Theses, Dissertations, and Student Research:
Department of Physics and Astronomy

Physics and Astronomy, Department of

Spring 4-2023

Diffractive Imaging of Laser Induced Molecular Reactions with Kiloelectron-Volt Ultrafast Electron Diffraction

Yanwei Xiong

University of Nebraska–Lincoln, ywxiong@huskers.unl.edu

Follow this and additional works at: https://digitalcommons.unl.edu/physicsdiss

Part of the Atomic, Molecular and Optical Physics Commons, Optics Commons, Physical Chemistry Commons, and the Quantum Physics Commons

DIFFRACTIVE IMAGING OF LASER INDUCED MOLECULAR REACTIONS WITH KILOELECTRON-VOLT ULTRAFAST ELECTRON DIFFRACTION

by

Yanwei Xiong

A DISSERTATION

Presented to the Faculty of

The Graduate College at the University of Nebraska

In Partial Fulfillment of Requirements

For the Degree of Doctor of Philosophy

Major: Physics and Astronomy

Under the Supervision of Professor Martin Centurion

Lincoln, Nebraska

April, 2023

DIFFRACTIVE IMAGING OF LASER INDUCED MOLECULAR REACTIONS WITH KILOELECTRON-VOLT ULTRAFAST ELECTRON DIFFRACTION

Yanwei Xiong, Ph.D

University of Nebraska, 2023

Advisor: Martin Centurion

Capturing the structural changes during a molecular reaction with ultrafast electron diffraction (UED) requires a high spatiotemporal resolution and sufficiently high signal-to-noise to record the signals with high fidelity. In this dissertation, I have focused on the development of a tabletop gas phase keV-UED setup with a femtosecond temporal resolution. A DC electron gun was employed to generate electron pulses with a high repetition rate of 5 kHz. The space charge effect in the electron pulse was ameliorated by compressing the 90 keV electron pulse longitudinally with a time varying electric field in an RF cavity. The velocity mismatch between electron and laser pulses was mitigated using a tilted laser pulse with an incident angle such that longitudinal component of the laser velocity is matched to the speed of electron pulse. The combination of these two techniques enabled the setup to reach a temporal resolution of 240 fs, more recently ~200 fs, and a timing drift of 50 fs rms over several hours. The UED was used to capture the laser induced alignment of linear and nonlinear molecules. The high beam current and femtosecond resolution allowed us to extract the molecular orientation distribution (MOD) of the molecular ensemble with high fidelity as it evolved from the prompt alignment to the past multiple revivals. To retrieve the MOD of nonlinear molecules, I developed a theory that

maps the MOD to the atom-pair angular distributions. The retrieval method does not require solving Schrödinger equation and works for any alignment methods. We also investigated ionization, fragmentation and isomerization of toluene generated by an IR strong laser field. Combined with the time-of-flight mass spectrometry, UED can determine the structure and yield of cations. A comparison of measurements to scattering calculations shows that scattering computation with independent atom model is inadequate to describe electron scattering from cations, and *ab-initio* calculation is required. Finally, the molecular photodissociation experiments with CF_3I and iodobenzene induced by a UV pulse were demonstrated with the keV-UED.

DEDICATION

To Haiyan Yu, my beloved wife,

and my children

Acknowledgement

I would like to express my deepest gratitude to everyone who helped and encouraged me throughout my Ph.D journey. I could not have undertaken this journey and made my research successful without the support, encouragement, and assistance from the extraordinary persons below, to whom I am forever indebted.

My research supervisor, professor Martin Centurion, for his consistent academic and personal support, and his commitment to excellent science throughout my entire Ph.D journey. Thank you for offering me the opportunity to develop my potential to be a physicist, which directed me to a better career and life. Your optimistic attitude, considerate thoughts, and patience always guided me to overcome academic challenges and inspired me to pursue high quality work throughout my research.

I am also grateful to my dissertation committee, professor Timothy J. Gay, professor Ilya Fabrikant, professor Xiaoshan Xu and professor Hui Li, for serving as the committee members, and presiding over my comprehensive exam and thesis defense. I express my special thanks to Dr. Timothy J. Gay and Dr. Ilya Fabrikant for reviewing my thesis and valuable comments.

My previous coworkers: Dr. Omid Zandi, Dr. Kyle J. Wilkin for their selfless instructions, kindness, and patience. They taught me numerous hands-on skills working in the lab without reservation, which is of importance for me to construct experiments independently. Their hard work is vital for the UED setup to be working successfully. Dr. João Pedro Figueira Nunes for his help in reviewing my paper and providing code for data analysis.

started to work in the department. Special thanks to Dallas Powell, Mark Gill, John Bruhl, and Joni Yang Bruhl for their enormous help and support over the years, who played significant roles to help me grow in faith and spirit.

My beloved wife, Haiyan Yu, for her unceasing love, support, and encouragement to make me confident and tenacious facing the challenges in work and life, and in pursuit of dreams. Her wisdom and faith motivated me to grow both spiritually and emotionally, and to be a man of principle and faith. Deep thanks to my parents, parents-in-law, sister, and brother-in-law for their consistent emotional and financial support throughout my entire collegiate career.

Contents

List of Figures

List of Tables

Chapter 1

Introduction to ultrafast electron diffraction

1.1 Introduction

Electron and X-ray diffraction are powerful techniques used to investigate the microscopic world on the atomic scale [1], and both have a similar history of development with respect to technology and theory. The X-ray diffraction technique has been used to determine the three-dimensional structures of samples, ranging from crystals, to DNA and complex proteins, with atomic resolution since the beginning of 20th century [2, 3]. These major advances have enabled us to obverse the static features or time-varying behaviors in molecules. Historically, the wave nature of electrons was first postulated by de Broglie in 1924, stating that all matter particles behave as waves and therefore can be diffracted [4]. The hypothesis was experimentally verified by the discovery of electron diffraction by Davisson and Germer using a crystal of nickel [5], and by Thomson and Reid using a thin film of celluloid [2, 6]. The discovery of electrons behaving as waves with wavelengths much shorter than the visible light opened up new opportunities to investigate the microscopic world of molecules where conventional microscopes were not able to. The first gas-phase electron diffraction (GED) was developed by Mark and Wierl to investigate the structure of CCl_4 in the 1930s [7]. Mourou and Williamson reported the first time-resolved electron diffraction experiment to probe a thin film of aluminum that demonstrates an electron pulse duration of 100 picoseconds (ps) generated by a streak camera in 1982 [8]. The first gas phase time-resolved electron diffraction experiments were conducted by synchronizing the electron pulses to either a microsecond laser pulse [9] or to a flash photolysis source [10] for the investigation of short-lived molecular species.

With the advent of femtosecond laser technology in the early 1990s, Zewail's group improved the temporal resolution of gas phase ultrafast electron diffraction (UED) into the picosecond regime [11-15], opening up new possibilities to study dynamics of molecules in real time. The pioneering works from Zewail's group achieved a series of groundbreaking UED results to capture the transient states of excited, isolated molecules with picosecond temporal resolutions. However, only slow immediate molecular states could be observed due to the limited temporal resolutions of their UED instrument. In these experiments, ultrafast laser pulses are used to both pump the sample and to produce the electron pulses to probe the sample. This idea has been considered as a standard methodology for the following development of UED setup.

In order to investigate atomic motion during a photoexcited chemical reaction, an overall temporal resolution of ~100 femtoseconds (fs) is required [16]. Recently a few techniques have been developed to achieve this goal, including compact setups [17, 18], relativistic electrons [19-21], electron pulse compression with radio-frequency (RF) fields [22, 23], tilted laser pulse [24, 25], *etc*. Gas phase UED experiments using megaelectron-volts (MeV) electron pulses have demonstrated a temporal resolution of 150 fs [19, 20, 26-28]. However, operating at the high energies requires a significantly larger infrastructure [26], and repetition rate and beam current are limited. For a sub-relativistic UED instrument, the RF compression technique has been developed to successfully compress electron pulses [22, 23, 29] to obtain an electron pulse duration of 150 fs [23]. The extra challenge of sub-relativistic, gas phase UED is that the velocity mismatch between the electron and laser pulses significantly deteriorates the overall temporal resolution [30]. The technique of tilted laser pulse has demonstrated the feasibility for compensating the velocity mismatch

in sub-relativistic electron diffraction [24, 25, 31, 32]. The combination of RF compression and tilted laser pulse techniques has allowed an overall temporal resolution of 240 fs for our sub-relativistic UED [32].

1.2 Motivations and thesis content

Recently, tremendous efforts have been devoted to improving the temporal resolution of gas phase UED instruments, mostly transitioning from kiloelectron-volt (keV) UED instruments [33-35] to relativistic MeV-UED [36-39]. However, these developments have not been able to increase the electron beam current significantly, which has been a limiting factor in gas phase UED experiments. The first application of a MeV-UED setup in a gas phase experiment has achieved a temporal resolution of 230 fs [19] and more recently 150 fs [40], compared to 240 fs for the gas phase keV-UED setup [32]. Low electron beam current has been the main limitation of gas phase MeV-UED, resulting in low signal levels and long acquisition times. Due to the presence of noise and timing instability that increases with time, low signal levels in many cases cannot be compensated by further increases the integration time. Furthermore, the limited beam time that is available to users has also been a major challenge, which has so far prevented systematic studies, i.e., exploring the wavelength dependence of the reaction dynamics and carrying out a set of experiments on similar molecules [32]. These systematic studies are essential to the understanding of the general mechanisms underlying photo-chemical reactions. One of the possible solutions is to develop a tabletop keV-UED setup with a higher electron beam current and a temporal resolution that is comparable to that of MeV-UED. Our first stage of experimentation has demonstrated a temporal resolution of 240 fs [32], more recently ~200 fs, for the gas phase keV-UED with an electron beam current that is more than an order of magnitude higher

than that obtained at MeV-UED facilities. The instrumental temporal resolution could be further improved by increasing the stability of the laser, RF system and tuning the parameters of the table-top setup.

The content of this thesis is organized as follows. In the chapter 1, I will give a brief introduction to ultrafast electron diffraction and the theory of electron scattering from a single molecule, including elastic and inelastic scattering, and then present the typical formulas for electron diffraction from a molecular ensemble and for molecular structure retrieval. In chapter 2, I demonstrate the electron pulse compression and tilted laser pulse techniques to improve the temporal resolution of the keV-UED. By combining these two techniques, the keV-UED has achieved a temporal resolution of 240 fs and a timing drift of 50 fs RMS for several hours, which is comparable to state-of-the-art facilities such as the MeV-UED setup at SLAC [32]. In chapter 3, I give a brief review of the theory of nonadiabatic alignment of molecules induced by an ultrafast laser pulse, and then demonstrate the theory to retrieve the molecular orientation distribution from atom-pair angular distributions. Also, I present in this chapter the theory to extract the angular distribution and internuclear distance of atom pairs with the UED measurement. In chapter 4, I show the rotational dynamics of impulsive molecular alignment, including linear and symmetric molecules, induced by a femtosecond laser pulse. Thanks to the high electron beam current, the keV-UED demonstrates the ability to capture a continuous temporal evolution of rotational dynamics of nitrogen with high fidelity and short acquisition times. We use the fast rotational dynamics of nitrogen to characterize the temporal resolution and timing drift of the setup. Also, we are able to retrieve the molecular orientation distribution for nonlinear molecules from experimentally measured atom-pair angular distributions,

which is demonstrated using rotational dynamics of trifluoro-iodomethane (CF₃I). In chapter 5, I demonstrate an ultrafast electron diffraction experiment from ions induced by a near infrared strong laser field. Combined with mass spectroscopy, UED can differentiate structures, including isomers, and determine the yield of products from ionization and fragmentation. In chapter 6, I demonstrate the preliminary experimental results of molecular dissociation dynamics induced by ultrafast UV pulses and captured by the keV-UED.

1.3 Principles of ultrafast electron diffraction

Electrons with wavelengths that are shorter than those of visible light can be easily obtained, allowing imaging devices with electrons to produce images with higher resolution than standard light microscopes. The first electron microscope was designed and built by Ernst Ruska in 1933 using a magnetic coil as a lens for electron beams [41]. The device provided a spatial resolution which far surpassed previous resolution capabilities and allowed scientists to observe things that cannot be seen with a light microscope [42]. Electrons behave as particles as well as waves due to the wave-particle duality. The wavelength of an electron is given by de Broglie's equation as

$$\lambda = \frac{h}{p}, \tag{1.1}$$

where h is Planck's constant, $p = \gamma m_e v$ is the electron momentum, $\gamma = 1/\sqrt{1 - v^2/c^2}$ is the Lorentz factor, m_e is the rest mass of an electron, v the velocity of the electron, and c the speed of light in vacuum. After being accelerated in an electric potential U, the total energy of the electron is given by

$$E = m_e c^2 + eU = \sqrt{p^2 c^2 + m_e^2 c^4}, \tag{1.2}$$

where e is the charge of an electron. Using the above two equations, the de Broglie wavelength is

$$\lambda = \frac{hc}{\sqrt{eU(2m_e c^2 + eU)}}. \tag{1.3}$$

For U=0.1 kV, the wavelength of electron λ= 1.2 Å, and for U=90 kV, λ= 3.9 picometers (pm).

Electron diffraction is a phenomenon resulting from the interaction between electrons and The potential of isolated molecules or atoms in crystalline materials, producing an interference pattern that characterizes the sample [43]. Unlike electron microscopy, UED instruments use coherent diffractive imaging (CDI), which is a lensless technique. The electrons scattered by the object generate a diffraction pattern which is recorded by a detector. The diffraction pattern is not a direct image of the object, but the information of the object is encoded in the pattern. We can use the classical Thomas Young's double slit experiment as an analogy to the electron diffraction experiment. The information, such as the wavelength of illuminating light, the width of the slits, and the distance between the slits are all encoded in the interference pattern. The width and distance can be successfully retrieved given the wavelength of the light. In a similar manner, electron diffraction patterns can be used to analyze objects which cause the diffraction. The advantage of CDI is that the diffraction pattern is aberration-free, and its spatial resolution is only determined by wavelength and electron beam quality, and not by the optics [44]. Thus, the CDI technique has been applied to probe ultrafast dynamics with high spatiotemporal resolutions [45].

Capturing the structural changes during a chemical reaction had been a challenge since it requires both a high spatiotemporal resolution on the order of sub-Angstroms and femtoseconds, and a sufficiently high signal-to-noise ratio to record the transient dynamics with high fidelity. Thanks to the advent of femtosecond laser technology, we are able to capture the ultrafast dynamics inside matter with experimental techniques, such as ultrafast X-ray diffraction and UED experiments, based on the combination of diffractive imaging and pump-probe spectroscopy. In the case of UED, a femtosecond laser pulse is split into two laser pulses, one of which is to excite the sample as a pump pulse, generating a non-equilibrium state, and the second one is used to first produce an electron pulse and then to probe the pump-induced changes in the sample. Each probe takes a snapshot of the transient state of the sample and the changes are measured as a function of time delays between the arrival time of the pump and probe pulses. When the overall temporal resolution is shorter than the intrinsic time scale of the change in the sample, the pump-induced dynamics can be captured accurately.

Recently, multiple experimental techniques have been developed to observe the change of molecular structures, such as Coulomb explosion imaging [46, 47], ultrafast X-ray diffraction [48-51], gas phase ultrafast electron diffraction (UED) [20, 21, 52-55], and laser-induced electron diffraction [56, 57]. The methods of diffractive imaging are directly sensitive to the spatial distribution of the constituent atoms of the molecule. In particular, UED has unique advantages compared to X-ray diffraction, as follows [2]. First, X-ray photons are scattered by the electron distribution through Thompson scattering, whereas UED electrons are scattered by both the nucleus and the electrons of the molecule through Coulombic interactions [2]. The cross section of electron scattering is about six orders of

magnitude stronger than that of X-ray scattering [34, 58], resulting in a much shorter exposure time for electron scattering. Second, electrons as a probe cause less damage to the sample being studied per useful scattering event. In each inelastic scattering event, the energy deposited to the sample using 1.5 Å X-ray photons is 400 times more than that of electrons, and the energy deposited in each useful elastic scattering event is 1000 times less for 80 to 500 keV electrons [2]. Third, due to the short penetration depth, electrons are suitable for experiments with gas phase targets, thin film samples, and surface characterization [2]. Fourth, tabletop UED instruments can be made through combination with ultrafast laser sources.

1.4 Theory of electron scattering

We start in this section with a description of elastic electron scattering from a potential with the first-Born approximation and briefly review the theory of correction of atomic form factors. We then show the total and inelastic scattering cross section from a single molecule in terms of charge density (or wave functions) by using the scattering matrix and the Morse approximation. Lastly, we show the analytic formalism of diffraction from a molecular ensemble, based on independent atom model, and the theory of retrieving the structural parameters.

1.4.1 Elastic scattering from a potential

The interaction between the probe electrons and the object of interest is through Coulomb interaction. Here, we give a brief review of the theory of electrons scattered elastically by a potential. *The following derivation follows the descriptions in ref.* [43, 59-62]. For an incident electron accelerated to 90 keV, the speed of the electron is ~0.53 c. Thus, the

potential of the scatterers, i.e., the atoms, appear to be frozen in time during the scattering event for one electron. Therefore, the wavefunction of the scattered electron can be described by the solution of the time-independent Schrödinger equation:

$$\left[-\frac{\hbar^2}{2m_e}\nabla^2 + V(\mathbf{r})\right]\psi(\mathbf{r}) = E\,\psi(\mathbf{r}), \tag{1.4}$$

where E is the energy of the electron, which is determined by the voltage used to accelerate the electron and is constant before and after the scattering. The potential energy $V(\mathbf{r})$ is due to Coulomb interaction of the fast electron and the object, such as an isolated molecule or atoms in crystals. The equation can be written in the form of the Helmholtz equation:

$$(\nabla^2 + k^2)\psi(\mathbf{r}) = \frac{2m_e}{\hbar^2}V(\mathbf{r})\,\psi(\mathbf{r}), \tag{1.5}$$

where $k^2 = \frac{2m_e}{\hbar^2}E = \frac{4\pi^2}{\lambda^2}$. Figure 1.1 shows the diagram of the electron scattered by the sample. The wavevector of the incident electron $\mathbf{k}_0$ is along the z axis, and the wavevector of the scattered wave is $\mathbf{k}$. By using the Green's function method, $\psi(\mathbf{r})$ can be written in this form [63, 64]:

$$\psi(\mathbf{r}) = \psi_0(\mathbf{r}) - \frac{m_e}{2\pi\hbar^2}\int \frac{\exp\left(ik|\mathbf{r}-\mathbf{r}'|\right)}{|\mathbf{r}-\mathbf{r}'|}V(\mathbf{r}')\,\psi(\mathbf{r}')\,d\tau', \tag{1.6}$$

where $\psi_0(\mathbf{r}) = \exp(i\mathbf{k}_0\mathbf{r})$ is the general solution (1.5) when $V(\mathbf{r}) = 0$ and describes the wavefunction of the incoming beam before scattering. The integrand is the scattering wavelet at $\mathbf{r}$, which is scattered by the infinitesimal volume $d\tau'$ of sample at $\mathbf{r}'$, and the integral is the summation of the wavelets scattered by all the sample [60]. However, equation (1.6) shows that the source for $\psi(\mathbf{r})$ is $\psi(\mathbf{r})$ itself. Thus, eqn. (1.6) is really not a solution, but an integral equation for $\psi(\mathbf{r})$. The advantage of converting the differential

equation to an integral form is that we can do a perturbative expansion for $\psi(\boldsymbol{r})$ by means of a series of iterative approximations, known as the Born series [59]. The zeroth order solution is $\psi_0(\boldsymbol{r})$, and the first order solution is obtained by inserting $\psi(\boldsymbol{r}') = \psi_0(\boldsymbol{r})$ into the integral. Continuing in this way, we can calculate $\psi(\boldsymbol{r})$ to any desired order.
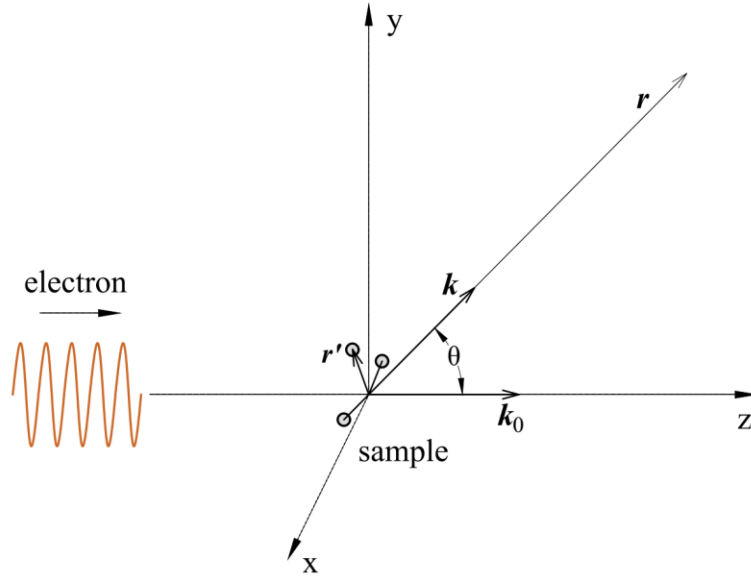
Figure 1.1: Diagram of electron scattering. The wavevector of the incident electron $\boldsymbol{k}_0$ is along the z axis, and the wavevector of the scattered wave is $\boldsymbol{k}$. The polar angle of $\boldsymbol{r}$ is θ, and its azimuthal angle is ϕ (not shown in the diagram). The point of observation is at a distance far away from the sample, $r \gg r'$.

The distance between the point of observation and sample is always much larger than the dimension of the scatterers in the sample, $r \gg r'$. Thus, $|\boldsymbol{r} - \boldsymbol{r}'|$ can be approximated by $|\boldsymbol{r} - \boldsymbol{r}'| \cong r\left(1 - \frac{\boldsymbol{r}\cdot\boldsymbol{r}'}{r^2}\right)$, which is called the far-zone approximation. Therefore, the asymptotic form of the wavefunction is given by

$$\frac{\exp(ik|\boldsymbol{r}-\boldsymbol{r}'|)}{|\boldsymbol{r}-\boldsymbol{r}'|} \cong \frac{\exp(ikr)}{r}\exp[-ik(\boldsymbol{r}/r)\cdot\boldsymbol{r}'], \tag{1.7}$$

where $k(\mathbf{r}/r) = \mathbf{k}$, and, for $r \to \infty$, (1.6) obtains the asymptotic form:

$$\psi(\mathbf{r}) \cong \exp(i\mathbf{k}_0\mathbf{r}) + f(\theta,\phi)\frac{\exp(ikr)}{r} \tag{1.8}$$

and

$$f(\theta,\phi) = -\frac{m_e}{2\pi\hbar^2}\int \exp(-i\mathbf{k}\cdot\mathbf{r}')V(\mathbf{r}')\,\psi(\mathbf{r}')\,d\tau', \tag{1.9}$$

where $f(\theta,\phi)$ is called the scattering amplitude, or atomic form factor when the wave is scattered by an isolated atom. Here we use the first Born approximation to evaluate $f(\theta,\phi)$ by replacing $\psi(\mathbf{r}')$ by $\exp(i\mathbf{k}_0\mathbf{r}')$. The wavefunction $\psi(\mathbf{r})$ consists of two parts: the incident wave $\exp(i\mathbf{k}_0\mathbf{r})$ and the scattered wave $f(\theta,\phi)\frac{\exp(ikr)}{r}$. The approximation neglects the scattered wave, which is equivalent to saying that the amplitude of the scattered wave is much smaller than that of the incident wave, and in particular, no phase shift occurs in the scattering process [60]. The first Born approximation provides a good approximation when the potential energy $eV(\mathbf{r})$ is much smaller than the kinetic energy of the incident electron such that the scattered wavefunction is only slightly different from the incident wavefunction. Under the first Born approximation, the scattering amplitude is the Fourier transform of the potential with respect to the variable $\mathbf{s} = \mathbf{k} - \mathbf{k}_0$ [65]. We can write the scattering amplitude as $f(\theta,\phi) = f(\mathbf{s})$, where

$$f(\mathbf{s}) = -\frac{m_e}{2\pi\hbar^2}\int V(\mathbf{r}')\exp(-i\mathbf{s}\cdot\mathbf{r}')\,d\tau' \tag{1.10}$$

and $\mathbf{s} = \mathbf{k} - \mathbf{k}_0$ is called the momentum transfer with $s = 2k\sin\frac{\theta}{2}$. The criterion of the validity of the first Born approximation is that modulus of the 2nd term is far smaller than the 1st term in (1.6). In electron diffraction experiments, the incident electron beam is blocked by a beam stop, and the scattering signal is collected by a detector. The differential cross section is related to the scattering amplitude by

$$\frac{d\sigma}{d\Omega} = |f(\theta, \phi)|^2. \tag{1.11}$$

Here, we derive the electron diffraction from an isolated molecule using the independent atom model (IAM). Under the IAM approximation, the bonding is neglected, and the potential of the molecule can be written as $V(\mathbf{r}') = \sum_n V_n (\mathbf{r}' - \mathbf{r}_n)$, where $V_n(\mathbf{r}' - \mathbf{r}_n)$ is the potential of the nth atom in the molecule, and the coordinate of its nucleus is $\mathbf{r}_n$. The scattering amplitude of the molecule is given by

$$f(\mathbf{s}) = \sum_n f_n(\mathbf{s}) \exp(-i\mathbf{s} \cdot \mathbf{r}_n), \tag{1.12}$$

where

$$f_n(\mathbf{s}) = -\frac{m_e}{2\pi\hbar^2} \int V_n(\mathbf{x}) \exp(-i\mathbf{s} \cdot \mathbf{x}) \, d\tau \tag{1.13}$$

and $f_n(\mathbf{s})$ is the scattering amplitude of nth atom in the molecule. The analytical form of $f_n(\mathbf{s})$ is given by (16) in ref. [60], which is a real function under the assumption of a spherically symmetric potential. The differential cross section is

$$\frac{d\sigma}{d\Omega} = |\sum_n f_n(\theta) e^{-i\mathbf{s} \cdot \mathbf{r}_n}|^2 = \sum_{m,n} f_m^*(\theta) f_n(\theta) e^{i\mathbf{s} \cdot \mathbf{r}_{mn}}, \tag{1.14}$$

where $\mathbf{r}_{mn}$ is the vector pointing from the nth atom to the mth atom. In the 1930s, the first Born approximation was shown to be sufficient to explain the electron diffraction results for a number of compounds using electronic kinetical energy around 10 keV or higher [60, 66]. In 1950s, Schomaker and Glauber showed that, for gas molecules consisting of heavy and light atoms, such as uranium hexafluoride, the first Born approximation was inadequate for describing the electron diffraction results, and the existence of the phase shift in the atomic scattering factor was suggested to address this issue [66]. The details are given in ref. [43, 62]. In the correction, the scattered wave from a molecule is still represented by a superposition of $f_j(\mathbf{k}, \mathbf{k}_0) \frac{\exp(ikr)}{r}$ scattered by the atoms from k_0 to $\mathbf{k}$;

however, the atomic form factors $f_j(\boldsymbol{k}, \boldsymbol{k}_0)$ for individual atoms are complex functions, $|f|e^{i\eta}$, of the scattering angle for a given kinetic energy of the electron. In particular, the difference between screened and unscreened scattering, corresponding to small and large angle diffraction, respectively, is of importance for the phase of the scattering amplitude. The principal term in the phase for an unscreened field is given by $\frac{Ze^2}{\hbar v}\log[kr(1-\cos\theta)]$, where v is the speed of the electron and r is the distance between electron and scatterer [63]. The imaginary part of $f(\boldsymbol{k}, \boldsymbol{k}_0)$, in the screened Coulomb fields, is related to the form factor by [43]

$$\text{Im}[f(\boldsymbol{k}, \boldsymbol{k}_0)] = \frac{k}{4\pi}\int f^*(\boldsymbol{k}, \boldsymbol{k}')\, f(\boldsymbol{k}', \boldsymbol{k})d\Omega_{\text{k}'}. \tag{1.15}$$

The phase in the screened case can be estimated by using the first Born approximation scattering amplitude $f_{\text{B}}(\boldsymbol{k}, \boldsymbol{k}')$, formulated as

$$\eta(\boldsymbol{k}, \boldsymbol{k}_0) = \frac{k}{4\pi f_{\text{B}}(\boldsymbol{k}, \boldsymbol{k}_0)}\int f_{\text{B}}(\boldsymbol{k}, \boldsymbol{k}')\, f_{\text{B}}(\boldsymbol{k}', \boldsymbol{k})d\Omega_{\text{k}'}. \tag{1.16}$$

The phase shift provides a few percent correction for atomic scattering factors at high values of momentum transfer s using electron kinetic energy in the keV range, and the correction is smaller for small s values or higher energy electrons, such as in the MeV range [66]. The IAM diffraction formula (1.14), using complex atomic scattering factors, has so far been found to be sufficiently accurate to describe electron diffraction from gas molecules in electronic ground states. In Table 4.3.3.1 from ref. [67], the complex atomic scattering factors of elements from H (Z=1) to U (Z=92) are calculated using the partial wave method based on relativistic Hartree-Fock fields [68] at a number of kinetic energies in the keV range.

1.4.2 Scattering amplitude of an isolated molecule

Recent UED experiments show that *ab initio* computation is needed for the analysis of electron diffraction from molecules in electronic excited states [52] and ions [69] since IAM simulations are inadequate for describing the UED signal, especially in the low *s* range. In *ab initio* computation, electronic wavefunctions (or charge density) of the molecules are used to obtain the molecular scattering amplitude instead of the potential $V(\boldsymbol{r})$. In this section, we derive the relation between the scattering amplitude and the charge density. *The following derivation follows the descriptions in ref.* [59, 61, 70-72]. The first Born approximation scattering amplitude (1.10) can be written as the scattering matrix (S-matrix) element using Fermi's Golden rule:

$$f(\boldsymbol{s}) = \frac{-m_e}{2\pi\hbar^2}\langle \boldsymbol{k}|V|\boldsymbol{k}_0\rangle. \tag{1.17}$$

The first Born approximation result agrees with scattering amplitude obtained by evaluating the S-matrix to the first order, considering $V(\boldsymbol{r})$ as a perturbation [59, 61]. Let's consider the sample to be an isolated molecule. The operator of Coulombic interaction between the scattered electron and the molecule is given by

$$\hat{V} = \frac{-e^2}{4\pi\varepsilon_0}\sum_{n=1}^{N}\left(\frac{Z_n}{R_{ns}} - \sum_{i=1}^{Z_n}\frac{1}{r_{is}}\right), \tag{1.18}$$

where Z_n is the charge number of the nth nucleus, R_{ns} is the distance between the *n*th nucleus and the scattered electron, and r_{is} is the distance of the ith electron of the molecule and the scattered electron. To calculate the potential, consideration must be given to the question of what role the nuclear wavefunctions play in the scattering process [73]. The answer has been given in [71] that the nuclear separation is instantaneously unaltered in

the scattering process according to the Franck-Condon principle. Therefore, the positions of the nuclei are fixed in space in the view of the fast electron. The potential can be evaluated by $V = \langle \emptyset_0 | \hat{V} | \emptyset_0 \rangle$, where $\emptyset_0$ is the electronic wavefunction of the molecule in the ground state. In elastic scattering, the scattering amplitude is given by

$$f(s) = \frac{-m_e}{2\pi\hbar^2} \langle k\emptyset_0 | \hat{V} | k_0 \emptyset_0 \rangle. \tag{1.19}$$

Evaluation of $f(s)$ comes down to the calculation of the matrix element, given by

$$\langle k\emptyset_0 | \hat{V} | k_0 \emptyset_0 \rangle = \int e^{-is \cdot r'} d\tau' \int \emptyset_0^*(r_1, r_2, \dots) \hat{V} \emptyset_0(r_1, r_2, \dots) d\tau_1 d\tau_2 \dots, \tag{1.20}$$

where r' is the coordinates of the scattered electron (r' is replaced by r_s in the following text for convenience), r_i is the coordinate of the ith electron in the molecule, and the integral is over the coordinates of all the electrons. Alternatively, we can calculate the scattering operator first, which is defined as [70, 71]

$$\hat{V}_1 = \langle k | \hat{V} | k_0 \rangle = \frac{-e^2}{4\pi\varepsilon_0} \int \sum_{n=1}^{N} \left(\frac{Z_n}{R_{ns}} - \sum_{i=1}^{Z_n} \frac{1}{r_{is}} \right) e^{-is \cdot r_s} d\tau_s. \tag{1.21}$$

The integral can be evaluated by using the transformation of coordinates $r_s = R_n + R_{ns}$ for the term consists of $\frac{Z_n}{R_{ns}}$, where R_n is the coordinates of the nth nuclei, R_{ns} is the vector pointing from the nuclei to the scattered electron, and $r_s = r_i + r_{is}$ for $\frac{1}{r_{is}}$. The Jacobians of the two coordinate transformations, $(r_s, r_i) \rightarrow (R_{ns}, r_i)$ and $(r_s, r_i) \rightarrow (r_{is}, r_i)$, are unity, so

$$\int \frac{Z_n}{R_{ns}} e^{-isr_s} d\tau_s = e^{-is \cdot R_n} \int \frac{Z_n}{R_{ns}} e^{-is \cdot R_{ns}} d\tau_{ns} \tag{1.22}$$

and $$\int \frac{1}{r_{is}} e^{-isr_s} d\tau_s = e^{-is \cdot r_i} \int \frac{1}{r_{is}} e^{-is \cdot r_{is}} d\tau_{is}. \tag{1.23}$$

Using the Yukawa potential, the integral is $\int \frac{1}{r_{is}} e^{-is \cdot r_{is}} d\tau_{is} = \frac{4\pi}{s^2}$. Thus, (1.21) and (1.20)

become [70, 71, 74]

$$\hat{V}_1 = \frac{-e^2}{\varepsilon_0 s^2} \sum_{n=1}^{N} (Z_n e^{-is \cdot R_n} - \sum_{i=1}^{Z_n} e^{-is \cdot r_i}) \tag{1.24}$$

and $$\langle k\emptyset_0 | \hat{V} | k_0 \emptyset_0 \rangle = \frac{-e^2}{\varepsilon_0 s^2} \left(\sum_n Z_n e^{-is \cdot R_n} - \sum_i \langle \emptyset_0 | e^{-is \cdot r_i} | \emptyset_0 \rangle \right), \tag{1.25}$$

where n indicates the nth nuclei, and i indicates the ith electron. The integral of the electron

part is [72]

$$\sum_i \langle \emptyset_0 | e^{-is \cdot r_i} | \emptyset_0 \rangle = \sum_i \int |\emptyset_0|^2 \, e^{-is \cdot r_i} d\tau_1 d\tau_2 \dots = \sum_i \int |\varphi(r_i)|^2 \, e^{-is \cdot r_i} d\tau_i =$$

$$\sum_i \int |\varphi_i(r)|^2 \, e^{-is \cdot r} d\tau = \int \rho_{el}(r) \, e^{-is \cdot r} d\tau \,, \tag{1.26}$$

where $|\emptyset_0|^2$ is the probability of finding the 1st, 2nd, …, ith, … electron in the unit volume

at $r_1, r_2, \dots r_i, , \dots$, and $|\varphi(r_i)|^2$ is the probability of finding the ith electron in a unit

volume at r_i, which can be written in an alternative way by labeling the wavefunction

$|\varphi_i(r)|^2$ for the ith electron [72]. The electron charge density $\rho_{el}(r) = \sum_i |\varphi_i(r)|^2$ is the

total charge density contributed from all the electrons in the molecule [72]. We can define

the charge density contributed from the nucleus as $\rho_{nc}(r) = \sum_n Z_n \delta(r - R_n)$, and

$\sum_n Z_n e^{-is \cdot R_n} = \int \rho_{nc}(r) \, e^{-is \cdot r} d\tau$. Therefore, the matrix element in SI units, which has

been shown in ref. [52, 66, 70, 72], is

$$\langle k\emptyset_0 | \hat{V} | k_0 \emptyset_0 \rangle = \frac{-e^2}{\varepsilon_0 s^2} \int [\rho_{nc}(r) - \rho_{el}(r)] e^{-is \cdot r} d\tau = \frac{-e^2}{\varepsilon_0 s^2} \int \rho_t(r) \, e^{-is \cdot r} d\tau, \tag{1.27}$$

where $\rho_t(r)$ is the total charge density from both the nuclei and electrons. Equation (1.27)

is a general form of electron scattering, which could be useful for systems other than a

molecule, such as ions.

Using the independent atom approximation (IAM), (1.27) can be converted to the commonly used IAM electron diffraction formula. The total charge density can be written as

$$\rho_t(\vec{r}) = \sum_n [\rho_{nc,n}(r - r_n) - \rho_{el,n}(r - r_n)],\tag{1.28}$$

where $\rho_{nc,n}(r - r_n)$ and $\rho_{el,n}(r - r_n)$ are the charge density of the nucleus and of electrons in the atom marked as n, and r_n is the coordinates of the nuclei of the atom. Here, $\rho_{nc,n}(r - r_n) = Z_n \delta(r - r_n)$ yields

$$\int \rho_t(r)\, e^{-is \cdot r} d\tau = \sum_n e^{-is \cdot r_n} \left[Z_n - \int \rho_{el,n}(x)\, e^{-is \cdot x} d\tau \right].\tag{1.29}$$

Here we show that the part in the bracket is the atomic form factor. $s \cdot x = 2k \sin\left(\frac{\theta}{2}\right) x \cos\alpha$, where α is the angle between s and x. The charge density contributed from the electrons in an atom is spherically symmetric, $\rho_{el,n}(x) = \rho_{el,n}(x)$, so [60]

$$\int \rho_{el,n}(x)\, e^{-is \cdot x} d\tau = \int_0^{2\pi} d\beta \int_0^{\pi} \sin\alpha\, d\alpha \int_0^{+\infty} \rho_{el,n}(x) e^{-isx\cos\alpha}\, x^2\, dx$$

$$= 2\pi \int_0^{+\infty} \rho_{el,n}(x) x^2\, dx \int_{-1}^{1} e^{-isx\cos\alpha}\, d(\cos\alpha) = 4\pi \int_0^{+\infty} \rho_{el,n}(x) \frac{\sin sx}{sx} x^2\, dx = F_n(\theta).\tag{1.30}$$

Therefore, the scattering amplitude is

$$f(s) = \frac{m_e e^2}{2\pi\varepsilon_0\hbar^2} \frac{1}{s^2} \int \rho_t(r)\, e^{-is \cdot r} d\tau = \frac{m_e e^2}{2\pi\varepsilon_0\hbar^2} \sum_n e^{-is \cdot r_n} \frac{[Z_n - F_n(\theta)]}{s^2} = \sum_n f_n(\theta) e^{-is \cdot r_n}\tag{1.31}$$

where $f_n(\theta) = \frac{m_e e^2}{2\pi\varepsilon_0\hbar^2} \frac{[Z_n - F_n(\theta)]}{s^2}$ is the famous Mott-Bethe formula [74, 75] that describes the atomic form factor of the nth atom in the molecule. The differential cross section gives the same result as eqn. (1.14).

1.4.3 Separation of core electrons and valence electrons

The *ab initio* computation using (1.27) is time consuming when the number of atoms in the molecule is large. The electrons in an atom can be classified as core electrons and valence electrons according to the orbitals that electrons occupy. The valence electrons that participate in the chemical bonds have a diffuse nature across the molecule. A possible approximation that could improve the IAM and save time for complex molecules is to treat the core electrons and valence electrons separately. The total charge density can be written as

$$\rho_t(\boldsymbol{r}) = \sum_n [Z_n \delta(\boldsymbol{r} - \boldsymbol{r}_n) - \rho_{el,n}^C(\boldsymbol{r} - \boldsymbol{r}_n)] - \rho_{el}^V(\boldsymbol{r}), \qquad (1.32)$$

where $\rho_{el,n}^C(\boldsymbol{r} - \boldsymbol{r}_n)$ is the charge density of core electrons in the nth atom, and $\rho_{el}^V(\boldsymbol{r})$ is the charge density of valence electrons in the molecule. Following the same process shown from (1.28) to (1.31), the scattering amplitude is

$$\frac{1}{s^2} \int \rho_t(\boldsymbol{r}) e^{-i\boldsymbol{s}\cdot\boldsymbol{r}} d\tau = \sum_n f_n^C(\theta) e^{-i\boldsymbol{s}\boldsymbol{r}_n} - f^V(\theta), \qquad (1.33)$$

where $f_n^C(\theta) = \frac{Z_n - F_n^C(\theta)}{s^2}$ is the atomic form factor of the nth ion that consists of the nucleus and the core electrons, and $f^V(\theta) = \frac{1}{s^2} \int \rho_{el}^V(\boldsymbol{r}) e^{-i\boldsymbol{s}\boldsymbol{r}} d\tau$ is the Fourier transform of charge density of valence electrons in the molecule, multiplied by $\frac{1}{s^2}$.

1.4.4 Inelastic electron scattering

The S-matrix element for the system with a transition from the initial state $|\boldsymbol{k}_0 \emptyset_0\rangle$ to final state $|\boldsymbol{k}\emptyset_\nu\rangle$ in the first Born approximation is given by $\langle \boldsymbol{k}\emptyset_\nu | \hat{V} | \boldsymbol{k}_0\emptyset_0 \rangle$, where $\nu \neq 0$ is corresponding to inelastic scattering process, $\emptyset_\nu$ is the excited state of the molecule, and

$\nu = 0$ represents elastic scattering. *The following derivation follows the description in ref.* [59, 61, 70, 72, 76]. In the scattering process, the momentum of the incident electron is far larger than that of the electrons in the molecule, leaving out the possibility that the incident electron changes places with the electrons of the molecule [59]. We evaluate the total scattering using the Morse approximation [67, 76], which is based on the three assumptions as follows: 1) all the molecular states are accessible since the energy of the incident electron is high, 2) the ratio $k/k_0 \cong 1$ for all inelastic scattering processes, and 3) momentum transfer of inelastically scattered electrons may be replaced by elastic momentum transfer. With these approximations, the differential cross section of the total scattering is

$$\frac{d\sigma}{d\Omega}\Big|_{\text{tot}} = \left(\frac{m_e}{2\pi\hbar^2}\right)^2 \sum_\nu |\langle k\emptyset_\nu|\hat{V}|k_0\emptyset_0\rangle|^2 = \left(\frac{m_e}{2\pi\hbar^2}\right)^2 \sum_\nu |\langle \emptyset_\nu|\hat{V}_1|\emptyset_0\rangle|^2$$

$$= \left(\frac{m_e}{2\pi\hbar^2}\right)^2 \sum_\nu \langle \emptyset_0|\hat{V}_1^*|\emptyset_\nu\rangle\langle \emptyset_\nu|\hat{V}_1|\emptyset_0\rangle = \left(\frac{m_e}{2\pi\hbar^2}\right)^2 \langle \emptyset_0|\hat{V}_1^*\hat{V}_1|\emptyset_0\rangle, \qquad (1.34)$$

where is the $\hat{V}_1 = \frac{-e^2}{\varepsilon_0 s^2}\left(\sum_n Z_n e^{-is\cdot R_n} - \sum_j e^{-is\cdot r_j}\right)$, and the first summation is over all the nuclei indicated by n and the second summation is over all the electrons indicated by j. The enclosure property is used to obtain (1.34). The operator $\hat{V}_1^*\hat{V}_1$ is given by

$$\hat{V}_1^*\hat{V}_1 = \frac{e^4}{\varepsilon_0^2 s^4}\left[\sum_{m,n} Z_m Z_n e^{is\cdot R_{mn}} - 2\sum_{j,n} Z_n \cos(s\cdot r_j - s\cdot R_n) + \sum_{j,k} e^{is\cdot r_{jk}}\right], \quad (1.35)$$

where m and n are the indices of nuclei, j and k are the indices for the electrons, and $R_{mn} = R_m - R_n$, $r_{jk} = r_j - r_k$. The differential cross section for the total scattering is written as

$$\frac{d\sigma}{d\Omega}\Big|_{\text{tot}} = \left(\frac{m_e}{2\pi\hbar^2}\right)^2 \frac{e^4}{\varepsilon_0^2 s^4}\left[\sum_{m,n} Z_m Z_n e^{is\cdot R_{mn}} - 2\sum_{j,n} Z_n\langle \emptyset_0|\cos(s\cdot r_j - s\cdot R_n)|\emptyset_0\rangle + \sum_{j,k}\langle \emptyset_0|e^{is\cdot r_{jk}}|\emptyset_0\rangle\right].$$

$$(1.36)$$

The terms are evaluated below. The 2nd term is given by

$$\sum_{j,n} Z_n \langle \emptyset_0 | \cos(\mathbf{s} \cdot \mathbf{r}_j - \mathbf{s} \cdot \mathbf{R}_n) | \emptyset_0 \rangle = \sum_n Z_n \sum_j \int |\emptyset_0(\mathbf{r}_1, \mathbf{r}_2, \dots)|^2 \cos(\mathbf{s} \cdot \mathbf{r}_j - \mathbf{s} \cdot \mathbf{R}_n) \, d\tau_1 d\tau_2 \dots$$

$$= \sum_n Z_n \sum_j \int |\varphi(\mathbf{r}_j)|^2 \cos(\mathbf{s} \cdot \mathbf{r}_j - \mathbf{s} \cdot \mathbf{R}_n) \, d\tau_j$$

$$= \sum_n Z_n \int \sum_j |\varphi_j(\mathbf{r})|^2 \cos(\mathbf{s} \cdot \mathbf{r} - \mathbf{s} \cdot \mathbf{R}_n) \, d\tau$$

$$= \sum_n Z_n \int \rho_{el}(\mathbf{r}) \cos(\mathbf{s} \cdot \mathbf{r} - \mathbf{s} \cdot \mathbf{R}_n) \, d\tau,$$

where $\rho_{el}(\mathbf{r})$ is the electron charge density of the molecule, s is the momentum transfer of the incident electron, and $\mathbf{R}_n$ are the coordinates of the nth nuclei which are fixed in space. The third term is given by

$$\sum_{j,k} \langle \emptyset_0 | e^{i\mathbf{s} \cdot \mathbf{r}_{jk}} | \emptyset_0 \rangle = \sum_{j,k} \int \emptyset_0^*(\mathbf{r}_1, \mathbf{r}_2, \dots) \, \emptyset_0(\mathbf{r}_1, \mathbf{r}_2, \dots) e^{i\mathbf{s} \cdot (\mathbf{r}_j - \mathbf{r}_k)} d\tau_1 d\tau_2 \dots$$

$$= N_e + \sum_{j \neq k} \int \emptyset_0^*(\mathbf{r}_1, \mathbf{r}_2, \dots) \emptyset_0(\mathbf{r}_1, \mathbf{r}_2, \dots) e^{i\mathbf{s} \cdot (\mathbf{r}_j - \mathbf{r}_k)} d\tau_1 d\tau_2 \dots$$

$$= N_e + \sum_{j \neq k} \int P(\mathbf{r}_j, \mathbf{r}_k) e^{i\mathbf{s} \cdot (\mathbf{r}_j - \mathbf{r}_k)} d\tau_j d\tau_k$$

$$= N_e + \int \sum_{j \neq k} P_{j,k}(\mathbf{r}, \mathbf{r}') e^{i\mathbf{s} \cdot (\mathbf{r} - \mathbf{r}')} d\tau d\tau'$$

$$= N_e + \int \rho_{el}(\mathbf{r}, \mathbf{r}') e^{i\mathbf{s} \cdot (\mathbf{r} - \mathbf{r}')} d\tau d\tau',$$

where N_e is the number of electrons in the molecule, $P(\mathbf{r}_j, \mathbf{r}_k)$ is the probability density of finding the jth electron at $\mathbf{r}_j$ and the kth electron at $\mathbf{r}_k$, and the two-electron density is $\rho_{el}(\mathbf{r}, \mathbf{r}') = \sum_{j \neq k} P_{j,k}(\mathbf{r}, \mathbf{r}')$. Therefore, the total scattering is given by

$$\frac{d\sigma}{d\Omega}_{tot} = \left(\frac{m_e}{2\pi\hbar^2}\right)^2 \frac{e^4}{\varepsilon_0^2 s^4} \left[\sum_{m,n} Z_m Z_n e^{i\mathbf{s} \cdot \mathbf{R}_{mn}} - 2 \sum_n Z_n \int \rho_{el}(\mathbf{r}) \cos(\mathbf{s} \cdot \mathbf{r} - \mathbf{s} \cdot \mathbf{R}_n) \, d\tau + \right.$$

$$\left. N_e + \int \rho_{el}(\mathbf{r}, \mathbf{r}') e^{i\mathbf{s} \cdot (\mathbf{r} - \mathbf{r}')} d\tau d\tau' \right].$$

The differential cross section of the elastic scattering is given by

$$\frac{d\sigma}{d\Omega}_{\text{ela}} = \left(\frac{m_e}{2\pi\hbar^2}\right)^2 |\langle \mathbf{k}\emptyset_0|\hat{V}|\mathbf{k}_0\emptyset_0\rangle|^2$$

$$= \left(\frac{m_e}{2\pi\hbar^2}\right)^2 \frac{e^4}{\varepsilon_0^2 s^4}\left[\sum_{m,n} Z_m Z_n e^{i\mathbf{s}\cdot\mathbf{R}_{mn}} - 2\sum_n Z_n \int \rho_{\text{el}}(\mathbf{r})\cos(\mathbf{s}\cdot\mathbf{r} - \mathbf{s}\cdot\mathbf{R}_n)\,d\tau + \left|\int \rho_{\text{el}}(\mathbf{r})\,e^{-i\mathbf{s}\cdot\mathbf{r}}d\tau\right|^2\right].$$

The inelastic scattering differential cross section is given by [52, 66, 72]

$$\frac{d\sigma}{d\Omega}_{\text{ine}} = \frac{d\sigma}{d\Omega}_{\text{tot}} - \frac{d\sigma}{d\Omega}_{\text{ela}}$$

$$= \left(\frac{m_e}{2\pi\hbar^2}\right)^2 \frac{e^4}{\varepsilon_0^2 s^4}\left[N_e + \int \rho_{\text{el}}(\mathbf{r},\mathbf{r}')e^{i\mathbf{s}\cdot(\mathbf{r}-\mathbf{r}')}d\tau d\tau' - \left|\int \rho_{\text{el}}(\mathbf{r})\,e^{-i\mathbf{s}\cdot\mathbf{r}}d\tau\right|^2\right]. \quad (1.37)$$

If the scatterer is an atom, instead of a molecule, the equations reduce to total inelastic scattering factors for individual atoms developed by Bethe [74], Heisenberg [77], and Morse [76], demonstrated below. The wavefunction of the target can be represented as a Slater determinant, and both spatial and spin coordinates are taken into account:

$$\emptyset_0(\mathbf{r}_1,\mathbf{r}_2,\dots) = \frac{1}{\sqrt{N_e!}}\det\{\phi_1\phi_2\dots\phi_{N_e}\} = \frac{1}{\sqrt{N_e!}}[\phi_a(\mathbf{r}_b)], \qquad a,b = 1,2,\dots,N_e,$$

where different ϕ's are orthogonal. Thus, the third term of eqn. (1.37) is given by

$$\frac{d\sigma}{d\Omega}_{\text{tot}} = \left(\frac{m_e}{2\pi\hbar^2}\right)^2 \frac{e^4}{\varepsilon_0^2 s^4}\left[Z^2 - 2Z\sum_j\langle\emptyset_0|\cos(\mathbf{s}\cdot\mathbf{r}_j)|\emptyset_0\rangle + \sum_{j,k}\langle\emptyset_0|e^{i\mathbf{s}\cdot\mathbf{r}_{jk}}|\emptyset_0\rangle\right]$$

$$= \left(\frac{m_e}{2\pi\hbar^2}\right)^2 \frac{e^4}{\varepsilon_0^2 s^4}\left[Z^2 - 2Z\int \rho_{\text{el}}(\mathbf{r})\cos(\mathbf{s}\cdot\mathbf{r})\,d\tau + Z + \int \rho_{\text{el}}(\mathbf{r},\mathbf{r}')e^{i\mathbf{s}\cdot(\mathbf{r}-\mathbf{r}')}d\tau d\tau'\right]$$

$$= \left(\frac{m_e}{2\pi\hbar^2}\right)^2 \frac{e^4}{\varepsilon_0^2 s^4}[Z^2 - 2Z^2 F(\mathbf{s}) + S], \qquad (1.38)$$

where the origin of the coordinate is at the nuclei, the function $F(\mathbf{s})$ is the X-ray form factor, and Z stands for the number of electrons and the number of charges in the nuclei. For a spherically symmetric electron charge density, $F(\mathbf{s})$ is given by [60, 76]

$$F(s) = \frac{1}{Z} \int \rho_{el}(r) \exp(is \cdot r) \, d\tau = \frac{4\pi}{Z} \int_0^\infty \rho_{el}(r) \frac{\sin sr}{sr} r^2 dr. \tag{1.39}$$

The third term is given by

$$S = \sum_{j,k} \langle \emptyset_0 | e^{is \cdot r_{jk}} | \emptyset_0 \rangle = \sum_{j,k} \int \emptyset_0^*(r_1, r_2, \dots) \, \emptyset_0(r_1, r_2, \dots) e^{is \cdot (r_j - r_k)} d\tau_1 d\tau_2 \dots$$

$$= Z + \sum_{j \neq k} \int \emptyset_0^*(r_1, r_2, \dots) \emptyset_0(r_1, r_2, \dots) e^{is \cdot (r_j - r_k)} d\tau_1 d\tau_2 \dots$$

$$= Z + \sum_{a,b=1}^{Z} \int |\phi_a(r)|^2 |\phi_b(r')|^2 e^{is \cdot (r - r')} d\tau d\tau' - \sum_{a,b=1}^{Z} \int \phi_a^*(r) \phi_b(r) \phi_b^*(r') \phi_a(r') e^{is \cdot (r - r')} d\tau d\tau'$$

$$= \left| \int \rho_{el}(r) \, e^{-is \cdot r} d\tau \right|^2 + Z - \sum_{a,b=1}^{Z} \int \phi_a^*(r) \phi_b(r) \phi_b^*(r') \phi_a(r') e^{is \cdot (r - r')} d\tau d\tau'$$

$$= [ZF(s)]^2 + S_i.$$

Therefore eqn. (1.38) yields

$$\frac{d\sigma}{d\Omega_{tot}} = \left(\frac{m_e}{2\pi\hbar^2} \right)^2 \frac{e^4 Z^2}{\varepsilon_0^2 s^4} \left\{ [1 - F(s)]^2 + \frac{S_i}{Z^2} \right\} \tag{1.40}$$

$$\frac{d\sigma}{d\Omega_{ela}} = \left(\frac{m_e}{2\pi\hbar^2} \right)^2 \frac{e^4 Z^2}{\varepsilon_0^2 s^4} [1 - F(s)]^2 \tag{1.41}$$

$$\frac{d\sigma}{d\Omega_{ine}} = \left(\frac{m_e}{2\pi\hbar^2} \right)^2 \frac{e^4}{\varepsilon_0^2} \frac{S_i}{s^4}, \tag{1.42}$$

where $S_i = Z - \int \sum_{a,b=1}^{Z} \phi_a^*(r) \phi_b(r) \phi_b^*(r') \phi_a(r') e^{is \cdot (r - r')} \, d\tau d\tau'$ is the inelastic scattering factor for X-rays. The summation is over those pairs of states, a and b, that have the same spins. The terms $\phi_a^*(r) \phi_b(r)$ describe the *exchange charge density* [74, 76, 77]. Equations (1.41), (1.42) are the differential cross section of elastic and inelastic electron scattering. The inelastic scattering factors (elements Z=1 to 92) for electrons and X-rays are calculated with Hartree–Fock wavefunctions [78, 79] and the Morse approximation, and are tubulated in Table 4.3.3.2 in ref. [67]. The inelastic electron scattering produces signals at very low *s* range. Thus, it can be isolated from the elastic scattering signals.

1.5 Electron diffraction from a molecule ensemble

We have shown in the last section the theory of electron scattering from a single molecule, including the elastic and inelastic scattering. In practical experiments, i.e., gas phase UED, the scattering signal is from all the molecules that are oriented differently in space. The scattering intensity from a molecular ensemble is obtained by averaging the electron scattering signal for molecules at all different orientations. This requires numerical computations for electron scattering calculated with *ab initio* methods. Since inelastic scattering is confined to small scattering angles, and can be isolated from the elastic scattering, we demonstrate here the commonly used formulas of elastic electron diffraction based on the independent atom model (IAM). Using IAM, electron diffraction from a molecular ensemble can be expressed as a simple, analytic form that provides an effective approximation to describe the diffraction pattern from a molecular ensemble. In IAM, the molecule is assumed to be made up of atoms that are independent, noninteracting; thus, the effect of chemical bonds of the molecule to the electron scattering is ignored. In the gas phase electron diffraction, the density of the gas molecules is low enough such that each molecule scatters independently. Therefore, the diffraction intensity (or differential cross section) is an incoherent sum of scattering from individual molecules, in which the scattered wavefunctions from the constituent atoms interfere. The diffraction intensity of a single molecule that consists of N atoms, shown in eqn. (1.14), can be separated into the atomic scattering term and molecular scattering term [60]:

$$I(\boldsymbol{s}) = \sum_{j=1}^{N}\left|f_j(s)\right|^2 + \sum_{j\neq k}^{N} f_j^*(s)f_k(s)e^{i\boldsymbol{s}\cdot\boldsymbol{r}_{jk}}, \qquad (1.43)$$

where $f_j(s) = |f_j(s)|e^{i\eta_j}$ is the atomic form factor of jth atom and $\mathbf{r}_{jk} = \mathbf{r}_j - \mathbf{r}_k$ is the vector pointing from the kth atom to jth atom. The first term is the atomic scattering term, which contains no information about the structure of the molecule, while the structure information is encoded in the second term. Eqn. (1.43) shows that the diffraction intensity is sensitive to the orientation and interatomic distance of atom pairs, denoted by $\mathbf{r}_{jk}$. Suppose the angular distribution of $\mathbf{r}_{jk}$ is $g_{jk}(\alpha, \beta)$, where α, β are polar and azimuthal angles of $\mathbf{r}_{jk}$, and the diffraction intensity of the molecule ensemble is given by

$$I_{\text{total}} = \iint \sum_{j=1}^{N} \sum_{k=1}^{N} f_j^*(s) f_k(s) e^{i\mathbf{s} \cdot \mathbf{r}_{jk}(\alpha,\beta)} g_{jk}(\alpha, \beta) \sin \alpha \, d\alpha \, d\beta, \tag{1.44}$$

where $g_{jk}(\alpha, \beta) = g_{kj}(\alpha, \beta)$. The angular distributions of all atom pairs are $g_{jk}(\alpha, \beta) = \frac{1}{4\pi}$ for the random distribution of molecular orientation. In this case, we can choose the angle between s and $\mathbf{r}_{jk}$ to be α to calculate the integral [60]:

$$I_{\text{total}} = \frac{1}{4\pi} \sum_{j=1}^{N} \sum_{k=1}^{N} f_j^*(s) f_k(s) \int_0^{2\pi} d\beta \int_0^{\pi} e^{isr_{jk} \cos \alpha} \sin \alpha \, d\alpha$$

$$= \sum_{j=1}^{N} \sum_{k=1}^{N} f_j^*(s) f_k(s) \frac{\sin(sr_{jk})}{sr_{jk}}, \tag{1.45}$$

where r_{jk} is the distance between the jth and kth atoms, $s = 2k\sin(\frac{\theta}{2})$, and θ is diffraction angle. Eqn. (1.45) was developed independently by P. Debye [80] and P. Ehrenfest [81] in 1915 for X-ray diffraction from molecules. For $j=k$, the terms reduce to the atomic scattering term, and the terms with $j \neq k$ are corresponding to the molecular scattering term:

$$I_{\text{atom}} = \sum_{j=1}^{N} |f_j(s)|^2 \tag{1.46}$$

and $$I_{\text{mol}} = \sum_{j=1}^{N} \sum_{k=1, j \neq k}^{N} f_j^*(s) f_k(s) \frac{\sin(sr_{jk})}{sr_{jk}}. \tag{1.47}$$

As the atomic form factor is proportional to s^{-2}, shown in Mott-Bethe formula, I_{mol} has a dependence of s^{-5}, and drops quickly with the increase of s [2], which makes the signal level extremely low in the experimental data set. The modified scattering intensity $sM(s)$ [58] is commonly used to address this issue, given by

$$sM(s) = \frac{sI_{\text{mol}}}{I_{\text{at}}}.$$
(1.48)

A corresponding pair distribution function, $p(r)$, which shows the interatomic distances in the molecule, is generated by the Fourier (sine) transform of $sM(s)$ [2]:

$$p(r) \cong \int_0^{s_{\max}} sM(s)\sin(sr)e^{-\kappa s^2}ds,$$
(1.49)

where $s_{\max}$ is the maximum value of momentum transfer s, and $e^{-\kappa s^2}$ is a Gaussian damping factor that filters out the high frequency oscillations at the high s end and mitigates artificial effect due to the cutoff, which is equivalent to a Gaussian smoothing in real space. The molecular and atomic scattering terms cannot be separated experimentally; thus, a processing procedure, shown in ref. [3, 82], is used to obtain the experimental $sM(s)$. Briefly, a theoretical model of the molecule is used to calculate the modified scattering intensity $sM^{\text{T}}(s)$ and $I_{\text{atom}}^{\text{T}}(s)$. The zeros of the $sM^{\text{T}}(s)$ are used to fit and remove a background $b^{\text{E}}(s)$ from the experimental $I_{\text{total}}^{\text{E}}(s)$, which consists of atomic scattering and other experimental background scattering and noise. Thus, the experimental modified scattering intensity is obtained $sM^{\text{E}}(s) = s\left[I_{\text{total}}^{\text{E}}(s) - b^{\text{E}}(s)\right]/I_{\text{atom}}^{\text{T}}(s)$, and the corresponding pair distribution function is calculated with (1.49). The degree of agreement between $sM^{\text{E}}(s)$ and $sM^{\text{T}}(s)$ indicates the accuracy of the theoretical model of the

molecular structure. The processing procedure is commonly used to check the theoretical model with the ground-state data.

To capture the structural change of the molecules at a particular temporal delay following excitation, we need the time-resolved structural analysis. In UED, all the molecules, including the unexcited and excited ones, scatter the incident electrons, thus, the vast majority (>85%-90%) of the diffraction signal is from the unexcited molecules and the signal from the excited ones is usually weak [2, 3]. To accentuate the scattering signal due to the excited molecules, we use the diffraction-difference method [83], wherein we take a difference of the diffraction pattern at time delay t with the pattern at a reference time t_{ref}:

$$\Delta I^E(s,t) = I^E_{total}(s,t) - I^E_{total}(s,t_{ref}) \cong \Delta I^E_{mol}(s,t), \tag{1.50}$$

where t_{ref} refers to the time delay that the arrival of electron probe pulse is ahead of the arrival of the reaction-initiating laser pulse. As the atomic scattering terms in $I^E_{total}(s,t)$ and $I^E_{total}(s,t_{ref})$ stay the same, the difference of the diffraction patterns at temporal delay t and t_{ref} is equal to the difference of molecular scattering terms, denoted as $\Delta I^E_{mol}(s,t)$. Similar to eqn. (1.48), the difference modified molecular scattering can be calculated, formulated as $\Delta sM(s,t) = s\Delta I^E_{mol}(s,t)/I_{at}$, and the corresponding difference of pair distribution function is given by [2]

$$\Delta p(r,t) \cong \int_0^{s_{max}} \Delta sM(s,t) \sin(sr) e^{-\kappa s^2} ds. \tag{1.51}$$

The structural changes of the molecules are reflected by the temporal evolution of $\Delta sM(s,t)$ and $\Delta p(r,t)$, where $\Delta p(r,t) < 0$ indicates a loss of interatomic distance r compared to the parent (reference) molecule and $\Delta p(r,t) > 0$ means an increase of

internuclear distance r in the transient structure or product. For example, the transient structures of $C_2F_4I_2$ after excitation with 277 nm femtosecond laser pulse has been shown in ref. [14], and pyridine and lutidine in ref. [15]. The structural parameters and relative fraction of the product are determined by fitting the experimental $\Delta sM^E(s,t)$ to the theoretical $\Delta sM^T(s,t)$ and minimizing χ^2:

$$\chi^2 = \sum_{s_{\min}}^{s_{\max}} \left[\frac{c \cdot \Delta sM^T(s,t) - \Delta sM^E(s,t)}{\sigma(s)} \right]^2, \qquad (1.52)$$

where c is the relative fraction of the product and $\sigma(s)$ refers to the standard error of the measurement at s. The possible structure of the product is employed to calculate $\Delta sM^T(s,t)$, and the minimum χ^2 determines the product structure. When there is more than one product species, $c \cdot \Delta sM^T(s,t)$ is replaced by $\sum_i c_i \cdot \Delta sM_i^T(s,t)$, where c_i and $\Delta sM_i^T(s,t)$ refer to the yield and theoretical difference modified diffraction intensity of the ith product, respectively.

1.6 Instrumental smearing effects

In this section, we discuss the instrumental resolution of the electron diffraction experiment. A reduction in sharpness or definition of the electron diffraction pattern can be due to several things: (a) wavelength spread of the electrons, (b) finite sample thickness, (c) finite resolution of the detector, (d) beam profile and (e) beam divergence at the sample [84-87]. The discussion of these aspects for small-angle X-ray or neutron scattering has been given in [84-87]. The first one can be ignored for the femtosecond UED since the electron momentum spread is approximated to be very small (~0.1%), and the second one ignored due to the small angle scattering. The detector of UED is a phosphor screen, which is imaged to a photon camera through an imaging system. The scattered electrons impinge on

the phosphor screen to produce photons, which are collected by the camera. A good imaging system makes each point on the phosphor screen mapped to the corresponding pixel on the photon camera; therefore, the diffraction pattern can be recorded by the camera with high fidelity. The smearing effect due to the finite spatial resolution of detector can be estimated by the spot size of the signal on the camera from one electron that impinges on the phosphor screen.
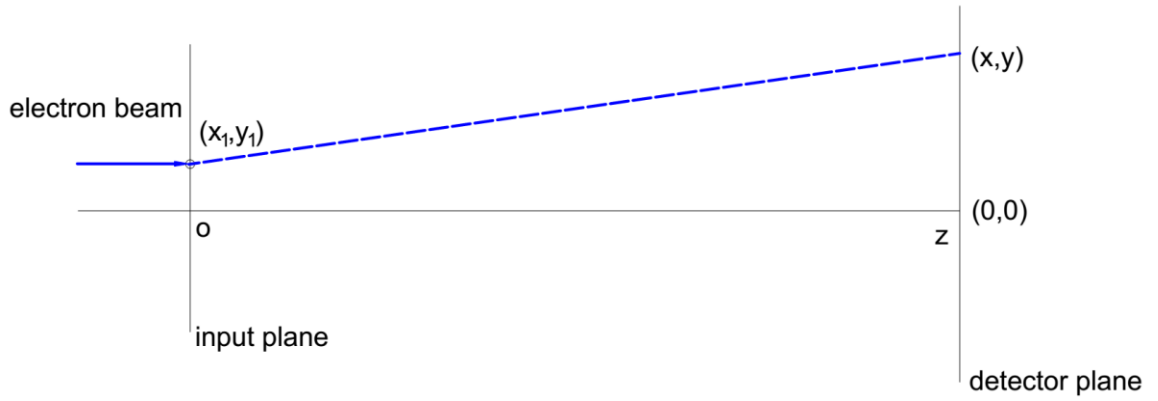
Figure 1.2: Diagram of electron diffraction with a finite beam size. The input plane indicates the sample. The momentum of the incident electron is along z axis.

Here we focus on the discussion of smearing effects due to the last two aspects. Since the smearing effect from the thickness of sample is much smaller in small angle scattering, we use a plane to simplify the scattering from the sample. Figure 1.2 shows the diagram of electron scattering with a finite beam size. The momentum of the incident electron is along z axis. The electron diffraction intensity from a small area of the sample (input plane) located at $(x_1, y_1, 0)$ can be written as $I_o(x - x_1, y - y_1)$. We usually express the diffraction intensity as a function of momentum transfer $s = c(x - x_1, y - y_1)$, where c is the ratio determined by the instrument. For example, the diffraction intensity from a gas

sample at $(x_1 = 0, y_1 = 0,0)$ is $I_o(x,y) = \sum_{j=1}^{N}\sum_{k=1}^{N} f_j^*(s)f_k(s)\frac{\sin(sr_{jk})}{sr_{jk}}$, where $\boldsymbol{s} =$ $c(x,y)$.

Suppose the 2-dimensional distribution of the scattering source on the input plane is $f_1(x_1, y_1)$, which accounts for the distributions of the electron beam and the sample. The total scattering signal contributed from the samples at different locations is given by the convolution:

$$I_T(x,y) = \iint f_1(x_1, y_1)\, I_o(x - x_1, y - y_1)dx_1 dy_1. \tag{1.53}$$
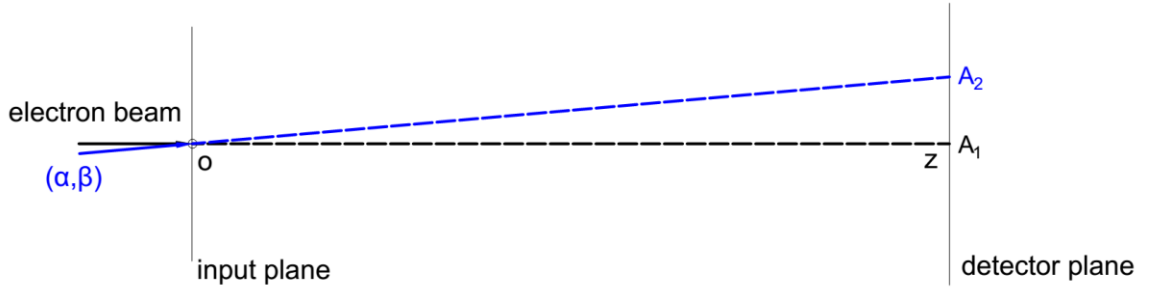
Figure 1.3: Diagram of electron diffraction with a different incident angle. The black arrow indicates the incident electron momentum along z axis. The blue arrow indicates that the electron incident direction is described by (α, β), where α is the polar angle with respect to z axis, and β is the azimuthal angle.

Now we show that the electron diffraction intensity with an electron beam with divergence can be written in a convolution form as well. Figure 1.3 shows the diagram of the diffraction with two different incident angles. The black arrow is the electron beam that is perpendicular to the input plane, and the diffraction intensity is $I_o(x,y)$ with the center of the diffraction rings at $A_1(0,0)$ on the detector plane. For an electron beam with incident angle (α, β), indicated by the blue arrow, the center of the diffraction rings ends up with

$A_2(z\alpha\cos\beta, z\alpha\sin\beta)$, where α is a small angle. The diffraction intensity can be further

approximated to be $I_o(x - z\alpha\cos\beta, y - z\alpha\sin\beta)$ for small angle scattering.

Suppose the distribution of the incident angle is $f_a(\alpha, \beta)$. The total diffraction intensity is

given by

$$I_T(x, y) = \iint f_a(\alpha, \beta) I_o(x - z\alpha\cos\beta, y - z\alpha\sin\beta) \sin\alpha d\alpha d\beta. \qquad (1.54)$$

By defining $x_2 = z\alpha\cos\beta, y_2 = z\alpha\sin\beta, f_2(x_2, y_2) = \frac{1}{z^2}f_a(\alpha, \beta)$ and using $\sin\alpha d\alpha d\beta =$

$\frac{1}{z^2}dx_2 dy_2$, equation (1.54) is

$$I_T(x, y) = \iint f_2(x_2, y_2) I_o(x - x_2, y - y_2) dx_2 dy_2, \qquad (1.55)$$

where $f_2(x_2, y_2)$ is a function determined by the angular distribution of the electron beam

on the sample. A general case is that the incident angle distributions at different position

of the electron beam are different. In this case, the distribution functions that account for

the beam intensity distribution and incident angle distribution are coupled, formulated as

$f(x_1, y_1, \alpha, \beta)$. The scattering intensity is given by

$$I_T(x, y) = \int f(x_1, y_1, \alpha, \beta) I_o(x - x_1 - z\alpha\cos\beta, y - y_1 - z\alpha\sin\beta) dx_1 dy_1 \sin\alpha d\alpha d\beta. \qquad (1.56)$$

By expressing the α, β by x_2, y_2, the eqn. (1.56) becomes

$$I_T(x, y) = \int f(x_1, y_1, x_2, y_2) I_o(x - x_1 - x_2, y - y_1 - y_2) dx_1 dy_1 dx_2 dy_2. \qquad (1.57)$$

Eqn. (1.57) shows that the center of the diffraction intensity on the detector is

$(x_1 + x_2, y_1 + y_2)$ when considering smearing effects from both the size and divergence

of the electron beam. The point $(x_1 + x_2, y_1 + y_2)$ is the intersection point of the detector

plane and the extended line of the vector of the incident electron is described by

$(x_1, y_1, \alpha, \beta)$. The resolution of the instrument can be improved by minimizing the size of

the $(x_1 + x_2, y_1 + y_2)$ distribution. If the trajectories of all the electrons in the main beam (unscattered electrons) can be approximated to be straight as propagating from the input plane to the detector plane, the beam distribution on the detector could be used to estimate the distribution of $(x_1 + x_2, y_1 + y_2)$. In this case, the total scattering intensity can be approximated by the convolution of the $I_o(x, y)$ with the direct beam distribution on the detector.

Chapter 2

Instrumental temporal resolution of gas phase kiloelectronvolts ultrafast electron diffraction

Portions of this material have previously appeared in the publication [32].

2.1 Introduction

Capturing the dynamics of transient molecular states requires the spatial and temporal resolution of the apparatus to be better than, or comparable to, the intrinsic dimension and time scale of molecules. The interatomic distance in a molecule is on the order of angstrom (10^{-10} m). The motion of atoms, or structure change of the molecules, in real time, could be as short at sub-picoseconds, and in some cases as short as ~10 fs for the dissociative channels. The overall temporal resolution of a pump-probe (laser-electron) experiment is given by

$$\tau_{\text{total}} = \sqrt{\tau_{\text{laser}}^2 + \tau_{\text{electron}}^2 + \tau_{\text{GVM}}^2 + \tau_{\text{jitter}}^2}, \qquad (2.1)$$

where τ_{laser} is the laser pulse duration, τ_{electron} is the electron pulse duration, τ_{GVM} is the temporal broadening due to group velocity mismatch between laser and electron pulse, and τ_{jitter} is the arrival jitter of the two pulses. A sub-100fs laser pulse can be easily obtained nowadays thanks to the advent of commercial ultrafast laser sources, and τ_{jitter} is normally determined by the instability of the laser and the voltage source that accelerates the electrons. The electron pulse duration τ_{electron} is dictated by momentum spread when electrons are generated on the cathode, and then the space-charge repulsion during the propagation from the cathode to the sample.

Three methods have been employed to obtain a femtosecond electron pulse duration. A compact design with a short distance from the cathode to the sample has been used to obtain a short electron pulse duration since electron pulse broadening due to space charge effects is proportional to the drift distance. This method has demonstrated a sub-200fs overall temporal resolution in solid state experiments [16, 17, 88] and a 850 fs resolution in gas phase UED experiments [18]. However, in gas phase UED experiments, the short distance between the cathode and sample limits the DC voltage that accelerates the electrons and electron beam current.

The use of relativistic electron pulses significantly suppresses the space charge effects between electrons [27], which has a scale of γ^3, where γ is the Lorentz factor. The electrons are accelerated by RF fields to a kinetic energy of MeV. Using MeV electrons as probes naturally circumvents the temporal broadening due to the group velocity mismatch between pump laser and probe electron pulses. Gas-phase UED has made significant progress recently with the application of relativistic MeV electron gun technology to reach a temporal resolution first of 230 fs [19] and recently 150 fs [19, 20, 26-28]. Several major scientific advances have been achieved by the use of relativistic electrons, including the observation of coherent rotation and vibrational motion [19, 89], structural dynamics in the electronic ground state [53], relaxation dynamics through a conical intersection [21], a ring opening reaction [90] and, more recently, simultaneously capturing nuclear motions and electronic excitations [52]. However, the main limitation of MeV-UED has been the low signal levels due to the low number of electrons per pulse needed to maintain the short electron pulse duration and the dilute nature of gas phase samples. This often limits the amount of data that can be recorded. For example, it is still challenging to carry out

experiments with a set of similar molecules or explore the dependence of a reaction on the excitation wavelength, which will be essential to the understanding of the general rules underlying the chemical reaction dynamics. Also, operating at the high energies requires a significantly larger infrastructure [26].

The radiofrequency (RF) compression technique has been able to successfully compress electron pulses longitudinally in sub-relativistic UED instruments [22, 23, 29], and, more recently, electron pulse duration with this technique has been reduced to 150 fs [23]. The tilted laser pulse-front technique has demonstrated the feasibility of compensating the velocity mismatch between the sub-relativistic electron pulse and the laser pulse [31, 32]. In order to reach femtosecond resolution for gas phase keV-UED experiment, we combined the RF compression and tilted laser pulse front techniques. A hybrid DC-RF electron gun is used to first accelerate the electrons in a DC electric field and then temporally compressed at the sample using an RF cavity [26, 91, 92]. A laser pulse with a tilted pulse front is used to excite the molecules in a geometry so that the velocity mismatch between laser and electrons can be significantly reduced [24, 25].

In this chapter, we discuss the RF compression technique used to optimize the electron pulse duration in our table-top gas phase keV-UED setup, which includes the mechanism of electron pulse compression, the updated RF generation electronics, and RF synchronization with a streaking field. Then we demonstrate the laser pulse-front tilting technique to compensate the laser-and-electron velocity mismatch. We have applied the setup to capture the rotational dynamics of laser aligned nitrogen molecules. The comparison of theoretical simulations and the experimental results shows that the keV-UED instrument reaches an overall temporal resolution of 240 fs. The electron beam

current of the UED setup is more than an order of magnitude higher than that of typical MeV-UED setups.

2.2 Longitudinal compression of an electron pulse

The work described in this section follows the descriptions in ref. [26, 29, 32]. The Coulomb repulsion of electrons in a high-charge density electron pulse inevitably leads to a linear expansion of the electron bunch during the propagation, in both longitudinal and transverse directions. The transverse expansion of electrons is effectively compressed by using time-invariant magnetic fields produced by a magnetic lens. The longitudinal expansion after propagation of the electron pulse in free space leads to a space-momentum chirp, with fast electrons situated at the front and slow electrons at the rear of the pulse [22, 93, 94]. The longitudinal compression of electron pulse is realized by reversing the space-momentum chirp by the use of a time-varying RF electric field in a cavity that is precisely synchronized to the electron pulse. The theory and simulation of propagation dynamics and compression of femtosecond electron packets have been demonstrated in [93, 94]. The details of transverse and longitudinal compression of an electron pulse have been described in detail in [95]. In this section, we give a review of the electron pulse compression with time-varying RF fields, show the updated RF compression electronics and synchronization implemented in our keV-UED setup.

2.2.1 Momentum modulation with time-varying fields

The electron pulse is generated by shining a femtosecond 266 nm laser pulse onto a photocathode made of pure copper. The kinetic energy of the photo-emitted electrons is quickly accelerated to 90 keV in a DC electric field across the cathode to the anode. The

details of electron generation and high voltage chamber are given in ref [95]. The electrons are guided by electron optics (omitted in the figure) into the RF cavity for bunch compression and then to the sample as a probe, shown in figure 2.1 (a).
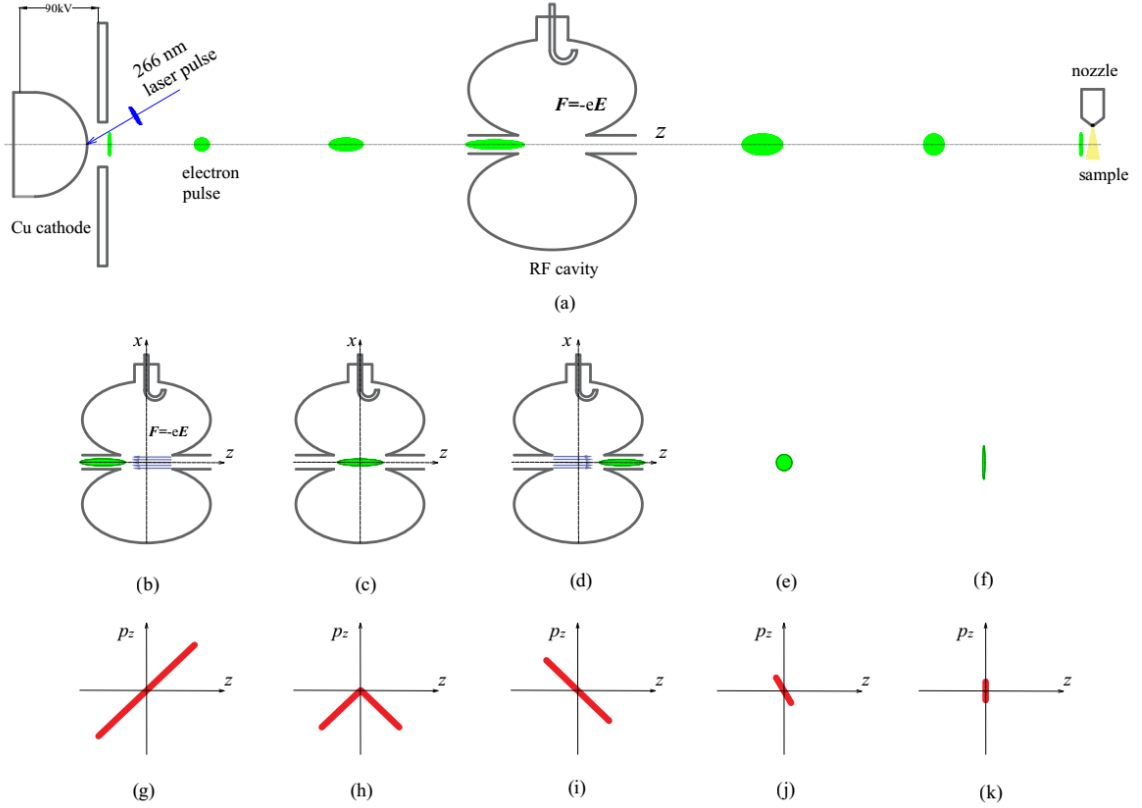
Figure 2.1: Schematic of electron pulse compression with a time-varying field using a RF cavity. (a) Schematics of electron bunch compression [22]. (b-f) the position of the electron pulse relative to the RF cavity at several key times [96]. (g-k) are the corresponding space-momentum distributions at the times in (b-f) [93]. The electron pulse is shown in green. A linear space-momentum distribution is developed as the electrons propagating from the cathode to the RF cavity. The electric fields in the RF cavity decelerate the electrons situated at the front while the pulse enters the cavity, and accelerate the electrons at the back while exiting the cavity. Thus, the space-momentum distribution is reversed.

A RF cavity with a resonant frequency at ~3GHz in the TM010 mode is used to longitudinally compress the electron pulse. As the transverse electron beam size is much smaller than the radius of the RF cavity, the paraxial electric field can be approximated as $E(z,t) = E_0 \cos(2\pi f t + \varphi)\hat{z}$, where $f = 3$GHz, and the cavity axis is along z. The schematic of the electron bunch compression at several key times are shown in figure 2.1 (b)-(f) and the corresponding space-momentum distribution in figure 2.1 (g)-(k). The electron bunch develops a linear spatial-momentum distribution after propagating from the cathode to the RF cavity, shown in figure 2.1 (b) and (g). The phase φ of the electric field is tuned such that the electrons at the front of the bunch are decelerated, shown in figure 2.1 (b), the electrons at the center are not accelerated, in figure 2.1 (c), and the electrons at the back are accelerated, in figure 2.1 (d), leading to a reversed space-momentum distribution [93] for the electron pulse exiting the cavity, in figure 2.1 (i). After that, the electrons at the back have a greater speed than that of electrons in the front, shown in figure 2.1 (e) and (j). Thus, the electrons with larger speeds at the back chase the electrons with lower speeds at the front during the propagation from the cavity to the sample, and a minimum pulse duration is obtained on the sample, shown in figure 2.1 (f) and (k).

The pulse duration before the RF cavity is on the order of 10 picoseconds due to the space charge repulsion for a pulse containing 10^5 electrons. The stretched electron pulse duration is still much smaller than the period of the oscillating fields ($1/f = 0.33$ ns). Second, the transit time of the electron pulse in the RF cavity is much smaller than the period of oscillating field, $d_{\text{cav}}/v_c \ll 1/f$, where d_{cav} is the length of the cavity and $v_c \sim 0.526c$ is the average speed of the 90 keV electrons. Third, the velocity change due to the RF field is small compared to the average speed of the electrons, resulting in a negligible change in

transit time. The momentum change Δp_z of a single electron entering the cavity at t_1 is given by [29, 93]

$$\Delta p_z = -\int_{t_1}^{t_1+\frac{d_{cav}}{v_c}} eE(t)\,dt, \tag{2.2}$$

where $\omega = 2\pi f$ is the angular frequency and the phase φ of the electric field is chosen such that the electric field is written as $E(t) = -E_0\sin\left(wt - \frac{\omega d_{cav}}{2v_c} + \varphi_0\right)$. The phase offset φ_0 is chosen to make the center electrons of the bunch gain no momentum after exiting the RF cavity [29]. We will show that the condition is $\varphi_0 = 0$. The phase offset φ_0 is kept here for later analysis of phase instability. The integral of (2.2) yields

$$\Delta p_z = \frac{2eE_0}{\omega}\sin\left(\omega t_1 + \varphi_0\right)\sin\left(\frac{\omega d_{cav}}{2v_c}\right). \tag{2.3}$$

The time to enter the RF cavity for electrons situated at the front of the pulse is $t_1 = -L/v_c$, where the length of the electron bunch is $2L$. For electrons at the center of the electron pulse, the time to enter the cavity is $t_1 = 0$, and for electrons at the back of the pulse, the time is $t_1 = L/v_c$. The condition of $\Delta p_z = 0$ for $t_1 = 0$ is that $\varphi_0 = 0$ or π. Inserting the times of electron at the front and back in the bunch into eqn. (2.3), we can calculate the difference of the momentum change as [29]

$$\Delta p_b - \Delta p_f = \frac{4eE_0}{\omega}\sin\left(\frac{\omega d_{cav}}{2v_c}\right)\sin\left(\frac{\omega L}{v_c}\right)\cos\left(\varphi_0\right). \tag{2.4}$$

Since $\frac{\omega d_{cav}}{2v_c}, \frac{\omega L}{v_c} \ll 1$, the difference is approximated as $\Delta p_b - \Delta p_f \cong \frac{eE_0\omega d_{cav}\tau_0}{v_c}$, where $\tau_0 = \frac{2L}{v_c}$ is the electron pulse duration when entering the RF cavity. Appropriate selection of φ_0 would reverse the space-momentum chirp to compress the electron bunch properly. The maximum difference of the momentum change corresponds to the condition $\varphi_0 = 0$.

The electron pulse would be stretched by the electric field if $\cos(\varphi_0) < 0$ and the maximum stretching corresponds to $\varphi_0 = \pi$. We discuss how to experimentally make this phase offset be zero in section 2.2.3. The electric field in the RF cavity for $\varphi_0 = 0$ and the times of electrons entering the cavity are shown in figure 2.2.
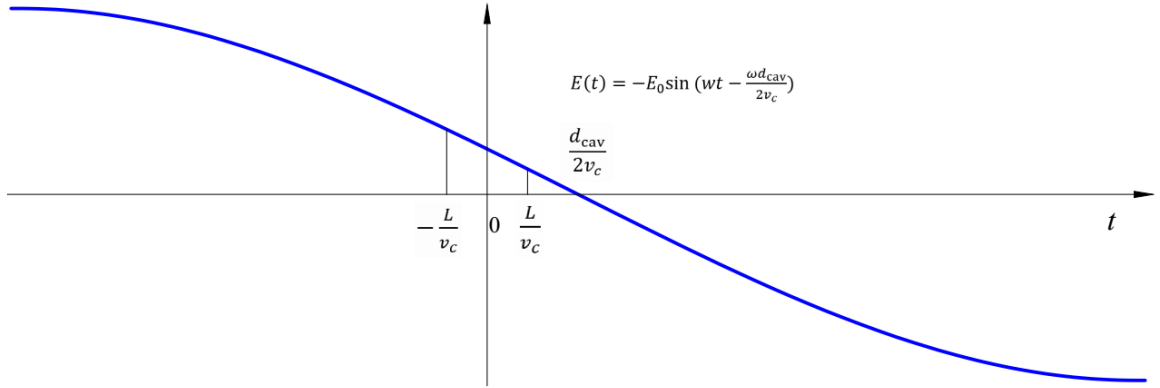
Figure 2.2: The electric field in the RF cavity with φ_0=0 for electron pulse compression. The times to enter the RF cavity for electrons situated at the front, the center, and the back of the electron pulse are $-L/v_c$, 0, L/v_c, respectively. The amount of time that an electron spends in the RF cavity is d_{cav}/v_c.

The above mentioned analysis is about compression of a single electron pulse. Now we analyze the arrival time of different electron pulses at the sample due to the phase instability. We consider the momentum change of the electrons at the center of the bunch to show how the phase instability affects the arrival time of the electron pulse. Suppose that the ideal phase offset φ_0 is set to be zero, but there is a phase instability denoted as φ_r. Thus, the momentum change is

$$\Delta p_z = \frac{2eE_0}{\omega} \sin\left(\frac{\omega d_{cav}}{2v_c}\right)\sin(\varphi_r). \tag{2.5}$$

The change of the arrival time of electrons at the sample is given by

$$\Delta t = -dm\gamma \frac{\Delta p_z}{p_z^2} = -\frac{2deE_0}{m\gamma_s \omega v_c^2} \sin\left(\frac{\omega d_{cav}}{2v_c}\right)\sin(\varphi_r), \tag{2.6}$$

where m is the mass of electron, d is the distance from the RF cavity to the sample (which is 255 mm in our case), and $\gamma = 1/\sqrt{1 - (\frac{v_c}{c})^2}$. Using the condition $\varphi_r \ll 1$, the parameters $E_0 = 1.6$ MV/m and $d_{cav} = 1$ cm [95], eqn. (2.6) yields

$$\Delta t = -160\varphi_r \text{ [ps]}, \tag{2.7}$$

where φ_r is a random variable for a certain amount of time. The overall electron pulse duration is $\sqrt{\tau_e^2 + \Delta t_{FWHM}^2}$, where τ_e is the single electron pulse duration and Δt_{FWHM} is the FWHM width of the distribution of Δt. Therefore, an RF field with a stable phase is of significance to the optimization of the electron pulse duration.

2.2.2 RF generation and phase fixing

We describe in this section the homemade electronic system for RF generation and synchronization, which is inspired from the method in ref. [23]. The diagram of the RF generation is shown in figure 2.3. A small fraction of the power (5 mW) from the laser oscillator (Coherent Mantis), running with a repetition rate at f_0 =74.940 MHz, is focused onto a fast photodiode (Newport 818-BB45) to generate a periodic pulse train, denoted as $f_1(t)$. The periodic pulse train from the photodiode runs through a rough bandpass filter (Mini Circuits VBF-2900+), followed by a low phase noise amplifier (Holzworth HX2400) and a cavity band pass filter with bandwidth of 80 MHz (Anatech AB3000B509) to select the 40th harmonic, which is a sinusoidal signal ($40f_0$~ 2.998 GHz) with a narrow band width, indicated as f_2(t). Two more low phase noise amplifiers (HMC8411LP2FE) and one

attenuator are used to make the power of the sinusoidal signal be 16 dBm before going through the RF switch, denoted as RF.S in figure 2.3, to chop the continuous RF signal into a pulsed signal. We use an analog phase shifter (Analog Devices HMC928LP5E), controlled by an adjustable DC voltage, to tune the phase offset φ_0 of the RF filed in the cavity relative to the arrival of electron pulse. The phase offset φ_0 is set to be zero by measuring the electron pulse through a streak camera, shown in section 2.2.3.

Figure 2.3: Schematic of RF generation and synchronization circuit. OSC = laser oscillator, PD = photo diode, FLT = filter, AMP = amplifier, ISO = isolator, SDG = synchronization and delay generator, Att. = attenuator, PS = phase shifter, RF.S = RF switch, DIV = power divider, C.V.= control voltage, F.E.= feedback electronics, P.DET = phase detector, D.C. = directional coupler, PDC = power detector, OSL = oscilloscope. The signal from the SDG is the electric 5 kHz trigger signal from the laser control unit to control the release timing of laser pulse and 3 GHz pulse.
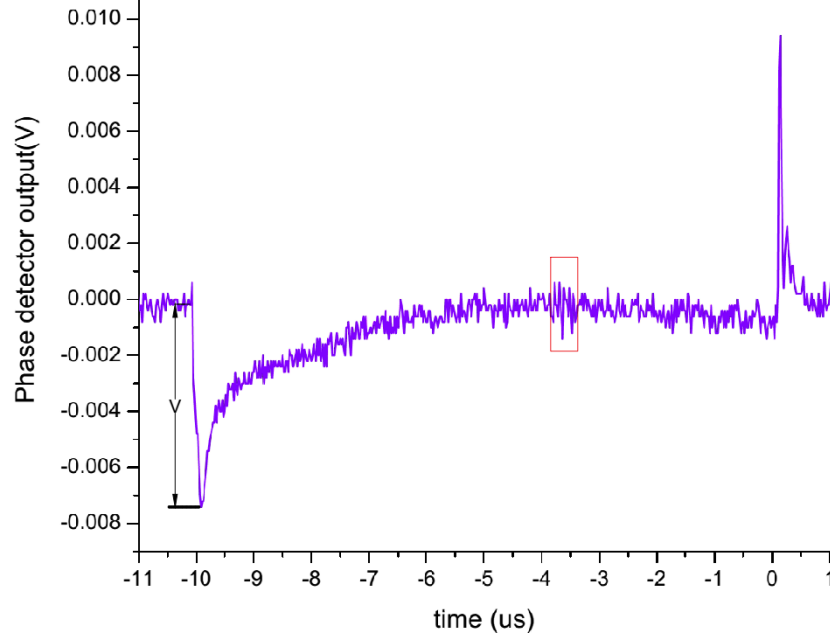
Figure 2.4: Voltage output of the phase detector. The phase of the RF wave inside the red rectangle, the arrival time window of electron pulse, is fixed, though the voltage V at the beginning of the pulsed RF field could be unstable due to the high gain amplifier. The noise peak in the red rectangle is the electromagnetic interference signal from the Pockels cells switching in the laser amplifier and can be used as an indicator of the time the electrons enter the RF cavity [95].

The sinusoidal RF signal is chopped to a pulsed RF signal $f_3(t)$ with duty cycle of 5% by the use of a RF switch (ZASW-2-50DRA+), triggered by a timing signal from the Coherent synchronization and delay generator (SDG). We split the pulsed RF power into two paths, making a feedback loop to correct the phase instability introduced by the high-gain amplifier (Microwave Amps AM83-3S-50-53R). One of the paths is sent through a phase shifter (HMC928LP5E) to correct the phase change, amplified by the high-gain amplifier, and then sent into the RF cavity through a directional coupler (e-MECA 722N-30-3.100). A small portion of the power from the coupled port is picked up and connected to the RF

port of a phase detector (Holzworth HX3400). The other path is directly from the power divider and is used as reference signal for the phase detector.
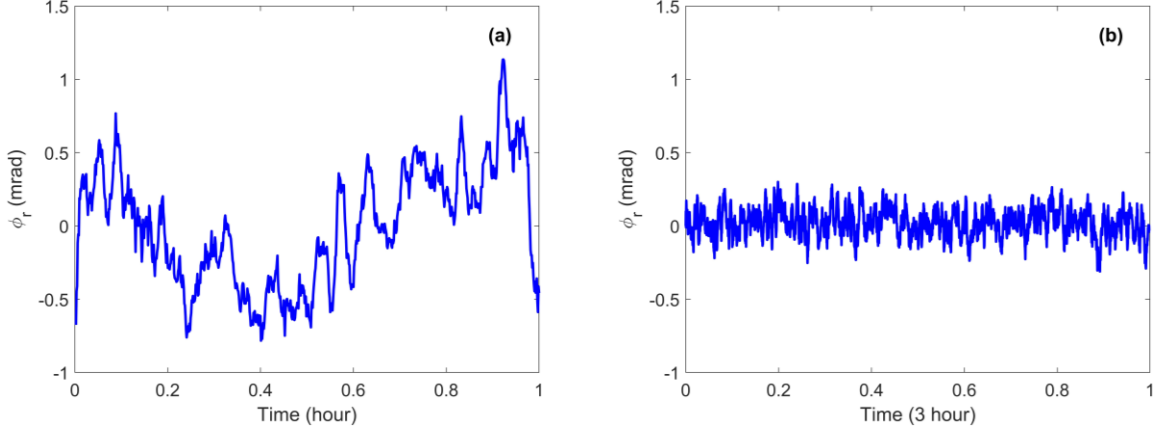
Figure 2.5: Comparison of outputs without and with the feedback electronics. (a) Phase change φ_r introduced by the high gain amplifier shown in figure 2.3. φ_r is measured by the voltage output of phase detector when the feedback loop is off. (b) φ_r is measured by the voltage output of phase detector when the feedback loop is on.

The output voltage $f_4(t)$ of the feedback electronics is used as the feedback signal to a phase shifter in the first path to fix the phase. The voltage output of the phase detector is shown in figure 2.4. While the voltage V at the beginning of the pulsed RF wave could be changed due to the amplifier, the voltage inside the red rectangle (window of arrival time for the electron pulse) is fixed, which indicates that the phase of the RF signal is corrected.

The isolated port of the directional coupler is connected to the power detector (ZX47-40LN-S+) to measure the reflected RF power from the RF cavity. By minimizing the reflection, the optimal repetition rate f_0 of the laser oscillator is obtained. A commercial RF cavity (AccTec BV) is used, and its temperature is stabilized within 1mK RMS with a temperature controller. We use phase stable cables (LL142 Harbour) to deliver the RF

signals. The feedback electronics amplify the output voltage of phase detector with a constant offset voltage V_{offset} and feeds the voltage to the phase shifter to correct phase instability from the high gain amplifier in real time. The function of feedback electronics (see Appendix A for details) is formulated as $f_4(t) = A \cdot V_{PDC} + V_{offset}$, where the gain factor $A = -1/(k_1 k_2)$, k_1 is the slope of phase to control voltage of the phase shifter, and k_2 is the slope of the output voltage to phase change of the phase detector. We use an operational amplifier (LT1028) in the feedback electronics for the voltage amplification, which provides a response time on the order of µs. Figure 2.5 shows a comparison of the phase change, converted from the voltage output of the phase detector, when the feedback loop is off and on. According to eqn. (2.7), the arrival time change (FWHM) of the electron pulse is on the order of 200 fs due to the phase instability. However, the timing change (FWHM) is ~43 fs when the phase is fixed.

2.2.3 RF synchronization

Portions of the work described in this section is based on the results in ref. [97]. We have shown that phase offset φ_0 needs to be zero for the optimal compression of the electron pulse duration in section 2.1. We demonstrate here the adjustment of the phase of the RF wave using a streak camera. The details of the home-made streak camera can be found in [95, 97]. First, we briefly review how the streak camera functions, and then show how to use it to synchronize the zero value of RF wave to the center of electron pulse. The function of a streak camera is to map the longitudinal profile of an electron pulse into a distribution of deflected angles by using a time-varying streaking field. Several methods, such as a discharging capacitor [97-100], a microwave cavity [101], and a laser standing wave [102-

104] have been used to generate such a time-varying streaking field. Here the time-varying

streaking field is produced by using a laser-activated discharging capacitor.

The diagram of the streak camera is shown in figure 2.6, in which C is the capacitance of

a pair of parallel metal plates used to deflect the electrons, L stands for the self-inductance

of the circuit, R(t) is the resistance of the photo-switch and R_0 is the time-independent

resistance in the circuit. The capacitor (two parallel metal plates) is charged to certain

voltage V_0 for $R(t < 0) = \infty$, and then is discharged after a laser pulse activates the photo-

switch (GaAs) leading to $R(t = 0) \cong 0 \ \Omega$.
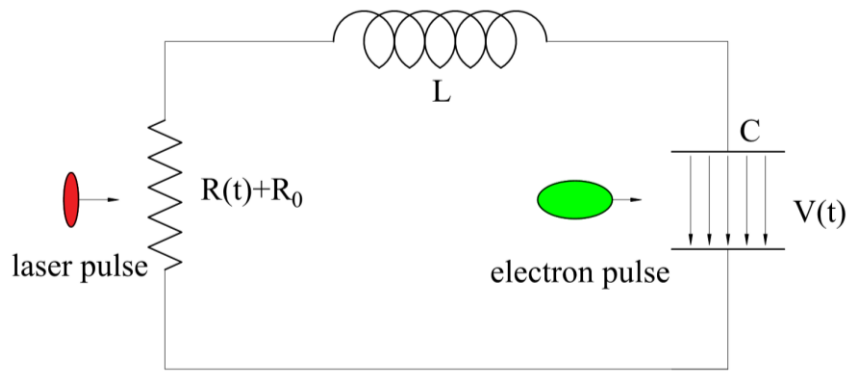
Figure 2.6: The diagram of the equivalent circuit for the streak camera. The capacitance of

a pair of parallel metal plates is denoted as C, and the time-varying electric field between

the two plates is used to deflect the electrons in green. The inductance of the circuit is

denoted as L. The resistance R(t) is time-varying due to the photo-switch triggered by the

laser pulse in red, and R_0 is the time-independent resistance in the circuit, which is

dominated by the Ohmic contacts of the photo-switch.

The streak camera can be considered to be an RLC circuit with a time-varying resistance.

According to Kirchhoff's voltage law, the voltage across the capacitor, denoted as V(t),

after the photo-switch is triggered by the laser pulse, can be described by the homogenous differential equation

$$L\frac{d^2V(t)}{dt^2} + [R(t) + R_0]\frac{dV(t)}{dt} + \frac{1}{C}V(t) = 0, \tag{2.8}$$

where $V(t = 0) = V_0$. The resistance of the photo-switch after being triggered by the ultrafast laser pulse is modeled by $R(t) = R_1 e^{\frac{t}{\tau_1}}$, where the time constant τ_1 is determined by the properties of the GaAs material, such as electron-hole recombination time, contact injection efficiency and carrier drift velocity [97, 105].

The parameters of the circuit are determined by experimental measurements and calculations [97] to be: $V_0 = 800$ V, $R_0 = 48$ Ω, $R_1 = 0.372$ Ω, $\tau_1 = 0.36$ ns, $C = 0.245$ pF and $L = 8.35$ nH. Eqn. (2.8) cannot be solved analytically due to the time dependence of R(t). However, an approximated solution can be obtained by comparing the R(t) to R₀ in the first few cycles of oscillations, which in practice is the time range of relevance to the experiment. By ignoring R(t), the oscillation frequency is $\omega_0 = \sqrt{\frac{1}{LC} - (\frac{R_0}{2L})^2} = 21.9$ GHz, and the damping constant $\zeta_0 = -\frac{R_0}{2L} = -2.89$ GHz. The 3rd oscillation of the V(t) corresponds to $t = 0.86$ ns, and the resistance of the photo-switch is $R(t = 0.86 \text{ ns}) = 4.06$ Ω, which is far smaller than R_0. Therefore, the approximate solution of V(t) within the first three cycles of oscillation can be obtained by ignoring R(t) in eqn. (2.8), which gives

$$V(t) = V_0 e^{\zeta_0 t} \cos(\omega_0 t). \tag{2.9}$$

The time zero $t=0$ is defined as the arrival time of the ultrafast laser pulse on the photo-switch in the abovementioned analysis. In the experiment, the arrival time of trigger laser

can be adjusted by using an optical stage for synchronization, which is denoted as t_{tri}. Therefore, the voltage across the capacitor can be written as $V_1(t) = V(t - t_{\text{tri}})$.

We now analyze the displacement of an electron by the time-varying electric field in the capacitor. The electron pulse duration τ_{electron} is on order of ~10 ps without the RF compression and is $\lesssim 200$ fs with the optimal RF compression. The speed of the electron pulse is ~0.53 c. Suppose t_s is the amount of time the electron spends in the capacitor, and in our case $t_s = l_s/v_z \cong 20$ ps, where v_z is the velocity in the longitudinal direction and l_s is the width of the capacitor. Both the t_s and τ_{electron} are far smaller than the period of the oscillation of the voltage across the capacitor, denoted as $2\pi/\omega_0$. When going through the capacitor with a voltage $V_1(t)$, the electron gains a transverse momentum from the electric field, given by

$$p_x(t) = \int_t^{t+t_s} \frac{eV_1(t)}{d_{\text{st}}} dt = \frac{eV_1(t_{\text{m}})}{d_{\text{st}}} t_s, \tag{2.10}$$

where d_{st} is the gap length of the capacitor, and t_{m} is a certain value between $t \sim t + t_s$. The eqn. (2.10) is obtained by the mean value theorem. The value of t_{m} can be approximated by $t_{\text{m}} \cong t + t_s/2$; or in a rough approximation, $t_{\text{m}} \cong t$. Therefore, if an electron enters the capacitor at time t, the transverse momentum is $p_x(t) \cong \frac{eV_1(t+t_s/2)}{d_{\text{st}}} t_s$.

Suppose the distance from the streak camera to the detector is D, the position of the electron (x) on the detector is determined by $\frac{x}{D} = \frac{p_x}{p_z} = \frac{eV_1(t+t_s/2)}{p_z d_{\text{st}}} t_s$, and we have

$$x(t) = \frac{eDl_s}{\gamma m_e v_z^2 d_{\text{st}}} V_1(t + \frac{t_s}{2}). \tag{2.11}$$

The transverse displacement of the electron entering the capacitor at time t is proportional to $V_1(t + \frac{t_s}{2})$. Therefore, the longitudinal profile of the electron pulse can be mapped into a transverse distribution when $V_1(t + \frac{t_s}{2})$ is a monotonic function, which can be done by using voltage around the first zero.
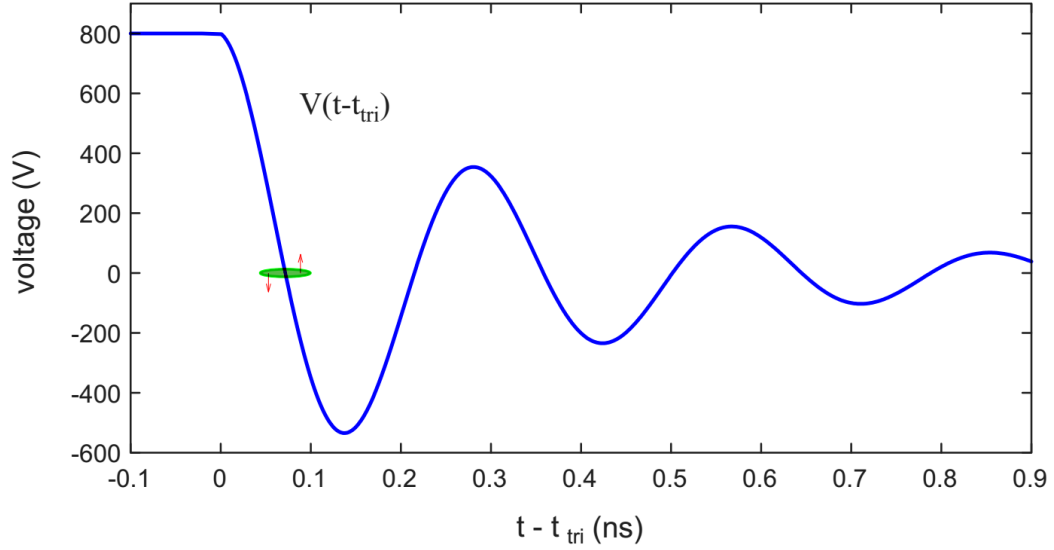
Figure 2.7: Damped oscillation of voltage across the capacitor. The equation is $V_1(t) = V(t - t_{\text{tri}})$. The electron pulse in green is streaked by the time-varying electric field transversely, in which the electrons on the left side gain a momentum downwards, and electrons on the right-side gain a momentum upwards.

Figure 2.7 shows the damped oscillation of voltage across the capacitor $V_1(t) = V(t - t_{\text{tri}})$, and a diagram of an electron pulse being streaked transversely. By choosing a proper t_{tri}, the electron pulse, in green, can be streaked transversely by the electric field around its first zero, in which the electrons on the left side gain a momentum downwards indicated by the red arrow, and the electrons on the right-side gain a momentum upwards while the electrons in the center gain no momentum. We demonstrate the diagram of RF

synchronization in figure 2.8. This is experimentally demonstrated in figure 2.9. The electron pulse through the streak camera, without the RF compression and streaking field, is shown in figure 2.9 (a) as a reference. By turning on the streaking field, the electron pulse without RF compression is streaked. By adjusting the arrival time of the trigger laser on the photo-switch t_{tri}, the center of the streaked electron pulse, shown in figure 2.9 (b), is overlapped with the center of reference in figure 2.9 (a). We then turn on the RF compression, and the electron pulse gains a momentum after going through the RF cavity according to eqn. (2.3), given by $\Delta p_z = \frac{2eE_0}{\omega}\sin(\varphi_0)\sin(\frac{\omega d_{cav}}{2v_c})$.
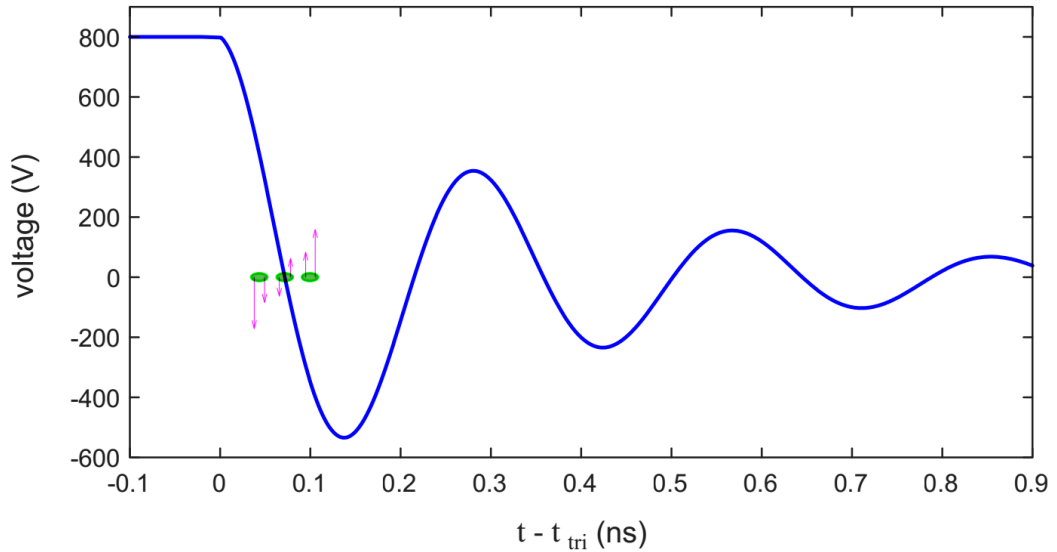
Figure 2.8: Diagram of RF synchronization by adjusting the phase shifter 1 in figure 2.3. For $\sin(\varphi_0) > 0$, the electron pulse is accelerated by the RF field, shown as the left electron pulse in green, and is deflected by the streaking field downwards indicated by the red arrows. The length of the arrow indicates the amplitude. For $\sin(\varphi_0) < 0$, the electron pulse is decelerated by the RF field and is deflected by the streaking field upwards. In the case of $\sin(\varphi_0) = 0$, the electron pulse is streaked but its center does not change.
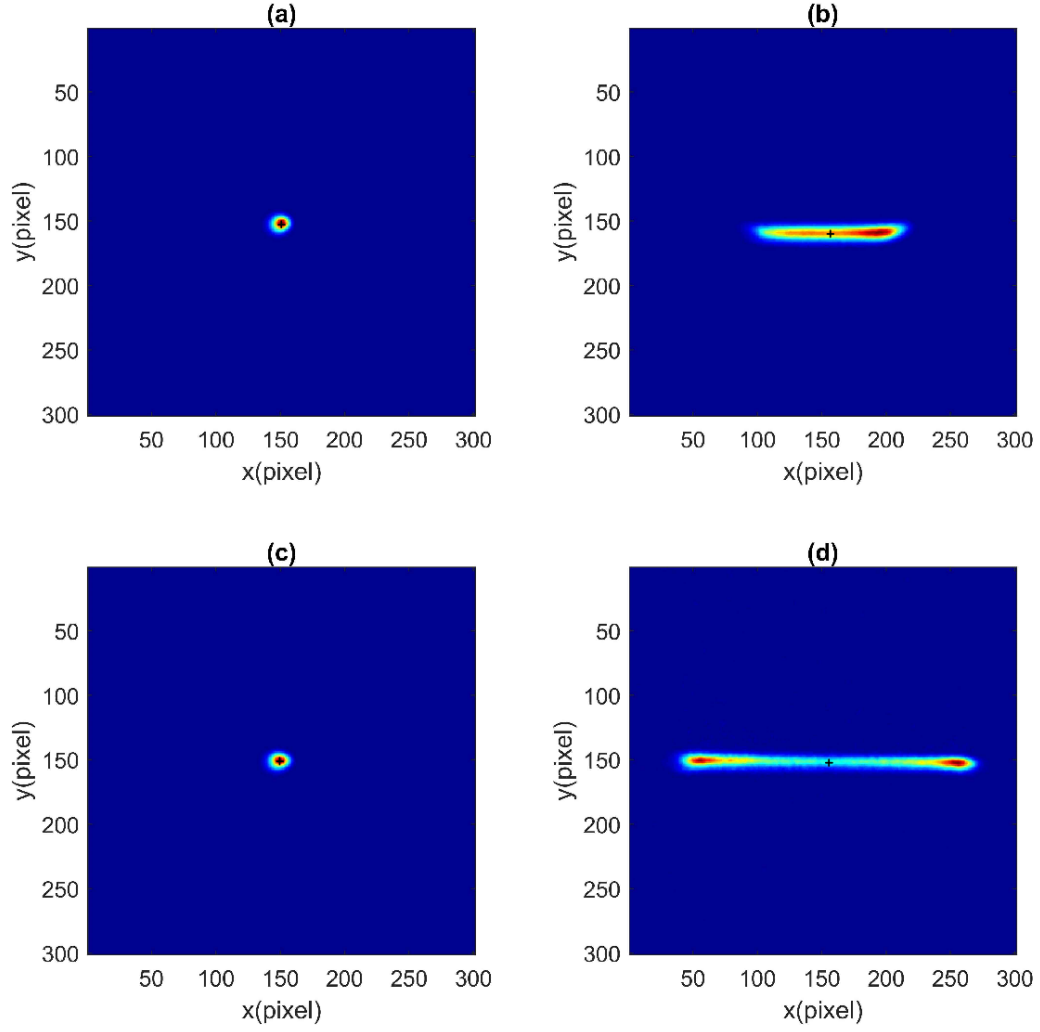
Figure 2.9: Demonstration of RF synchronization using a streaking camera. (a) electron pulse going through the streak camera without RF compression and streaking field is off. The center of signal is considered as a reference. (b) electron pulse through the streaking field, without RF compression. By adjusting the arrival time of the trigger laser on the photo-switch, the center of the streaked electron signal overlaps with the reference center in (a). (c) electron pulse goes through the streak camera and RF cavity with both fields on. By adjusting the phase shifter 1 in figure 2.3 to make $\varphi_0 = 0$ such that the center of the center of the signal overlaps with the reference center. (d) The phase shifter 1 is adjusted

to obtain $\varphi_0 = \pi$, corresponding to maximum stretching of the electron pulse by the RF field.

If $\sin(\varphi_0) > 0$, the electron pulse is accelerated by the RF field, shown as the left electron pulse in green, and is deflected by the streaking field downwards indicated by the red arrow, shown in figure 2.8. If $\sin(\varphi_0) < 0$, the electron pulse is decelerated by the RF field and is deflected by the streaking field upwards. In both cases, the electron pulse is displaced away from the reference center shown in 2.9 (a). By adjusting the control voltage for phase shifter 1 (PS1 in figure 2.3), we obtain $\varphi_0 = 0$ for the optimal compression, shown in figure 2.9 (c), such that the center of the streaked electron pulse overlaps with the reference center in figure 2.9 (a). We adjust the phase shifter 1 to make $\varphi_0 = \pi$, corresponding to the maximum stretching of the electron pulse, shown in figure 2.9 (d).

The other two factors that affect the electron pulse duration on the sample are the amplitude of the RF field and the number of electrons in each pulse. After the synchronization is done, we tune these two parameters to find the minimum electron pulse duration with the laser induced nitrogen alignment experiment, which will be discussed in chapter 4.

2.3 Tilted laser pulse for group velocity match

Portions of the work described in this section are based on results presented in the previous publications [26, 32]. Ultrafast electron diffraction with relativistic electron pulses does not have the issue of group velocity mismatch since the speed of the laser and electron pulse are very close. However, the speed of the electrons at kinetic energy 90 keV is about half of the speed of light. The difference of speeds makes it impossible to maintain the same time delay between the pump and probe pulses across the sample. According to the

analysis given in ref. [30], the temporal broadening due to the velocity mismatch is $\gtrsim 600$ fs for our keV-UED when the diameter of the laser, the electron beam, and the gas jet are 200 μm. In this section, I discuss the method to compensate group velocity mismatch between the laser and the electron pulse using a tilted laser pulse.

2.3.1 Design
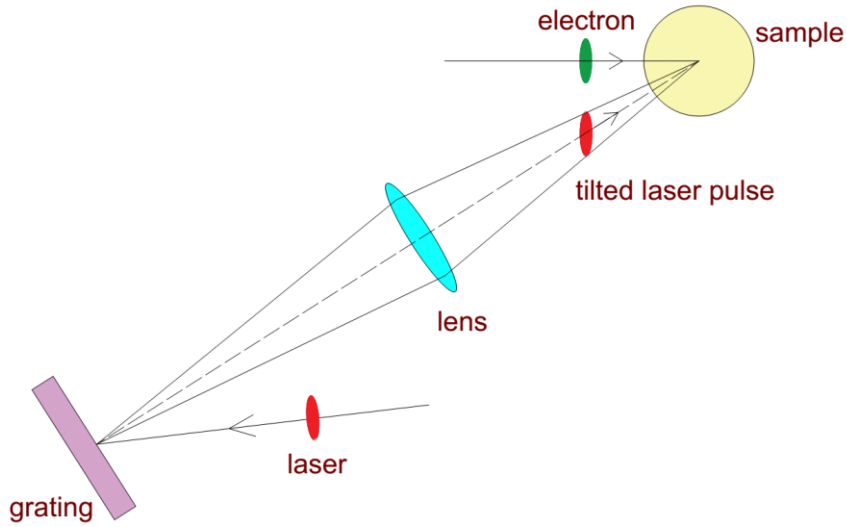
Figure 2.10: Diagram of group velocity match using a tilted laser pulse generated with a grating, not to scale.

Figure 2.10 shows the diagram of velocities match using a tilted laser pulse. The idea is to make the component of the laser velocity along the electron propagation equal to the speed of the electron pulse such that the time delays across the sample are the same. A tilted pulse front of a femtosecond laser pulse can be generated by introducing a spatial chirp to the laser beam with a dispersive element, e.g., a grating or a prism. In the case of diffraction grating, the tilted angle ψ of the pulse front relative to the phase front, right after the grating [106-108], is given by

$$\tan\psi = \lambda_0 \frac{d\theta_{out}}{d\lambda},$$

where λ_0 is the central wavelength of the laser pulse, and θ_{out} is the output angle of the diffracted beam. To make the tilted angle adjustable for the application in the keV-UED, we use a grating and an imaging system. Suppose the imaging system is ideal with a magnification factor M and the amplitude spectrum of the laser pulse on the grating is $a(x, \omega)$, the amplitude spectrum on the image plane, denoted as $a_{IM}(x_i, \omega)$, is equal to $a(-x_i/M, \omega)$ [109]. The spatial frequency of the laser on the image plane is related to that on the grating surface by $d\theta_{im}/d\lambda = -M_D\, d\theta_{out}/d\lambda$, where the demagnification factor is $M_D = 1/M$. Thus, the tilted angle γ_t of the pulse front on the image plane is given by [110]

$$\tan\gamma_t = M_D \lambda_0 \left(\frac{d\theta_{out}}{d\lambda}\right)_{\lambda_0}. \tag{2.12}$$

The angular dispersion is determined by the diffraction order k, the grating constant d (grooves/mm) and the output angle. The equation of angular dispersion is

$$\left(\frac{d\theta_{out}}{d\lambda}\right)_{\lambda_0} = \frac{kd}{\cos\theta_{out}}. \tag{2.13}$$

To remove velocity mismatch between the 90 keV electron pulse ($v_e = 0.526c$) and the laser pulse, the tilt angle is $\gamma_t = \cos^{-1}\left(\frac{v_e}{c}\right) = 58.24°$. A gold-coated ruled grating with a grating constant d=150 mm^{-1} is used to generate the tilted laser pulse with an efficiency 80% of the incident laser power to the first diffraction order ($k = 1$). Using the grating equation $\sin\theta_{in} + \sin\theta_{out} = d\lambda_0$ with $\theta_{out} = 0$ and $\lambda_0 = 800$ nm, the incident angle is $\theta_{in} = 6.9°$. The demagnification factor is $M_D = \tan(\gamma_t)/(d\lambda_0) = 13.46$. We use a thin lens with a focal length of 25.5 cm to image the grating surface to the sample. The distance from the grating to the lens is 368.7 cm and from the lens to the sample target is 27.4 cm.

The time duration of the tilted laser pulse at Δz after the grating is given by [107, 110]

$$\tau \simeq \tau_0 \sqrt{1 + \frac{(4\ln2)^2 \lambda_0{}^6 \Delta z^2}{\pi^2 c^4 \tau_0{}^4} \left(\frac{d\theta_{\text{out}}}{d\lambda}\right)^4} \, , \tag{2.14}$$

where τ_0 is the pulse duration of the incident laser pulse. The amplitude spectrum on the image plane is $a_{\text{IM}}(x_i, \omega) = a(-x_i/M, \omega)$, indicating that the tilted pulse has the same temporal frequency distribution as that on the grating. Thus, the pulse duration around the image plane is obtained by replacing $d\theta_{\text{out}}/d\lambda$ with $d\theta_{\text{im}}/d\lambda = -M_D \, d\theta_{\text{out}}/d\lambda$ in eqn. (2.14). When the grating surface is not parallel to the lens, the demagnification factor M_D is a function of lateral distance from the center of image. Thus, the pulse duration is a function of lateral distance from the center. A geometry with the output laser beam that is perpendicular to the grating was suggested to address this issue such that $\tau \simeq \tau_0$ is obtained on the image plane [110]. The measurement of tilted pulse duration, as a function of the displacement Δz from the image plane, shows that $\tau \simeq \tau_0$ within $\pm$ 500 µm around the image plane [25]. The diameter of the gas jet in our experiment is ~200 µm. Thus, the minimum pulse duration can be obtained by imaging the grating surface to the target.

2.3.2 Measurements of the tilted angle and pulse duration

The tilted angle and pulse duration can be measured by cross correlation between the tilted pulse and a reference pulse [25], shown in figure 2.11. The reference and tilted pulse are propagating along z axis. By changing the relative timing ($\Delta z/c$) between the two pulses, we measure the interference at different transverse positions Δx, and the tilted angle is given by $\tan\gamma_t = \Delta z/\Delta x$. Figure 2.12 shows the cross correlation measurements: five relative delays (z) between the two pulses and the corresponding interferences are recorded. The five measurements are combined into one picture, shown in figure 2.12 (a). The tilted

angle is determined to be $\gamma_t = 57° \pm 2°$ by fitting the interference centers as a function of delays to a linear function, shown in figure 2.12 (b).
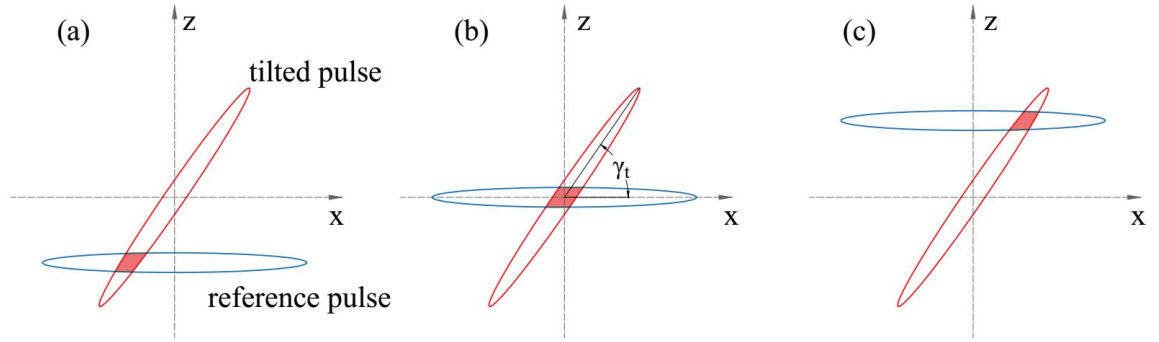
Figure 2.11: Diagram of cross correlation between the tilted pulse and the reference pulse. The reference and tilted pulses are propagating along z axis. The red area is the overlapping between the two pulses.
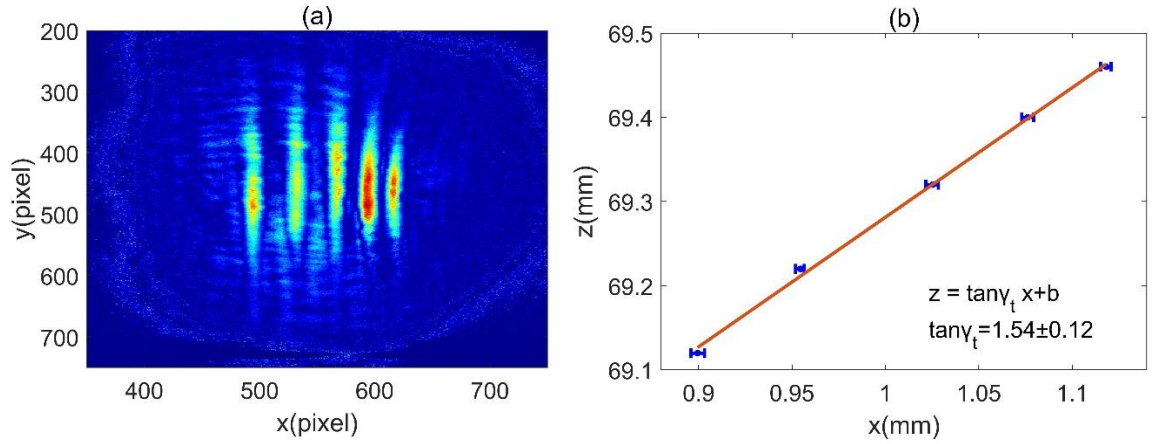
Figure 2.12: Cross correlation measurement of the tilted and reference pulse. (a) Five delays (z) and the corresponding interferences are recorded and combined into one picture. (b) The fitting of delays vs. interference centers to a linear function. The tilted angle is determined to be $\gamma_t = 57° \pm 2°$.

The pulse duration can be measured by the width of the interference. Here we consider the tilted pulse to be propagating along z, and the wavevector of the reference beam has a small component along x. The electric amplitude of the reference E_r and the tilted pulse E_t can be written as

$$E_r = f_r(x,y)e^{-\alpha_r t^2}e^{i(k_2 z + k_1 x - \omega t)} , \qquad (2.15)$$

$$E_t = f_t(x,y)e^{-\alpha_t(t-\frac{x\tan\gamma_t}{c})^2}e^{i(kz - \omega t + \phi)} , \qquad (2.16)$$

where $f(x,y)$ represents amplitude distribution, $\alpha = 4\ln 2/\tau^2$, τ is the pulse duration, and t=0 corresponds to the center of both pulses at the origin of the coordinate. The relative phase of the two pulses is ϕ, and the condition of the wavevector components is $k_2 \gg k_1$. Since the response time of the detector is much larger than the pulse duration, the measured intensity $I(x,y) = \int_{-\infty}^{+\infty}|E_r + E_t|^2 dt$ yields

$$I(x,y) = G(x,y) + f_r(x,y)f_t(x,y)\exp\left(-\frac{\alpha_r\alpha_t}{\alpha_r+\alpha_t}\frac{x^2}{c^2}\tan\gamma_t^2\right)\cos(k_1 x + \phi'), \qquad (2.17)$$

where $G(x,y) \propto f_r(x,y)^2 + f_t(x,y)^2$ is the background and the phase is $\phi' = \phi + (k_2 - k_1)z$. The background $G(x,y)$ can be measured by changing the time delay such that there is no interference. The term $f_r(x,y)f_t(x,y)$ is assumed to be a Gaussian function with a width that is much larger than the width of the signal from the interference.

The pulse duration is encoded in the term $\exp\left(-\frac{\alpha_r\alpha_t}{\alpha_r+\alpha_t}\frac{x^2}{c^2}\tan\gamma_t^2\right)\cos(k_1 x + \phi')$, and can be retrieved by fitting a Gaussian function multiplied by a sinusoidal function, formulated as $a \cdot \exp[-(x-b)^2 w^{-2}] \cdot \cos(dx + e)$. The measurement of the tilted pulse duration is shown in figure 2.13. The FWHM is $l = 2\sqrt{\ln 2}w$, and the tilted pulse duration τ_t is given by

$$\tau_t = \sqrt{\left(\frac{l}{c}\tan\gamma_t\right)^2 - \tau_r^2} \,, \tag{2.18}$$

where τ_r is the reference pulse duration, which is measured with a frequency-resolved optical gating (FROG) [111]. The measured tilted pulse duration τ_t is close to the reference pulse duration τ_r when a good imaging is obtained.
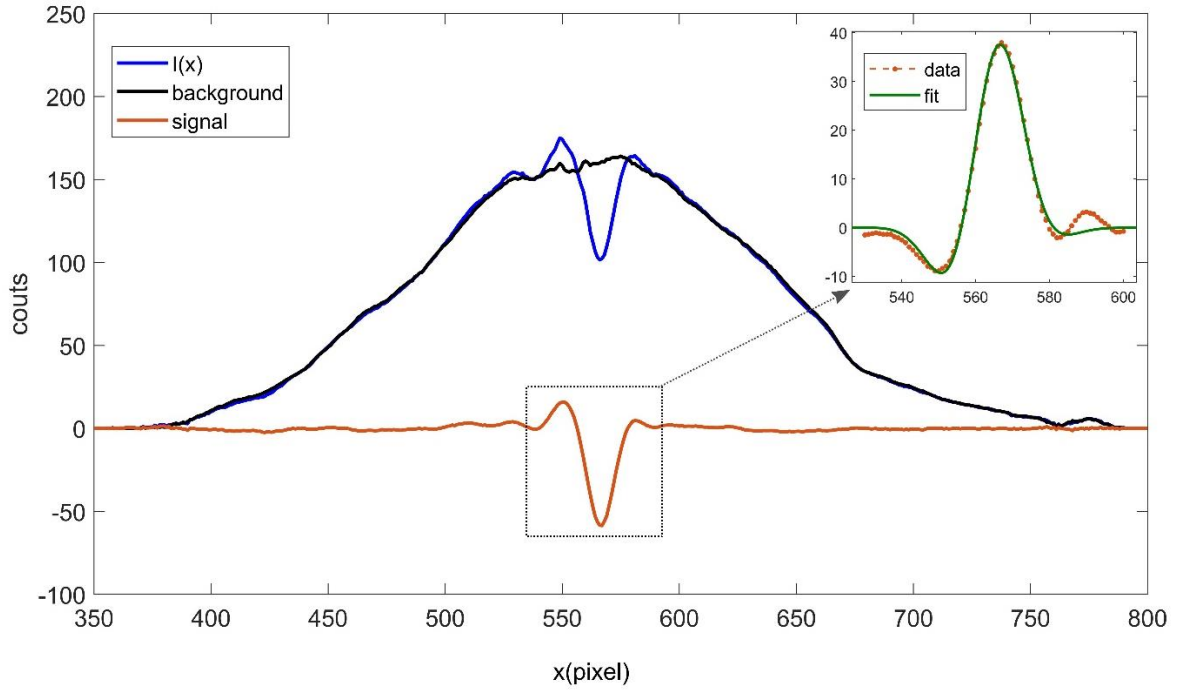
Figure 2.13: Measurement of tilted pulse duration. The intensity $I(x)$ (blue) is calculated by integrating the image of the interference signal along the y axis. The background (black) is the measurement with no interference signal. The signal (orange) that contains the tilted pulse duration is obtained by taking the difference of $I(x)$ and the background. The signal is fitted to a Gaussian function multiplied by a sinusoidal function, shown in the inset.

2.3.3 Residual velocity mismatch

Ideally, the velocity mismatch can be removed by using the tilted laser pulse technique. However, the tilted angle and the incident angle in practice could be off. Here, we analyze

the dependence of the residual temporal broadening on the angle misalignments using the method described in [30]. Since the size of the sample is much smaller than the object and image distances, the tilted angle is considered to be constant across the sample. To analyze the temporal broadening due to the velocity mismatch, the electron (probe) and laser (pump) pulses are described as delta functions in time and Gaussian functions in space, shown as $\rho_1(x)$ and $\rho_2(u)$ in figure 2.14. The tilted angle of the laser pulse is γ_t, and the angle between the laser and electron beams is θ.
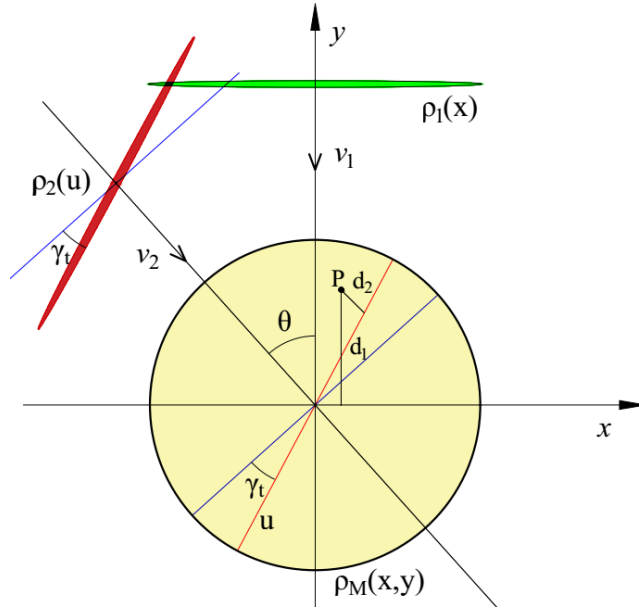
Figure 2.14: Diagram of pump-probe experiment with a tilted laser pulse. The electron pulse (green) and the laser pulse (red) intersect at the center of a molecular beam (yellow), which is introduced in the direction perpendicular to both the laser and electron beams. The angle between the laser energy plane and the phase plane is the titled angle γ_t. When the phase plane rotates to the energy plane counter-clock wisely, the tilted angle is defined positive ($\gamma_t > 0$) and vice versa.

The time zero is defined when the centers of two pulses are overlapped at the origin of x-y coordinate. The time delay between pulse 1 and 2 for molecules at point P(x, y) is given by

$$\Delta t(x, y) = \frac{d_1}{v_1} - \frac{d_2}{v_2},$$

where $d_1 = y$, $d_2 = y\cos\theta - x\sin\theta - (x\cos\theta + y\sin\theta)\tan\gamma_t$. Let $k = v_2/v_1$, and the time delay is

$$\Delta t = \frac{x(\sin\theta + \cos\theta \, \tan\gamma_t) + y(\sin\theta \, \tan\gamma_t + k - \cos\theta)}{v_2}. \qquad (2.19)$$

For a specific Δt, all the molecules along the line described by eqn (2.19) experience the same time delay between the laser and electron pulses. The equation with a specific Δt can be written as $y = ax + b$, where a and b are given by

$$a = -\frac{\sin\theta + \cos\theta \, \tan\gamma_t}{\sin\theta \, \tan\gamma_t + k - \cos\theta},$$

$$b = -\frac{v_2 \Delta t}{\sin\theta \, \tan\gamma_t + k - \cos\theta}.$$

Taking an integral along the line with a weighting factor, the signal contributed from all the molecules experiencing a time delay Δt is given by [30]

$$I(\Delta t) = \int_{-\infty}^{+\infty} f(x, ax + b) \sqrt{1 + (dy/dx)^2} \, dx \ ,$$

where $f(x, y) = \rho_1(x)\rho_2(u)\rho_M(x, y)$ is the weighting factor that accounts for the distributions of the electron, the laser, and the molecular beams. Spatial distributions of the pulses are assumed to be Gaussian functions with a FWHM width w_1, w_2 and w_M for the electron and laser pulse, and molecular beam, respectively. The corresponding spatial distributions for the electron, laser and molecular beams are formulated as $\rho_1(x) =$

$\exp\left(-4\ln2x^2/w_1{}^2\right)$, $\rho_2(u) = \exp\left(-4\ln2u^2/w_2{}^2\right)$, and $\rho_M(x,y) = \exp\left[-4\ln2(x^2 + y^2)/w_M{}^2\right]$. The integral is given by

$$I(\Delta t) = \sqrt{\frac{\pi(1+a^2)}{4\ln2\,\mathcal{A}}}\exp[-4\ln2\,\mathcal{M}\,(\Delta t)^2]. \tag{2.20}$$

The temporal broadening (FWHM) is given by

$$\tau_{\text{GVM}}(\theta, \gamma_t, k) = \frac{1}{\sqrt{\mathcal{M}}} \tag{2.21}$$

where

$$\mathcal{M} = \frac{\left(\mathcal{C} - \frac{\mathcal{B}^2}{4\mathcal{A}}\right)v_2{}^2}{(\sin\theta\,\tan\gamma_t + k - \cos\theta)^2}, \tag{2.22}$$

$$\mathcal{A} = \frac{1}{w_1{}^2} + \frac{[a\sin(\theta + \gamma_t) + \cos(\theta + \gamma_t)]^2}{w_2{}^2} + \frac{a^2+1}{w_M{}^2}, \tag{2.23}$$

$$\mathcal{B} = \frac{2\sin(\theta + \gamma_t)[a\sin(\theta + \gamma_t) + \cos(\theta + \gamma_t)]}{w_2{}^2} + \frac{2a}{w_M{}^2}, \tag{2.24}$$

and

$$\mathcal{C} = \frac{\sin^2(\theta + \gamma_t)}{w_2{}^2} + \frac{1}{w_M{}^2}. \tag{2.25}$$

The eqn. (2.21) gives the temporal broadening due to the GVM , which recoveries to eqn. (18) in ref. [30] using a untitled laser pulse ($\gamma_t = 0$). In our experiment $k = 1.8997$, w_1, w_2 and w_M are estimated to be 200 μm. The temporal broadening $\tau_{\text{GVM}}(\theta, \gamma_t, k)$ is calculated numerically using the parameters in the experiment, shown in figure 2.15. The minimum of τ_{GVM} is corresponding to $\theta = 58.25°$ and $\gamma_t = -58.24°$, which are in good agreement to the direct calculation given in section 2.3.1. The first and second ovals in figure 2.15 correspond to $\tau_{\text{GVM}} \cong 50\text{ fs}, 100\text{ fs}$, respectively. The temporal broadening $\tau_{\text{GVM}}(\theta, \gamma_t, k)$ is more sensitive on γ_t than θ. The rectangle shows the range of τ_{GVM} defined by $56° \leq \gamma_t \leq 60°$ and $56° \leq \theta \leq 60°$. In this range the τ_{GVM} is less than 100 fs,

indicating that the temporal broadening due to the residual velocity mismatch can be kept below 100 fs when both angles are kept within $58.24° \pm 2°$.
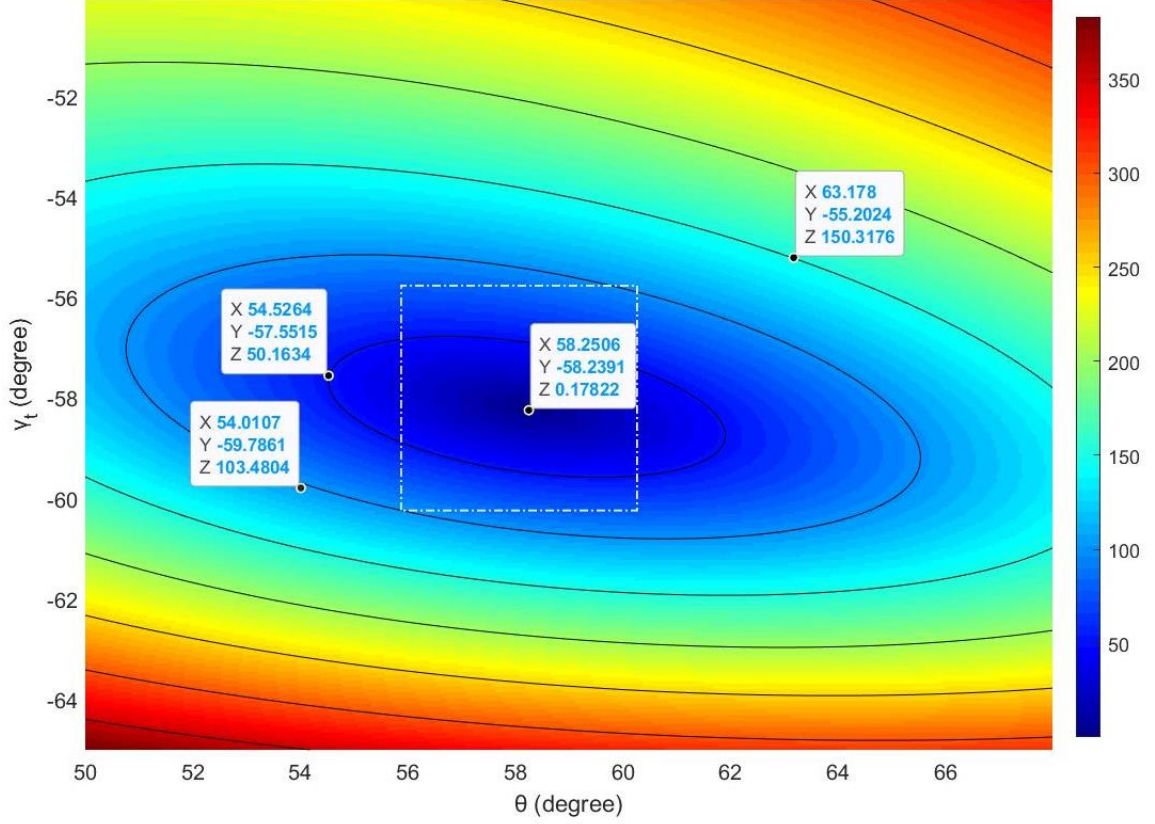
Figure 2.15: Temporal broadening $\tau_{GVM}(\theta, \gamma_t, k)$ due to the residual group velocity mismatch. The parameters in the experiment are used to calculate the temporal broadening numerically with $k = 1.8997$ and $w_1 = w_2 = w_M = 200 \, \mu m$. The unit of temporal broadening is fs. The first and second ovals correspond to $\tau_{GVM} \cong 50 \, fs, 100 \, fs$, respectively.

2.4 Gas phase kiloelectron-volts ultrafast electron diffraction

We demonstrate here a table-top keV-UED setup that combines electron pulse compression and velocity mismatch compensation, which allows us to reach a temporal resolution of

240 fs, more recently ~200 fs, with a low timing drift of 50 fs RMS over several hours. By running the setup at a high repetition rate of 5 kHz, the electron beam current is more than an order of magnitude higher than that has been achieved by MeV-UED facilities. The high repetition rate is made possible by the use of a DC voltage accelerator. The high beam current significantly shortens the experimental beamtimes and enables systematic studies beyond those currently possible. The UED instrument with a small scale is suitable for university laboratories and thus is more accessible.

2.4.1 UED instrument

In order to reach a femtosecond pulse duration of the electron bunch, a DC-RF electron gun is employed where electrons are first accelerated to 90 keV in a DC electric field and then longitudinally compressed by using an time-vary electric field in a RF cavity [26, 91, 92]. The advantage of using a DC accelerator is that the gun can be run at high repetition rates, which is only limited by the repetition rate of the laser system. DC-RF UED setups have been used for solid phase diffraction experiments. However additional challenges due to the low sample density and extended size of the sample target are present in gas phase UED experiments. Particularly, the group velocity mismatch due to the difference of the speeds in laser and electron pulses causes their relative time delay to vary across the gas jet, leading to a degradation of the overall temporal resolution. The minimum temporal broadening due to the velocity mismatch in our keV-UED is estimated to be ~600 fs. We fixed this issue by using a laser pulse with a tilted wavefront and an angled incidence to the propagation direction of electrons such that the projection of the laser velocity along the propagation direction of electrons is equal to the speed of electrons. The schematic of the keV-UED instrument is shown in figure 2.16, described in detail as follows.
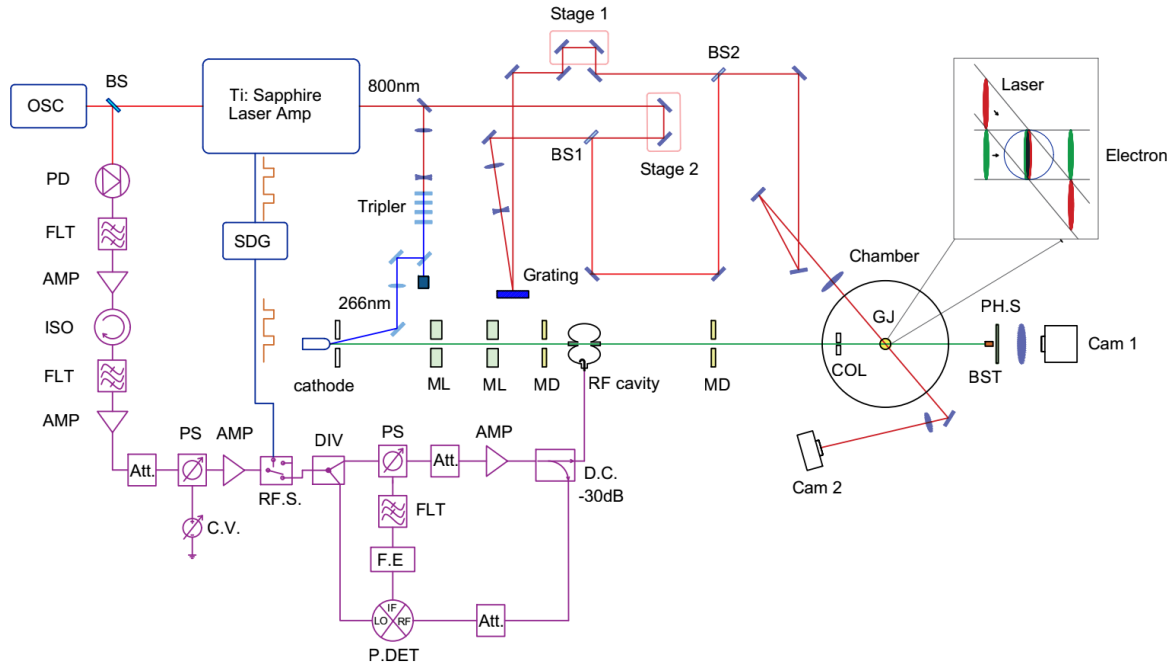
Figure 2.16: Schematic of UED experimental layout. The path drawn in red color represents the pump laser pulse at 800 nm wavelength. A pulse energy of 0.2 mJ is converted to the third harmonic at 266 nm to drive the photocathode, shown here in light blue. BS1 and BS2 are used to pick up a reference pulse for measurement of the tilted pulse duration or making florescence in the sample but are removed when taking diffraction data. The path drawn in green corresponds to the electron beam trajectory, guided by the electron optics, from the photocathode to the detector. The path in purple corresponds to the RF signal used to compress the electron bunch with the RF cavity. Camera 1 captures the light generated by the electrons impinging on the phosphor screen. Camera 2 is used to monitor the laser beam that pumps the sample. The yellow square wave signal from SDG is the electric 5 kHz trigger signal from the laser control unit used to control the release timing of laser pulse and the timing window of the RF pulse. The inset shows a sketch showing the matching of velocities in the gas jet using a laser pulse with a tilted intensity front travelling at an angle with respect to the electron beam. OSC = oscillator, BS = beam

splitter, PD = photo diode, FLT = filter, AMP = amplifier, ISO = isolator, SDG = synchronization and delay generator, Att. = attenuator, RF.S = RF switch, DIV = power divider, PS = phase shifter, C.V.= control voltage, F.E.= feedback electronics, P.DET = phase detector, D.C. = directional coupler, ML = magnetic lens, MD = magnetic deflector, COL = collimator, GJ = gas jet, BST= beam stop, PH.S = phosphorus screen, Cam = camera. (This figure is reproduced from ref [32], used in accordance with the Creative Commons Attribution 4.0 International license.)

The setup consists of three major parts: the pump laser beam (in red color), the electron beamline (in green), and the RF compression system (in purple). The laser pulses (60 fs, 800 nm, 2mJ) are produced by the amplifier (Legend Elite Duo) at a repetition rate of 5 kHz. Most part of the laser pulse energy is used to pump the sample molecules, such as producing impulsive alignment of the nitrogen molecules, and about 10% of the energy is used to generate electrons on a photoelectron gun after being frequency tripled to a UV pulse with a central wavelength of 266 nm. The group velocity mismatch between the electron and laser pulses can be successfully removed using a tilted laser pulse, shown in the inset of figure 2.16. We use two beam splitters (BS1 and BS2) to pick up a reference pulse to measure the pulse duration of the tilted pulse, and to generate fluorescence to overlap the beams to the sample. The two beam splitters are removed when taking diffraction data. The electrons are accelerated to a kinetic energy of 90 keV by a DC voltage, guided by magnetic lens and deflectors and temporally compressed on the sample using a time-varying electric field in the RF cavity. The generation and synchronization of the RF fields is achieved with a home-made RF system, described in section 2.2, based on the design by Otto et al [92]. The RF system enables the setup to run the experiment with high

stability for several hours. The setup is used to capture the rotational dynamics of impulsively aligned molecules, such as nitrogen, CF_3I and CH_3Cl, induced by a short, non-resonant laser pulse. The high beam current has enabled the setup to record the rotational dynamics continuously with high signal levels.

The laser pulse with a tilted pulse front has a time duration of 60 fs and energy of 1mJ and a spot size of 190 µm (H)× 260 µm (V) on the gas jet. We use a 100 µm platinum aperture to collimate the electron beam which delivers on the sample 10,000 electrons per pulse. The repetition rate of the laser and electron pulses is 5 kHz. More electrons per pulse is possible with a larger collimator. A de Laval nozzle with an inner diameter of 30 µm is used to introduce the gas sample to the interaction region as a supersonic gas, and the nozzle backing pressure is 900 torr. We use an electron-multiplying-charge-coupled-device (EMCCD) camera to record the electron scattering patterns from the gas jet, and an optical stage to control the time delay between the laser and electron pulses.

2.4.2 Spatial and temporal overlapping

We overlap the electron beam and the gas jet by moving the nozzle in the direction that is perpendicular to the electron beam to optimize the diffraction intensity. A maximum diffraction intensity indicates that optimal overlapping between the electron beam and the gas jet is obtained. To overlap the laser beam and the gas jet, we use a florescence produced by focusing the laser onto the gas jet. For molecules with a low ionization energy, such as CF_3I, the florescence can be generated with the tilted pulse directly. However, for molecules with a higher ionization energy, such as nitrogen, we use the reference pulse picked from beam splitters (BS1 and BS2), shown in figure 2.16, and make a tighter focus to produce the fluorescence. A camera is used to view the fluorescence from the gas jet,

shown in figure 2.17 (a). A fluorescence generated from CF_3I is shown in figure 2.17 (b). The overlapping of the laser beam and the gas jet is obtained by moving the laser beam perpendicular to the gas jet to maximize the brightness of the fluorescence. When the laser intensity is very high, a dark spot appears in the center of the florescence, indicating a strong plasma produced. In this case, the laser power can be lowered to reduce the size of the dark spot.
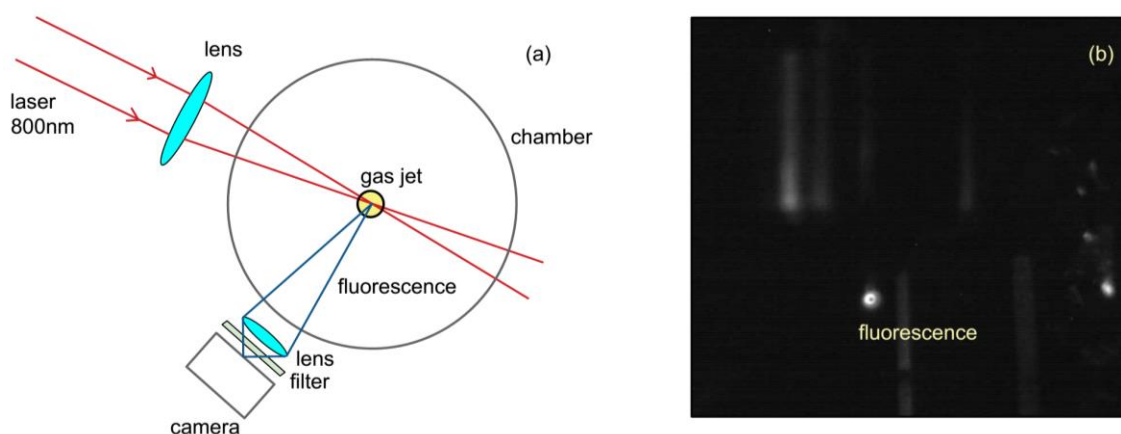
Figure 2.17: Fluorescence generated by an ultrafast laser. (a) A laser beam is focused onto the gas jet to generate fluorescence, and a camera is used to image the fluorescence. (b) Fluorescence generated from CF_3I.

The spatial and temporal overlapping of the laser and electron pulse are obtained by using plasma lensing effect. When the arrival time of the laser pulse is ahead of the electron pulse, the electrons are affected by the charges generated in the gas jet through plasma lensing effect [112, 113]. We adjust the laser power to observe an obvious lensing effect in the electron beam. Figure 2.18 (b) and (c) show the electron beam being affected by plasma. We move the laser along the gas jet to put the stripe due to plasma lensing effect in the middle of the electron beam to optimize the spatial overlapping of the electron and laser

beams. The temporal overlapping, defined by the synchronization of the electron and laser pulses, is determined by observing the appearance of plasma lensing effect while changing the relative time delay between the two pulses, shown in figure 2.18. The total count of the stripe in the middle of the electron beam is used to check the appearance of the plasma lensing effect, displayed by the inset. The time zero is determined to be when the stripe starts to appear, shown as inset 2.18 (b). The time zero is determined to be the corresponding position of the optical stage. We take scans around time zero to record time-dependent signal of molecules due to the laser excitation.
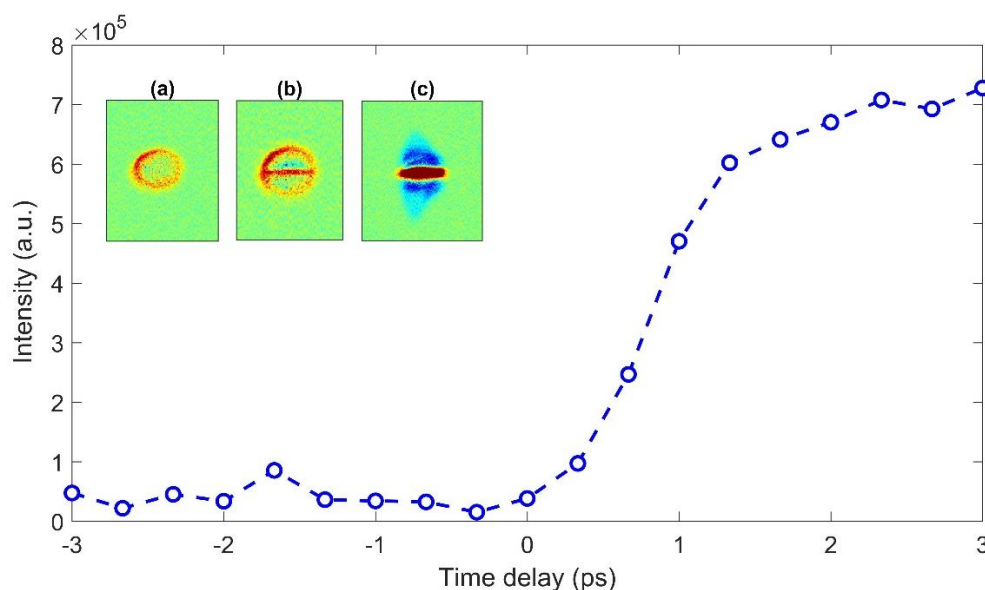
Figure 2.18: Variation of plasma lensing effect by changing the relative time delay between the laser and electron pulses. The intensity is the total count in the area that electrons are affected by plasma. Inset (a) is the profile of electrons (background subtracted) with the arrival time of -333 fs before that of the laser. The background is obtained by setting the arrival time of electron pulse way before that of the laser. Inset (b) corresponds to the electrons with the arrival time of 333 fs after that of the laser. Inset (c) corresponds to the electrons with the arrival time of 2 ps after the laser pulse.

2.4.3 Temporal resolution and timing drift

Impulsive molecular alignment induced by femtosecond laser pulses will be demonstrated experimentally in detail in chapter 4. We use rotational dynamics of laser-induced nitrogen alignment to characterize the temporal resolution and the timing drift of the keV-UED. Rotational wave packets of nitrogen molecules are excited by a femtosecond laser pulse nonadiabatically. The maximum alignment of the nitrogen ensemble is reached shortly after the laser pulse excitation, followed by a dephasing and subsequent periodic revivals. The electron diffraction pattern from aligned nitrogen molecules shows anisotropy, which contrasts against the circular diffraction pattern of randomly oriented molecules. The fast-changing dynamics of nitrogen molecules provides a good measure to evaluate the temporal resolution of the instrument by comparing the experimental result to the theoretical calculation. The temporal resolution is contributed from both the laser and electron pulse durations, the temporal broadening due to residual velocity mismatch, the arrival timing jitter of the electron and laser pulses. The temporal resolution FWHM is determined to be 240 fs by comparing the experiment to the theory, and timing drift over 4.5 hours was on the order of 50 fs RMS, which is comparable to that obtained by the use the MeV-UED setup at SLAC [28].

Chapter 3

Impulsive laser-induced molecular alignment and molecular orientation distribution retrieval

The theoretical work of retrieving molecular orientation distribution and atom-pair angular distribution described in this chapter have previously appeared in the publications [32, 114]. *Used with permission.*

3.1 Introduction

Laser-induced molecular alignment has been an active field in recent years due to new capabilities for manipulating molecular arrangement in space and an increasing number of applications [115-120]. The methods of molecular alignment using laser pulses generally can be classified into two categories: adiabatic alignment, and nonadiabatic alignment. Adiabatic alignment experiments are conducted using a laser with a long pulse duration: $\tau_{\text{pulse}} \gg \tau_{\text{rot}}$, where τ_{pulse} is the laser pulse duration and τ_{rot} is the rotational period for linear or symmetric tops, or the rotational time scale for asymmetric top molecules. For adiabatic alignment, the molecules can be aligned by the use of an intense, continuous wave (CW) field, proposed in ref. [121, 122], where dynamical considerations do not play a role [117, 123]. When the CW field is on, the eigenstates of the field-free Hamiltonian are evolving adiabatically into the corresponding pendular states of the complete Hamiltonian, including kinetic and potential energy, whereas when the field is off, the pendular states return to the original field-free states [117, 123]. The main drawback of adiabatic alignment is that the alignment is lost once the field is turned off.

We focus on nonadiabatic alignment induced by a femtosecond laser pulses for current experimental interests in this chapter. Nonadiabatic alignment requires a short laser pulse $\tau_{\text{pulse}} \ll \tau_{\text{rot}}$. The molecules in nonadiabatic alignment remain in coherent wave packets after interacting with the short laser pulse, which produces a prompt alignment peak, followed by the process of dephasing and rephasing that produces the alignment revivals. Thus, the field-free aligned molecules can be obtained [117, 123]. Nonadiabatic alignment allows the molecules to be investigated in a field-free environment.

There has been an increasing number of applications for molecular alignment induced by ultrafast lasers in recent years. Some of the applications include: investigation and manipulation of chemical reactions [124-127], molecular orbital tomography [128-131], imaging of molecular structure and capturing dynamics with ultrafast laser or electron pulses [18, 19, 132-136], generation of ultra-short light pulses [137] and high-order harmonics of light [138-142], determination of photoelectron angular distributions in dissociating and spinning molecules [143-145], control of the rotational and torsional motion in molecules [146], control of photoionization dynamics [125, 147, 148], transient-absorption spectroscopy [149], optical image storage [150], and quantum information processing [151]. To take advantage of these applications, it is of great importance to accurately retrieve the full dynamics of molecular orientation distribution (MOD), as a function of Euler angles, because it contains the most direct knowledge of the ensemble. MOD here is defined to be the probability density distribution of the principal axes of inertia tensor of the molecule (body-fixed frame) with respect to the axes of the space-fixed (lab) frame.

The rotational dynamics of molecules induced by an ultrafast laser have been widely investigated theoretically [121, 123, 152-155] and experimentally [117, 156-158]. Coulomb explosion imaging has been employed to quantitatively characterize the spatial alignment of molecules by recording the three-dimensional momentum and angular distributions of the fragmented ions following the explosion event [156-163]. The information of angular distributions can be extracted from the ion signal distributions. The MOD has only been directly measured in special cases in which the ions are generated along the symmetry axis of the molecule, which is corresponding to one of its principal inertia directions [160, 164, 165]. Another method that can characterize the MOD is rotational Raman spectroscopy. In this method, the amplitude, frequency, and phase of rotational wave packets in nonadiabatic alignment can be obtained by a Fourier transform of an appropriate time-domain trace that corresponds to the full dynamics of the alignment of molecular ensemble [166, 167]. However, this method requires capturing multiple periods of a trace that reflects the molecular alignment in field-free environment and is thus mainly feasible to the case of free-space dynamics after impulsive interaction between the molecule and laser pulse is complete. Ultrafast electron diffraction (UED) has been used to successfully capture rotational dynamics of laser induced alignment of nitrogen molecules [19, 113] and characterize the degree of alignment in symmetric top molecules [18]. UED is directly sensitive to the internuclear distances and atom-pair angular distributions of the molecules, and for the simplest case of a linear molecule, the atom-pair angular distribution is identical to the MOD [32].

The measurement of MOD for nonlinear molecules in general cases to date remains an unresolved challenge except for special cases mentioned above. Therefore, methods of

retrieving the MOD from the experimental measurement are of great importance. Several methods and experiments have been reported to obtain MOD and angular distribution of ions for linear [168], symmetric [169], and asymmetric top molecules [170]. However, the reported methods [168-171] require the solution of the time-dependent Schrödinger equation (TDSE) to obtain the best matching between the theoretical calculation and experimental measurement such that the MOD and corresponding experimental parameters initiating the rotational alignment could be determined, i.e. laser fluence and rotational temperature of the molecular ensemble.

In this chapter, I demonstrate the theory that maps the MOD to the atom-pair angular distributions for nonlinear molecules in general case. With the theory, the methods for retrieving the MOD from measured atom-pair distribution are developed for different cases. The methods do not require solving the TDSE with experimental parameters, work for both adiabatic and nonadiabatic alignment. The contents of this chapter, which are organized below, will prepare the theories for experimental results in chapter 4. First, I will give a brief review of the theory of nonadiabatic alignment of molecules induced by an ultrafast laser pulse. Second, I present the derivations of the theory that relates the MOD to the atom-pair angular distributions of molecular ensemble, and the corresponding retrieval methods in different cases. At last, I demonstrate that the atom-pair angular distributions can be extracted by applying the inverse Fourier transform, followed by the Abel inversion, to the molecular scattering intensity.

3.2 Theory of nonadiabatic molecular alignment

Here we briefly review the theory of molecular alignment by use of a short, linearly polarized, non-resonant laser field. *The review of the theory of laser induced nonadiabatic*

alignment of molecules follows the descriptions in ref. [123, 172-176]. The content

includes the field-free molecular rotation, the potential energy due to the interaction of the

induced dipole and the electric field, the rotational wave packet of a single molecule, and

the observables of rotational wave packets in a molecular ensemble.

3.2.1 Field-free molecular rotation
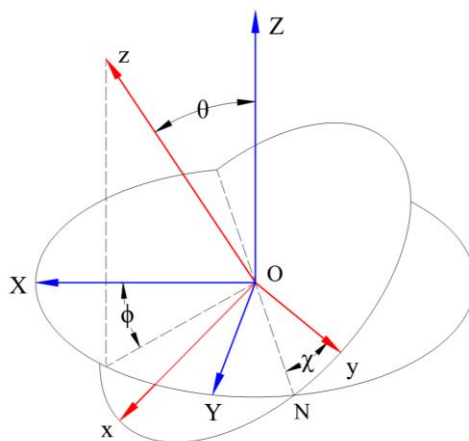
Figure 3.1: The space-fixed (lab) frame XYZ and molecule-fixed (body) frame xyz are

related by the three rotations defined by the Euler angles (ϕ, θ, χ). The polarization of the

electric field is along the Z axis. (This figure is reproduced from ref. [114], with the

permission of APS Publishing.)

The motion of a rigid body is described by the use of two systems of coordinates: a space-

fixed system (lab frame) XYZ, and a molecule-fixed system (body frame) xyz which

participates the motion [172]. Figure 1 shows the molecule-fixed frame xyz, typically

defined by the principal axes of the moment of inertia [172], and space-fixed frame XYZ.

The body frame of the molecule and the lab frame are related through three rotations

defined by the Euler angles (ϕ, θ, χ) (the details of the rotations are shown in ref. [173]).

Within the rigid rotor approximation and assumption that the molecule is in ground vibronic state, the rotational kinetic energy is given by

$$H_{\text{rot}} = \frac{J_x^2}{2I_{xx}} + \frac{J_y^2}{2I_{yy}} + \frac{J_z^2}{2I_{zz}} , \tag{3.1}$$

where J_k, k=x, y, z is the components of the total angular momentum in Cartesian coordinate defined by the body frame and I_{kk} is the corresponding principal moments of inertia. If all the three principal moments of inertia are equal, the molecule is a spherical top. If two are equal ($I_{xx} = I_{yy} \neq I_{zz}$), the molecule is a symmetric top, which can be further divided into two categories: prolate symmetric top ($I_{xx} = I_{yy} > I_{zz}$), and oblate symmetric top ($I_{xx} = I_{yy} < I_{zz}$). In the case of linear molecule, $I_{zz} = 0$ and $I_{xx} = I_{yy}$. The molecule is called an asymmetrical top if the three principal moments of inertia are all different. The kinetic energy is commonly expressed in terms of the rotational constants using $\frac{1}{2I_{kk}}$. In convention, the I_{xx}, I_{yy}, I_{zz} are denoted as I_{aa}, I_{bb}, I_{cc} with $I_{aa} \leq I_{bb} \leq I_{cc}$. By defining the corresponding rotational constants, $A_e = \frac{1}{2I_{aa}}, B_e = \frac{1}{2I_{bb}}, C_e = \frac{1}{2I_{cc}}$, and $A_e \geq B_e \geq C_e$ we have

$$H_{\text{rot}} = A_e J_a^2 + B_e J_b^2 + C_e J_c^2 . \tag{3.2}$$

For *prolate symmetric top* molecules ($A_e > B_e = C_e$), we can choose $J_a = J_z$. Thus, H_{rot} can be written as

$$H_{\text{rot}} = C_e \boldsymbol{J}^2 + (A_e - C_e)J_z^2 . \tag{3.3}$$

The eigenvalues and corresponding eigenfunctions of time-independent Schrödinger equation (TISE), formulated as $H_{\text{rot}}\Psi = E\Psi$, are

$$E^{JK} = C_e J(J+1) + (A_e - C_e)K^2, \tag{3.4}$$

$$|JKM\rangle = \left(\frac{2J+1}{8\pi^2}\right)^{\frac{1}{2}} e^{iM\phi} d^J_{MK}(\theta) e^{iK\chi}, \tag{3.5}$$

where J is the quantum number of the total angular momentum, K is quantum number of the projection of the angular momentum on z axis, M is the quantum number of the projection of angular momentum on Z axis, and $d^J_{MK}(\theta)$ is the Wigner's d-matrix, defined in ref. [173]. Note that the $\hbar^2$ is omitted for the energy levels. For *oblate symmetric top* molecules $(A_e = B_e > C_e)$, $J_c = J_z$ and $H_{\text{rot}} = A_e \mathbf{J}^2 + (C_e - A_e)J_z^2$. Thus, the eigenvalues of TISE are $E^{JK} = A_e J(J+1) + (C_e - A_e)K^2$. In the case of a *linear molecule* (rigid rotor), $I_{zz} = 0$ and $H_{\text{rot}} = B_e \mathbf{J}^2$. Thus, the eigenvalues and eigenfunctions of TISE are

$$E^J = B_e J(J+1), \tag{3.6}$$

$$|JM\rangle = Y_{JM}(\theta, \phi), \tag{3.7}$$

where Y_{JM} is the spherical harmonics. The energy levels and wavefunctions of the *asymmetric top* molecules cannot be represented by an explicit form that is analogous to those of the symmetric tops. The eigenfunctions are expanded by the linear combinations of symmetric top wave functions, and the coefficients are obtained by the corresponding secular equations. Numerical calculations are required to obtain the energy levels and the eigenfunctions, see [174, 177] for details. The energy levels can be written in different forms, and two of these quantitative formulas are given below (first one due to ref. [178], and second one ref. [179, 180])

$$E = \frac{1}{2}(B_e + C_e)J(J+1) + \left[A_e - \frac{1}{2}(B_e + C_e)\right]W_\tau, \tag{3.8}$$

$$E = \frac{1}{2}(A_e + C_e)J(J+1) + \frac{1}{2}(A_e - C_e)E_\tau, \tag{3.9}$$

where W_τ and E_τ are quantities that depend in a complicated manner on A_e, B_e, C_e and J, and $2J + 1$ different energy levels are assumed for a given J.

3.2.2 Interaction potential

The potential energy due to the interaction between a molecule and the laser field is given by [181-183]

$$V(t) = -\boldsymbol{\mu} \cdot \boldsymbol{E}(t) - \frac{1}{2}\boldsymbol{\alpha}\boldsymbol{E}(t) \cdot \boldsymbol{E}(t) - \frac{1}{6}\boldsymbol{\beta}\boldsymbol{E}(t)\boldsymbol{E}(t) \cdot \boldsymbol{E}(t) + \cdots, \tag{3.10}$$

where $\boldsymbol{\mu}$ is the permanent electric dipole moment of the molecule, $\boldsymbol{E}(t)$ is the electric field of the laser pulse, $\boldsymbol{\alpha}$ is the polarizability tensor, and $\boldsymbol{\beta}$ is the hyperpolarizability tensor. For a femtosecond laser pulse with a central wavelength of 800 nm, the period of the fast carrier wave is 2.67 fs. Thus, the fast oscillation of the electric field does not affect the rotational motion of the molecule. The terms in eqn. (3.10) with odd orders of $\boldsymbol{E}(t)$ vanish after averaging over the cycles of the fast carrier wave. The interaction potential is represented by the second term in eqn. (3.10) since the terms with a higher even order can be negligible for the level of laser intensity ($\sim 10^{13}$W/cm^2) in the experiment. The electric field $\boldsymbol{E}(t)$ is linearly polarized along the Z axis in the lab frame, given by

$$\boldsymbol{E}(t) = \frac{1}{2}\big[\varepsilon(t)e^{i\omega t} + \text{c.c.}\big]\boldsymbol{e}_Z, \tag{3.11}$$

where $\varepsilon(t)$ is the envelope of the electric field of the laser pulse, ω is the central frequency of the laser, or the frequency of the carrier wave, c.c. stands for the complex conjugate and $\boldsymbol{e}_Z$ is the unit vector along Z axis. In the case where the laser frequency is much lower than any vibronic transition frequencies of the molecule, the molecule is in the ground vibronic state and only the rotationally excited states need to be considered. The interaction potential in this situation can be written as [123, 175, 176]

$$H_{\text{ind}} = \sum_j \varepsilon_j \, \mu_j^{\text{ind}} = -\frac{1}{4}\sum_{jk} \varepsilon_j \, \alpha_{jk}\varepsilon_k^* \,, \tag{3.12}$$

where j and k are the indices of the Cartesian coordinates in lab frame, $\mu_j^{\text{ind}} = \sum_k \alpha_{jk}\varepsilon_k^*$ is

the component of the induced electric dipole moment, and α_{jk} is the component of the

polarizability tensor in lab frame. The polarizability tensor can be expressed in the body

frame of the molecule according to the tensor transformation rule under coordinate change

[123], formulated as $\alpha_{\rho\rho'} = \sum_{kk'}\langle\rho|k\rangle\,\alpha_{kk'}\langle k'|\rho'\rangle$, where ρ,ρ' are the indices of the

coordinates in the lab frame, k, k' are indices of body frame coordinates, and $\langle\rho|k\rangle$ is the

components of the direction cosine matrix, given in [173, 184]. The polarizability tensor in

body frame can be calculated by the use of the *ab initio* quantum chemistry program,

ORCA [185]. By using the polarizability tensor in the body frame of the molecule, the

interaction potential is given by [123]

$$H_{\text{ind}}(t) = -\frac{\varepsilon^2(t)}{4}[\alpha^{zx}\cos^2\theta + \alpha^{yx}\sin^2\theta\sin^2\chi]$$

$$= -\frac{\varepsilon^2(t)}{4}\left\{\frac{\alpha^{zx}+\alpha^{zy}}{3}D_{00}^2(\phi,\theta,\chi) - \frac{\alpha^{yx}}{\sqrt{6}}[D_{02}^2(\phi,\theta,\chi) + D_{0-2}^2(\phi,\theta,\chi)]\right\}, \tag{3.13}$$

where $\alpha^{zx} = \alpha_{zz} - \alpha_{xx}$, $\alpha^{yx} = \alpha_{yy} - \alpha_{xx}$, α_{kk} are the components of polarizability

tensor in the body frame, $D_{MK}^J(\phi,\theta,\chi) = e^{iM\phi}d_{MK}^J(\theta)e^{iK\chi}$ is Wigner D-matrix, defined

in ref. [173]. Eqn. (3.13) omits the terms that are independent of the angles since they

simply shift the potential and have no effect on the alignment dynamics. The interaction

potential H_{ind} has no dependence on ϕ, leading to the conservation of the eigenvalue $(M\hbar)$

of J_Z, the projection of total angular momentum $\boldsymbol{J}$ on the Z axis. Alternatively, according

to classical mechanics, the torque exerted on the induced dipole due to the electric field $\boldsymbol{E}$

is perpendicular to $\boldsymbol{E}$, resulting in the conservation of J_Z. The dependence of H_{ind} on θ and

χ produces a wave packet in J and K spaces, giving rise to a larger probability density of the molecule that orients at certain θ and χ angles. In the case of a symmetric top or linear top molecule, $\alpha_{xx} = \alpha_{yy} \neq \alpha_{zz}$, eqn. (3.13) is simplified to [123]

$$H_{\text{ind}}(t) = -\frac{\varepsilon^2(t)}{4}\Delta\alpha\cos^2\theta, \qquad (3.14)$$

where $\Delta\alpha = \alpha^{zx} = \alpha_{\parallel} - \alpha_{\perp}$, and $\alpha_{\parallel}, \alpha_{\perp}$ are the polarizability components along and perpendicular to the symmetric axis of the molecule. Since the interaction potential has no dependence on both ϕ and χ in this case, both the quantum numbers K and M are conserved during the interaction. The complete Hamiltonian contains both the rotationally kinetic energy H_{rot} and the interaction potential H_{ind}.

3.2.3 Rotational wave packets

Here we introduce the theory of nonadiabatic alignment of a symmetric top molecule by a non-resonant, linearly polarized ultrafast laser pulse. The alignment process can be described by the time-dependent Schrödinger equation (TDSE) [123]

$$i\hbar\frac{\partial\Psi(t)}{\partial t} = H(t)\Psi(t), \qquad (3.15)$$

$$H(t) = H_{\text{rot}} + H_{\text{ind}}(t). \qquad (3.16)$$

For a *prolate symmetric* top, the solution of eqn. (3.15) can be expanded by $|JKM\rangle$ as a basis. Since the J_Z is conserved, the wavefunction $\Psi(t)$ is written as

$$\Psi_{J_i K_i M_i}(t) = \sum_{J,K} c^{JKM_i}(t)\,|JKM_i\rangle, \qquad (3.17)$$

where the inital state of the molecule before the interaction is $|J_i K_i M_i\rangle$, and $c^{JKM_i}(t)$ are the parameters as a function of time. Inserting (3.17) into (3.15), and using the orthonormalimity of the basis functions, we have

$$i\hbar\dot{c}^{JKM_i}(t) = \sum_{J',K'} c^{J'K'M_i}(t)\langle JKM_i|H(t)|J'K'M_i\rangle$$

$$= \sum_{J',K'} c^{J'K'M_i}(t)\delta_{KK'}\left[E^{J'K'}\delta_{JJ'} - \frac{\varepsilon^2(t)\Delta\alpha}{6}\langle JKM_i|D_{00}^2|J'K'M_i\rangle\right]. \qquad (3.18)$$

The rotaional matrix can be represented and calculated by the Wigner 3-j symbols and Clebsch-Gordan coefficents according to the eqn. (3.118), (3.125), (2.27) and (2.25) in ref. [173].

$$\langle JKM|D_{mn}^l|J'K'M'\rangle = (-1)^{M'-K'}\sqrt{(2J+1)(2J'+1)}\begin{pmatrix} J & l & J' \\ M & m & -M' \end{pmatrix}\begin{pmatrix} J & l & J' \\ K & n & -K' \end{pmatrix}. \qquad (3.19)$$

The conditions for the matrix element to be nonzero are $|J-l| \leq J' \leq J+l$, $M' = M+m$, $K' = K+n$. Therefore the selection rules of the interaction, shown in eqn. (3.18), are $|J-2| \leq J' \leq J+2$, and $K' = K$. Since $|J_iK_iM_i\rangle$ is the initial state and quantum number K is conversved, eqn. (3.18) can be further simplified to

$$i\hbar\dot{c}^{JK_iM_i}(t) = \sum_{J'} c^{J'K_iM_i}(t)\left[E^{JK_i}\delta_{JJ'} - \frac{\varepsilon^2(t)\Delta\alpha}{6}\langle JK_iM_i|D_{00}^2|J'K_iM_i\rangle\right]. \qquad (3.20)$$

The coefficients $c^{JK_iM_i}(t)$ can be solved numerically by the use of the Matlab function ode45 [186], and the one-molcule wavepacket during the interaction is a pure state, formulated as $\Psi_{J_iK_iM_i}(t) = \sum_J c^{JK_iM_i}(t)|JK_iM_i\rangle$. The differential equation indicates that, given an initial state $|J_iK_iM_i\rangle$, a series of new states are produced through the interaction of the induced dipole and the electric field with selection rule $|J-2| \leq J' \leq J+2$, and both the quantum number K_i and M_i do not change during the excitation. After the interaction, the wavepacket evolves in free space according to

$$\Psi_{J_iK_iM_i}(t) = \sum_J \tilde{c}^{JK_iM_i}e^{-i\frac{E^{JK_i}}{\hbar}t}|JK_iM_i\rangle, \qquad (3.21)$$

where $\tilde{c}^{JK_iM_i}$ are the coeffecents when the interaction is complete, and E^{JK_i} are energy levels given in eqn. (3.4). The equations for symmetric top mentioned above can be also employed to calculate the excitation process of *linear molecules* with $K_i = 0$, and the basis functions are reduced to spherical harmonics, shown in eqn. (3.7). The matrix element is given by

$$\langle J0M|D_{00}^2|J'0M'\rangle = (-1)^{M_i}\sqrt{(2J+1)(2J'+1)} \begin{pmatrix} J & 2 & J' \\ M & 0 & -M' \end{pmatrix} \begin{pmatrix} J & 2 & J' \\ 0 & 0 & 0 \end{pmatrix}.$$

The conditions for the matrix element to be nonzero are $|J-2| \leq J' \leq J+2$, $M' = M$ and $J' + J + 2 =$ even. Therefore the selectrion rules for excitation of *linaer molecules* are $J' = J \pm 2$ and $M' = M$.

3.2.4 Observables of a molecule ensemble

We showed in the last section the rotational wave packet of a single molecule produced by the interaction between the induced dipole and the electric field. In gas phase laser induced molecular alignment experiments, the initial states are in a thermal distribution, determined by the Boltzmann distribution and nuclear spin statistics. The distribution of the initial state $|n\rangle$ is given by [123, 187]

$$W_{|n\rangle} = \frac{S_{|n\rangle}\exp\left(-\frac{E^n}{k_BT_{\text{rot}}}\right)}{Q_{\text{rot}}}, \tag{3.22}$$

where $S_{|n\rangle}$ is the weight factor due to nuclear spin statistics, $|n\rangle$ represents $|J_iK_iM_i\rangle$ for symmetric top and $|J_iM_i\rangle$ for linear molecules, E^n is the energy level of the state $|n\rangle$, k_B is the Boltzmann constant, T_{rot} is the rotational temperature of the ensemble, and Q_{rot} is the partition function.

Ref. [187, 188] show that for the general case in which a molecule has C_{3v} symmetry and the spin of the three identical nuclei is I, the weight factors due to nuclear spin statistics are: $\frac{1}{3}(2I + 1)(4I^2 + 4I + 3)$ for K divisible by 3, and $\frac{1}{3}(2I + 1)(4I^2 + 4I)$ for K not divisible by 3. The discussion of nuclear spin weights for homonuclear diatomic molecules has been shown in detail in ref. [189, 190]. Upon the permutation $(\hat{P}_{AB})$ of two identical nuclei A, B, the total wavefunction, formulated as $\psi = \psi_{ele}\psi_{vib}\psi_{rot}(\theta, \phi)\psi_{spin}(A, B)$, is symmetric for bosons, and antisymmetric for fermions. For the ground state $^1\Sigma_g^+$, the electronic and vibrational wavefunctions are not affected by the $\hat{P}_{AB}$ operator. However, for rotational wavefunctions $\hat{P}_{AB}\psi_{rot}(\theta, \phi) = (-1)^J\psi_{rot}(\theta, \phi)$, and for nuclear spin function $\hat{P}_{AB}\psi_{spin} = \psi_{spin}$ in symmetric nuclear spin states, and $\hat{P}_{AB}\psi_{spin} = -\psi_{spin}$ in antisymmetric spin states. In general, the ratio of the symmetric to antisymmetric spin states is $(I + 1)/I$, where I is the spin of the nuclei. For example, ^{14}N is a boson as $I=1$, and the total wavefunction must be symmetric upon the permutation. Therefor the rotational wavefunction $\psi_{rot}(\theta, \phi)$ with even J is twice of that with odd J.

The MOD (probability density distribution of molecule orientation) in the general case is given by [123]

$$\rho(\phi, \theta, \chi, t) = \sum_n W_{|n\rangle}|\Psi_n(\phi, \theta, \chi, t)|^2 . \tag{3.23}$$

In the case of symmetric top molecules (or linear molecules) aligned by a linearly polarized laser field, the probability density of the wavepacket after the interaction is given by

$$\left|\Psi_{J_iK_iM_i}(t)\right|^2 = \sum_{J'J''} \tilde{c}^{J'K_iM_i}{}^* \tilde{c}^{J''K_iM_i} e^{-i\frac{\Delta E_{J'J''}}{\hbar}t} |J'K_iM_i\rangle^*|J''K_iM_i\rangle , \tag{3.24}$$

where $|J'K_iM_i\rangle^*$ is the complex conjugate of $|J'K_iM_i\rangle$, and $\Delta E_{J'J''} = C_e[J'(J'+1) - J''(J''+1)] = 2nC_e$. The difference in the energy leves implies that there are revivals of the alignment with period $\tau = \frac{\pi\hbar}{C_e} = \frac{2\pi I_{cc}}{\hbar}$, which has the same form as the revival period for linear molecules shown in [191]. Since the MOD has no dependence on ϕ and χ for linear and symmetric top molecules, it can be written as

$$\rho(\phi, \theta, \chi, t) = \left(\frac{1}{2\pi}\right)^2 \rho_1(\theta, t). \tag{3.25}$$

The degree of alignment, which is commonly used to describe the evolution of the alignment, is defined as [123]

$$\langle\cos^2\theta\rangle(t) = \sum_n W_{|n\rangle}(T) \langle\Psi_n(t)|\cos^2\theta|\Psi_n(t)\rangle. \tag{3.26}$$

However, this metric reduces the dynamics to a single number at a certain time t and thus contains far less information than the MOD.

3.3 Molecular orientation distribution

The ultrafast electron diffraction (UED) patterns of laser aligned molecules contains information about the angular distribution and interacomic distance of each atom pair in the molecule, as shown in eqn. (1.44). For the case of linear molecules, the atom-pair angular distribution is equivalent to the MOD. For nonlinear molecules, however, the angular distribution of the atom pairs does not directly reflect the MOD. The exception is the special case where there is an atom pair along the axis of symmetry of the molecule and the interatomic distance of this atom pair does not overlap with any other interatomic distances in the molecule, but this condition is generally not satisfied. Atom-pair angular distributions can be measured experimentally by the use of Coulomb explosion imaging [156-164], UED [19, 32, 192], X-ray diffraction [133, 193, 194], *etc*. However, the

function $\rho(\phi, \theta, \chi)$ cannot be measured directly. In this section we show the relation between the MOD and the atom-pair angular distributions. *The derivations shown here were first published in ref.* [114].
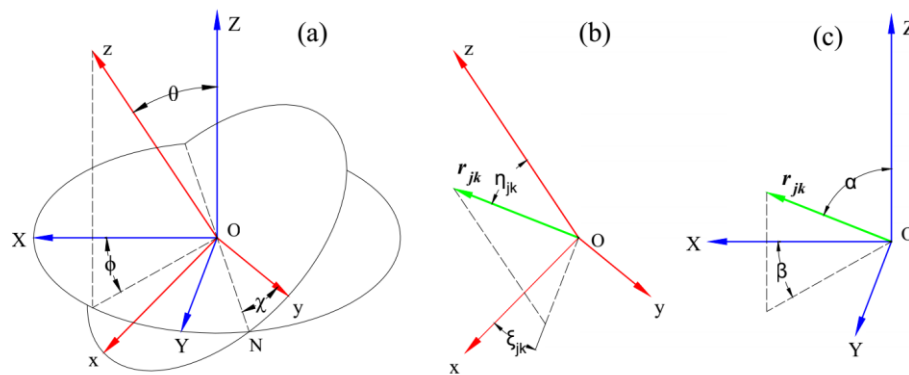
Figure 3.2: Description of a vector (atom pair) in lab and body frames. (a) lab frame XYZ and body frame xyz are related by the three rotations defined by the Euler angles (ϕ, θ, χ). (b) The orientation of an atom pair $\boldsymbol{r}_{jk}$ is described by the polar and azimuthal angles (η_{jk}, ξ_{jk}) defined in the body frame. (c) The orientation of $\boldsymbol{r}_{jk}$ in the lab frame is described by the angles (α, β). (This figure is reproduced from ref. [114], with the permission of APS Publishing.)

For illustration purposes, figure 3.1 is again displayed in figure 3.2(a), showing the body frame xyz and lab frame XYZ. The orientation of an atom pair (labeled as jk) in a molecule is indicated by its corresponding vector $\boldsymbol{r}_{jk}$ and is described by the polar and azimuthal angles (η_{jk}, ξ_{jk}), shown in figure 3.2(b). For a rigid molecule, the angles (η_{jk}, ξ_{jk}) are fixed in the body frame. After the rotations, the orientation of $\boldsymbol{r}_{jk}$ in the lab frame is described by the angles (α, β), shown in figure 3.2(c). The orientation distribution of the molecule is $\rho(\phi, \theta, \chi)$, and correspondingly, the orientation of the atom pair jk has an

angular distribution denoted as $g_{jk}(\alpha, \beta)$. Here we show how $g_{jk}(\alpha, \beta)$ is related to $\rho(\phi, \theta, \chi)$. First, we will show how the angles (α, β) are related to the (ϕ, θ, χ) and (η_{jk}, ξ_{jk}). Second, we derive the probability distribution of $\boldsymbol{r}_{jk}$ from $\rho(\phi, \theta, \chi)$ by using the transformation theory of bivariate random variables.

Suppose $\boldsymbol{r}$ is an arbitrary vector having the Cartesian components (X, Y, Z) in the lab frame and the components (x, y, z) in the body frame. The body frame is obtained by applying the unitary transformation expressed by the product of three Euler angle rotations $\boldsymbol{\Phi}(\phi, \theta, \chi) = \mathbf{R_z}(\chi)\mathbf{R_N}(\theta)\mathbf{R_Z}(\phi)$ to the lab frame, as shown in figure 3.2(a). The details are shown in ref. [173]. The two representations of the vector $\boldsymbol{r}$ in two frames are related by the transformation, eqn. (3.37) in ref. [173], below

$$\begin{pmatrix} X \\ Y \\ Z \end{pmatrix} = \begin{bmatrix} c\phi c\theta c\chi - s\phi s\chi & -c\phi c\theta s\chi - s\phi c\chi & c\phi s\theta \\ s\phi c\theta c\chi + c\phi s\chi & -s\phi c\theta s\chi + c\phi c\chi & s\phi s\theta \\ -s\theta c\chi & s\theta s\chi & c\theta \end{bmatrix} \begin{pmatrix} x \\ y \\ z \end{pmatrix}, \qquad (3.27)$$

where cosine and sine are denoted by c and s for simplification when the expression is long. The atom pair (η_{jk}, ξ_{jk}) defined in the body frame of the molecule ends up with an orientation described by (α, β) after the three rotations defined by the directional cosine matrix. For convenience, we use (η, ξ), instead of (η_{jk}, ξ_{jk}), to indicate the orientation of the atom pair jk in a molecule. The corresponding unit vector of the atom pair jk is $\boldsymbol{b} = (\sin\eta \cos\xi, \sin\eta \sin\xi, \cos\eta)$. Note that we do not distinguish the row and column vectors here. The orientation of the atom pair vector in the lab frame after the rotations can be obtained using eqn. (3.27):

$$\boldsymbol{B} = \begin{pmatrix} c\phi c\theta s\eta c(\chi + \xi) - s\phi s\eta s(\chi + \xi) + c\phi s\theta c\eta \\ s\phi c\theta s\eta c(\chi + \xi) + c\phi s\eta s(\chi + \xi) + s\phi s\theta c\eta \\ -s\theta s\eta c(\chi + \xi) + c\theta c\eta \end{pmatrix}. \qquad (3.28)$$

The atom pair in the lab frame is described by the polar and azimuthal angles (α, β) and $\boldsymbol{B} = (\sin\alpha\cos\beta, \sin\alpha\sin\beta, \cos\alpha)$. Thus, we have

$$c\alpha = -s\theta s\eta c(\chi + \xi) + c\theta c\eta , \tag{3.29}$$

$$s\alpha s\beta = s\phi c\theta s\eta c(\chi + \xi) + c\phi s\eta s(\chi + \xi) + s\phi s\theta c\eta, \tag{3.30}$$

$$s\alpha c\beta = c\phi c\theta s\eta c(\chi + \xi) - s\phi s\eta s(\chi + \xi) + c\phi s\theta c\eta. \tag{3.31}$$

By organizing right side of eqn. (3.30), we have

$$\sqrt{[c\theta s\eta c(\chi + \xi) + s\theta c\eta]^2 + [s\eta s(\chi + \xi)]^2} \left[s\phi \frac{c\theta s\eta c(\chi+\xi)+s\theta c\eta}{\sqrt{[c\theta s\eta c(\chi+\xi)+s\theta c\eta]^2+[s\eta s(\chi+\xi)]^2}} + \right.$$

$$\left. c\phi \frac{s\eta s(\chi+\xi)}{\sqrt{[c\theta s\eta c(\chi+\xi)+s\theta c\eta]^2+[s\eta s(\chi+\xi)]^2}} \right].$$

It is easy to check that $[c\theta s\eta c(\chi + \xi) + s\theta c\eta]^2 + [s\eta s(\chi + \xi)]^2 + [-s\theta s\eta c(\chi + \xi) + c\theta c\eta]^2 = 1$. Thus $s\alpha = \sqrt{[c\theta s\eta c(\chi + \xi) + s\theta c\eta]^2 + [s\eta s(\chi + \xi)]^2}$. Eqn. (3.30) yields

$$s\beta = s\phi c\delta + c\phi s\delta = s(\phi + \delta) . \tag{3.32}$$

A similar organization of (3.31) yields

$$c\beta = c(\phi + \delta) . \tag{3.33}$$

Eqn. (3.32) and (3.33) indicate:

$$\beta = \phi + \delta, \tag{3.34}$$

where $s\delta = \frac{s\eta s(\chi+\xi)}{\sqrt{[c\theta s\eta c(\chi+\xi)+s\theta c\eta]^2+[s\eta s(\chi+\xi)]^2}}$ and $c\delta = \frac{c\theta s\eta c(\chi+\xi)+s\theta c\eta}{\sqrt{[c\theta s\eta c(\chi+\xi)+s\theta c\eta]^2+[s\eta s(\chi+\xi)]^2}}$. The relation between (α, β) and (ϕ, θ, χ) is given by (3.29) and (3.34). Using $c(\chi + \xi) = \frac{c\theta c\eta - c\alpha}{s\theta s\eta}$ from (3.29), we have

$$c\delta = \frac{c\theta s\eta c(\chi+\xi)+s\theta c\eta}{\sqrt{[c\theta s\eta c(\chi+\xi)+s\theta c\eta]^2+[s\eta s(\chi+\xi)]^2}} = \frac{c\eta-c\theta c\alpha}{s\theta s\alpha}.$$ (3.35)

According to (3.29), (3.34) and (3.35), (ϕ, χ) can be expressed in terms of (α, β) as follows, and θ can be considered as a parameter or an arbitrary variable. There are two solutions of (ϕ, χ) corresponding to (α, β). For $\chi + \xi \leq \pi$

$$\begin{cases} \phi_1 = \beta - \cos^{-1}(\frac{\cos\eta-\cos\theta\cos\alpha}{\sin\theta\sin\alpha}) \\ \chi_1 = \cos^{-1}(\frac{\cos\eta\cos\theta-\cos\alpha}{\sin\theta\sin\eta}) - \xi \end{cases}.$$ (3.36)

For $\chi + \xi > \pi$

$$\begin{cases} \phi_2 = \beta - 2\pi + \cos^{-1}(\frac{\cos\eta-\cos\theta\cos\alpha}{\sin\theta\sin\alpha}) \\ \chi_2 = 2\pi - \cos^{-1}(\frac{\cos\eta\cos\theta-\cos\alpha}{\sin\theta\sin\eta}) - \xi \end{cases}.$$ (3.37)

Now we calculate the probability density function of (α, β) for a certain θ as a parameter, denoted as $w(\alpha, \beta, \theta)$, according to the theory of bivariate transformation in [195]. The Jacobians are given by

$$J_1 = \begin{vmatrix} \frac{\partial\phi_1}{\partial\alpha} & \frac{\partial\phi_1}{\partial\beta} \\ \frac{\partial\chi_1}{\partial\alpha} & \frac{\partial\chi_1}{\partial\beta} \end{vmatrix} = -\frac{\partial\chi_1}{\partial\alpha} = \frac{\sin\alpha}{\sqrt{(\sin\theta\sin\eta)^2-(\cos\theta\cos\eta-\cos\alpha)^2}},$$ (3.38)

$$J_2 = \begin{vmatrix} \frac{\partial\phi_2}{\partial\alpha} & \frac{\partial\phi_2}{\partial\beta} \\ \frac{\partial\chi_2}{\partial\alpha} & \frac{\partial\chi_2}{\partial\beta} \end{vmatrix} = -\frac{\partial\chi_2}{\partial\alpha} = \frac{-\sin\alpha}{\sqrt{(\sin\theta\sin\eta)^2-(\cos\theta\cos\eta-\cos\alpha)^2}}.$$ (3.39)

If θ is considered as an arbitrary variable, the Jacobians are determinants of the 3×3 Matrix, but the results are the same since $\partial\theta/\partial\alpha$, $\partial\theta/\partial\beta$=0 and $\partial\theta/\partial\theta$=1. The joint probability density function of (ϕ, θ, χ) is $\rho(\phi, \theta, \chi)$, which is in our case the MOD. Then $w(\alpha, \beta, \theta)$ is given by

$$w(\alpha,\beta,\theta) = |J_1|\rho(\phi_1,\theta,\chi_1) + |J_2|\rho(\phi_2,\theta,\chi_2)$$

$$= \frac{\sin\alpha}{\sqrt{(\sin\theta\sin\eta)^2-(\cos\theta\cos\eta-\cos\alpha)^2}}[\rho(\phi_1,\theta,\chi_1) + \rho(\phi_2,\theta,\chi_2)] , \qquad (3.40)$$

where $\phi_1, \chi_1, \phi_2, \chi_2$ are given by (3.36) and (3.37). The inequality $(\sin\theta\sin\eta)^2 - (\cos\theta\cos\eta - \cos\alpha)^2 > 0$ must be fulfilled such that the Jacobian term is nonzero. Therefore, we can write $w(\alpha,\beta,\theta)$ as

$$w(\alpha,\beta,\theta) = u(\alpha,\theta,\eta)[\rho(\phi_1,\theta,\chi_1) + \rho(\phi_2,\theta,\chi_2)],$$

where $u(\alpha,\theta,\eta)$ is defined as

$$u(\alpha,\theta,\eta) = \begin{cases} \frac{\sin\alpha}{\sqrt{(\sin\theta\sin\eta)^2-(\cos\theta\cos\eta-\cos\alpha)^2}} & \text{if } (\sin\theta\sin\eta)^2 - (\cos\theta\cos\eta - \cos\alpha)^2 > 0 \\ 0 & \text{otherwise} \end{cases}.$$

$$(3.41)$$

The atom-pair angular distribution $g(\alpha,\beta)$ is given by

$$g(\alpha,\beta)\sin\alpha = \int_0^\pi w(\alpha,\beta,\theta)\,\sin\theta\,d\theta .$$

Therefore, we have

$$g(\alpha,\beta)\sin\alpha = \int_0^\pi u(\alpha,\theta,\eta)[\rho(\phi_1,\theta,\chi_1) + \rho(\phi_2,\theta,\chi_2)]\sin\theta\,d\theta.$$

Now we can switch (η,ξ) back to (η_{jk}, ξ_{jk}) for angular distribution of the atom pair marked by jk:

$$g_{jk}(\alpha,\beta)\sin\alpha = \int_0^\pi u(\alpha,\theta,\eta_{jk})[\rho(\phi_1,\theta,\chi_1) + \rho(\phi_2,\theta,\chi_2)]\sin\theta\,d\theta . \qquad (3.42)$$

The $\phi_1, \chi_1, \phi_2, \chi_2$ are calculated using (3.36) and (3.37) by replacing (η,ξ) with (η_{jk}, ξ_{jk}), and $u(\alpha,\theta,\eta_{jk})$ is calculated by (3.41) with η replaced by η_{jk}. In eqn. (3.42), $\sin\alpha$ can be cancelled on both sides, and the equation is:

$$g_{jk}(\alpha, \beta) = \int_0^\pi \tilde{u}(\alpha, \theta, \eta_{jk})[\rho(\phi_1, \theta, \chi_1) + \rho(\phi_2, \theta, \chi_2)] \sin \theta \, d\theta, \tag{3.43}$$

where $\tilde{u}(\alpha, \theta, \eta)$ is given by

$$\tilde{u}(\alpha, \theta, \eta_{jk}) = \begin{cases} \dfrac{1}{\sqrt{(\sin\theta\sin\eta_{jk})^2 - (\cos\theta\cos\eta_{jk} - \cos\alpha)^2}} & \text{if } (\sin\theta\sin\eta_{jk})^2 - (\cos\theta\cos\eta_{jk} - \cos\alpha)^2 > 0 \\ 0 & \text{otherwise} \end{cases} \tag{3.44}$$

The inequality $(\sin\theta\sin\eta_{jk})^2 - (\cos\theta\cos\eta_{jk} - \cos\alpha)^2 > 0$ requires that $|\eta_{jk} - \theta| <$ $\alpha < \eta_{jk} + \theta$ for $\eta_{jk} + \theta \leq \pi$, and $|\eta_{jk} - \theta| < \alpha < 2\pi - (\eta_{jk} + \theta)$ for $\eta_{jk} + \theta > \pi$.

3.4 Retrieval of molecular orientation distribution

We demonstrate in this section the retrieval of MOD for nonlinear molecules using the atom-pair angular distributions g_{jk} that can be measured experimentally by using Coulomb explosion imaging [156-164], UED [19, 32, 192], *etc*. We demonstrate the retrieval methods for different cases, which depend on the polarization of the pump laser for the alignment. *The derivations shown here were first published in ref. [114].*

We first present the method to retrieve the MOD with the form $\rho(\phi, \theta, \chi) = (\frac{1}{2\pi})^2 \rho_1(\theta)$, referring to the one-dimensional (1-D) alignment. In the case of symmetric top molecules aligned by a linearly polarized laser field along Z axis in figure 3.2, the ρ has no dependence on ϕ and χ such that it can be written as a function of θ [123, 196, 197]. By inserting $\rho = (\frac{1}{2\pi})^2 \rho_1(\theta)$ into eqn.(3.42), we have the equation $g_{jk}(\alpha, \beta) \sin \alpha = \int_0^\pi \frac{1}{2\pi^2} u(\alpha, \theta, \eta_{jk}) \rho_1(\theta) \sin \theta \, d\theta$. As $g_{jk}(\alpha, \beta)$ has no dependence on β, and by defining $g_{jk}(\alpha)\sin\alpha = \int_0^{2\pi} g_{jk}(\alpha, \beta)\sin\alpha \, d\beta$, we have

$$g_{jk}(\alpha) \sin \alpha = \frac{1}{\pi} \int_0^\pi \rho_1(\theta) u(\alpha, \theta, \eta_{jk}) \sin \theta \, d\theta. \tag{3.45}$$

Eqn. (3.45) can be calculated numerically by the discrete integral:

$$g_{\mathrm{jk}}(\alpha)\sin\alpha \cong \textstyle\sum_{q=1}^{N}\rho_1(\theta_q)u(\alpha,\theta_q,\eta_{\mathrm{jk}})\sin\theta_q\frac{\Delta\theta}{\pi},$$

where $\Delta\theta = \pi/N$ and $\theta_q = q\Delta\theta$. By defining $y_p = g_{\mathrm{jk}}(\alpha_p)\sin\alpha_p$, $x_q = \rho_1(\theta_q)\sin\theta_q$,

and $\mathrm{U}_{pq} = u(\alpha_p,\theta_q,\eta_{\mathrm{jk}})\frac{\Delta\theta}{\pi}$, we can write the equation as

$$y_p = \textstyle\sum_{q=1}^{N}\mathrm{U}_{pq}\cdot x_q. \tag{3.46}$$

The matrix U_{pq} is a square matrix when we choose the number of elements in x and y to

be equal to N. Thus eqn. (3.45) can be expressed as a linear transformation $y = \mathrm{U}x$, where

vector y is measured experimentally, and the matrix U can be calculated using the known

structure of the molecule. The retrieval of MOD is to find the solution of x in a system of

linear equations.

If ρ is a function of more than one variable, we can expand it with a basis set, formulated

as $\rho = \sum_i f_i S_i$, where the f_i are the coefficients to be determined, and S_i are the basis

functions. In the general case ρ is function of (ϕ,θ,χ), and S_i can be chosen to be the

eigenfunctions of the free-space symmetric top. When ρ is a function of θ,χ, we can use

the real spherical harmonics for S_i. With the expansion, the retrieval of MOD is equivalent

to looking for the solution of a system of linear equations, demonstrated as follows.

Here we show the retrieval method in the case of $\rho(\phi,\theta,\chi) = \frac{1}{2\pi}\rho_2(\theta,\chi)$, referring to the

2-D alignment. For an asymmetric top molecule aligned by a linearly polarized laser, the

quantum number M is conserved during the interaction, and the MOD has the form:

$$g_{jk}(\alpha,\beta)\sin\alpha = \frac{1}{2\pi}\int_0^\pi u(\alpha,\theta,\eta_{\mathrm{jk}})[\rho_2(\theta,\chi_1)+\rho_2(\theta,\chi_2)]\sin\theta\,d\theta.$$

Since χ_1 and χ_2 are not functions of β, the $g_{jk}(\alpha, \beta)$ has no dependence on β. By defining

$g_{jk}(\alpha)\sin\alpha = \int_0^{2\pi} g_{jk}(\alpha, \beta)\sin\alpha \, d\beta$, we have

$$g_{jk}(\alpha)\sin\alpha = \int_0^{\pi} u(\alpha, \theta, \eta_{jk})[\rho_2(\theta, \chi_1) + \rho_2(\theta, \chi_2)]\sin\theta \, d\theta, \qquad (3.47)$$

where ρ_2 is a real function, which can be expanded by the real spherical harmonics $S_{lm}(\theta, \chi)$ introduced in ref. [198]:

$$\rho_2(\theta, \chi) = \sum_{lm} f_{lm} S_{lm}(\theta, \chi), \qquad (3.48)$$

where f_{lm} are the coefficients to determine for each S_{lm}. Inserting (3.48) into (3.47), we have

$$g_{jk}(\alpha)\sin\alpha = \sum_{lm} f_{lm} \int_0^{\pi} u(\alpha, \theta, \eta_{jk})[S_{lm}(\theta, \chi_1) + S_{lm}(\theta, \chi_2)]\sin\theta \, d\theta. \qquad (3.49)$$

By defining $V_{lm}(\alpha) = \int_0^{\pi} u(\alpha, \theta, \eta_{jk})[S_{lm}(\theta, \chi_1) + S_{lm}(\theta, \chi_2)]\sin\theta \, d\theta$, we can calculate $V_{lm}(\alpha)$ numerically. Eqn. (3.49) yields

$$g_{jk}(\alpha)\sin\alpha = \sum_{lm} f_{lm} V_{lm}(\alpha). \qquad (3.50)$$

By using one index p for data bins of α, and another index q to represent lm, we can write eqn. (3.50) as a linear transformation $y_p = \sum_q V_{pq} f_q$, where $y_p = g_{jk}(\alpha_p)\sin\alpha_p$, $V_{pq} = V_q(\alpha_p)$. The retrieval of MOD is to find the solution of f in the system of linear equations $y = Vf$, where y is a vector of experimental measurements, and the matrix V can be calculated using the known structure of the molecule and the spherical harmonicas. Since there will be many more data points of y than f, it is likely to be an equation with an overdetermined matrix. However such equations are solvable by methods such as Moore-

Penrose Inverse [199]. For *m*=0, eqn. (3.50) can be applied to the retrieval of 1-D alignment as well, which indicates that $\rho_1(\theta)$ is expanded by the Legendre polynomials.

Now we consider retrieval of MOD in the general case in which ρ is a function ϕ, θ, χ, refereeing to 3-D molecular alignment, such as asymmetric top molecules aligned by using elliptically polarized laser pulses or two linearly polarized pulses with orthogonal polarization. In this case, $g_{jk}(\alpha, \beta)$ is a function of both α and β, and $\rho(\phi, \theta, \chi)$ is a non-negative function. We can use the eigenfunctions of free-space symmetric top $|JKM\rangle$ as a basis set to expand $\rho(\phi, \theta, \chi)$, where $|JKM\rangle = \left(\frac{2J+1}{8\pi^2}\right)^{\frac{1}{2}} e^{iM\phi} d^J_{MK}(\theta) e^{iK\chi}$. However, as $|JKM\rangle$ are complex funcitons, the coefficient of each $|JKM\rangle$ must fullfill certain conditions. Eqn. (3.70) in ref. [173] shows that $d^J_{MK}(\theta)$ has the following properties:

$$d^J_{MK}(\theta) = (-1)^{M-K} d^J_{KM}(\theta) = (-1)^{M-K} d^J_{-M-K}(\theta). \tag{3.51}$$

Therefore, for $M - K = $ even,

$$|JKM\rangle + |J - K{-}M\rangle = 2\left(\frac{2J+1}{8\pi^2}\right)^{\frac{1}{2}} d^J_{MK}(\theta)\cos(M\phi + K\chi). \tag{3.52}$$

For $M - K = $ odd,

$$|JKM\rangle + |J - K{-}M\rangle = 2i\left(\frac{2J+1}{8\pi^2}\right)^{\frac{1}{2}} d^J_{MK}(\theta)\sin(M\phi + K\chi). \tag{3.53}$$

We use $D_{JKM}(\phi, \theta, \chi)$ to denote $|JKM\rangle$ for convenience of formulism below. The MOD is expanded as

$$\rho(\phi, \theta, \chi) = \sum_{JKM} f_{JKM} D_{JKM}(\phi, \theta, \chi), \tag{3.54}$$

where $D_{JKM}(\phi, \theta, \chi) = |JKM\rangle$. The conditions for the right side of (3.54) to be real are that

$f_{JKM} = f_{J-K-M}$, f_{JKM} is real for $M - K =$ even, and f_{JKM} is purely imaginary for $M - K =$ odd. Equivalently, the coefficients for $M - K =$ odd can be predefined as $i \cdot f_{JKM}$ such that all f_{JKM} are real. Inserting (3.54) into eqn. (3.42), we have

$$g_{jk}(\alpha, \beta)\sin\alpha = \sum_{JKM} f_{JKM} W_{JKM}(\alpha, \beta) , \qquad (3.55)$$

$$W_{JKM}(\alpha, \beta) = \int_0^\pi u(\alpha, \theta, \eta_{jk})[D_{JKM}(\phi_1, \theta, \chi_1) + D_{JKM}(\phi_2, \theta, \chi_2)] \sin\theta \, d\theta, \qquad (3.56)$$

where $W_{JKM}(\alpha, \beta)$ can be calculated with the basis functions and the structure of the molecule. Eqn. (3.55) can be written as a linear transformation by properly manipulating the indices of the data bins and the basis functions. In practice both $g_{jk}(\alpha, \beta)\sin\alpha$ and $W_{JKM}(\alpha, \beta)$ are two-dimensional arrays, whereas they can be converted into one-dimensional arrays by using one index p to map each data point at (α_i, β_n), and another index q to represent JKM. The number of p equals the multiplication of number of α_i and number of β_n. Therefore eqn. (3.55) can be written as a linear transformation $y_p = \sum_q W_{pq} f_q$, where $y_p = g_{jk}(\alpha_i, \beta_n)\sin\alpha_i$ and $W_{pq} = W_{JKM}(\alpha_i, \beta_n)$ with the mapping relation $p \leftrightarrow (i, n)$ and $q \leftrightarrow$ JKM. Retrieval of the MOD is again to find the solution of vector f in a system of linear equations $y = Wf$ with the certain constraint conditions discussed below eqn. (3.54), where y is the measurement, and W is the matrix given by eqn. (3.56). Eqn. (3.54) reduces to the retrieval of the MOD in 2-D alignment for K=0.

When two or more atom-pair angular distributions are measured, the measured data sets can be combined such that the retrival is equivalent to finding the solution of one system of linear equations. For example, when two data sets y_1, y_2 are available, the linear transformation is written as

$$\begin{bmatrix} y_1 \\ y_2 \end{bmatrix} = \begin{bmatrix} W_1 \\ W_2 \end{bmatrix} f, \tag{3.57}$$

where the matrix W are contributed from two parts W_1, W_2 which are calculated according to parameters of the two atom pairs repesctively. The coefficients f here can be determined by sovling the linear equations, whereas they can also be obtained by minimazing the residual sum of squares between the measurement and the theoretical modeling, shown in ref. [197]. The retrival methods demonstrated here do not require solving the TDSE with experimental parameters that launch the rotational wavepacket, provided that the atom-pair anglur distribution is experimentally measured, and the methods are applicable independent of the means to produce the molecular alignment.

3.5 Measurement of atom-pair angular distributions

We have derived the method to retrieval MOD in section 3.4. Here we show that the atom-pair angular distribution can be obtained by applying the Fourier transform, followed by the Abel inversion, to the experimentally measured two-dimensional diffraction pattern measured by UED. *The derivations shown here were first published in ref.* [32, 114]. Define a Cartesian coordinate system x_1-x_2-x_3 for the molecules in real space, where the plane x_1-x_2 is parallel to the surface of 2-dimensinoal (2D) flat detector (s_1-s_2), the x_2-axis corresponds to the direction of the laser polarization, and the x_3-axis represents the direction of propagation of the incident electron beam. Comparing to the lab coordinate defined figure 3.2 (a), x_2-axis is the Z axis, and x_3-axis the X axis. For a general function $u(s)$, the Abel transform of $\text{FT}_{3D}^{-1}[u(s)]$ is

$$\int_{-\infty}^{+\infty} dx_3 \, \text{FT}_{3D}^{-1}[u(s)] = \int_{-\infty}^{+\infty} dx_3 \iiint ds_1 ds_2 ds_3 \, u(s) e^{i(s_1 x_1 + s_2 x_2 + s_3 x_3)}$$

$$= \iiint ds_1 ds_2 ds_3 \, u(\boldsymbol{s}) e^{i(s_1 x_1 + s_2 x_2)} \delta(s_3) = \iint ds_1 ds_2 \, u(s_1, s_2, s_3 = 0) e^{i(s_1 x_1 + s_2 x_2)} \, ,$$

(3.58)

where FT_{3D}^{-1} represents inverse Fourier transform. Eqn. (3.58) can be written in the inversion form when $\mathrm{FT}_{3D}^{-1}[u(\boldsymbol{s})]$ is cylindrically symmetric to axis x_2, shown below

$$\mathrm{FT}_{3D}^{-1}[u(s_1, s_2, s_3)] = \mathrm{Abel}^{-1}\mathrm{FT}_{2D}^{-1}[u(s_1, s_2, s_3 = 0)].$$

(3.59)

The molecular scattering intensity of an ensemble of molecules is a summation over molecules with all orientations. For molecules aligned by a linear polarized laser, the quantum number M is conserved (see section 3.2), and $\rho(\phi, \theta, \chi)$ has no dependence on ϕ. Therefore, according to eqn. (3.36), (3.37), (3.42), the angular distribution of atom pairs in the general case can be written as $g_{jk}(\alpha)$, which refers to one-dimensional alignment. The molecular scattering is given by

$$I_{\mathrm{mol}}(\boldsymbol{s}) = \iint \sum_{j=1}^{n} \sum_{k=1, j \neq k}^{n} f_j^*(s) f_k(s) \, e^{-i \boldsymbol{s} \cdot \boldsymbol{r}_{jk}(\alpha_0, \beta_0)} \, g_{jk}(\alpha_0) \sin\alpha_0 d\alpha_0 d\beta_0 \, ,$$

(3.60)

where $g_{jk}(\alpha_0) = g_{kj}(\alpha_0)$. The inverse Fourier transform of $I_{\mathrm{mol}}(\boldsymbol{s})$ is

$$\mathrm{FT}_{3D}^{-1}[I_{\mathrm{mol}}(\boldsymbol{s})] = \sum_{j,k=1, j \neq k}^{n} \iint g_{jk}(\alpha_0) \sin\alpha_0 \delta[\boldsymbol{r} - \boldsymbol{r}_{jk}(\alpha_0, \beta_0)] \, d\alpha_0 d\beta_0 \otimes F_j(-\boldsymbol{r}) \otimes F_k(\boldsymbol{r}), \text{(3.61)}$$

where α_0, β_0 are the polar angle, azimuthal angle with respect to the laser polarized direction along x_2 axis, F is the Fourier transform of the atomic scattering amplitude f, and is proportional to the atomic potential [60]. By definition, we have $F_j(-\boldsymbol{r}) \otimes F_k(\boldsymbol{r}) = F_j(\boldsymbol{r}) \star F_k(\boldsymbol{r})$, where $\otimes$ signifies convolution and $\star$ stands for correlation. The delta function in spherical coordinate is $\delta[\boldsymbol{r} - \boldsymbol{r}_{jk}(\alpha_0, \beta_0)] = \frac{1}{r^2 \sin\alpha} \delta(r - r_{jk}) \delta(\alpha - \alpha_0) \delta(\beta - \beta_0)$. Thus, the integral in eqn. (3.61) becomes:

$$\iint g_{jk}(\alpha_0) \sin\alpha_0 \delta[\boldsymbol{r} - \boldsymbol{r}_{jk}(\alpha_0, \beta_0)] d\alpha_0 d\beta_0 = \frac{g_{jk}(\alpha)\delta(r-r_{jk})}{r_{jk}{}^2} . \tag{3.62}$$

Equation (3.61) becomes:

$$\text{FT}_{3D}^{-1}[I_{mol}(\boldsymbol{s})] = \sum_{j=1}^{n} \sum_{k=1, j \neq k}^{n} g_{jk}(\alpha) \, \delta(r - r_{jk}) \otimes \frac{F_j(r) \star F_k(r)}{r_{jk}{}^2} . \tag{3.63}$$

The $\delta(r - r_{jk})$ are part of the pair distribution function (PDF), which has a peak with position corresponding to the internuclear distance between each pair of atoms in the molecule. The term $g_{jk}(\alpha)$ is the angular distribution of the atom pair marked as jk in real space. Equation (3.63) shows that each component of the PDF is convoluted with a correlation of the Fourier transform of the atomic form factors. Here we define the right hand of eqn. (3.63) as a modified pair distribution function (MPDF).

We now show how the molecular scattering intensity measured on a 2D detector with limited dimensions relates to eqn. (3.63). We define a truncating function h(s) that corresponds to the effective measurement area, which can be formulated as $h(s)=1$ for $s \leq s_{max}$, and $h(s)=0$ for $s > s_{max}$, with its Fourier inversion H(r). For small angle diffraction experiments, the momentum transfer component along the x_3-axis can be approximated to be zero $s_3 \cong 0$. Define $I_{mol}^{E}(\boldsymbol{s}) = h(s) \cdot I_{mol}(\boldsymbol{s})$, and $I_{mol}^{E}(\boldsymbol{s})$ measured on the detector is $I_{mol}^{E}(s_1, s_2, s_3 = 0) = h(s_1, s_2, s_3 = 0) \cdot I_{mol}(s_1, s_2, s_3 = 0)$. Replacing $I_{mol}(\boldsymbol{s})$ with $I_{mol}^{E}(\boldsymbol{s})$ in (3.63), and using eqn. (3.59), we have

$$\text{Abel}^{-1}\text{FT}_{2D}^{-1}[I_{mol}^{E}(s_1, s_2, s_3 \cong 0)] = H(r) \otimes \sum_{j,k=1, j \neq k}^{n} g_{jk}(\alpha) \, \delta(r - r_{jk}) \otimes \frac{F_j(r) \star F_k(r)}{r_{jk}{}^2} ,$$

$$\text{Abel}^{-1}\text{FT}_{2D}^{-1}[I_{mol}^{E}(s_1, s_2, s_3 \cong 0)] = \sum_{j,k=1, j \neq k}^{n} g_{jk}(\alpha) H(r - r_{jk}) \otimes \frac{F_j(r) \star F_k(r)}{r_{jk}{}^2} , \tag{3.64}$$

where $H(r - r_{jk})$ is the measured pair distribution function (PDF) for atom pair jk, which is the convolution of the ideal PDF and the Fourier inversion of the function truncating the diffraction signal due to the limited size of the detector. Using the symmetry of the alignment with respect to the laser polarization, the 3-dimensional MPDF is shown in two-dimensional form by the use of $r = (\rho, x_2)$, where $\rho = \sqrt{x_1^2 + x_3^2}$ and $\tan\alpha = \frac{\rho}{x_2}$. Alternatively, the MPDF is generated by the Fourier inversion, followed by the Abel inversion, of the ratio of the molecular and atomic scattering intensities:

$$\text{Abel}^{-1}\text{FT}_{2D}^{-1}\left[\frac{I_{mol}^E(s_1,s_2,s_3\cong 0)}{I_{atom}}\right] = \sum_{j=1}^{n}\sum_{k=1,j\neq k}^{n} g_{jk}(\alpha)\, H(r-r_{jk}) \otimes \frac{\tilde{F}_j(r)\star\tilde{F}_k(r)}{r_{jk}^2}, \quad (3.65)$$

where $\tilde{F}$ is the Fourier transform of the normalized atomic scattering amplitude $\frac{f(s)}{\sqrt{I_{atom}}}$, which has a narrower distribution than F. The ratio is used to narrow the broad profile of the Fourier transform of the atomic scattering amplitude.

Chapter 4

Diffractive imaging of molecular alignment induced by an ultrafast laser

Portions of this material have previously appeared in the publications [32, 114, 196]. *Used with permission.*

4.1 Introduction

Capturing the fast structural change of molecules requires a high spatiotemporal resolution on the order of femtosecond and sub-Angstrom, and a sufficiently high signal-to-noise level to detect the continuous evolution of dynamics with high fidelity. Multiple experimental methods recently have been developed to capture nuclear motions during chemical reactions or laser induced molecular alignment, such as Coulomb explosion ion imaging [46, 47], ultrafast X-ray scattering [51], laser-induced electron diffraction [56, 57], and gas phase ultrafast electron diffraction [54, 55]. The diffractive methods have the advantage of being directly sensitive to the internuclear distances and spatial orientation of the atom pairs in the molecule. UED has the additional advantages that it does not disturb the sample and its scattering cross section is six orders of magnitude stronger than that of X-ray scattering, resulting in a much shorter exposure time. And dynamical structural information directly from the experimental data could be obtained by using UED, without theoretical modeling of the effect of the probe on the system.

MeV-UED with a temporal resolution of 150 fs has enabled several major scientific advances [19, 20, 26-28, 32], such as the capturing coherent rotation [19] and vibrational motion [20], observation of molecular relaxation through conical intersections and photon-

dissociation dynamics upon UV excitation [21], resolving molecular vibrations and transient structural dynamics in the electronic ground state [53], capturing a ring opening reaction [90], and more recently simultaneously observing nuclear and electronic motions [52]. However, the main limitation of MeV-UED has been the low signal-to-noise levels because of the low electron current needed to maintain the high temporal resolution and the dilute nature of gas phase samples. This often limits the amount of data that can be recorded. Previous experiments have demonstrated that MeV-UED is able to capture the rotational dynamics of laser aligned nitrogen molecules [19], whereas the measurement was limited to a few frames of the diffraction patterns due to the low signal-to-noise level that requires long integration times to obtain high fidelity data.

Imaging the full temporal evolution of the dynamics during a photoinduced reaction is essential for elucidating the reaction mechanisms. We demonstrate here that a table-top gas phase keV-UED setup is able to capture the full dynamics to understand the reactions. The keV-UED setup has a temporal resolution of 240 fs and an electron beam current that is more than an order of magnitude higher than those at typical MeV-UED setups. We present the rotational dynamics of laser aligned molecules captured by our keV-UED in this chapter. By using the high current keV-UED setup, we captured the full rotational dynamics of impulsively aligned nitrogen molecules that allows us to retrieve a movie of the rotational motion with high fidelity. The rapid rotational dynamics of nitrogen molecules is used to characterize the overall temporal resolution and timing drift of the UED instrument. We also captured the rotational dynamics of laser aligned trifluoro-iodomethane (CF_3I) molecules and show that we can directly retrieve the full evolution of molecular orientation distribution (MOD) of symmetric top molecules. In the last

experiment, molecules with different isotopes are differentiated by impulsively aligning the molecules and observing the time dependent anisotropy over multiple revivals. We demonstrated the technique experimentally by investigating the rotational dynamics of chloromethane with two naturally occurring chlorine isotopes ^{35}Cl and ^{37}Cl.

4.2 Experiment setup
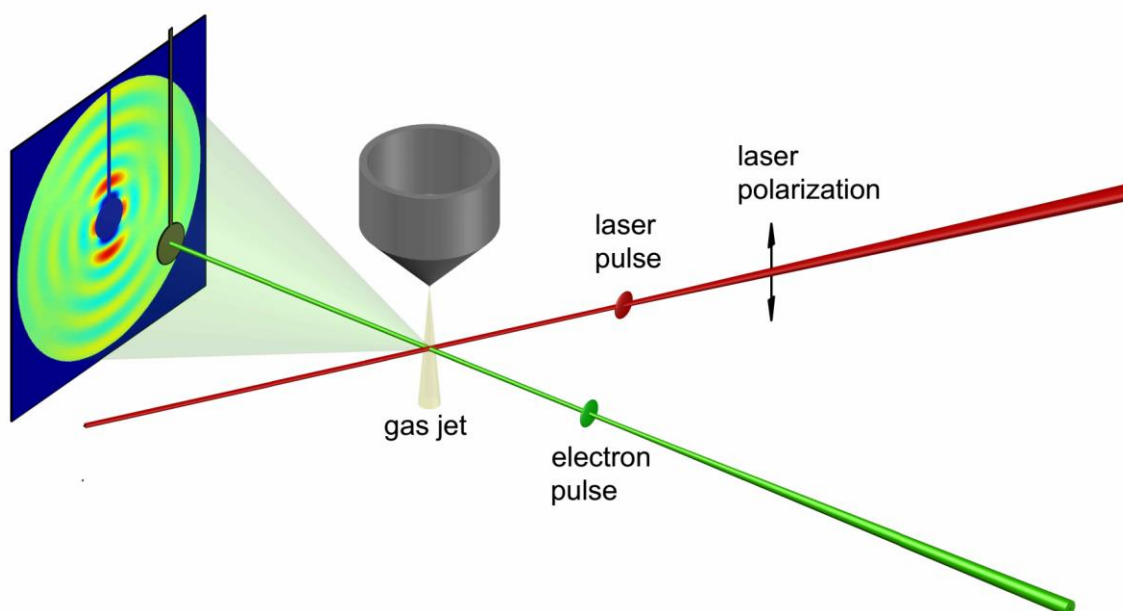
Figure 4.1: Diagram of the keV-UED experiment. The diagram shows a gas jet being introduced into the chamber from the nozzle, with the laser and electron pulses traveling from right to left. The polarization of the laser (Z axis) is orthogonal to the propagation direction of both the electron (X axis) and laser beams. A tilted laser pulse is used to compensate the group velocity mismatch between the laser and electron pulses. The directly transmitted electron beam is blocked by a copper beam stop, and the scattering electrons are recorded by an imaging detector (parallel to Y-Z plane). (This figure is reproduced from ref. [114], with the permission of APS Publishing.)

We use a keV-UED instrument to capture diffraction patterns from a sample of laser aligned molecules as a function of the time delay between the pump laser pulse and the probe electron pulse. The details of the KeV-UED setup have been demonstrated in chapter 2 and ref. [26, 32]. Each diffraction pattern is a snapshot in which the information of molecular ensemble is encoded. Figure 4.1 shows a diagram of the interaction region containing a gas jet of the target molecules, and the laser and electron beams. Each laser pulse is split into an infrared (IR) pulse as a pump and a pulse for photoelectron generation after being frequency tripled. The pump laser pulse has a wavelength of 800 nm, minimum pulse duration of 40 fs FWHM, energy of 1 mJ, and beam diameter of 190 µm (horizontal) × 260 µm (vertical) FWHM at the sample. The laser pulse duration can be stretched to longer pulse durations to minimize ionization while remaining in the impulsive alignment regime. The polarization of the laser is orthogonal to the propagation direction of both the electron and laser beams. The group velocity mismatch between laser and electron pulses is compensated by using a tilted intensity front of the laser pulse and setting up a certain angle between the laser and electron beams [25, 32].

The probe electron pulse is generated by shining a 266 nm ultraviolet laser pulse onto a copper cathode. A hybrid DC-RF electron gun is employed to deliver the keV electron pulse, where the electrons are first accelerated to 90 keV (speed of 0.53 c) in a DC field and then is temporally compressed at the sample utilizing a time-varying electric field in a RF cavity. The electron pulse is guided by electron optics and collimated by a platinum aperture and is then delivered to the sample for scattering measurements. The electron beam current is adjustable by changing the size of the platinum aperture. Using a platinum

aperture with a 200 μm diameter enables a beam current of 20 picoamperes, corresponding to 25,000 electrons per pulse. The repetition rate of the instrument is 5 kilohertz.

The sample gas is seeded in helium with an adjustable ratio to lower the rotational temperature. We use a backing pressure of 900 torr to produce a supersonic jet through a de Laval nozzle with an inner orifice of 30 μm diameter. The gas jet is perpendicular to the plane made up of the electron and laser beams, with the laser incident at an angle of ~60° with respect to the electron beam propagation. The electron scattering patterns are recorded using an electron-multiplying charge-coupled device (EMCCD) through a phosphor screen that is imaged onto the EMCCD.

4.3 Rotational dynamics of impulsively laser-aligned nitrogen molecules

A moderately intense ultrafast laser pulse is used to excite the rotational wavepackets of nitrogen molecules. For the nitrogen alignment experiment, the sample is pure nitrogen without a carrier gas, and the intensity of the laser pulse is $\sim 2.8 \times 10^{13} \text{W/cm}^2$, pulse duration 60 fs. The maximum alignment of the molecular ensemble is reached shortly after the interaction with the ultrafast laser field, followed by a dephasing and rephasing processes, leading to revivals of the alignment. The revivals for linear and symmetric top molecules are periodic due to the quantization of the energy levels of rotational states. Electron diffraction is sensitive to both the angular distribution and the internuclear distance of atom pairs in the molecule. The main signature of aligned molecules in the diffraction pattern is the appearance of anisotropy as opposed to the circularly symmetric patterns from randomly oriented molecules. Therefore, we can use the temporal evolution of anisotropy to demonstrate the evolution of the molecular alignment, similar to the degree of alignment. The anisotropy is defined by

$$A = \frac{S_\text{H} - S_\text{V}}{S_\text{H} + S_\text{V}}, \tag{4.1}$$

where S_H and S_V are the sum of the counts in horizontal and vertical cones in the diffraction pattern, respectively, within a chosen range of the amplitude of momentum transfer (*s*).

4.3.1 Characterization of temporal resolution and slow timing drift

The fast-changing dynamics of laser induced impulsive alignment of nitrogen molecules provides a good metric to characterize the overall temporal resolution and timing drift of the keV-UED instrument through the comparison of experimental measurement to its simulated counterpart. The overall instrumental temporal resolution determined in this way includes all the factors that contribute to the resolution, including the laser and electron pulse durations, the residual temporal broadening due to group velocity mismatch, and the time of arrival jitter between the two pulses.

Figure 4.2 shows the time-dependent anisotropy calculated from 2D diffraction patterns at different time delays using eqn. (4.1) with opening angle of 60° and the *s* range from 3 to 4.5 Å^{-1}. The *t*=0 ps was defined to be the maximum anisotropy of the prompt alignment. The acquisition time of the diffraction pattern at each time step is 25 seconds, and the time step of the experiment is 100 fs. The temporal resolution of the setup is determined by the best fitting of the temporal evolution of experimental anisotropy to its theoretical counterpart using four parameters: the laser fluence ($\mathcal{F}$), the rotational temperature of the molecular ensemble (T_rot), the instrumental temporal resolution (τ) and a rescaling factor (*ef*) that accounts for the percentage of molecules being excited in the interaction region. The dynamics of rotational nitrogen ensemble from the prompt alignment to the ¾ revival

is recorded. The experimental and simulated anisotropy are shown in blue and red, respectively.
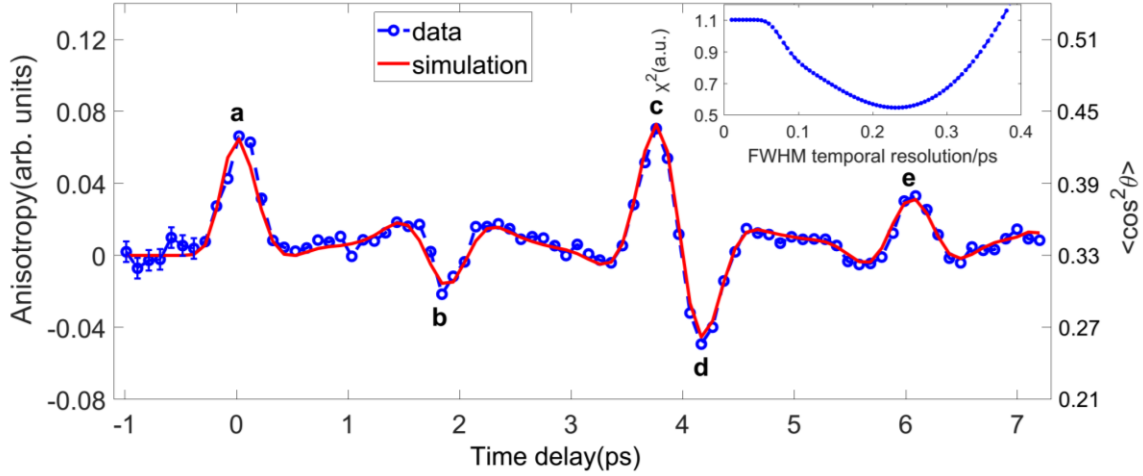
Figure 4.2: Temporal evolution of anisotropy calculated from nitrogen alignment induced by a femtosecond laser pulse. The experimental and simulated anisotropy are shown in blue and red, respectively. The exposure time for each data point is 25 s. The inset shows χ^2 fitting as a function of the temporal resolution of the setup. The error bars for the first 7 points are evaluated by calculating the standard deviation of the anisotropy of 10 images before the prompt revival. The error bars are used to show the uncertainty of measurement $\sigma(t)$ at each data point. (This figure is reproduced from [32]; used in accordance with the Creative Commons Attribution 4.0 International license.)

The temporal evolution of anisotropy measured by the instrument is modeled by the convolution of the theoretically calculated time-dependent anisotropy $A_{\mathrm{th}}(t; \mathcal{F}, T_{\mathrm{rot}})$ with a Gaussian function with a width (τ) that reflects the temporal resolution of the experiment, formulated as $h(t; \tau) = \frac{2}{\tau}\sqrt{\frac{\ln 2}{\pi}} \exp\left(-4\ln 2\, t^2/\tau^2\right)$. To compare the theory and experiment, simulated diffraction patterns are produced using the calculated angular distributions

obtained through solving the time-dependent Schrodinger's equation with the parameters that launch the rotational wave packets, and then the anisotropy is calculated in the same manner as in the experiment. The χ^2 fitting is given by

$$\chi^2 = \frac{1}{N-w}\left[\frac{A_{\text{ex}}(t)-ef\times A_{\text{th}}(t;\mathcal{F},T_{\text{rot}})\otimes h(t;\tau)}{\sigma(t)}\right]^2, \tag{4.2}$$

where $A_{\text{ex}}(t)$ is the temporal evolution of anisotropy measured in the experiment, N is the number of anisotropy data points, w is the number of fitted parameters, $\otimes$ stands for convolution, and $\sigma(t)$ is the error of each data point. Simulated diffraction patterns are produced by using the simulated angular distribution with parameters: the pump laser fluence and the rotational temperature of nitrogen ensemble. The anisotropy is calculated with the same conditions as in the experiment.

The best fit of χ^2 gives a laser fluence $\mathcal{F} = 1.7$ J/cm^2, rotational temperature T$_{\text{rot}}$= 45 K, rescaling factor $ef = 0.35$ and instrument response time $\tau =$230 fs, which are in good agreement to the approximated experimental parameters. Figure 4.2 shows a very good fit between the experimental and simulated anisotropies. Error bars that indicate the measurement uncertainty were determined by the standard error from the first few points before the pump pulse and are shown in the figure. The left axis shows the anisotropy in arbitrary units, and the right axis shows the value of degree of alignment <cos$^2\theta$>, where θ is the angle between the axis of nitrogen molecule and the laser polarization. The degree of alignment of the rotational dynamics has a maximum value of 0.44 and variations on the order of 0.01 are well resolved experimentally, indicating the high sensitivity of the keV-UED measurement. We repeated the nitrogen alignment experiment four times and achieved consistent results. The temporal resolutions from the fittings are 240 fs, 240 fs, 230 fs and 250 fs. A constant electron beam current is required to optimize the temporal

resolution, and a larger fluctuation (>10%) could lead to an obvious deterioration of the temporal resolution.
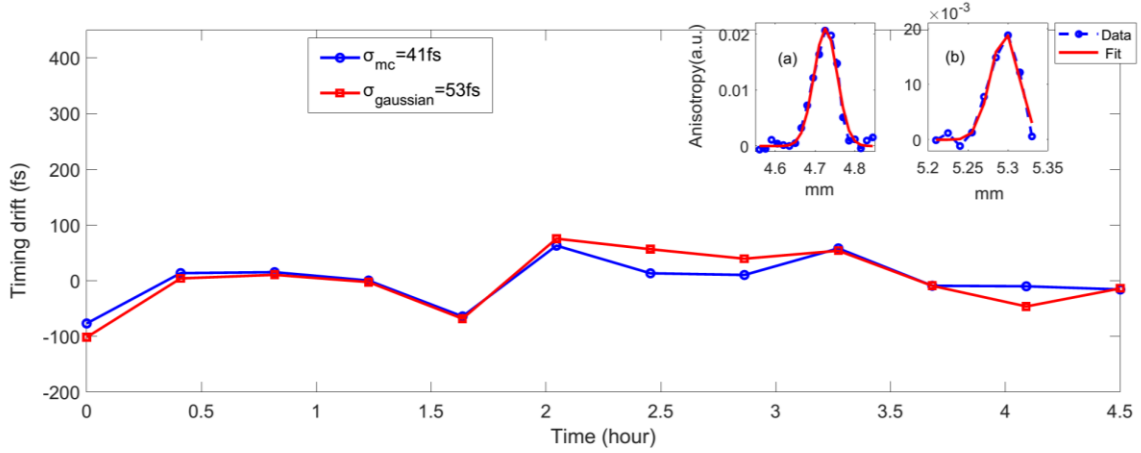
Figure 4.3: Characterization of slow timing drifts. The center of the revivals is calculated by two methods: gaussian fitting (red) and calculation of center of mass (blue). The insets show the fitting of revivals with a gaussian function.

The fitting that determines the temporal resolution shown in figure 4.2 does not account for the slow timing drifts that take place over many hours. We characterized the slow timing drifts by evaluating the center of the prompt alignment peak and the positive part of the half revival. The shift of the time delays of these anisotropy peaks provides a measure to estimate the timing drift of the setup. Figure 4.3 shows the slow timing drift over 4.5 hours. The center of the revivals is calculated by two methods: gaussian fitting (red) and center of mass (blue). The inset shows the fitting of anisotropy peaks with a gaussian function, in which the prompt revival is shown in figure 4.3 (a) and the positive part of the half revival in (b). The timing drift over 4.5 hours was evaluated to be on the order of 50 fs RMS, which is comparable to that obtained by the MeV-UED setup at SLAC [28]. The setup is sufficient for performing gas phase UED experiments over many hours.

4.3.2 Modified pair distribution function
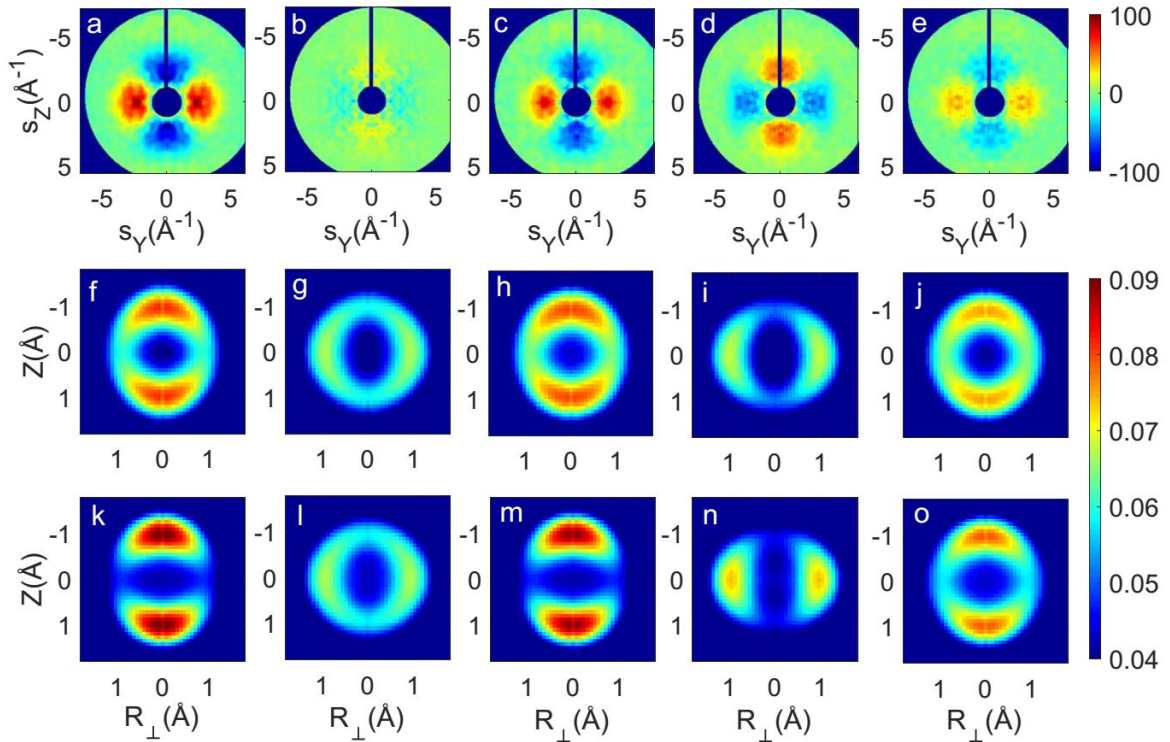
Figure 4.4: Diffraction patterns and modified pair distribution functions. (a-e) $\Delta I_{\mathrm{mol}}(\boldsymbol{s}, t)$ corresponding to the features marked in figure 4.2 at different time delays (a) t=0 ps, (b) t= 1.9 ps, (c) t= 3.8 ps, (d) t= 4.2 ps, (e) t= 6.1 ps. The dark circle and vertical line correspond to the regions where the incident beam is blocked by the beam stop. (f-j) The experimental MPDFs corresponding to the diffraction patterns in (a-e). (k-o) The simulated MPDF at the same time delays as the experimental data. The direction of the laser polarization is along Z axis, and $R_{\perp} = \sqrt{X^2 + Y^2}$, $\tan \alpha = \frac{R_{\perp}}{Z}$. (This figure is reproduced from [32]; used in accordance with the Creative Commons Attribution 4.0 International license.)

We now focus on calculating molecular scattering intensity and retrieving the angular distribution of laser-aligned nitrogen molecules. For linear molecules, the angular

distribution can be trivially converted to the molecular orientation distribution. Figure 4.4 (a)-(e) show the 2-dimensional diffraction difference patterns $\Delta I_{mol}(\boldsymbol{s}, t)$ at the prompt alignment peak, the ¼ revival, the peak and trough that correspond to the half-revival and the peak at the ¾ revival. At the half-revival, the angular distribution changes completely from alignment along the laser polarization direction to anti-alignment within ~300 fs, which is clearly resolved by the keV-UED.

The diffraction patterns are obtained by averaging images from four different scans, corresponding to the total integration time of 100 seconds at each time delay. In comparison to a similar measurement by the state-of-the-art gas phase MeV-UED instrument [19, 113], our results demonstrate a much higher signal-to-noise (SNR) ratio with a shorter acquisition time. The experiment of laser-aligned nitrogen molecules was carried out by Yang et al. using the SLAC MeV-UED with an electron beam current of 0.7 pA (37.5k e/pulse at a repetition rate of 120 Hz) [19, 113], and integration times between 60 minutes to 90 minutes were needed to acquire high quality 2D diffraction difference images. The long integration times prevented the experiment from retrieving more than a couple of images of the diffraction-difference patterns and the angular distributions. Their laser and electron beam sizes were similar in the interaction region, which reduces the efficiency of excitation. In our setup, we reduced the diameter of the electron beam to be half of the diameter of the laser beam using a platinum aperture, which results in a more uniform excitation at the cost of reduced beam current.

We now show that the increased SNR in our experiment allows us to retrieve a full movie of the dynamics. The data analysis procedure is described as follows. First, hot pixels in each image are removed, and each image is normalized by its total counts. The diffraction

difference patterns are calculated with $\Delta I_{\mathrm{mol}}(\boldsymbol{s}, t) = I(\boldsymbol{s}, t) - I(\boldsymbol{s}, t < -1\mathrm{ps})$ for each image, where $I(\boldsymbol{s}, t < -1\mathrm{ps})$ is taken by setting the arrival time of electron pulse more than 1 ps before the laser pulse. The diffraction patterns are averaged over four quadrants based on their symmetry as the laser field is vertically polarized. The transmitted electron beam is blocked by a copper beam stop held by a thin metal wire. The data in the detector area blocked by beam stop is extrapolated smoothly to zero at $s{=}0$, and the data area behind the wire is replaced by the data using the symmetry of the diffraction pattern. The molecular diffraction intensity $I_{\mathrm{mol}}(\boldsymbol{s}, t)$ is obtained by adding the calculated molecular scattering with random distribution back to $\Delta I_{mol}(\boldsymbol{s}, t)$, after rescaling by a factor $ef{=}0.35$, formulated as $I_{\mathrm{mol}}(\boldsymbol{s}, t) = \Delta I_{\mathrm{mol}}(\boldsymbol{s}, t) + ef \cdot I_{\mathrm{mol}}^{\mathrm{random}}(s)$. For an ensemble of laser-aligned nitrogen molecules with an angular distribution $g(\alpha)$, the molecular scattering intensity is given by

$$I_{\mathrm{mol}}(\boldsymbol{s}) = 2 \iint |f_N(s)|^2 \cos[\boldsymbol{s} \cdot \boldsymbol{r}(\alpha_0, \beta_0)] g(\alpha_0) \sin \alpha_0 \, \mathrm{d}\alpha_0 \mathrm{d}\beta_0 \ , \qquad (4.3)$$

where f_N is the complex scattering amplitude of the nitrogen atom, $\boldsymbol{s}$ is the momentum transfer vector, $\boldsymbol{r}$ is the vector pointing in the direction of the molecular bond of nitrogen, and α_0, β_0 are the polar and azimuthal angles with respect to the laser polarization. The MPDF is constructed by applying a 2-dimensional inverse Fourier transform, followed by Abel inversion, to the $I_{\mathrm{mol}}(\boldsymbol{s}, t)$.

$$\mathrm{MPDF}(r, \alpha) = \mathrm{Abel}^{-1}\mathrm{FT}_{2D}^{-1}[I_{\mathrm{mol}}(\boldsymbol{s})] = 2g(\alpha)H(r - r_{\mathrm{N}}) \otimes \frac{F_N(r) \star F_N(r)}{r_{\mathrm{N}}^2} , \qquad (4.4)$$

where r_{N} is the bond distance and $\otimes$ denotes a convolution and $\star$ stands for correlation, F is the Fourier transform of the atomic scattering amplitude $f(s)$. The term $H(r - r_{\mathrm{N}})$ is the measured pair distribution function (PDF), which is the convolution of the ideal PDF and the Fourier inversion of the function truncating the diffraction signal due to the limited

size of the detector. The MPDF contains information on both the internuclear distance of the nitrogen molecule and the angular distribution of the molecular ensemble.

A Gaussian damping function with RMS width of 6 Å^{-1} is applied to $I_{\mathrm{mol}}(\mathbf{s})$ to suppress noise in the data at high s and to minimize the effects of the discontinuity due to limited detector dimension, and zero padding is used to improve the resolution of the MPDF in the region of interest. Analyzing the MPDF at a fixed radius, corresponding to the interatomic distance of the nitrogen molecule, reveals the angular distribution of the ensemble. The angular distribution of nitrogen molecules is extracted by converting the MPDF into a polar representation where the horizontal axis is the polar angle α. By integrating the MPDF in the polar representation along the radius, the angular distribution for each angle is obtained. The angular distribution is normalized by $\int_0^\pi g(\alpha) \sin \alpha \, d\alpha = 1$.

The simulated angular distribution is calculated by solving the TDSE described in Chapter 3 with the experimental parameters. The molecular scattering patterns, and corresponding MPDF are produced with the same procedures as the experimental patterns. Figure 4.4 (f)-(j) show the modified pair distribution function (MPDF) retrieved from the corresponding diffraction patterns (a)-(e), and (k)-(o) are the corresponding simulated MDPF. Figures 4.4 (f), (h), (j) show that an increased population of molecules are aligned along the alignment axis (vertical) with decreased population in the perpendicular direction whereas the distributions in (g) (i) show that more nitrogen molecules are aligned along the direction perpendicular to the laser excitation, which agrees with the expected results for alignment along the direction of the laser polarization. The experimental MPDFs are in good agreement with the theoretical counterparts.

4.3.3 Temporal evolution of molecular orientation distribution

In the case of linear molecules, the molecular orientation distribution (MOD) is identical to the atom-pair angular distribution. Thus, we have $\rho(\theta, t) = g(\alpha, t)$, where θ is one of the Euler angles defined in figure 3.2 of chapter 3, and α is the polar angle of N-N defined in the lab frame. In addition to the MPDFs at several key times shown in figure 4.4, we calculated a series of MPDFs from the initial alignment to the revivals up to 7 ps, through which the full temporal evolution of angular distribution (or MOD) is retrieved. The MOD evolution shows the continuous dynamics of laser induced impulsive alignment of nitrogen molecules captured by our keV-UED instrument, shown in figure 4.5 (a). The experimentally measured MOD evolution is a convolution of the real MOD evolution with the instrumental response function, which is determined by the overall temporal resolution and slow timing drift of the instrument. Therefore, by deconvolving the instrument response function [200-202], we can remove the smearing effect due to the instrumental response function from the temporal evolution of MOD. The instrument response function of keV-UED is assumed to be a Gaussian function with a width (FWHM) of 0.25 ps.

Figure 4.5 (b), (c) show the deconvolved and theoretically calculated MOD evolution. The full rotational dynamics of the nitrogen ensemble are clearly displayed in figure 4.5 with time-dependent MOD, labeled as $\rho(\theta, t)$ as a function of θ (horizontal axis) and time t (vertical axis). The experiment accurately captures all details of the rotational dynamics, including small changes in the distribution, and is in very good agreement with the theoretical calculation. This time-dependent MOD has been used to successfully retrieve the complete quantum states of laser induced alignment of nitrogen ensemble using the quantum tomography technique in ref. [131].
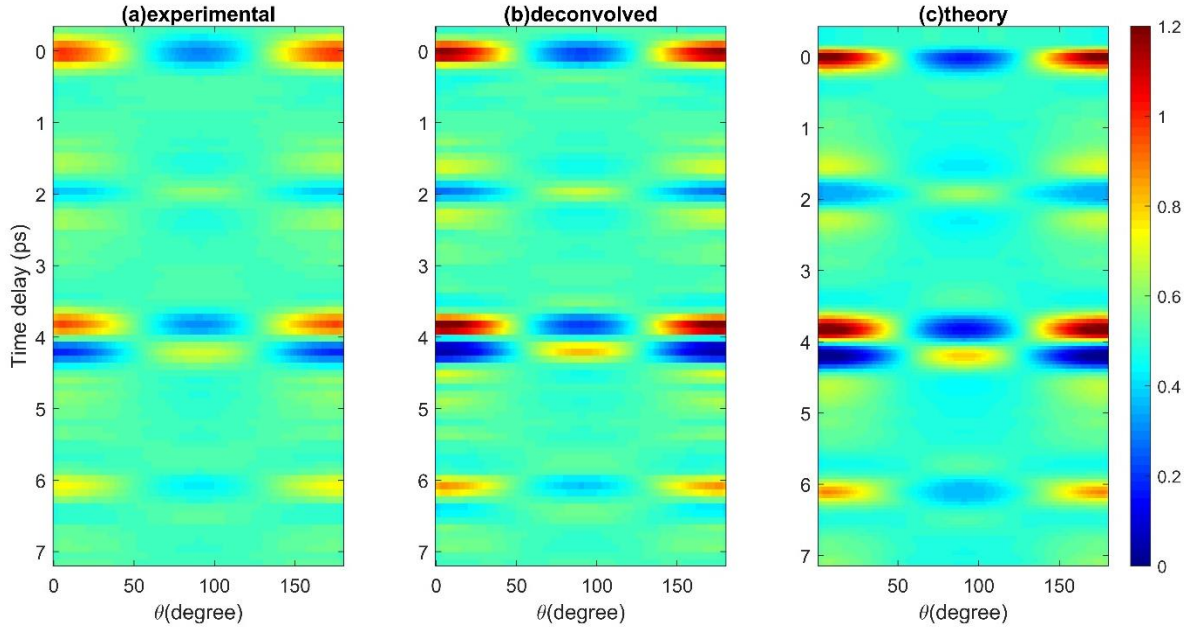
Figure 4.5: Comparison of experimental and calculated angular distributions. (a) Temporal evolution of MOD, denoted as $\rho(\theta, t)$, retrieved from experimental diffraction patterns. (b) Deconvolved MOD which removes the broadening effect due to the instrumental response function that accounts for the limit temporal resolution of the setup. (c) Theoretically calculated MOD evolution obtained by solving TDSE.

Figure 4.6 shows the quantitative comparison between the experimentally measured, deconvolved and theoretically calculated MOD at six different times. There is an improved agreement between the deconvolved MOD and its simulation after accounting for the smearing effect from the instrumental response function. The experimental results demonstrate the ability of the keV-UED to achieve high spatiotemporal resolutions comparable to those reported by gas-phase MeV-UED experiments. Thanks to high electron beam current, keV-UED provides higher signal levels and requires much shorter acquisition time. This increase in the SNR and decrease of acquisition time could be transformative to gas phase UED experiments, since it allows better capturing of the

dynamics, investigating additional reaction parameters such as excitation conditions (laser wavelength, pulse energy), and investigating molecules with similar structures.
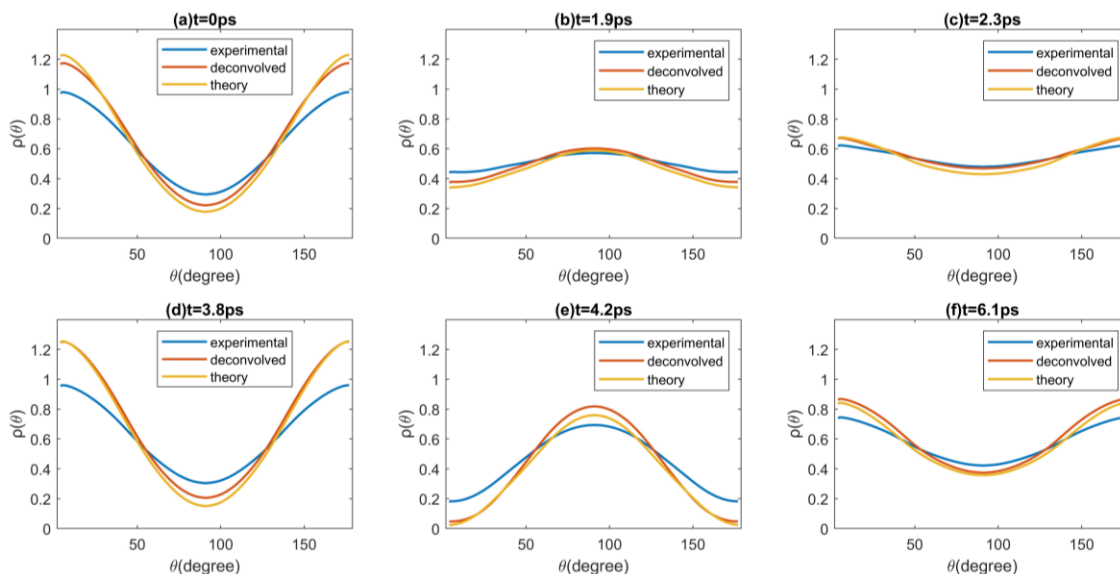
Figure 4.6: Comparison of experimental, deconvolved and theoretically calculated $\rho(\theta, t)$ at different time delays.(a) t=0 ps; (b) t=1.9 ps; (c) t=2.3 ps; (d) t=3.8 ps; (e) t=4.2 ps; (f) t=6.1 ps.

4.4 Rotational dynamics of laser aligned CF₃I molecules

In this section, we use the keV-UED to capture diffraction patterns from a sample of laser-aligned CF_3I molecules as a function of time delay between the pump laser pulse and the probe electron pulse. The setup has been introduced in section 4.2, and reported in details in [26, 32]. In this experiment, we stretched the pump laser pulse duration to 200 fs to minimize ionization of CF_3I while still impulsively aligning the molecules. The overall temporal resolution of the keV-UED setup is estimated to be 310 fs based on the pump laser pulse duration and the instrumental temporal resolution previously measured in the last section and in ref. [32]. A platinum aperture with diameter of 200 μm is used to

collimate the electron beam to deliver a beam current of 20 pA to the sample, corresponding to 25,000 electrons per pulse. The sample gas CF_3I is seeded in the carrier gas helium with a ratio of 1:4 to lower the rotational temperature of the sample. We use a de Laval nozzle that has an inner orifice diameter of 30 μm to produce a supersonic gas jet with a backing pressure of 950 torr.

4.4.1 Retrieval of MOD in 1D alignment
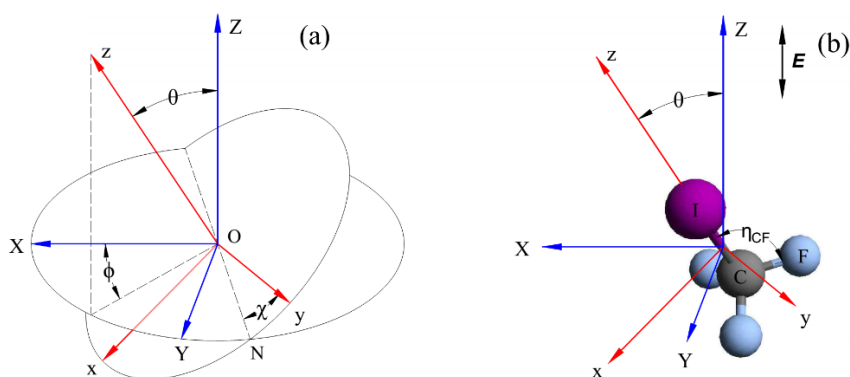
Figure 4.7: Orientation of a CF_3I molecule. (a) The lab frame XYZ and body frame xyz are related by the three rotations defined by the Euler angles (ϕ, θ, χ). The details are shown in chapter 3. (b) The orientation of the CF_3I molecule depicted by the Euler angles, with the xyz coordinates defined in the body frame. The laser polarization is along the Z axis. (This figure is reproduced from ref. [114], with the permission of APS Publishing.)

Figure 4.7 (a) shows the lab frame (XYZ) and body frame (xyz), which are related by the rotations defined by Euler angles. Figure 4.7 (b) shows the orientation of the CF_3I molecule described by the Euler angles. The z axis is along the molecular axis CI, the origin of xyz is defined by the center of mass of the molecule, and one of x, y axes can be chosen arbitrarily in the plane perpendicular to the z axis in the case of a symmetric top [172]. Here we briefly review the method to retrieve the MOD for symmetric top molecules

aligned by a linearly polarized laser field, and the details have been demonstrated in section 3.4. The MOD has the form $\rho = (\frac{1}{2\pi})^2 \rho_1(\theta)$, referring to the one-dimensional (1D) alignment. The MOD has no dependence on ϕ and χ for a symmetric top molecule aligned by a linearly polarized laser pulse since both the quantum number K and M are conserved during the interaction between the molecule and the laser pulse [123, 196, 197]. The atom-pair angular distributions $g_{jk}(\alpha, \beta)$ have no dependence on β, and the relation between the $g_{jk}(\alpha)$ and the MOD is given by eqn. (3.45), shown below

$$g_{jk}(\alpha) \sin \alpha = \frac{1}{\pi} \int_0^\pi \rho_1(\theta) u(\alpha, \theta, \eta_{jk}) \sin \theta \, d\theta,$$

where $u(\alpha, \theta, \eta_{jk}) =$

$$\begin{cases} \dfrac{\sin\alpha}{\sqrt{(\sin\theta\sin\eta_{jk})^2 - (\cos\theta\cos\eta_{jk} - \cos\alpha)^2}} & \text{for } (\sin\theta\sin\eta_{jk})^2 - (\cos\theta\cos\eta_{jk} - \cos\alpha)^2 > 0 \\ 0 & \text{otherwise} \end{cases}.$$

This equation shows that $g_{jk}(\alpha)$ has dependence on η_{jk}, but has no dependence on ξ_{jk}, indicating that the three FI atom pairs have the same angular distribution for CF$_3$I. This property is applicable to the atom pairs CF and FF as well. Actually, $\rho_1(\theta)$ is identical to $g_{CI}(\alpha)$, which is the angular distribution of the molecular axis CI. However, the angular distribution of CI cannot be isolated from that of FF because the internuclear distances r$_{CI}$ = 2.14 Å and r$_{FF}$ =2.15 Å are very close and the peaks corresponding to these distances cannot be separated in the MPDF. Therefore, the angular distribution of FI is used to retrieve $\rho_1(\theta)$, which represents the MOD in the following text.

The integral of (3.45) in discrete form is $g_{jk}(\alpha) \sin \alpha \cong \sum_{q=1}^N \rho_1(\theta_q) u(\alpha, \theta_q, \eta_{jk}) \sin\theta_q \frac{\Delta\theta}{\pi}$, where $\Delta\theta = \pi/N$ and $\theta_q = q\Delta\theta$. By defining $y_p = g_{jk}(\alpha_p)\sin\alpha_p$, $x_q = \rho_1(\theta_q)\sin\theta_q$, and

$U_{pq} = u(\alpha_p, \theta_q, \eta_{jk}) \frac{\Delta\theta}{\pi}$, we can write the equation as $y_p = \sum_{q=1}^{N} U_{pq} \cdot x_q$. Therefore, we have

$$\boldsymbol{y} = U\boldsymbol{x} .\tag{4.5}$$

The matrix U is chosen to be a square matrix with dimension N×N. Vector $\boldsymbol{y}$ is the experimental measurement, matrix U can be calculated from the known structure of the CF₃I molecule, and vector $\boldsymbol{x}$ is the vector being computed which contains the information of the MOD. The retrieval of the MOD is therefore to find a solution of $\boldsymbol{x}$ in a system of linear equations shown by eqn. (4.5). The angle between $\boldsymbol{r}_{\mathrm{FI}}$ and $\boldsymbol{r}_{\mathrm{CI}}$ is $\eta_{\mathrm{FI}} = 25.51°$. The matrix U is calculated using η_{FI} and N=18,000 values of α and θ from 0 to π. The transpose-free quasi-minimal residual method (MATLAB function TFQMR) is used to find the solution of $\boldsymbol{x}$ through iterations.

Here we show how to extract the $g_{\mathrm{FI}}(\alpha)$ from the experimental measurement. The MPDF is calculated from the 2D molecular scattering intensity normalized by the atomic scattering term, denoted by $I_{\mathrm{mol}}(\boldsymbol{s})/I_{\mathrm{atom}}$, by using eqn. (3.65):

$$\mathrm{MPDF} = \mathrm{Abel}^{-1}\mathrm{FT}_{2D}^{-1}\left[\frac{I_{\mathrm{mol}}(\boldsymbol{s})}{I_{\mathrm{atom}}}\right] = \sum_{j=1}^{n}\sum_{k=1,j\neq k}^{n} g_{jk}(\alpha)\, H(r - r_{jk}) \otimes \frac{\tilde{F}_j(r)\star\tilde{F}_k(r)}{r_{jk}^2} ,$$

where $H(r - r_{jk})$ is the measured pair distribution function that accounts for the limited size of the detector, $\otimes$ stands for convolution and $\star$ signifies correlation; $\tilde{F}$ is the Fourier transform of the normalized atomic scattering amplitude $f(s)/\sqrt{I_{\mathrm{atom}}}$. The MPDF is then converted into the polar representation to extract $g_{\mathrm{FI}}(\alpha)$. The raw $g_{\mathrm{FI}}(\alpha)$ is fitted to a 4th order polynomial to remove the noise and artifacts for the data with a low signal-to-noise ratio, such as the data other than the alignment peaks.

4.4.2 Degree of alignment

The interaction of the induced dipole of a molecule with the femtosecond laser pulse produces a rotational wave packet $\Psi_{J_i K_i M_i}(t)$, described in section 3.2.3. A prompt alignment of the molecular ensemble is shortly obtained after the pump laser, followed by the dephasing and rephasing process, giving rise to periodic revivals of the alignment for symmetric tops. The diffraction signal from molecules being partially aligned along the laser polarization or anti-aligned shows up an anisotropy, as opposed to the circularly symmetric diffraction patterns for molecules in a randomly orientated distribution. In the experiment, the difference of molecular scattering is calculated to enhance the anisotropic part of the diffraction signal, given by

$$\Delta I_{mol}(\boldsymbol{s}, t) = I_{total}(\boldsymbol{s}, t) - I_{total}^{random}(\boldsymbol{s}) = I_{mol}(\boldsymbol{s}, t) - I_{mol}^{random}(\boldsymbol{s}) , \qquad (4.6)$$

where the diffraction pattern I_{total}^{random} from randomly oriented molecules is measured by setting the electron arrival time at the sample to be before the arrival of the laser, corresponding to a negative time delay. The advantage of generating the difference is that it removes the atomic scattering along with most of the background noise and artifacts.

The process of data analysis is described as follows. First, we removed the outliers in each experimental image by using a filter with a window of A $\pm$ 3σ, where A is the average counts at each momentum transfer s, and σ corresponds to the standard deviation of the counts. Each image is normalized by its total counts. The diffraction difference patterns are calculated by $\Delta I_{mol}^{exp}(\boldsymbol{s}, t) = I_{total}(\boldsymbol{s}, t) - I_{total}(\boldsymbol{s}, t < -5ps)$ for each time delay and are averaged over the four quadrants based on the symmetry of diffraction pattern due to the vertical polarization of the laser. We use a copper beam stop held by a thin wire to block

the transmitted electron beam and measure its current. The range of momentum transfer s for the useful data in the diffraction pattern is from 1.25 Å^{-1} to 9.40 Å^{-1}. The data corresponding to the area blocked by the beam stop is extrapolated smoothly to zero at $s = 0$. We filled the data behind the wire using the symmetric data of the pattern. The noise of the diffraction pattern is reduced by using a pixel-wise adaptive low-pass Wiener filter. The molecular scattering intensity $I_{mol}(\boldsymbol{s}, t)$ can be reconstructed by adding $\Delta I_{mol}^{exp}(\boldsymbol{s}, t)$ to the theoretical I_{mol}^{random} with a scale factor (ef) to account for the scattering signal from both the excited and unexcited molecules, given by

$$I_{mol}(\boldsymbol{s}, t) = \Delta I_{mol}^{exp}(\boldsymbol{s}, t) + ef \cdot I_{mol}^{random}(s) , \qquad (4.7)$$

where the theoretical I_{mol}^{random} is computed from the known structure of the CF$_3$I molecule.
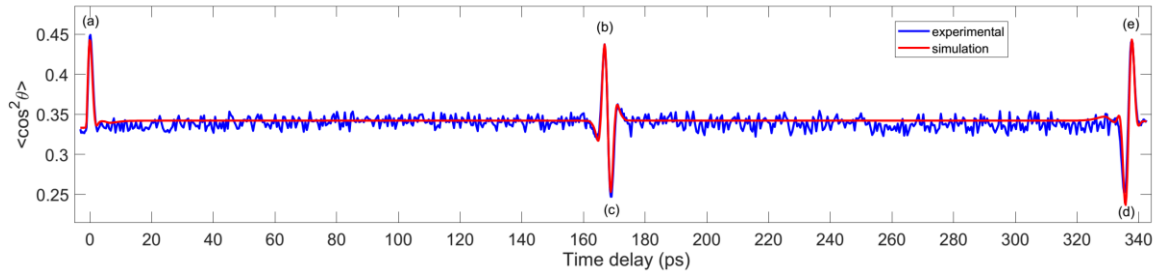
Figure 4.8: Temporal evolution of the degree of alignment of laser aligned CF$_3$I molecules. The experimentally measured and theoretically simulated degree of alignment are shown in blue and red, respectively. The time delays of the marked peaks and troughs are (a) t=0 ps, (b) t= 166.8 ps, (c) t= 168.8 ps, (d) t= 335.5 ps, (e) t= 337.7 ps. (This figure is modified from ref. [114], with the permission of APS Publishing.)

To determine the scale factor, we calculate a series of $I_{mol}(\boldsymbol{s}, t; ef)$ by using different ef from 0.14 to 0.60, and the corresponding MPDF is generated by eqn. (3.65), from which the $\rho_1(\theta, t; ef)$ is extracted. The corresponding experimental degree of alignment is

calculated using the definition $\langle\cos^2\theta\rangle^{\exp}(t;ef) = \int_0^\pi \cos^2\theta \cdot \rho_1(\theta,t;ef)\sin\theta\,d\theta$. Theoretical $\langle\cos^2\theta\rangle(t)$ is simulated using the laser parameters in the experiment according to the theory described in section 3.2. The laser fluence is 1.7 J/cm^2, and the laser pulse duration is 200 fs. We calculated a series of $\langle\cos^2\theta\rangle^{\text{th}}(t;T)$ using T from 30 K to 80 K. The excitation factor and rotational temperature of the ensemble were determined to be 0.28, 53 K by the best matching of $\langle\cos^2\theta\rangle^{\exp}(t;ef)$ to $\langle\cos^2\theta\rangle^{\text{th}}(t;T)$ through χ^2 fitting, shown in figure 4.8.

4.4.3 Modified pair distribution function

In this section we present the MPDFs calculated from the measured diffraction patterns with eqn. (4.7) and (3.65), which is the first step to extract the atom-pair angular distribution. Figure 4.9 (a-e) shows the experimentally measured diffraction-difference patterns normalized by the atomic scattering intensity, denoted as $\Delta I_{\text{mol}}^{\exp}(\boldsymbol{s},t)/I_{\text{atom}}$, at five time delays: (a) the prompt alignment peak (t=0), (b) the peak and (c) trough of the half revival, and (d) the trough and (e) peak of the full revival, as shown in figure 4.8. The corresponding MPDFs at the same time delays as in parts (a-e) are shown as figures 4.9 (f-j), and the atom pairs are marked for each pair distribution function in figure 4.9 (f), in which the rings are corresponding to the internuclear distances r_{CF}= 1.33 Å, r_{CI} = 2.14 Å, r_{FF} =2.15 Å and r_{FI} =2.89 Å. The angular distribution of each atom pair is represented by the intensity distribution of each ring as a function of the polar angle. The spatially resolved internuclear distance and angular distribution of the atom pairs are displayed in the experimental MPDFs, which are in good agreement with the simulated MPDFs at corresponding time delays are shown in figures 4.9 (k-o).
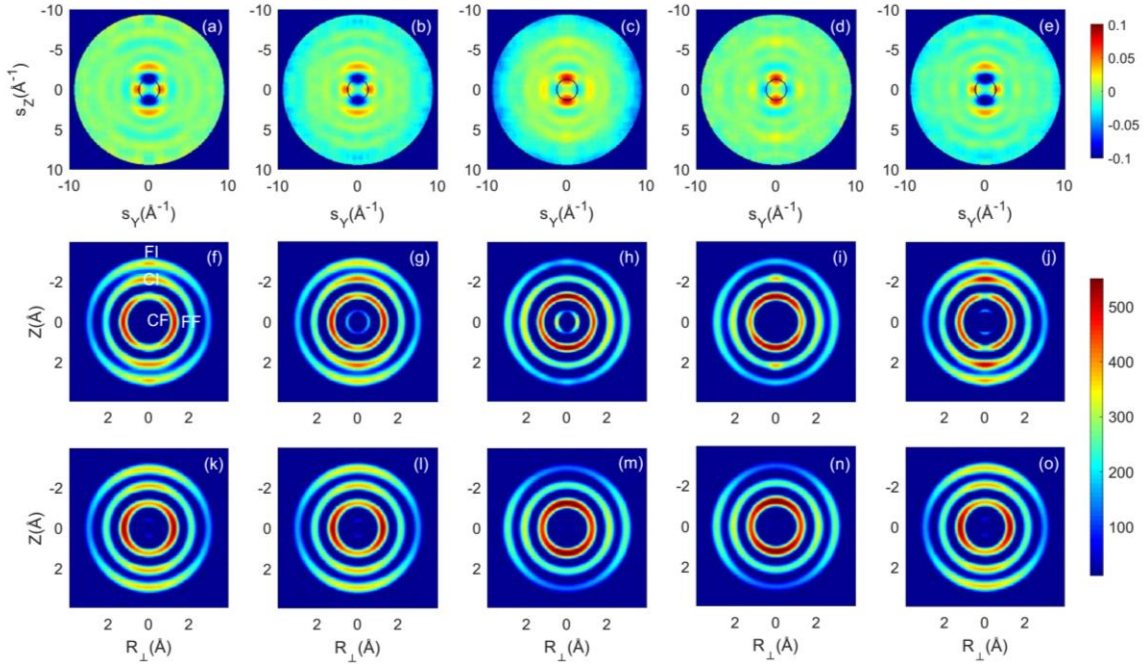
Figure 4.9: Diffraction patterns and modified pair distribution functions (MPFDs). (a-e) normalized diffraction-difference pattern $\Delta I_{\mathrm{mol}}(s,t)/I_{\mathrm{atom}}$ corresponding to the features marked in figure 4.7 at five different time delays (a) t=0 ps, (b) t= 166.8 ps, (c) t= 168.8 ps, (d) t= 335.5 ps, (e) t= 337.7 ps. The data inside of the black circle is extrapolated to zero at s=0. (f-j) The experimentally retrieved MPDFs corresponding to the diffraction patterns in (a-e). The atom pairs are marked for each pair distribution function in (f). (k-o) The simulated MPDFs at the same time delays as the experimental data. The direction of the laser polarization is along Z axis, and $R_\perp = \sqrt{X^2 + Y^2}$. (This figure is reproduced from ref. [114], with the permission of APS Publishing.)

We calculated the simulated MPDFs by applying the Fourier inversion, followed by the Abel inversion, to the simulated $I_{\mathrm{mol}}(s,t)/I_{\mathrm{atom}}$. The simulated $I_{\mathrm{mol}}(s,t)$ is calculated by averaging the single molecule scattering intensity at different orientations, parametrized with Euler angles, by the MOD calculated by numerical solution of TDSE. Figures 4.9 (f),

(g), (j) show that atom pairs FI and CI are aligned along the polarization direction of the laser field (Z axis), yet CF is anti-aligned, which is expected for the alignment of prolate symmetric top molecules. Figure 4.9 (h) (i) show that FI and CI are anti-aligned to the laser excitation, while CF is aligned to it. The signals with an internuclear distance below 1 Å in figure 4.9 (g), (h), (j) are from the residual background of the diffraction-difference pattern discussed in [69], which are spatially separated from the signal of the atom pairs.

4.4.4 Molecular orientation distribution
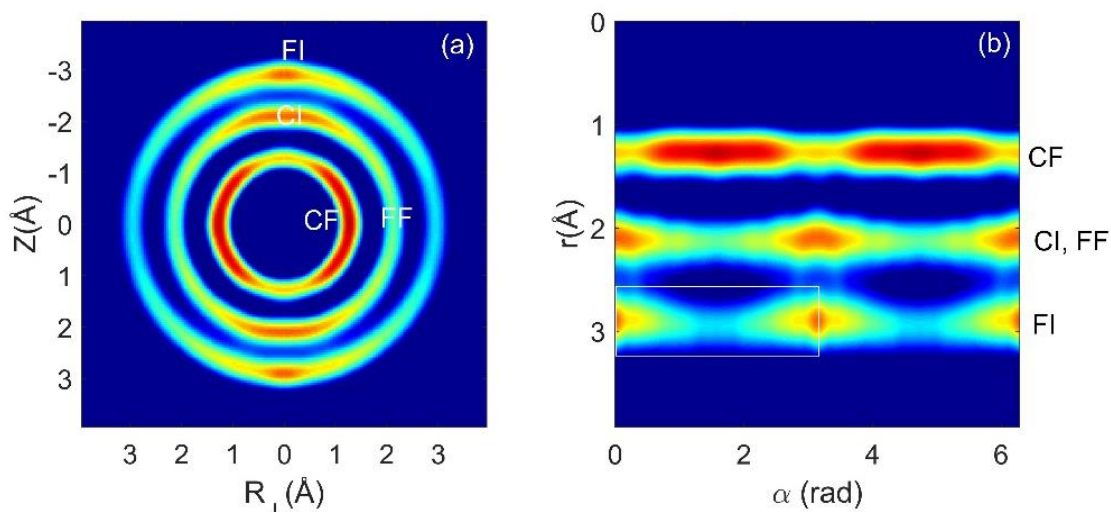
Figure 4.10: Converting a MPDF to the polar representation. MPDF calculated from the experimental diffraction pattern at t=0. (b) The MPDF is converted into its polar representation with angle α as the horizontal axis and interatomic distance as the vertical axis.

The MPDF is converted into a polar representation to extract the angular distribution of FI, shown in figure 4.10. We integrate the intensity distribution from FI, in figure 4.10 (b), along the vertical axis within a width of 1/e from the peak at a certain α to obtain $g_{\text{FI}}(\alpha)$, which is normalized by $\int_0^\pi g_{\text{FI}}(\alpha) \sin\alpha \, d\alpha = 1$. The extracted $g_{\text{FI}}(\alpha)$ at t=0 and retrieved

$\rho_1(\theta)$ with methods described in section 4.4.1 are shown in figure 4.11. The MOD, as expected, is significantly narrower than the angular distribution of FI.
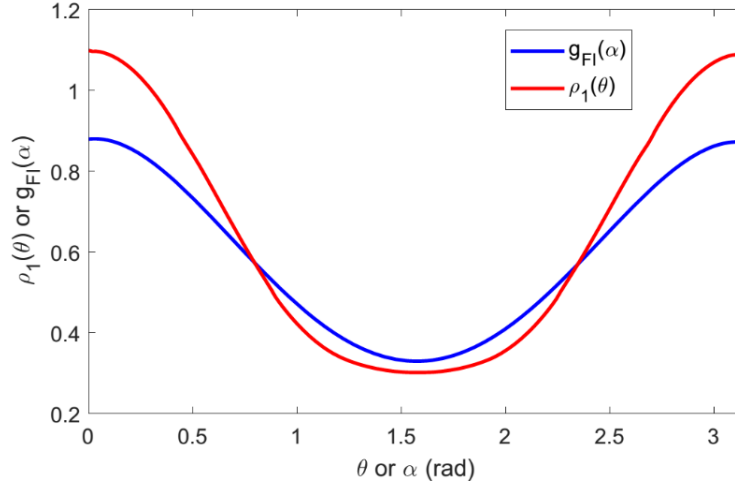
Figure 4.11: The experimentally determined angular distribution $g_{FI}(\alpha, t=0)$ of atom pair FI in blue, and the retrieved probability density distribution $\rho_1(\theta)$ in red. (This figure is reproduced from ref. [114], with the permission of APS Publishing.)

We retrieved the MOD from the experimental diffraction patterns and calculated the theoretical MOD at the five-time delays labeled in figure 4.8, which are shown in figure 4.12. The theoretical MOD is directly calculated from the wave packets obtained by numerically solving the TDSE. Figure 4.12 (a) (b) (e) show that the peaks of MODs are localized around $\theta = 0, \pi$, indicating alignment along the polarization direction of the laser field, while the peaks of MODs in (c) (d) are localized at $\theta=\pi/2$, referring to the anti-alignment. The comparison of the experimental and theoretical MODs demonstrates a very good agreement. The small discrepancies between the experimental and theoretical MODs at $\theta=\pi/2$ in figure 4.12 (c) and (d) are because of the noises at $g_{FI}(\alpha = 0, \pi)$ shown in figure 4.9 (h) and (i) that lower the amplitude of $g_{FI}(\alpha)$.
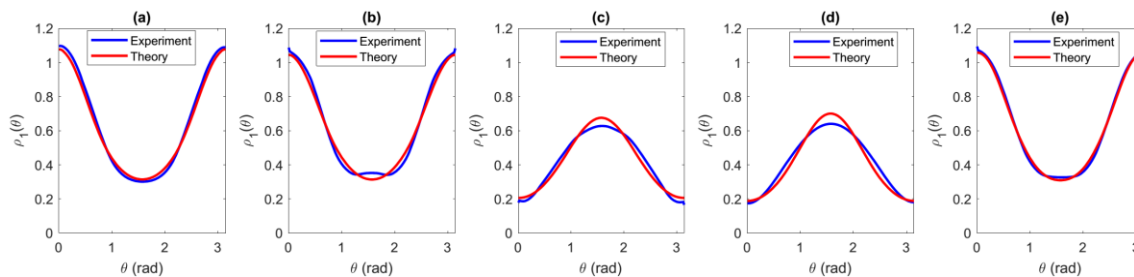
Figure 4.12: Experimentally retrieved $\rho_1(\theta, t)$ of the CF$_3$I molecules (in blue) and corresponding simulated counterparts at 5-time delays (in red). (a) t=0 ps, (b) t= 166.8 ps, (c) t= 168.8 ps, (d) t= 335.5 ps, (e) t= 337.7 ps (This figure is reproduced from ref. [114], with the permission of APS Publishing.)

We retrieved the MOD of the laser induced CF$_3$I alignment from the prompt alignment to the full revival, shown in figure 4.13 (a). The dynamics of the alignment of the molecular ensemble are clearly demonstrated by the temporal evolution of the MOD. The theoretically calculated temporal evolution of MOD is shown in figure 4.13 (b) as a comparison. The theoretical MOD is calculated directly from the coefficients of the wave packets obtained by solving the TDSE. The retrieved MOD is in good agreement with the theoretical counterpart. The time step of the data around the revivals is 250 fs and is 500 fs for the data between the two revivals. A weak, oscillatory alignment signal shows up in the theoretical MOD around the ¼ and ¾ of the full revival period, which is not captured in the experimental data, because of the coarse sampling and lower signal-to-noise level of the signals in the experiment. Three close-ups of the experimentally retrieved MOD evolution at prompt alignment and the revivals are displayed in figure 4.13 (c), (d), and (e) and the corresponding calculated counterparts are shown in figure 4.13 (f), (g) and (h). Quantization of rotational energy levels in the rotational wave packets result in the alignment revivals. The molecules are first aligned along the direction of laser polarization

in the half revival, followed by anti-alignment, as shown in figure 4.13 (d). The alignment

process is reversed in the full revival, shown in figure 4.13 (e). The experiment accurately

captures the dynamics of molecular alignment induced by an ultrafast laser pulse and is in

good agreement with the theoretically calculated results.
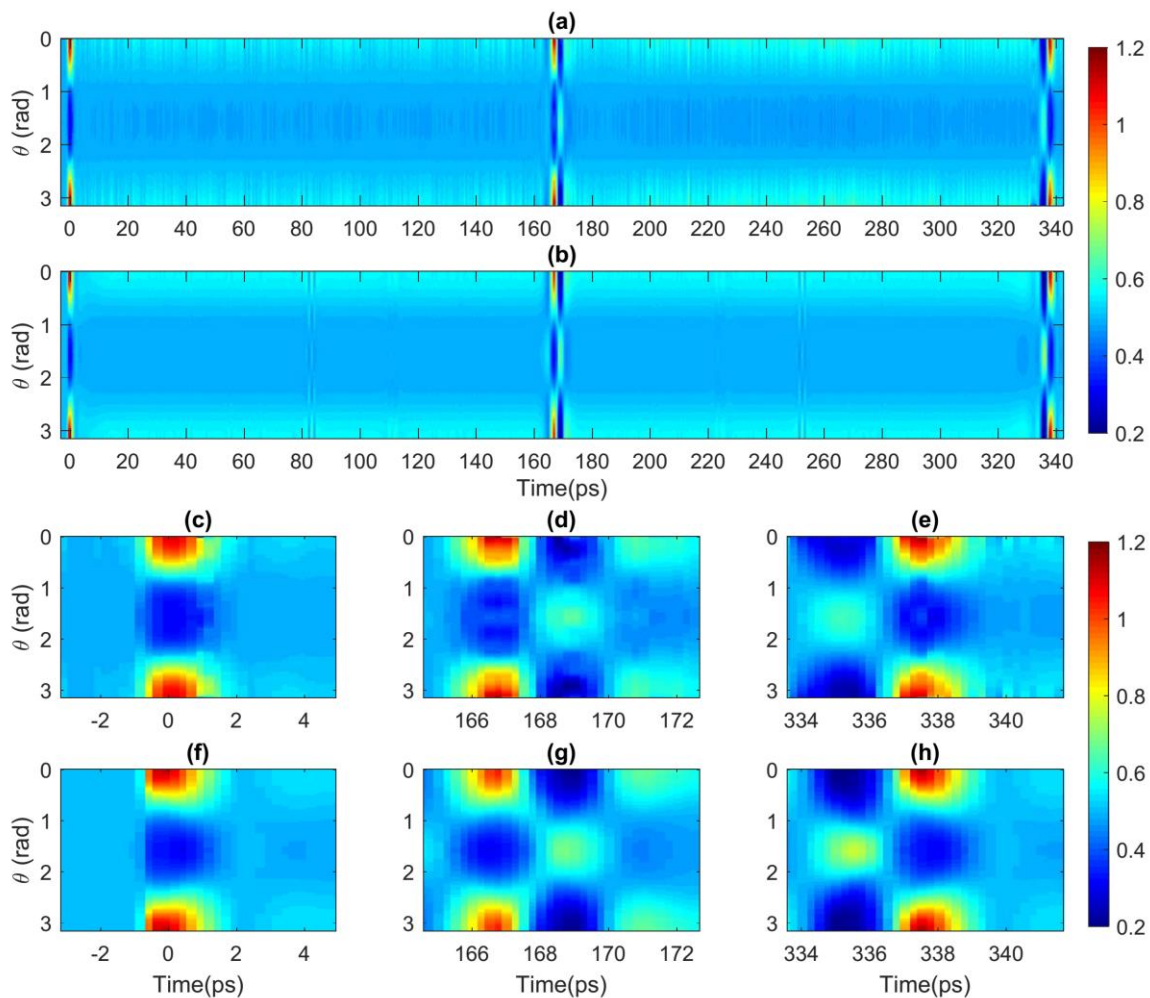
Figure 4.13: Comparison of experimental and theoretical MOD. (a) Temporal evolution of

MOD retrieved from experimental data. (b) Theoretically calculated MOD. (c-e) The close-

up of experimentally determined MOD at the prompt, half, and full revivals, respectively.

(f-h) are the close-ups of the calculated MOD at the corresponding revivals in (c-e). (This

figure is reproduced from ref. [114], with the permission of APS Publishing.)

4.5 Isotope detection with impulsive laser-induced alignment

Gas phase ultrafast electron diffraction (UED) has been proven to be a powerful tool to determine the structure [203, 204] and structural changes of isolated molecules on femtosecond and picosecond time scales [54, 205, 206]. Gas phase UED has been used to successfully capture the rotational dynamics of molecules impulsively aligned by femtosecond laser pulses [19, 32], in which the angular distributions and interatomic distances can be retrieved. In addition, diffraction patterns from aligned molecules allow for the retrieval of three-dimensional molecular structures [55, 207]. UED is directly sensitive to the internuclear distance and angular distribution of atom pairs in the molecule. However, not all internuclear distances can be experimentally resolved because of the limited spatial resolution of the measurement that results from the low signal-to-noise level of the data at high momentum transfer and the limited dimension of the detector. The electron scattering signal is determined by the charge distribution in the molecule [208]. Thus, it is not directly sensitive to the neutrons in the molecule and cannot differentiate different isotopologues (molecules where one or more nuclei are substituted by its isotopes).

We show here that it is possible to distinguish isotopologues by analysis of the rotational dynamics of the molecular ensemble induced by a femtosecond laser pulse. Mass spectrometry has been a sophisticated method to identify isotopologues but is not sensitive to the structures [69]. The advantage of a gas phase UED measurement is that it can determine the structure and isotopic composition in a single measurement. We demonstrate that gas phase UED is able to determine the abundance of ^{35}Cl and ^{37}Cl in a sample of CH_3Cl molecules by analyzing the temporal evolution of the anisotropy.

Rotational wave packets are produced through the interaction between the induced dipole and the ultrafast laser field, resulting in a prompt alignment of molecular ensemble, followed by dephasing and revivals of alignment. In case of linear and symmetric top molecules, quantization of rotational energy levels in the wave packets produces periodic revivals where the MOD changes between the alignment and anti-alignment [19, 117, 157]. The period of the MOD is determined by the moment of inertia, which is sensitive to the masses of the constituent atoms and structure of the molecule. Therefore, the measurement of the revival period in the nonadiabatic molecular alignment can be used to determine the isotope substitution in molecules. While we demonstrate an accurate measurement of the relative abundance of $CH_3{}^{35}Cl$ and $CH_3{}^{37}Cl$, which are symmetric top molecules, in a mixing gas phase sample, this technique in principle can be applied to asymmetric top molecules and can be used to identify molecules with small differences in their moments of inertia. This new methodology adds another capability to the existing technique of ultrafast electron diffraction.

4.5.1 Experimental measurement

We use the keV-UED instrument to capture the rotational revivals of the chloromethane isotopologues $CH_3{}^{35}Cl$ and $CH_3{}^{37}Cl$ induced by an infrared ultrafast laser pulse. The chloromethane sample was purchased from Sigma-Aldrich with chemical purity $\geq$ 99.5%. The diagram of the experiment has been shown in section 4.1. The pulse energy of pump laser is 0.8 mJ, the pulse duration is 200 fs, and the overall temporal resolution is around 300 fs. The chloromethane is mixed with helium at a ratio of 1:1, and the sample is introduced into the chamber using a de Laval nozzle with a backing pressure of 900 torr.

In section 3.2.4, we have shown that the quantazation of rotational energy levels results in the periodic revivals for linear and symmteric top molecules. The period of the revivals is given by [191, 196]

$$\mathcal{T} = \frac{\pi\hbar}{C_e} = \frac{2\pi I_{cc}}{\hbar}, \tag{4.8}$$

where I_{cc} is the principal moment of inertia of the molecule corresponding to the principal axis that is perpendicular to the symmetry axis of the CH_3Cl molecule. Here we derive the change of the revival period due to the isotope substitution. We use the rigid molecule approximation and assume that the two isotopologues have the same structure. Figure 4.7 (b) can be used to calculate I_{cc}, with fluorine being replaced by hydrogen, and iodine by chlorine. The z axis is along the symmetry axis of the molecule (C-Cl), with x and y axes perpendicular to it, and the origin is at the center of mass of the molecule. The moment of inertia is

$$I_{cc} = \sum_k m_k(z_k^2 + y_k^2), \tag{4.9}$$

where k indicates all the constituent atoms. The mass change of the isotope is small $\delta m_{Cl}/m_{Cl} \cong 0.057$ and the change of the coordinates is $|\delta z_k/z_k| \leq |\delta z_{Cl}/z_{Cl}| \cong 0.046$. Thus, we calcualte the variation of I_{cc} by keeping only the first order terms, given by

$$\delta I_{cc} = \delta m_{Cl} \cdot z_{Cl}^2 + 2\sum_k m_k \cdot z_k \cdot \delta z_k,$$

where $\delta m_k = 0$ for $k \neq Cl$, $y_{Cl}^2 = 0$ and $\delta y_k^2 = 0$ are used to obtain the above equation. Also, the shift of z_k due to the change of the center of mass shows that $\delta z_k = -\delta z_{MC}$, where δz_{MC} is the shift of the center of mass. The origin of the coordinate system is at the center of mass, leading to $\sum_k m_k \cdot z_k = 0$ and $\delta I_{cc} = \delta m_{Cl} \cdot z_{Cl}^2$. Therefore, change of the rotational period $\delta\mathcal{T}$ is given by

$$\delta\mathcal{T} = \frac{2\pi}{\hbar} \cdot \delta I_{cc} = \frac{2\pi}{\hbar} \cdot z_{Cl}^2 \cdot \delta m_{Cl},\tag{4.10}$$

where $|z_{Cl}|$ is the distance from the Cl atom to the center of mass of the molecule.
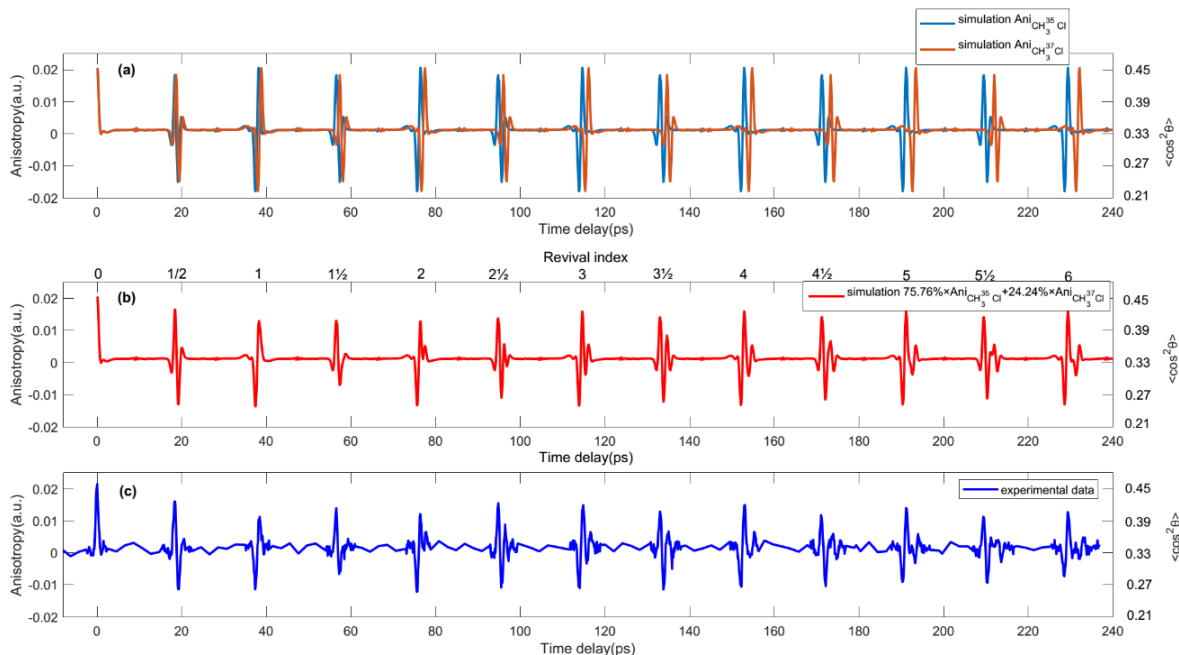
Figure 4.14: Temporal evolution of anisotropy. (a) Theoretically calculated anisotropy of $CH_3{}^{35}Cl$ and $CH_3{}^{37}Cl$ using the laser parameters from the experiment and assuming the rotational temperature of the molecular ensemble to be 50 K. (b) Simulated anisotropy contributed from the two isotopologues by using eqn. (4.11). (c) Experimental anisotropy $A_{ex}(t)$. The revival indices are listed at the top of graph (b). The simulated anisotropy is scaled by an excitation ratio of 0.45, which indicates the percentage of excited molecules in the interaction region. (This figure is reproduced from [196]; used under the terms of the Creative Commons Attribution 4.0 licence.)

The temporal evolutions of the simulated anisotropy for $CH_3{}^{35}Cl$ and $CH_3{}^{37}Cl$ displayed together in the same graph are shown in figure 4.14 (a). The structure of the isotopologues are optimized with ORCA [185] and the level of theory (B3LYP, DEF2-SVP). The laser

parameters in the experiment are used to solve the TDSE and rotational temperature of the molecular ensemble is assumed to be 50 K based on previous operation of the gas jet. The MOD and degree of alignment can be obtained from the coefficients of wavepackets and the weight factor determined by Boltzmann distribution and nuclear spin statistics. The simulated diffraction pattern at each time delay is calculated by averaging the scattering intensity of a single molecule, which is parametrized by the Euler angles, with the theoretically calculated MOD. The anisotropy of each simulated diffraction pattern is calculated using eqn. (4.1) with the range $1.4 \text{ Å}^{-1} < s < 3 \text{ Å}^{-1}$ and an opening angle of 60 degrees for the horizontal and vertical cones. The maximum degree of alignment at the revival peak is 0.45. The revivals in the time dependent signal from the two isotopologues overlap in the prompt peak and the first few revivals since their difference is much smaller than the duration of each revival. The difference in the revival periods can be seen more clearly as the revival index increases.

The relative abundances of ^{35}Cl and ^{37}Cl are 75.76% and 24.24% respectively according to the previous reports in [209-211]. In order to compare with the data, the simulated anisotropy contributed from $CH_3{}^{35}Cl$ and $CH_3{}^{37}C$, shown in figure 4.12 (b), is calculated by

$$A_{\text{total}}(t) = 75.76\% \times A_{CH_3{}^{35}Cl}(t) + 24.24\% \times A_{CH_3{}^{37}Cl}(t). \qquad (4.11)$$

The temporal evolution of anisotropy calculated from the experimental data is shown in figure 4.14 (c). The indices for revivals are listed at the top part of figure 4.14 (b). The excitation factor is determined to be 0.45 by the comparison of the amplitudes of the experimental $A_{\text{total}}(t)$ to the simulated counterpart. For better comparison between the simulation and experiment, the simulated anisotropy, figure 4.14 (a) and (b) are scaled by

an excitation factor of 0.45, indicating 45% of the molecules in the interaction region are excited. The experimental signal is in good agreement with the simulated anisotropy signal in figure 4.14 (b).

The acquisition time of each experimental image is 8 seconds, and we use a variable time step for each scan, in which a time step of 133.33 fs is used for the revivals and 3.33 ps for the region between the revivals. As figure 4.14 (c) shows, the signal has a complex structure in the first few revivals due to the overlapping of the revivals from the two isotopologues. However, the revivals begin to separate in time and a double revival structure shows up in the signal for time delays longer than 200 ps. The two revivals have different amplitudes due to the different abundance of the two isotopes.

We now demonstrate that the rotational periods, mass difference, and relative abundance of the two isotopologues can be determined by the temporal evolution of the experimental anisotropy $A_{total}(t)$. The revival period from laser aligned $CH_3{}^{35}Cl$ and $CH_3{}^{37}Cl$ can be calculated by using the time delay and the indices of revivals, formulated as

$$\mathcal{T} = \frac{\Delta t}{\Delta n}, \qquad\qquad (4.12)$$

where Δt is the difference of time delays at two revival peaks in $A_{ex}(t)$ and Δn is the difference of revival indices. The rotational periods of the two isotopologues are shown in table 1. By using eqn. (4.10) and (4.12), we can calculate the mass difference of the two Cl isotopes, denoted as δm_{Cl}, shown in table 1.

The relative abundance of the two isotopologues can be determined by using the relative amplitudes of their anisotropy signals, shown in figure 4.14 (c), at longer time delays where the two revival peaks are separated. At these longer time delays, the main revival peaks are

separated, whereas there is still some overlapping of the smaller features around the revival, which needs to be corrected. A close-up of the revivals with index 0 and ½ are shown in figure 4.15 (a), and revivals 4½ and 5 in figure 4.15 (b). The time at the peak of the 0th revival is defined to be t = 0, and t_1, t_2, t_3 are time delays of the peak at revival ½, the main peak and minor peak of revival 4½, respectively. The main peak and minor peak of index 4½ are separated, whereas the anisotropy at t_3 is not only from $CH_3{}^{37}Cl$ but also is affected by the base line of the main peak at t_2.
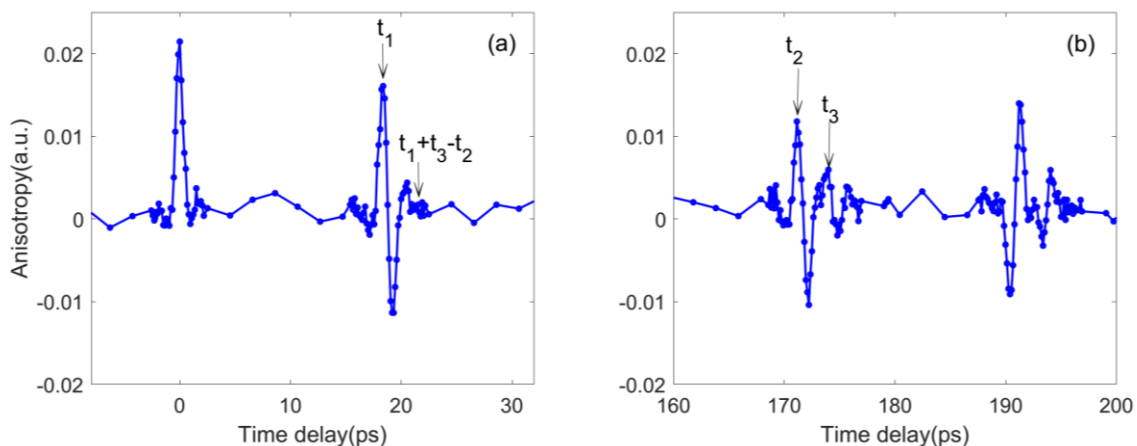
Figure 4.15: Anisotropy at different times. (a) The revival 0 (left) and ½ (right). The time delay of the peak in revival ½ is t₁, and the anisotropy at time delay $t_1 + t_3 - t_2$ is $A_{ex}(t_1 + t_3 - t_2)$. (b) The revival 4½ (left) and 5 (right). The main peak is from the revival of $CH_3{}^{35}Cl$ and the minor one is mostly from $CH_3{}^{37}Cl$. The time delay and anisotropy at the peak of the $CH_3{}^{35}Cl$ revival are $t_2, A_{ex}(t_2)$, respectively. The time delay and anisotropy at the peak of the $CH_3{}^{37}Cl$ revival are $t_3, A_{ex}(t_3)$, respectively. (This figure is reproduced from ref [196]; used under the terms of the Creative Commons Attribution 4.0 licence.)

The anisotropy at t_3 in figure 4.15 (b) is contributed from two parts. The major portion is from the signal of $CH_3{}^{37}Cl$, and the other part is the base line at $t_3 - t_2$ after the peak at t_2

from the signal of $CH_3{}^{35}Cl$. We use the anisotropy value of revival ½ at $t_1 + t_3 - t_2$ in figure 4.15 (a), in which the two revivals are well overlapped in time (timing difference is 0.22 ps), to estimate the base line for the anisotropy at t_3 in figure 4.15 (b).

By assuming the abundance ratio of $CH_3{}^{37}Cl$ to $CH_3{}^{35}Cl$ to be $p:1$, we can calculate the anisotropy contribution from $CH_3{}^{35}Cl$ at t_3 to be $\frac{1}{p+1} A_{ex}(t_1 + t_3 - t_2)$ and the anisotropy from $CH_3{}^{37}Cl$ at t_3 to be $A_{ex}(t_3) - \frac{1}{p+1} A_{ex}(t_1 + t_3 - t_2)$. The anisotropy at t_2 is from $CH_3{}^{35}Cl$ and has a value of $A_{ex}(t_2)$. The ratio of the two anisotropies should be equal to p:

$$\frac{A_{ex}(t_3) - \frac{1}{p+1} A_{ex}(t_1 + t_3 - t_2)}{A_{ex}(t_2)} = p . \tag{4.13}$$

The solution of p can be found by solving the quadratic equation, and $A_{ex}(t)$ is determined by the experimental measurement, shown in figure 4.14 (c). The solution of p is

$$p = \frac{A_{ex}(t_3) - A_{ex}(t_2) + \sqrt{[A_{ex}(t_3) - A_{ex}(t_2)]^2 - 4A_{ex}(t_2)[A_{ex}(t_1 + t_3 - t_2) - A_{ex}(t_3)]}}{2A_{ex}(t_2)} . \tag{4.14}$$

The abundance ratio is calculated using eqn. (4.14) and listed in table 1. The experimental results of the rotational periods, mass difference and abundance ratio of the isotopologues are average measurements of three independent measurements, and the uncertainty, which is the standard deviation of the measurements, indicates the meaningful range of the results determined by the experiment. The measurement could be improved by increasing the data acquisition time and capturing the anisotropy evolution at longer time delays such that the revivals are well separated. The theoretical calculation of the rotational periods, isotopic mass difference, and abundance ratio from ref. [209-211] are listed in table 4.1 for

comparison. The experimental measurements are in good agreement with the theoretical calculations and previous reports.

Table 4.1. Comparison of experimental results to theoretical calculations or values given in literature. Experimental measurement and theoretical calculation, or previous reports in ref. [209-211], of the rotational period, mass difference, and abundance ratio of $CH_3{}^{37}Cl$ to $CH_3{}^{35}Cl$. (This table is reproduced from [196]; used under the terms of the Creative Commons Attribution 4.0 licence.)

	$\mathcal{T}_{CH_3{}^{35}Cl}$ (ps)	$\mathcal{T}_{CH_3{}^{37}Cl}$ (ps)	δm_{Cl} (amu)	Abundance ratio p
Measurement	38.08±0.11	38.79±0.08	2.28±0.44	0.347±0.022
Theory or literature	38.13	38.73	2.00	0.320

By capturing the dynamics of impulsively aligned molecules with UED, we are able to determine the isotopic composition in a sample of gas phase molecules. The rotational period, mass difference, and relative abundance were determined from experiment in chloromethane with ^{35}Cl and ^{37}Cl isotopes. This technique in principle could be used to differentiate molecules with small differences in their moments of inertia and is not limited to only linear and symmetric top molecules. For asymmetric top molecules, there is no periodic revival structure. However, the dynamics of the revival spectra are still sensitive to the moment of inertia of the molecule [123]. The nonadiabatic laser-induced alignment of asymmetric top molecules can be produced in the same manner with an ultrafast laser pulse, and the temporal evolution of the anisotropy can be captured by UED. By comparing the measurements to the simulations, the moment of inertia of each isotopologue in the sample can be determined.

4.5.2 Discussions

The technique could also be used to determine the end products of a reaction more accurately with small structural differences. In cases when a reaction produces multiple products, it is challenging to determine the end products of the reaction based on UED data alone because it consists of the superposition of the diffraction signal from all products. It has been shown that this problem can be circumvented by combining UED and mass spectrometry measurements in ref. [69]. When combining two different measurements, it is always a challenge to match the experimental conditions exactly. An alternative method would be to carry out two measurements using a UED setup. In this scenario, a reaction is triggered by a laser pulse and is probed by an electron pulse in a UED configuration. A second laser pulse could be brought in to impulsively align the products after the reaction is completed. Different products would show different revival structures. The combination of the UED signal and the moment of inertia of the products from the rotational dynamics would help to accurately determine the outcome of a reaction when multiple products are present. The interpretation of the measurements could be more challenging if the reaction products are in highly excited vibrational states, which might modify the revival structure. However, in most cases it should be possible to identify at least some of the reaction products.

Another possible application would be to bring in the second laser pulse (the alignment pulse) during the reaction as a way to determine the timescale for product formation. Here, one would expect to see the rotational revivals of the products only if the alignment pulse is applied after the products are formed. Thus, the time delay between the pump and

alignment laser pulses could serve as a probe of the reaction timescale to enhance the temporal resolution of UED experiments.

Chapter 5

Ultrafast electron diffraction of ionized toluene molecules produced by a near-infrared strong laser field

Portions of this material have previously appeared in the publication [69].

5.1 Introduction

The toluene system (C_7H_8) has been investigated extensively in recent years by the use of mass spectrometry, such as the exploration of the isomer pathway of $C_7H_7^+$ [212-218]. Multiple fragments can be generated, and structure rearrangement reactions take place during the ionization of toluene, including the sigmatropic shifts of hydrogen atoms and the formation of the symmetric 7-ring tropylium cation (see figure 5.1). The ionization products and the corresponding yields produced from intense laser fields depend on the laser intensity [219-222] and wavelength [223]. Mass spectrometry is able to differentiate different ionization products by mass but is unable to identify isomers alone. Therefore, measurements by mass spectrometry are often combined with other experimental methods to determine isomers, such as Coulomb explosion imaging [224]. Gas phase electron diffraction has recently been combined with synchronous mass spectrometry to study molecular structure and intermolecular inversions [225, 226]. Electron diffraction has also been used to investigate the structure of cluster ions captured in a Paul trap [227-230]. Gas phase ultrafast electron diffraction (UED) has been proven to be a powerful tool to determine the structure of neutral molecules and to capture molecular structural dynamics induced by femtosecond laser pulses with great details, but there has not been reports of gas phase ionized molecules studied with UED.
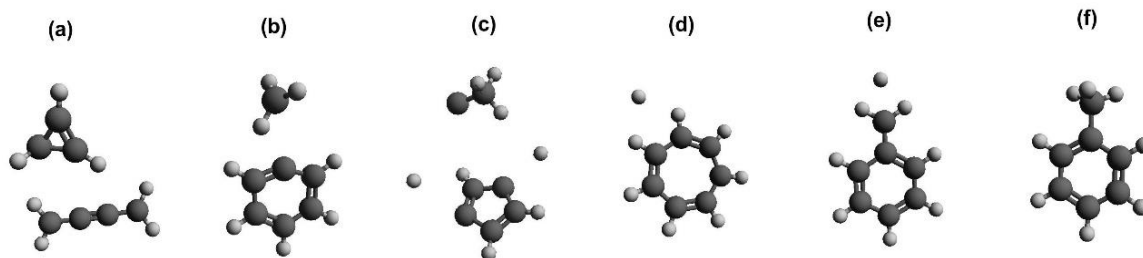
Figure 5.1: Three-dimensional models of some of the products generated from toluene ionization. The structures were calculated using the methods described in section 5.4.2. The fragments are: (a) $(C_4H_4^+, C_3H_4^+)$, (b) $(C_6H_5^+, CH_3^+)$, (c) $(C_5H_3+, C_2H_3^+)$, (d) tropylium Tr^+, (e) benzylum (Bz^+), and (f) ionized toluene (Tol^+). (The figure is reproduced from Faraday Discuss., 2021, 228, 39 DOI: 10.1039/D0FD00125B)

Gas phase UED experiments for ions are more challenging when compared to UED experiments with neutral gas phase molecules. The first challenge is that ionization in the gas sample generates a plasma which distorts the incident electron beam through the plasma lensing effect [231]. The second challenge is that the electron scattering theory based on the independent atom model (IAM) is not a good approximation to describe the electron diffraction from ions. The IAM scattering theory [60] approximates the scattered wavefunction as a sum of the scattering from the constituent atoms making up the molecule, which neglects effects of bonding electrons and any net charge. Corrections have been made to improve the IAM scattering theory by inducing the bonding effect to determine the structure of neutral molecules more accurately [232]. However, for scattering from ions, there is no straightforward way to make corrections for the net charge since the charge might not be localized in one of the constituent atoms but may instead be diffused across the molecule. Thus, an *ab-initio* scattering calculation is necessary.

Here we present an experimental investigation of ionization, fragmentation and isomerization of toluene molecules produced by a near-infrared strong laser field. The ionic products and fragments from the laser-induced ionization of toluene molecules are measured using gas phase keV-UED and momentum-resolved coincidence time-of-flight ion mass spectrometry (TOF-MS). The TOF-MS measurement determines the mass-to-charge ratio, momentum, and yield of each ion product, but is not sensitive to structure of the products. For example, it cannot differentiate the $C_7H_7^+$ isomers tropylium and benzylum (see figure 5.1). In the measurements of keV-UED, electrons are scattered from the products a few picoseconds after the ionization of toluene molecules produced by the strong laser field. The diffraction signal consists of neutral molecules and multiple ionic products. Since there are multiple products with unknown structures present, unambiguous determination of molecular structures is generally not possible. Therefore, we use the TOF-MS measurement to identify the most abundant products, which is helpful to determine the structures for analysis of the UED results. Based on the TOF-MS measurements, we perform *ab-initio* computation to determine the structure of each product using the level of theory (complete active space self-consistent field, CASSCF), and then conduct an *ab-initio* scattering computation to simulate the electron scattering from each product. By comparing the measured signal to the simulated scattering signals, the UED measurement is able to determine the relative yields of different fragments, including isomers, which is in good agreement with the TOF-MS measurement. The UED result is in good agreement with the *ab-initio* scattering calculation, while the electron diffraction calculation based on the IAM is not able to provide a good approximation for scattering from ions. This work establishes a method to conduct UED measurement from ions, and to combine the

measurement from TOF-MS and UED. It shows that electron diffraction from ions cannot be accurately described with the electron scattering theory based on the IAM but is in good agreement with the *ab-initio* scattering calculation.

5.2 Experiment

A brief introduction of the UED and TOF-MS is given in this section.

5.2.1 Ultrafast electron diffraction
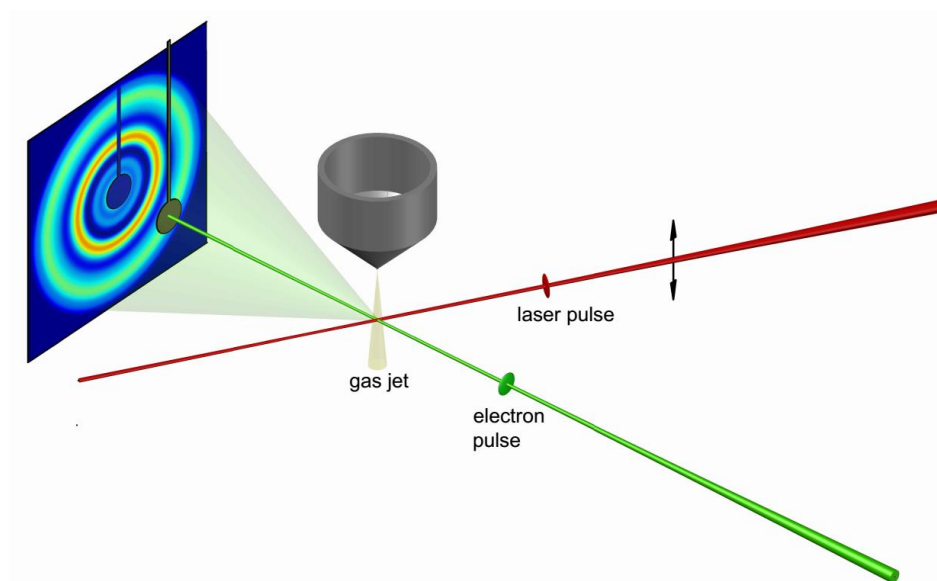
Figure 5.2: Diagram of the UED experiment. An ultrafast, near-infrared laser pulse is used to produce the ionization and fragmentation of toluene molecules, and an electron pulse is used to probe the products. The arrow indicates the polarization of the laser field. The toluene sample is introduced into the chamber using a nozzle with an orifice of 50 µm. The toluene molecules are seeded in helium as a carrier gas and the ratio of helium to toluene is 6 to 1. (This figure is modified from ref. [114], with the permission of APS Publishing.)

The keV-UED instrument has been described in detail in chapter 2, 4 and ref. [26, 32]. We use an ultrafast near-infrared laser pulse to ionize the toluene molecules, and an electron

pulse with a kinetic energy of 90 keV to probe the products generated from the ionization and fragmentation. The time delay between the laser and electron pulses is controlled by a translational optical stage. Figure 5.2 shows the diagram of the interaction region of the experiment. The toluene sample is seeded in helium with a helium to toluene mixture ratio of 6 to 1, which is introduced into the chamber using a nozzle with a 50 µm diameter orifice. The total backing pressure in the nozzle is 140 torr, and the diameter of the gas jet at the interaction region is estimated to be 350 µm (FWHM). The gas jet is perpendicular to the plane made up of the electron and laser beams, with the laser incident at an angle of 60° with respect to the electron beam.

To increase the laser intensity on the sample, we use here an untilted laser pulse, instead of the titled pulse demonstrated in chapters 2 and 4, to create the ionization and fragmentation of toluene molecules. The laser pulse has a temporal duration of 50 fs (FWHM), an energy of 1.2 mJ and a spot size of 100 µm (H) × 170 µm (V) FWHM on the sample. The peak intensity of the laser pulse is 116 ± 20 TW/cm^2. The peak laser intensity is obtained based on measurements of the pulse duration, laser pulse energy, beam size, and assumption of Gaussian temporal and spatial profiles. The uncertainty in the peak intensity is due to the uncertainty in the measurement of the beam size. The overall temporal resolution of the experiment is estimated to be 600 fs based on the diameters of the laser and electron beams, and the angle between the laser and electron beam. The resolution of keV-UED is dominated by the temporal broadening due to the group velocity mismatch between the electron and laser pulses [30], which can in principle be improved by using a tilted laser pulse [32]. The spatial overlap of the gas jet, laser, and electron pulses is determined by the maximum florescence intensity generated by focusing the laser beam onto the gas jet,

described in chapter 2. The temporal overlap of the laser and electron pulses is obtained by using the plasma lensing effect. The transmitted electron beam is blocked by a copper beam stop held by a thin metal wire. The electron diffraction signal is recorded using a phosphor screen which is imaged onto an electron-multiplying charge-coupled device (EMCCD).

5.2.2 Momentum-resolved coincidence ion time-of-flight mass spectrometry

We use a complementary momentum-resolved coincidence ion time-of-flight mass-spectrometry (TOF-MS) to determine the ionic products generated from the strong-field ionization of toluene molecules with the laser peak intensity similar to that used in the keV-UED experiment. The TOF-MS instrument has been reported in ref. [69, 233], and the only difference is that the laser beam in this experiment is not split into pump and probe pulses. Briefly, a linearly polarized ultrafast laser pulse is focused on a gaseous toluene sample with a 75 mm back-focusing spherical mirror. The focal spot diameter ($1/e^2$) of the laser beam is estimated to be ~ 3 µm. The laser pulse duration in the experiment is measured to be 29 fs. The laser peak intensity can be adjusted ranging from 30 to 220 TW/cm^2 to produce the ionization of toluene molecules. The toluene sample is introduced continuously into the chamber as a supersonic molecular beam with a 30 µm flat nozzle and is collimated by a series of skimmers and apertures that separate the expansion chamber from the interaction chamber. The molecular beam is mixed with 250 torr of helium as a carrier gas. The molecular beam is crossed by the laser beam at an angle of 90°, and the diameter of the molecular beam at the interaction region is about 4000 µm. Ions generated from the strong field ionization of toluene molecules are detected by using a COLTRIMS-type [234, 235] ion momentum imaging spectrometer with a uniform electric field with a strength of 125 V/cm. The electric field is parallel to the laser polarization to

guild all the ions emitted in the full 4π solid angle to a temporal-spatially sensitive delay-line anode microchannel plate (MCP) detector with a -2950 V bias at the front of the detector, which provides an approximately uniform detection efficiency for all ions independent of their mass-to-charge ratio. The amplified MCP and delay-line signals for all ions are processed by a constant fraction discriminator and a multi-hit, time-to-digital converter and are recorded shot-by-shot in a list-mode event file. The mass-to-charge ratio and three-dimensional momentum of each ion are determined from the time-of-flight and hit positions on detector with the assumption of classic motion in the homogeneous electric field of the spectrometer.

5.3 Theory

5.3.1 Electron scattering based on IAM

The theory of electron scattering has been described in detail in chapter 1. Based on the approximation of the IAM, the elastic scattering from a neutral molecule is given by $I(s) = \left| \sum_{j=1}^{N_a} f_j(s) \exp(-i\mathbf{s} \cdot \mathbf{r}_j) \right|^2$, where N_a is the total number of constituent atoms in the molecule, $f_j(s)$ is the atomic scattering amplitude of the jth atom, $\mathbf{s}$ is the vector of momentum transfer with magnitude $s = \frac{4\pi}{\lambda} \sin\left(\frac{\theta}{2}\right)$, θ is the scattering angle, λ is the de Broglie wavelength of the electron wave and $\mathbf{r}_j$ is the location of the jth atom. The total electron scattering cross-section of a randomly oriented molecular ensemble is obtained by averaging over all possible orientations of the molecules. The total scattering cross-section I_{total} can be separated into the atomic scattering term I_{at} and molecular scattering term I_{mol}. The modified scattering intensity sM is defined by using the I_{at} and I_{mol} to highlight

the information of the molecular structure encoded in I_{mol}. The scattering intensities are given below:

$$I_{\text{total}} = I_{\text{at}} + I_{\text{mol}} \,, \tag{5.1}$$

$$I_{\text{at}} = \sum_{j=1}^{Na} |f_j(s)|^2 \,, \tag{5.2}$$

$$I_{\text{mol}} = \sum_{j=1}^{Na} \sum_{k=1,j\neq k}^{Na} f_j^*(s) f_k(s) \frac{\sin(sr_{jk})}{sr_{jk}} \,, \tag{5.3}$$

$$sM = \frac{sI_{\text{mol}}}{I_{\text{at}}} \,, \tag{5.4}$$

where r_{jk} is the distance between jth and kth nucleus, and $*$ stands for the complex conjugate. To investigate the change of the molecular structure experimentally, we calculate the diffraction-difference intensity, formulated as $\Delta I(s,t) = I_{\text{total}}(s,t) - I_{\text{total}}(s, t_{\text{ref}}) \cong \Delta I_{\text{mol}}(s,t)$, where t_{ref} refers to the time before the arrival of the reaction-initiating laser pulse. $I_{\text{total}}(s, t_{\text{ref}})$ is a reference diffraction pattern used to remove the atomic scattering intensity and most of the experimental background. Correspondingly, we can define the ΔsM as

$$\Delta sM = \frac{s\Delta I_{\text{mol}}(s,t)}{I_{\text{at}}} \,. \tag{5.5}$$

5.3.2 *Ab-initio* computation of electron scattering

The elastic electron scattering intensity of a single molecule has been given by eqn. (1.27). Omitting the constants, we can write the total scattering intensity of a single molecule as [52, 66, 70, 72]

$$I^a = \frac{1}{s^4} \left| \int \rho_t(\boldsymbol{r}) \, e^{-i\boldsymbol{s}\cdot\boldsymbol{r}} d\tau \right|^2 \,, \tag{5.6}$$

where $\rho_t(\boldsymbol{r})$ is the distribution of total charge density including both the nuclei and electrons, which can be calculated by the molecular electronic wavefunction and the geometry of the molecule. Eqn. (5.6) not only provides a better description of the elastic electron scattering than the theory based on the IAM, but also enables a correct representation of the cationic products generated in the strong field ionization of molecules. The distribution of total charge density can be written as

$$\rho_t(\boldsymbol{r}) = \sum_j Z_j \delta(\boldsymbol{r} - \boldsymbol{R}_j) - \rho_{el}(\boldsymbol{r}) , \qquad (5.7)$$

where $\sum_j Z_j \delta(\boldsymbol{r} - \boldsymbol{R}_j)$ is the charge density due to the nuclei in the molecule, $\boldsymbol{R}_n$ is the vector indicating the coordinates of the nth nucleus, and $\rho_{el}(\boldsymbol{r})$ is the charge density of the electrons. Inserting eqn. (5.7) into eqn. (5.6), we have

$$s^4 I^a = \sum_{j=1}^{N_a} \sum_{k=1}^{N_a} Z_j Z_k e^{i\boldsymbol{s}\cdot\boldsymbol{R}_{jk}} - 2\sum_{j=1}^{N_a} Z_j \int \rho_{el}(\boldsymbol{r}) \cos\left[\boldsymbol{s}\cdot(\boldsymbol{r}-\boldsymbol{R}_j)\right]d\tau + \left|\int \rho_{el}(\boldsymbol{r})\, e^{i\boldsymbol{s}\cdot\boldsymbol{r}} dr\right|^2. \quad (5.8)$$

The three terms in eqn. (5.8) represent the interferences of the scattered electron wavefunctions contributed from different parts of the molecule. The first term is the interference of scattered wavefunctions due to the pair of nuclei, which only depends on the charge of the nuclei and the vector pointing from jth nucleus to kth nucleus. The second term is due to the scattering interaction from the electronic and nucleic charge densities. The third term stands for the interference of scattered wavefunctions due to the electron charge density distribution. In the electron scattering theory based on the IAM, the interference is due to the electron wavefunctions scattered from the constituent atoms of the molecule, which does not account for the effect of the chemical bonding and the extra charges in the system.

For a molecular ensemble with a randomly oriented distribution, the total scattering intensity I_{total}^a is obtained by the rotational average of eqn. (5.8), given by

$$s^4 I_{total}^a = \sum_{j,k} Z_j Z_k \frac{\sin(sR_{jk})}{sR_{jk}} - 2\sum_j Z_j \langle \int \rho_{el}(\boldsymbol{r}) \cos[\boldsymbol{s} \cdot (\boldsymbol{r} - \boldsymbol{R}_j)] d\tau \rangle + \langle |\int \rho_{el}(\boldsymbol{r}) e^{i\boldsymbol{s}\cdot\boldsymbol{r}} dr|^2 \rangle, \quad (5.9)$$

where $\langle .. \rangle$ stands for the average over randomly distributed orientations. The analytical evaluation of (5.9) using *ab-initio* molecular wavefunctions can be performed according to the methods described in ref. [236, 237]. The *ab-initio* calculation adequately accounts for distortion of the electron density in the molecule due to chemical bonding [238], and is valid to describe electron scattering from a charged system and excited molecule. The modified diffraction intensity *sM* can be calculated using the atomic scattering term I_{atom}, and I_{total}^a. The molecular scattering term is $I_{mol}^a = I_{total}^a - I_{atom}$. The atomic scattering amplitude term can be calculated by using the *ab-initio* calculated electronic wavefunctions and the charge of nuclei.

5.4 Results

In this section, we first demonstrate the measurement of TOF-MS, by which the most prevalent products of the ionization of toluene molecules are determined. We then show the results of the *ab-initio* electron scattering calculations for products from the toluene ionization and fragmentation. Finally, the yield of fragments and isomers are determined by fitting the UED measurement to the electron scattering intensity of the most prevalent products from the *ab-initio* calculation.

5.4.1 Momentum-resolved ion time-of-flight mass spectra

The momentum-resolved ion time-of-flight mass spectra of the toluene molecules being ionized by the strong-field laser are recorded at the peak laser intensity which ranges from

30 to 220 TW/cm^2. Figure 5.3 shows the TOF spectrum at a peak laser intensity of 130 TW/cm^2. The TOF spectrum shows that strong contributions from the parent ion ($C_7H_8^+$), parent dication ($C_7H_8^{2+}$), and the parent ion with one hydrogen or proton lost ($C_7H_7^+$) are observed, and that several broad distributions corresponding to the singly charged $C_mH_n^+$ fragments (m = 1 to 6, n = 0 to 8) are also present. The broad width of the distribution is due to the significant range in the amount of kinetic energy released as a result of the fragmentation of the various dicationic intermediate states. Therefore, in the TOF spectrum, we can resolve the groups of products with different numbers of carbon atoms (m), but we are not able to resolve individual peaks corresponding to a certain number of hydrogen atoms (n). The abundances of $C_7H_8^{2+}$, $C_7H_7^+$, and each of the $C_mH_n^+$ fragment groups, which are normalized to that of the $C_7H_8^+$ parent ion, for a series of laser peak intensities are shown in table 5.1.

The kinetic energy of the fragments can be obtained by analyzing the detector hit position as a function of the TOF, shown in the two-dimensional mass spectrum of figure 5.3. The ions that have very low kinetic energies, corresponding to ionic fragments generated by dissociative single ionization, are recorded around the center (Y = 0 mm) of the detector, and their time-of-flight are approximately equal to the nominal values expected for the corresponding mass-to-charge ratio. In most cases, these ions are generated along with one neutral fragment that carries the remaining mass. In contrast, fragment ions can be generated by the Coulomb explosion of a dication stemming from double ionization of a toluene molecule and carry a significant kinetic energy. The distribution of these ions spread out in both the detector hit position and the time-of-flight, leading to a ring or disk like profile in the two-dimensional spectrum in figure 5.3.
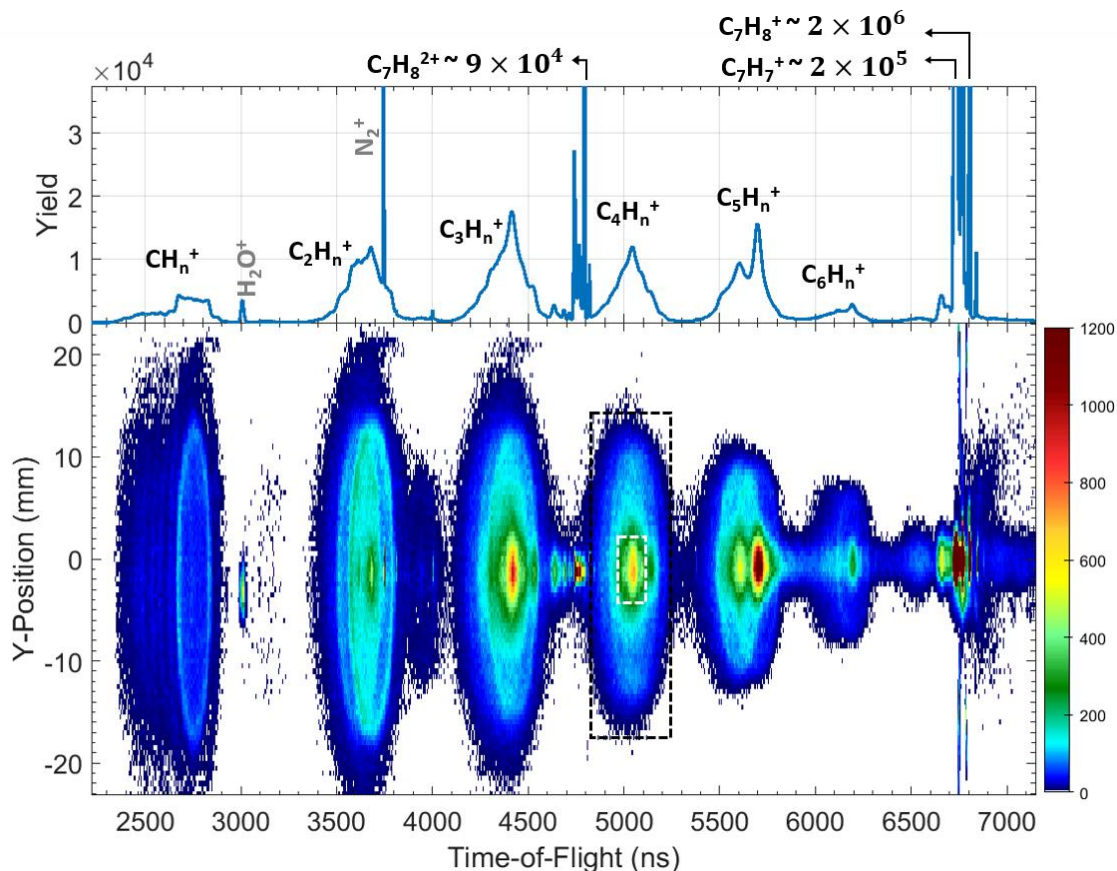
Figure 5.3: TOF mass spectrum of ions and two-dimensional spectrum on the detector. The 1D (top) and 2D spectrum are plotted as a function of ion time-of-flight (bottom) after the toluene molecules are ionized by an infrared strong laser field. The peak laser intensity is 130 TW/cm^2. The direction of laser polarization is along the time-of-flight axis. Contributions from residual gas are labeled in grey, i.e. N_2^+. The spectra contributed the parent ion, dication, and the parent ion with one hydrogen loss are cut highlight the distribution of fragment ions. The white and black dashed rectangles show the regions of interest used to extract the yield of fragments due to the single and double ionization, respectively. (This figure is reproduced from Faraday Discuss., 2021, 228, 39 DOI: 10.1039/D0FD00125B)

Table 5.1. Abundance of fragment ions normalized to the yield of the $C_7H_8^+$ parent ion. The time scale of the TOF measurements is on the order of microseconds. (This table is reproduced from Faraday Discuss., 2021, 228, 39 DOI: 10.1039/D0FD00125B.)

I (TW/cm²)	CH_n^+	$C_2H_n^+$	$C_3H_n^+$	$C_4H_n^+$	$C_5H_n^+$	$C_6H_n^+$	$C_7H_8^{2+}$	$C_7H_7^+$
220	17.1%	26.3%	30.9%	17.6%	17.2%	2.3%	4.8%	16.0%
170	8.6%	17.2%	21.0%	12.9%	13.9%	1.8%	3.5%	15.8%
130	4.7%	11.2%	13.9%	9.1%	10.9%	1.4%	2.5%	15.1%
90	1.2%	3.7%	5.0%	3.7%	5.7%	0.6%	1.1%	12.3%
65	0.5%	1.6%	2.4%	1.9%	3.4%	0.4%	0.6%	10.0%
30	0.4%	0.5%	0.8%	0.7%	1.3%	0.1%	0.1%	6.3%

Table 5.2. Abundance of fragment ions with high kinetic energies, normalized to that of the $C_7H_8^+$ parent ion. The peak laser intensity is denoted as I, and the unit is TW/cm². (This table is reproduced from Faraday Discuss., 2021, 228, 39 DOI: 10.1039/D0FD00125B.)

I (TW/cm²)	CH_n^+(high)	$C_2H_n^+$(high)	$C_3H_n^+$(high)	$C_4H_n^+$(high)	$C_5H_n^+$(high)	$C_6H_n^+$ (high)
220	14.2%	20.2%	22.3%	12.9%	10.5%	0.6%
170	7.0%	13.6%	15.4%	9.2%	8.0%	0.5%
130	3.8%	8.9%	10.2%	6.4%	5.8%	0.4%
90	1.0%	2.9%	3.6%	2.5%	2.4%	0.2%
65	0.4%	1.2%	1.6%	1.2%	1.2%	0.1%
30	0.4%	0.3%	0.5%	0.4%	0.4%	0.0%

The ion signal of each $C_mH_n^+$ group from single and double ionizations can be obtained by integrating the counts within the regions of interest. For example, for the $C_4H_n^+$ group shown in figure 5.3, the data inside the white dashed rectangle indicates the ions with low

kinetic energies, and the black rectangle for ions with high kinetic energies. The abundance of ions with high and low kinetic energies are given in table 5.2 and 5.3. Note that the separation of ion signals with low and high kinetical energies is approximated based on the distribution of the spectrum on the detector. A precise measurement of the three-dimensional momentum and kinetic energy is not possible for signals with different mass-to-charge ratios since their signals are overlapped on the detector.

Table 5.3. Abundance of fragment ions with low kinetic energies, normalized to that of the $C_7H_8^+$ parent ion. (This table is reproduced from Faraday Discuss., 2021, 228, 39 DOI: 10.1039/D0FD00125B.)

I (TW/cm²)	CH_n^+(low)	$C_2H_n^+$(low)	$C_3H_n^+$(low)	$C_4H_n^+$(low)	$C_5H_n^+$(low)	$C_6H_n^+$(low)
220	2.9%	6.1%	8.6%	4.7%	6.7%	1.7%
170	1.6%	3.6%	5.6%	3.6%	5.9%	1.3%
130	0.9%	2.3%	3.7%	2.7%	5.1%	1.0%
90	0.2%	0.8%	1.5%	1.3%	3.3%	0.4%
65	0.0%	0.4%	0.8%	0.7%	2.2%	0.3%
30	0.0%	0.3%	0.3%	0.3%	0.9%	0.1%

Nevertheless, the abundances in table 5.2 and 5.3 show that the majority of $C_mH_n^+$ fragments have high kinetic energies and are therefore created from double ionization, except for $C_6H_n^+$ fragments produced at the lower end of the covered intensity range. These measurements are in agreement with the analysis of a photoion-photoion coincident spectrum, which is not shown here. We use this spectrum and the 2D TOF *vs*. position spectra to identify the most prevalent ion species in each of the $C_mH_n^+$ fragment groups, which are listed in parentheses for each group below. The strongest fragments for each

group are shown in bold font: CH_n^+(CH_2^+, **CH_3^+**), $C_2H_n^+$(**$C_2H_2^+$, $C_2H_3^+$**), $C_3H_n^+$(**$C_3H_3^+$**, $C_3H_4^+$, $C_3H_5^+$), $C_4H_n^+$(**$C_4H_3^+$, $C_4H_4^+$**, $C_4H_5^+$), $C_5H_n^+$(**$C_5H_3^+$, $C_5H_5^+$**, $C_5H_6^+$), $C_6H_n^+$(**$C_6H_5^+$**, $C_6H_6^+$). This information is used to restrict the number of ions and fragment pairs for fitting of the UED measurements, explained in the following section.

5.4.2 *Ab-initio* calculated electron scattering of fragments

The fragmentation products of strong laser field induced toluene ionization captured by the UED instrument are assumed to be the same as those measured in the TOF-MS, shown in table 5.1. Neutral fragments generated from dissociative single ionization cannot be measured by TOF-MS, whereas their diffraction signal can be recorded by the UED measurement. The abundance of the neutral fragments corresponding to each $C_mH_n^+$ group can be estimated with table 5.3.

To simplify the *ab-initio* calculations, the structure optimization of the fragments after the ionization is performed in their respective electronic ground states, even though some of the fragments might be generated in electronically and/or vibrationally excited states. An accurate computation for fragments at excited states is challenging and is beyond the scope of this work. Previous X-ray diffraction experiments [49, 239, 240] have demonstrated that the electronic excitation manifests as a secondary contribution to the scattering signal and is approximately an order of magnitude smaller than the effect of molecular geometry changes. Most of the fragments, many of which are open-shell systems, are expected to return to their electronic ground state very quickly. The inclusion of fragments in vibrationally excited states is unlikely to make a significant difference in the scattering signal. Furthermore, no corrections are made to account for the effect on the electron scattering signal due to the vibrational excitation of the fragments, since very little is known

about the internal energy with which fragments are born in the photoionization process. Previous reports have demonstrated that the effect from vibrational excitation on the scattering signal, at least for rigid molecules, is small even at very high temperatures [241, 242]. Therefore, it is reasonable to model the electron scattering signal of the fragments in the experiment by using the structure of the fragments in their ground states.

Table 5.4. CASSCF level of theory is used for the structure optimization and electron scattering intensity computation. The number of active orbitals is denoted by α, and the number of active electrons by β. Each fragment is considered to be in its cationic or neutral form. The multiplicity of the fragments is changed accordingly. (This table is reproduced from Faraday Discuss., 2021, 228, 39 DOI: 10.1039/D0FD00125B.)

Ions	$CH_3{}^+$	CH_3	$CH_2{}^+$	CH_2	$C_2H_3{}^+$	C_2H_3	$C_2H_2{}^+$	C_2H_2	$C_3H_4{}^+$	$C_3H_5{}^+$
(α, β)	8,6	8,7	7,7	7,8	10,11	10,12	10,9	10,10	12,17	12,18
$C_3H_3{}^+$	$C_3H_2{}^+$	C_3H_3	C_3H_4	C_3H_5	C_3H_2	$C_4H_3{}^+$	C_4H_4	$C_4H_4{}^+$	$C_4H_5{}^+$	C_4H_5
12,16	10,17	12,17	12,18	12,19	10,18	8,10	8,12	8,11	8,12	8,13
C_4H_3	$C_5H_6{}^+$	C_5H_3	C_5H_6	$C_5H_3{}^+$	C_5H_5	$C_5H_5{}^+$	$C_6H_6{}^+$	C_6H_3	C_6H_6	$C_6H_3{}^+$
8,10	11,15	11,13	11,16	11,12	11,15	10,14	9,11	9,9	9,12	9,8
$C_6H_5{}^+$	C_6H_5	Bz^+	CHT^+	Tr^+	Tol^+	Tol^{2+}	Tol	H		
8,10	9,11	8,9	8,9	8,8	8,9	8,8	8,10	3,1		

We calculate the geometry of the neutral and ionic fragments in their ground states by use of the complete active space self-consistent field (CASSCF) level of theory and 6-311G basis sets with the electronic structure package Molpro [243]. The multiconfigurational

character of the method correctly accounts for static electron correlation and improves the accuracy of the molecular structure in the ground state in comparison to other single reference methods. The number of active orbitals (denoted as α) and electrons (β) considered in the electron scattering computation of each fragment are listed in table 5.4. They are chosen to allow for a multideterminant wavefunction which yields an accurate description of the system, while maintaining a balance between accuracy and computational time. The electron scattering intensity of each product is calculated using the method described in section 5.3.2 and in ref. [236, 238].

To model the electron scattering from the ionization fragments, we assume that only two fragments are produced from one fragmentation event, resulting in a pair of fragments. These fragment pairs scatter the high-speed incident electrons in the UED experiment. This assumption does not consider the possibility of one event leading to more than two fragments, since the contribution to the signal from these events is assumed to be small at the given peak laser intensities. The distance between the fragment pairs is long enough such that there is no interference produced from the scattered wavefunction between the two fragments. Furthermore, according to the TOF-MS measurement, one of the fragments is considered to be charged and the other one neutral in the case of dissociation after single ionization, and both fragments are charged, when they are formed from double ionization and subsequent Coulomb explosion.

The theoretically calculated diffraction difference signal for a certain fragment pair, i.e., C_6H_5, CH_3^+, is given by

$$\Delta I(s) = I_{C_6H_5}(s) + I_{CH_3^+}(s) - I_{\text{toluene}}(s), \tag{5.10}$$

and for benzylum (Bz⁺, $C_7H_7^+$) and hydrogen, $\Delta I(s) = I_{\text{Bz}^+}(s) + I_{\text{H}}(s) - I_{\text{toluene}}(s)$. The corresponding modified diffraction signal is defined as

$$\Delta sM(s) = \frac{s \cdot \Delta I(s)}{I_{\text{atom\_toluene}}}, \tag{5.11}$$

where $I_{\text{atom\_toluene}}$ is the atomic scattering intensity of the neutral toluene molecule. The *ab-initio* calculation of the electron scattering for fragment pairs is shown in figure 5.4 using the $sM(s)$ convention.
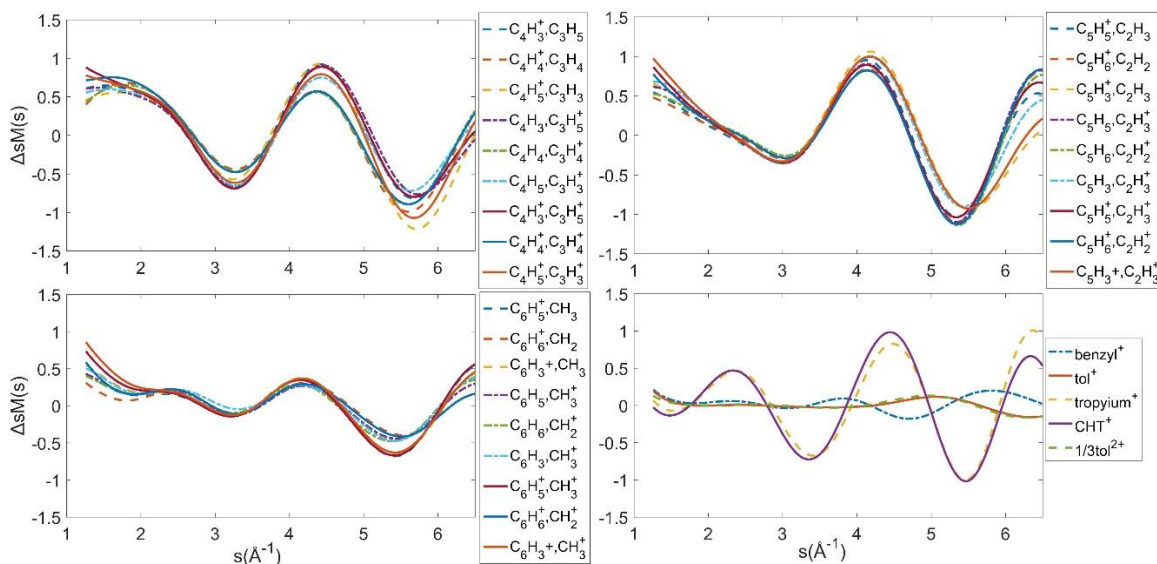
Figure 5.4: Theoretically calculated ΔsM(s) of fragment pairs and other ionic products using the *ab-initio* method. (This figure is reproduced from Faraday Discuss., 2021, 228, 39 DOI: 10.1039/D0FD00125B)

In the last panel of figure 5.4, the $\Delta sM(s)$ of tropylium (Tr⁺) is similar to that of cycloheptatriene (CHT⁺), and the $\Delta sM(s)$ of the toluene cation (tol⁺) is close to the $\Delta sM(s)$ of Tol²⁺ scaled by a factor of 1/3. Therefore, the $\Delta sM(s)$ of fragment pairs can be

approximately classified into 6 groups, (C_3H_m, C_4H_n), (C_6H_m, CH_n), (C_2H_m, C_5H_n), (Tr^+, CHT^+), (Tol^+, Tol^{2+}), and Bz^+.

The electron scattering intensities of the abovementioned fragment pairs using the theory based on the IAM described in section 5.3.1 are shown in figure 5.5 for comparison. The most obvious difference is the scattering intensity at the low *s* values, corresponding to the large impact parameters in Rutherford scattering. The *ab-initio* calculated $\Delta sM(s)$ of most prominent cations from each group determined by the TOF-MS measurement described in section 5.4.1 are used to fit the UED signals, explained in the following section.
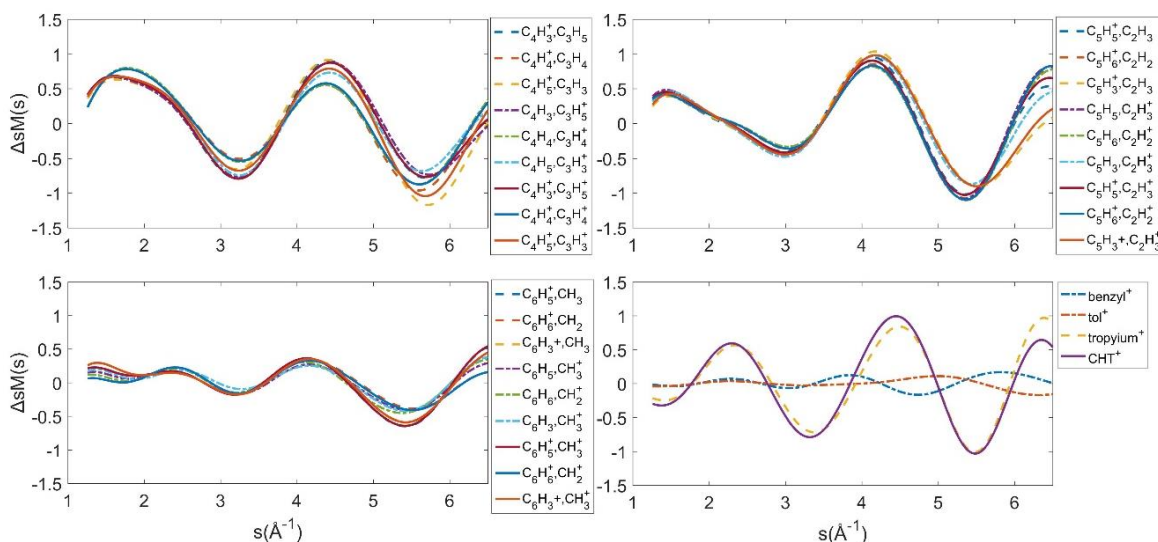
Figure 5.5: Simulated ΔsM(s) for fragment pairs using the diffraction theory based on the IAM. (This figure is reproduced from Faraday Discuss., 2021, 228, 39 DOI: 10.1039/D0FD00125B)

5.4.3 Ultrafast electron diffraction measurements

In this section, we show the electron diffraction signal of the fragments formed from the ionization and fragmentation of toluene induced by the strong laser field. We show the

static diffraction pattern of toluene which is taken by setting the arrival time of the electron pulse to before that of the laser pulse, corresponding to a negative time delay. We then demonstrate the diffraction signal at different positive time delays between the electron and laser pulses.

5.4.3.1 Static diffraction of toluene
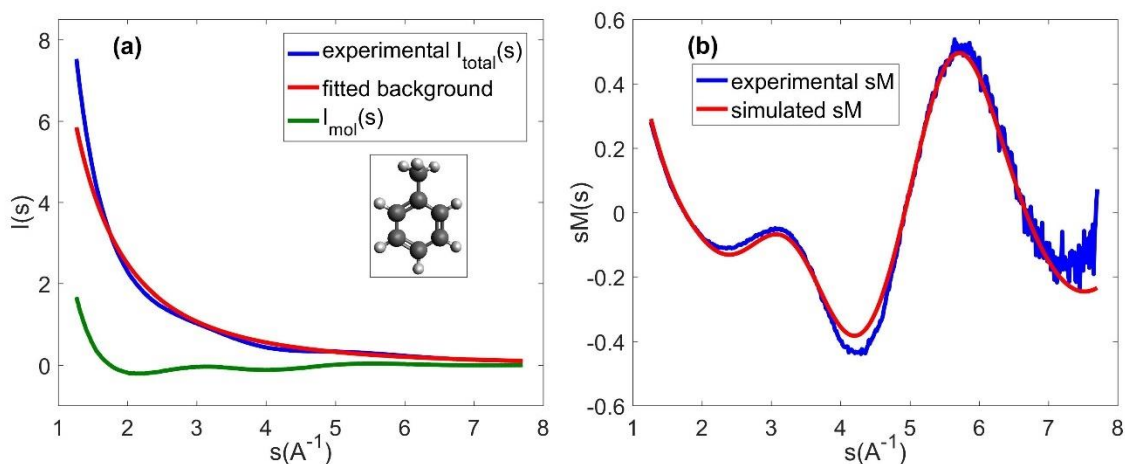
Figure 5.6: Static diffraction signal of neutral toluene molecules. The blue curve is the total diffraction intensity, denoted as $I_{total}(s)$, which is the azimuthal average of the 2D experimental diffraction pattern. The red curve is the background fitted using the zeros of the theoretical $sM(s)$, including the atomic scattering and other background scattering. The green curve is $I_{mol}(s)$, obtained by taking the difference of $I_{total}(s)$ and the fitted background. The inset shows the molecular structure of toluene. (b) The theoretical (red) and experimental (blue) $sM(s)$ of toluene. The experimental $sM(s)$ is calculated from the experimental $I_{mol}(s)$ using eqn. (5.4). (This figure is reproduced from Faraday Discuss., 2021, 228, 39 DOI: 10.1039/D0FD00125B.)

Figure 5.6 shows the static diffraction signal of toluene in ground state. The circularly symmetric 2-dimensional static diffraction pattern is azimuthally averaged to obtain the 1-

dimensional $I_{total}(s)$. We use the zero values of the theoretically calculated $sM(s)$ of toluene, which is based on the IAM, to fit and remove a background of the experimental $I_{total}(s)$ to obtain the experimental $I_{mol}(s)$ according to the method described in ref. [3]. The removed background consists of the atomic scattering, and most of the experimental background scattering and noise. The $I_{total}(s)$, $I_{mol}(s)$ and the background being removed are shown in figure 5.6 (a). The fitting of the experimental to theoretical $sM(s)$ is shown in figure 5.6 (b). There is good agreement between the experimental and theoretical $sM(s)$.

5.4.3.2 Diffraction signal of ions

The electron scattering at small angles from ions can be distorted by the laser-induced plasma through the lensing effect [231], described in section 2.4.2 of chapter 2. Macroscopic electric fields are present in the plasma which distort and deflect the incident electron beam, preferentially in the direction along the laser polarization [244, 245]. This results in a small amount of electron beam leaking out of the beam stop at small s values. However, the signal at low s on the detector due to the plasma deflection shows a strong anisotropy, while the diffraction signal from the randomly oriented fragments is isotropic. We apply a Legendre projection on to the 2D diffraction patterns to get rid of the anisotropic contributions and keep the isotropic part of the diffraction intensity. By doing so, we are able to remove the plasma-deflected electrons in the diffraction patterns.

The pump-probe diffraction patterns are recorded at four delay times: -5 ps, 5 ps, 10 ps, and 15 ps. The total diffraction intensity $I_{total}(s, t = -5 \text{ ps})$ contains scattering from the toluene molecules in the ground state and other background signals, such as scattered laser light and background electrons, which is used as a reference. The total integration time of the diffraction pattern at each time delay is 100 minutes. The procedures of calculating the

experimental $\Delta sM(s)$ are described below. First, the data behind the beam stop and outliers are removed from each image for the analysis, and each image is normalized by the average number of data counts within 60×60 pixels around s=2.4 Å^{-1}. Second, the 2D diffraction-difference patterns are calculated by taking the difference between the pattern at positive time delays and the reference pattern at -5ps, formulated as $\Delta I_{2D}(s,t) = I_{2D}(s,t) - I_{2D}(s, t_{ref} = -5ps)$. Third, the Legendre projection is applied to the $\Delta I_{2D}(s,t)$ to obtain the isotropic component in the 2D pattern [246], which is then azimuthally averaged to calculate the 1D diffraction-difference intensity $\Delta I_{exp}(s,t)$ and the standard error $\sigma(s,t)$ at each s. The experimental $\Delta sM(s)$ at each time delay is calculated using eqn. (5.11) and is shown in figure 5.7. The signal shows larger statistical variations at larger s due to the lower signal level.
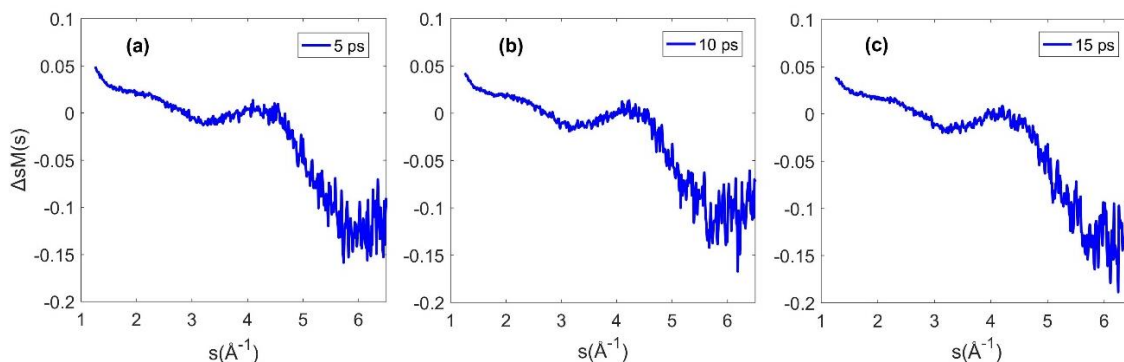
Figure 5.7: ΔsM_{exp} for different time delays using reference time t$_{ref}$=-5 ps. (a) 5 ps, (b) 10 ps, (c) 15 ps. (This figure is reproduced from Faraday Discuss., 2021, 228, 39 DOI: 10.1039/D0FD00125B.)

A residual background shows up in the ΔsM_{exp}, which can be fitted using the zero values of the theoretical $\Delta sM(s)$, a similar method to the one used to find the background for the static diffraction signal of toluene [3]. However, the ΔsM_{exp} contains more than one

structure, as fragments shown in the measurement of TOF-MS. Therefore, we model the $\Delta sM(s)$ by using the linear expansion of the *ab-initio* calculated $\Delta sM(s)$ for fragment pairs: $(C_4H_4^+, C_3H_4^+)$, $(C_6H_5^+, CH_3^+)$, $(C_5H_3^+, C_2H_3^+)$, Tr^+, Bz^+ and Tol^+, which are the most prevalent fragments determined by the measurement from TOF-MS, as shown in section 5.4.1. The fragments in parenthesis are fragment pairs generated after the breakup of the parent ions. All fragments are assumed to have a charged fragment partner since the TOF-MS measurements show that most of the fragments are generated by double ionization. Figure 5.1 shows three-dimensional models of the fragment pairs from the calculated structures.

The fitting procedure is described in the following section of text. The *ab-initio* calculated $\Delta sM(s)$ of each fragment pair is labeled as $y_i(s)$ for convenience. We construct a linear combination of $y_i(s)$ to model the experimental $\Delta sM(s)$, formulated as

$$\Delta sM_t(s, c_i) = \sum_{i=1}^{n} c_i \, y_i(s) \,, \tag{5.12}$$

where *n* is the number of fragment pairs and ionization products, and c_i are the coefficients to be determined by the fitting, which indicate the amplitude of each component in the experiment. To remove the residual background, we use the zero values of $\Delta sM_t(s, c_i)$ to fit a background, denoted as $b(s, c_i)$, with a 2nd order polynomial. The set of coefficients c_i is determined by the minimum of χ^2, given by

$$\chi^2(c_1, c_2, \dots, c_n) = \frac{1}{N_s - n} \sum_s \left[\frac{\Delta sM_{\exp}(s) - b(s, c_i) - \Delta sM_t(s, c_i)}{\sigma(s)} \right]^2, \tag{5.13}$$

where the sum is over all the *s* values in the experimental data, and the number of s values is N_s. The coefficient c_i gives the abundance of each fragment pair produced after ionization and fragmentation of toluene molecules. The sum of the coefficients obtained

by the fit, formulated as $ef = \sum_{i=1}^{n} c_i$, indicates the percentage of the toluene ionized in the interaction region. Bootstrapping is used to obtain the standard error of the fitted parameters. We use the combined data set, which is the average of the ΔsM_{exp} at three-time delays, to obtain the ef, and keep it the same in the fitting for all the time delays. The fittings of the experimental ΔsM_{exp} to the theoretical ΔsM_t for the three-time delays are displayed in figure 5.8.
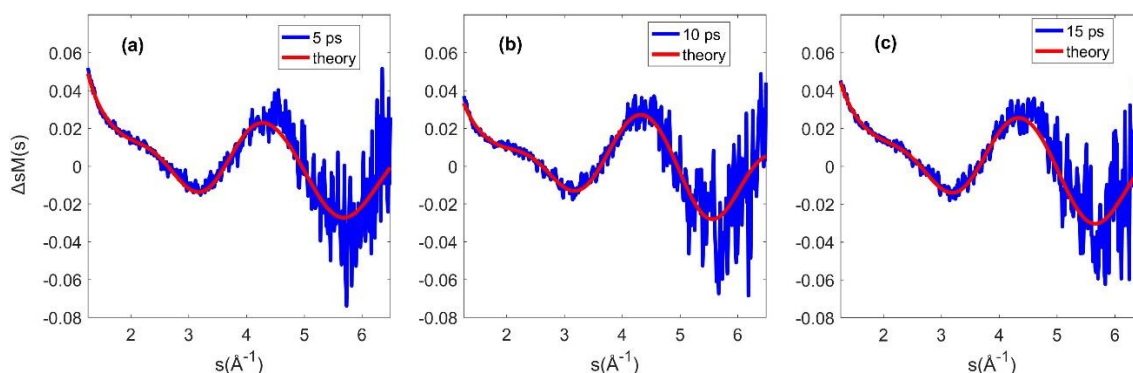
Figure 5.8: The fitting of the experimental ΔsM_{exp} (blue) to the theoretical ΔsM_t (red) for time delays : (a) 5ps, (b) 10ps, (c) 15ps. (This figure is reproduced from Faraday Discuss., 2021, 228, 39 DOI: 10.1039/D0FD00125B)

The coefficients c_i and the corresponding confidence intervals obtained from the least-squares fit are shown in table 5.5. The last row is the fit result with the averaged ΔsM_{exp} data at the three-time delays. Although there is some indication that yields of some fragment pairs might increase or decrease after 5 ps, further investigations are needed to reduce the uncertainties to address this point. Overall, fitting to the individual time steps gives the fragment yields observed at different time delays, which are consistent within the experimental uncertainties. The fitting of the combined data set, which is an average of the

ΔsM at 3-time delays, reduces the uncertainties. The results of the fitting are similar when using the theoretical ΔsM of different fragment pairs from each group, other than the ones chosen here, to do the fitting [69].

Table 5.5 Fitted abundance of the experimental ΔsM at different time delays. The last row (C) is the fitted parameters with the combined data at the 3-time delays. The total excitation fraction is denoted as *ef*. (This table is reproduced from Faraday Discuss., 2021, 228, 39 DOI: 10.1039/D0FD00125B.)

%	C_4H_m, C_3H_n	C_6H_m, CH_n	C_5H_m, C_2H_n	Tr^+, CHT^+	Bz^+	Tol^+, Tol^{2+}	*ef*	χ^2
5ps	3.13±2.14	1.48±2.08	15.77±2.79	4.41±1.41	1.44±3.17	73.78±3.41	0.12	1.88±0.09
10ps	7.26±2.19	4.37±2.51	13.73±2.91	3.70±1.45	9.78±6.34	61.18±6.70	0.12	1.85±0.11
15ps	8.09±2.31	4.95±2.15	13.79±2.34	2.29±1.47	4.63±5.63	66.27±5.58	0.12	1.82±0.09
C	**7.30±1.71**	**5.40±1.82**	**13.14±2.01**	**2.66±1.15**	**5.31±4.68**	**66.20±4.44**	**0.12**	**1.88±0.08**

The analysis gives an excitation fraction of 12%, denoted as *ef* in the table, corresponding to the percentage of molecules within the interaction volume that are ionized by the laser field. The most prevalent products obtained by the fit are the parent ion, as expected. In our analysis, we included also the doubly ionized parent (Tol^{2+}) since the *ab-initio* calculated $\Delta sM(s)$ of Tol^+ and Tol^{2+} are very similar and cannot be separated by the UED measurement. The singly ionized parent (Tol^+) is supposed to be more prevalent according to the TOF-MS measurements. The abundances of fragment pairs produced in descending order are (C_5H_m, C_2H_n), (C_4H_m, C_3H_n) and (C_6H_m, CH_n). The UED experiment also detects

a significant amount of Benzyl$^+$ and (Tr$^+$, CHT$^+$). However, the structure of tropylium and CHT cations are very similar. Thus, their abundances cannot be determined independently by the UED measurement.

5.5 Discussions

5.5.1 Comparison of UED and TOF-MS measurements

In this section, we compare the abundance of the fragments generated from the measurements by TOF-MS and by UED. We hope to make the measurements as comparable as possible though there are some significant differences in the experimental conditions. The first difference is the time scale of the two measurements. The UED data are recorded within 5 ps to 15 ps after the ionization by the laser pulse, while the spectra of TOF-MS are detected when the ions reach the detector, which is on the order of micro-seconds after the ionization. This leaves the possibility that there could be further fragmentations during the time between the ionization and when the ions are captured by the TOF-MS. Furthermore, the pulse duration of the laser used to induce the fragmentation for TOF-MS was 30 fs, while it was 50 fs for UED measurement, which might lead to some differences in the branching ratios.

The other significant difference is the intensity distribution of the laser field that creates the ionization of the toluene molecules. In the TOF-MS experiment, fragments are generated from the focal volume determined by the intersection of the molecular beam and the laser beam, in which the size of molecular beam is much larger than that of the laser beam. In the UED experiment, the probe electron beam is smaller than the laser beam.

Thus, the scattering signal is mostly from the higher intensity region of the laser focus when compared to the TOF-MS measurement.

Here we analyze the difference in the laser intensity distribution and signal collection in the TOF-MS and UED experiments. Assume $P(k, I)$ is the probability of the cation k being created from one toluene molecule per laser pulse with an intensity I, and $\rho(I)dI$ is the number of molecules ionized by the laser field in the intensity range $I \sim I + dI$. The number of cations k generated is $dN(k, I) = P(k, I)\rho(I)dI$. The molecule number density can be numerically calculated according to the interaction geometry. The total number of cations k is given by the integral over all the laser intensities, $N(k) = \int P(k, I)\rho(I)dI$. The relative abundance of cation k is $N(k)/\sum_k N(k)$. While $P(k, I)$ cannot be determined by the experiments, we are able to determine $\rho(I)$ by analyzing the interaction region of the UED and TOF-MS configurations.
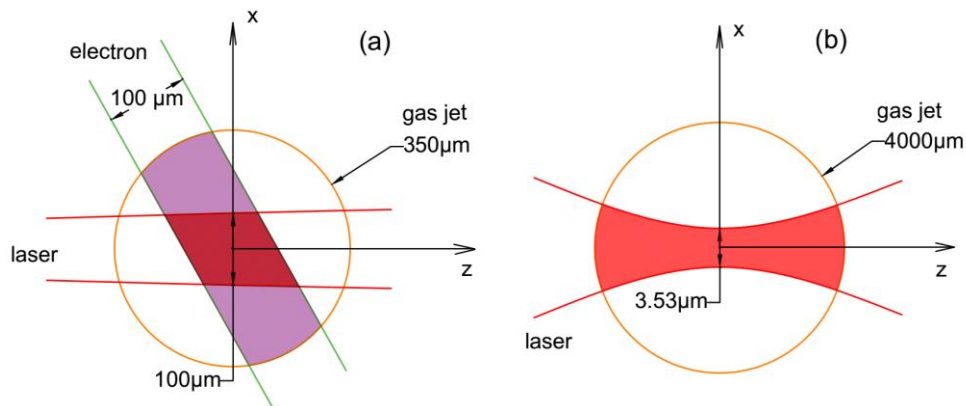
Figure 5.9: Geometry of the interaction region. (a) In the UED experiment, the gas jet is perpendicular to the plane made up of the electron and laser beams, with the laser incident at an angle of 60° with respect to the electron beam. (b) In TOF-MS, the laser beam is focused on a gas jet with a much larger beam size. The signal is produced from the red

region in both measurements. (This figure is reproduced from Faraday Discuss., 2021, 228, 39 DOI: 10.1039/D0FD00125B.)

Figure 5.9 shows the geometry of the interaction region in the UED and TOF-MS experiments. In the UED experiment, the diameter (FWHM) of the gas jet is 350 μm, laser beam 100 μm (H) × 170 μm (V), and electron beam 100 μm. The Rayleigh length is 1.13 mm, and the laser focus (diameter 20 μm) is 5 mm upstream of the interaction region, where the laser, electron and molecule beams intersect. The size of the laser beam can be approximated as a constant over the 350 μm gas jet. Therefore, the laser intensity distribution in the gas jet for the UED experiment can be written as

$$I_{\text{laser\_UED}}(x, y) = I_0 e^{-\left(\frac{x^2}{2c_x^2} + \frac{y^2}{2c_y^2}\right)}. \tag{5.14}$$

The integral of $I_{\text{laser\_UED}}(x, y) \exp\left(-\frac{t^2}{2c_t^2}\right)$ over space and time is equal to the pulse energy E. For example, based on measurements of pulse duration, energy, and spot size, the peak intensity in UED is $I_0 = \frac{E}{(2\pi)^{3/2} c_x c_y c_t} = 116 \text{ TW/cm}^2$. The intensity of the electron beam and gas jet can be written as

$$I_{\text{e\_UED}} = \frac{1}{2\pi c_e^2} e^{-\frac{\left(\frac{1}{2}x + \frac{\sqrt{3}}{2}z\right)^2 + y^2}{2c_e^2}}, \tag{5.15}$$

$$I_{\text{gas\_UED}} = \frac{1}{2\pi c_g^2} e^{-\left(\frac{x^2 + z^2}{2c_g^2}\right)}. \tag{5.16}$$

The toluene molecules in the interaction region that contribute to the electron diffraction signal are given by the three-dimensional distribution, formulated as $I_{\text{e\_UED}} \times I_{\text{gas\_UED}}$. In this distribution, molecules at different positions are pumped by the laser intensity given

by $I_{\text{laser\_UED}}(x, y)$. We use the $1/e^2$ width of the electron beam and gas jet to determine the effective interaction region and assume that the relative yield of fragments generated below the laser intensity I_{L} (1 TW/cm^2 is used below) is negligible. The laser intensity with a range from I_{L} to I_0 is considered to calculate the molecule number density $\rho(I)$ numerically.
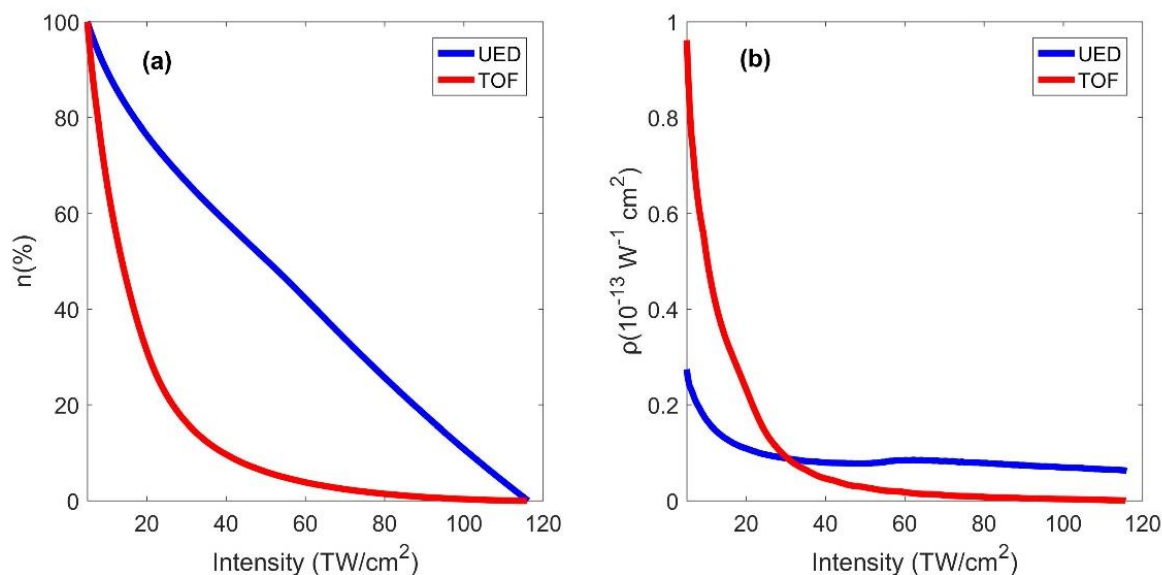
Figure 5.10: The cumulative number of molecules and number density distribution. (a) Cumulative number of molecules $n(I)$. (b) number density $\rho(I) = -dn(I)/dI$. UED is displayed in blue, and TOF-MS in red. Cumulative number of molecules $n(I)$ is the number of molecules pumped by an intensity larger than I. (This figure is reproduced Faraday Discuss., 2021, 228, 39 DOI: 10.1039/D0FD00125B.)

In TOF-MS, the diameter of the gas jet is 4000 μm, the diameter of laser focus 3.53 μm, and Rayleigh length is 10 μm, as shown in figure 5.9 (b). The laser intensity can be written as

$$I_{\text{laser\_TOF}} = I_0 \left[\frac{w_0}{w(z)}\right]^2 e^{\frac{-2(x^2+y^2)}{w(z)^2}} , \qquad (5.17)$$

where $w(z) = w_0\sqrt{1 + (z/z_R)^2}$, waist radius $w_0 = 1.5$ μm, and Rayleigh length $z_R = \pi w_0{}^2/\lambda$. The gas jet can be expressed as eqn. (5.16) with c_g=4000 μm. The $1/e^2$ width of the gas jet and the laser intensity ranging from 1 TW/cm^2 to I_0 are used for the numerical calculation.

The cumulative number of molecules $n(I)$, which is normalized to 1, and number density $\rho(I) = dn(I)/dI$ for UED and TOF-MS are shown in figure 5.10. Figure 5.10 (b) shows that the UED measurement will sample more molecules at higher intensities in comparison to the TOF-MS measurement.

5.5.2 Fragment yields in UED and TOF-MS

UED is sensitive to all fragments, whereas TOF-MS is not able to capture the neutral fragments. To compare the fragment abundances in the two measurements, we assume that for singly ionized fragments (low kinetic energy fragments in the TOF spectra) captured in TOF-MS, shown in table 5.3, there is a complementary neutral fragment. For example, the abundance of the neutral fragment C_3H_m is taken to be equal that of the $C_4H_n{}^+$ fragment in table 5.3. In the case of double ionization (high kinetic energy fragments, shown in table 5.2), the molecule is assumed to be broken into two fragments, both of which are detected by the TOF-MS. Based on this assumption, the two complementary charged fragments should have the same yield in the double ionization, but the TOF-MS measurement shows some differences, most likely due to three-body fragmentation events that have been neglected here, or due to the non-uniformity of the detection efficiency for different fragments in the detector.

To calculate the total yield for a fragment pair including neutrals, we take the sum of the yield of complementary pairs in the single ionization signal (table 5.3), and the yield of one of the complementary fragments in the doubly ionized signal (table 5.2). Using the lower or higher yield of the certain fragments in table 5.2 gives the lower or higher bounds of the total yield of the fragment pair, respectively. For example, for the fragment pair (C_4H_m, C_3H_n), the lower bound is given by $C_4H_m^+(SI) + C_3H_n^+(SI) + C_4H_m^+(DI)$, where SI and DI indicate fragments produced by single and double ionization, respectively. The corresponding higher bound for the yield of (C_4H_m, C_3H_n) is given by $C_4H_m^+(SI) + C_3H_n^+(SI) + C_3H_m^+(DI)$. Table 5.6 demonstrates the relative fragment pair yields including both charged and neutral fragments, obtained from the TOF-MS data.

Table 5.6. Relative yield of fragment pairs normalized to that of $C_7H_8^+$ in TOF-MS measurement. The two values in each column represent the lower and upper bounds for the yield of the fragment pair. (This table is reproduced from Faraday Discuss., 2021, 228, 39 DOI: 10.1039/D0FD00125B.)

I (TW/cm^2)	C_4H_m, C_3H_n (%)	C_6H_m, CH_n (%)	C_5H_m, C_2H_n (%)
170	18.86~24.56	3.44~9.95	17.44~23.15
130	12.98~16.51	2.30~5.68	13.19~16.29
90	5.15~6.30	0.78~1.62	6.54~6.98

Table 5.7 shows the equivalent yields of fragment pairs in the UED measurement, normalized with respect to the yield of the parent ion, as calculated from data in the last row of table 5.5. The comparison shows that the fragment yield in the UED measurement best agrees with TOF-MS measured yield in the peak laser intensity range between 130

TW/cm^2 and 170 TW/cm^2. The peak laser intensity for the UED experiment is 116 ± 20 TW/cm^2. However, due to the different sampling distribution described in the last section, we expect that the yield in UED measurement would best match the TOF-MS data at a higher laser intensity. Overall, the results from the two measurements are consistent. The possible reasons for the discrepancy are listed below. First, the laser intensity distributions over the sample volume in the two experiments are different, leading to the fragments being sampled differently. Second, the fragments are assumed to be in their vibronic ground state for the *ab-initio* computation of electron scattering. Thus, the other possible fragment structures that might give a different fitting result are ignored. Third, three-body fragmentation events could in principle have a role in the strong-field induced fragmentation, although the TOF-MS suggests that it is a minor fragmentation pathway.

Table 5.7. Relative yield of fragment pairs normalized to $C_7H_8^+$ in UED measurement. (This table is reproduced from Faraday Discuss., 2021, 228, 39 DOI: 10.1039/D0FD00125B)

I (TW/cm^2)	C_4H_m, C_3H_n (%)	C_6H_m, CH_n (%)	C_5H_m, C_2H_n (%)
116 ± 20	11.03±2.69	8.16±2.80	19.85±3.32

5.4.1 Comparison of *Ab-initio* and IAM scattering calculations

In this section, we demonstrate the comparison of modelling the UED signal with *ab-initio* scattering calculations and with a calculation based on IAM. A previous UED experiment on photo-excited pyridine has shown that the electron diffraction theory based on the IAM does not provide an accurate description of the diffraction signal at low *s* for time delays

within 1.5 ps after excitation [247]. An enhancement of the electron scattering signal shows up at low s due to the increased inelastic scattering from the molecules in electronically excited states, and the diffraction signal can be well simulated by using *ab-initio* scattering calculations and high-level computation of the excited state dynamics. Here we demonstrate that the elastic electron scattering theory based on the IAM does not provide a good approximation for the diffraction signals from ions, and that an *ab-initio* calculation for elastic electron scattering is needed. The main difference between the two is present at small s, in which the electron scattering from the charged system approaches Rutherford scattering.

Figure 5.11 shows a comparison of the modeling of the experimental $\Delta sM(s)$ with the *ab-initio* scattering calculations, figure 5.11 (a), and with the electron scattering simulation based on the IAM, figure 5.11 (b). The same fitting procedure, described in section 5.4.3.2, was used in both cases. The fit displayed in figure 5.11 (a) corresponds to the fitting parameters given in the last row of table 5.5. Figure 5.11 (c-d) display the difference between the experimental and best fit plots of $\Delta sM(s)$. A clear upward trend shows up in the $\Delta sM(s)$ at low s values, which is accurately modeled in the *ab-initio* calculations and is completely missed in the scattering calculation based on the IAM. This upward trend at low s is due to the net charge of the ions. There is also a significant discrepancy in the signal at larger s when compared to the calculation based on the IAM, in part because a good fit cannot be obtained with the low-s signal. The residuals show that the fit of the signal using the *ab-initio* calculation is very accurate. Figures 5.11 (c-d) show that the trend in the residuals is a flat line for the fit with the *ab-initio* calculations but contains significant

modulations for the fit with the IAM, with the modulations being larger than the statistical variations in the data.
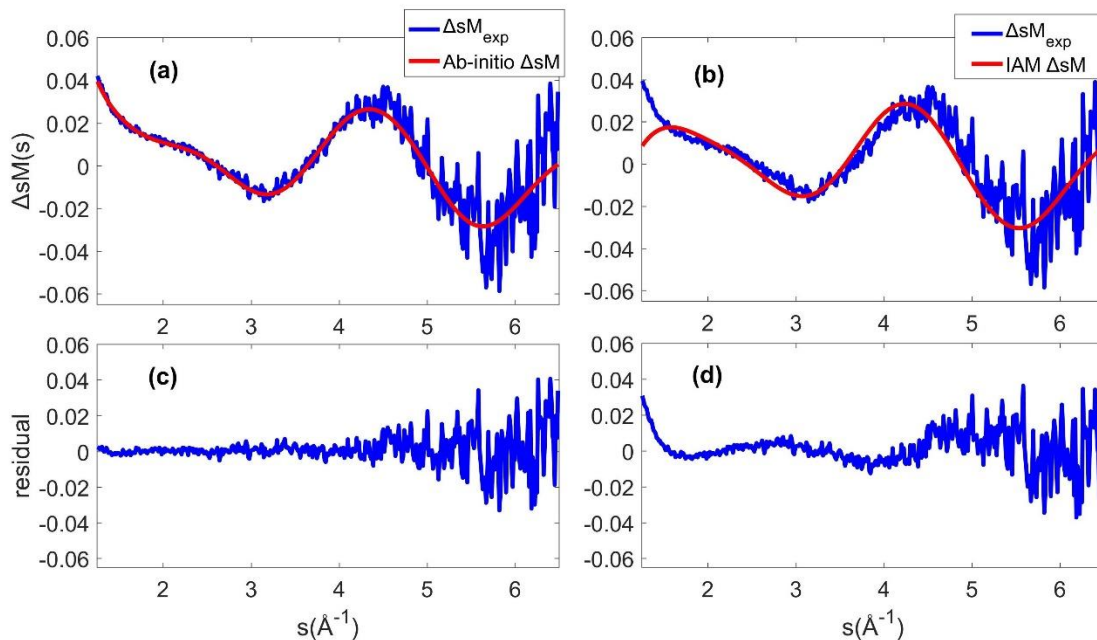
Figure 5.11: Fitting of the ΔsM(s) from the combined data at 3-time delays in the UED measurement. (a) Fitting with *ab-initio* electron scattering calculation; (b) Fitting with electron diffraction calculation based on the IAM; (c-d) are the residuals of the fits displayed in (a-b). (This figure is reproduced from Faraday Discuss., 2021, 228, 39 DOI: 10.1039/D0FD00125B)

Chapter 6

Ultrafast electron diffraction of UV-induced molecular dissociation

6.1 Introduction

Investigating structural changes of molecules upon photoexcitation is of importance to the understanding, and ultimately controlling of chemical reactions [248]. The energy of photons are converted into chemical and mechanical energy of molecules through the molecular photoexcitation process [66], which plays an essential role in biological processes, like photosynthesis [249], vision [250], the photodamage of DNA [251, 252] and the formation of vitamin D [253]. After photoexcitation, the absorbed energy leads to the generation of photoproducts often driven by the complex interplay of electronic and nuclear dynamics, including isomerization, bonding breaking and formation of new bonds, and energy dissipation by hot vibrations [66]. The transformation of the molecules from excited state to the end products takes place on ultrafast timescales. Understanding the mechanisms of the photochemical reaction requires capturing the full dynamics of the molecular structure change upon the photoexcitation.

Experiments that is able to capture such dynamics with enough temporal and spatial resolution can be used to accurately mode the photochemical reactions. Time-resolved spectroscopic experiments have been applied to study the energy landscape of the molecule and the relevant dynamics upon photoexcitation on the timescales of femtoseconds to attoseconds [254-256]. As a complementary to the spectroscopic measurements, time-resolved diffraction methods are sensitive to the molecular structure, and thus directly provide the spatial information of the molecule as it evolves in time [248]. Recently, both

ultrafast X-ray diffraction and UED have demonstrated the capacity to capture the dynamics of structural change of molecule upon photoexcitation on the order of femtosecond time scales [20, 21, 48-50, 52, 53]. However, in comparison to ultrafast X-ray diffraction, UED has the advantage of higher cross section that is about six orders of magnitude stronger than that of X-ray scattering [58]. More recently, sufficient spatiotemporal resolution of gas phase UED experiments has been achieved by the use of MeV-UED instrument, enabling the scientific advances of ultrafast molecular dynamics upon photoexcitation [19, 21, 52, 53, 89, 90].

In this chapter, I present the preliminary experimental results of dissociation of trifluoroiodomethane (CF_3I) and iodobenzene (C_6H_5I) upon UV excitation, captured by the keV-UED. In previous chapters, the keV-UED has demonstrated the capability to capture the ultrafast dynamics of laser-induced molecular alignment with a temporal resolution of 240 fs. Here we replace the IR pump pulse with a UV pump pulse with a central wavelength of 266 nm. The femtosecond UV laser pulse excites the molecules, such as CF_3I, C_6H_5I, to A-band electronically orbitals, followed by the relaxation associated with the fission of C-I bond. The electron pulse with a kinetic energy of 90 keV is used to probe the sample upon the photoexcitation. Using the rapid relaxation dynamics of CF_3I, the overall temporal resolution of the keV-UED setup is estimated to be ~200 fs.

6.2 Experiment setup

The details of the keV-UED setup with an IR laser as a pump have been previously reported in ref. [26, 32] and described in chapter 2. The diagram of the UED instrument with the UV laser pulse as a pump is shown in figure 6.1, including the RF compression, UV laser as a pump and electron pulse as a probe.
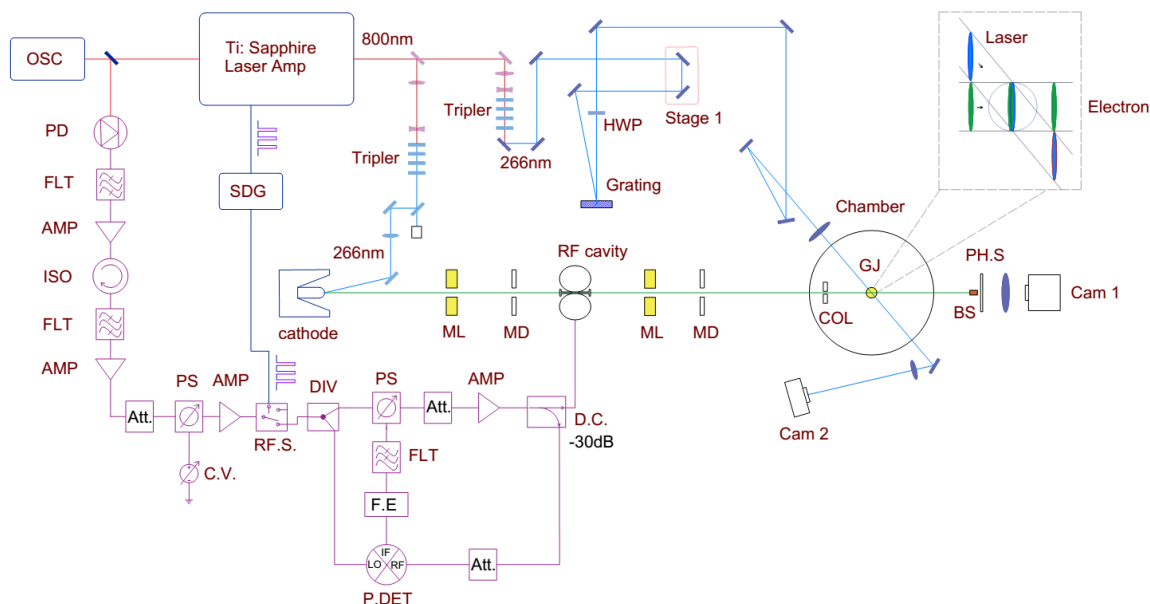
Figure 6.1: Schematic of experimental layout using a UV laser pulse as the pump. The path drawn in red color represents the laser pulse at 800 nm wavelength. The IR pulse with an energy of 2.9 mJ is frequency tripled to 266 nm as a pump laser. The UV pulse from the trippler has a maximum energy of ~400 µJ, and after considering the efficiency of the grating and reflectance of the mirrors, ~46% of the pulse energy can be delivered onto the gas jet to pump the sample. A pulse energy of 0.2 mJ is converted to the third harmonic at 266 nm to generate the electron as a probe, shown here in light blue. The path drawn in green corresponds to the electron beam, guided by the magnetic lenses and deflectors, from the photocathode to the phosphor screen. The path in purple represents the RF signal used to compress the electron pulse with the RF cavity. OSC = oscillator, BS = beam splitter, PD = photo diode, FLT = filter, AMP = amplifier, ISO = isolator, SDG = synchronization and delay generator, HWP= zero order half wave plate, Att. = attenuator, RF.S = RF switch, DIV = power divider, PS = phase shifter, C.V.= control voltage, F.E.= feedback electronics, P.DET = phase detector, D.C. = directional coupler, ML = magnetic lens, MD = magnetic deflector, COL = collimator, GJ = gas jet, BST= beam stop, PH.S = phosphorus screen,

Cam = camera. (This figure is modified from ref [32], used in accordance with the Creative Commons Attribution 4.0 International license.)

Each laser pulse from Ti: Sapphire amplifier is split into two parts, both of which are frequency tripled. One of the UV pulses with a higher energy is used to pump the molecules, and the other one with a lower energy to produce the photoelectrons as a probe. The pulse duration of the pump laser is estimated to be ~60 fs, the maximum pulse energy is 180 μJ and the beam diameter is 200 μm on the sample. We use a zero-order half wave plate to adjust the polarization of the UV laser pulse. The probe electron pulse is produced by shining the UV laser pulse with a lower energy onto a copper cathode. The electron pulse is accelerated to 90 keV in a DC electric field and then longitudinally compressed by using a time-varying field with an RF cavity. The electron pulse is guided by magnetic lens, deflectors, collimated by a platinum aperture, and then is delivered to the sample to probe the sample. The beam current is 8 pA on the sample, corresponding to 50,000 electrons per pulse, when using a 300 μm platinum aperture. The repetition rate of the instrument is 1 kHz.

The group velocity mismatch between UV and electron pulses is compensated by using a tilted UV laser pulse with a certain incident angle between the laser and electron beams [25, 32]. To remove velocity mismatch between the 90 keV electron pulse ($v_e = 0.526c$) and the laser pulse, the tilted angle of the UV pulse is 58.24°. The tilted intensity front is produced by introducing an angular chirp to the UV laser pulse using grating. An aluminum-coated grating with the grating constant d =400 mm^{-1} is used to generate the tilted pulse with an efficiency of ~50% for the energy of the incident pulse diffracted into the first order ($\hbar = 1$). Using the theory described in section 2.3.1, the incident angle of

the UV beam is $\theta_{in} = 6.1°$. The demagnification factor is $M_D = \tan(\gamma_t)/(d\lambda_0) = 15.18$.

The velocity matching between the laser and electron pulses within the gas jet is shown in

the inset of figure 6.1. We use the method described in section 2.4.2 of chapter 2 to overlap

the gas jet, electron, and laser beams. The electron scattering signals are recorded using an

electron-multiplying charge-coupled device (EMCCD) through a phosphor screen that is

imaged onto the EMCCD.

6.3 Electron diffraction measurement

The electron scattering theory has been introduced in detail in chapter 1. Electron

diffraction theory based on the IAM is able to provide a good approximation that describes

the electron scattering signals from neutral molecules. The total diffraction intensity for a

molecule ensemble in a random distribution is given by

$$I_{total}(s) = \sum_{j=1}^{N_a} \sum_{k=1}^{N_a} f_j^*(s) f_k(s) \frac{\sin(sr_{jk})}{sr_{jk}}, \tag{6.1}$$

where N_a is the total number of constituent atoms in the molecule, $f_j(s)$ is the atomic

scattering amplitude of the jth atom, $s = \frac{4\pi}{\lambda} \sin\left(\frac{\theta}{2}\right)$ is the amplitude of momentum transfer,

θ is the scattering angle, λ is the de Broglie wavelength of the electron wave and r_{jk} is the

distance between jth and kth nucleus. The total scattering intensity can be separated into

two parts: the atomic scattering term I_{atom} and molecular scattering term I_{mol}, given by

$$I_{atom} = \sum_{j=1}^{N_a} |f_j(s)|^2, \tag{6.2}$$

$$I_{mol} = \sum_{j=1}^{N_a} \sum_{k=1,j\neq k}^{N_a} f_j^*(s) f_k(s) \frac{\sin(sr_{jk})}{sr_{jk}}. \tag{6.3}$$

The modified scattering intensity $sM(s) = sI_{mol}/I_{atom}$ is used to get rid of the damping terms, and to highlight the features of oscillations in I_{mol}, in which the molecular structure is encoded [2]. The pair distribution function $f_r(r)$, which shows the peaks that corresponds to the internuclear distance r_{jk} between atom pairs, is obtained by the sine-transform of $sM(s)$:

$$f_r(r) \cong \int_0^{s_{max}} sM(s)\sin(sr)e^{-\kappa s^2}ds , \tag{6.4}$$

where s_{max} is the maximum measured value of s, and κ is a damping constant that suppresses the noises at high s range and minimizes the edge effects of the transform. To investigate to change of molecular structure experimentally, we calculate the diffraction-difference intensity, formulated as

$$\Delta I(s,t) = I_{total}(s,t) - I_{total}(s,t_{ref})$$

$$= I_{mol}(s,t) - I_{mol}(s,t_{ref}) \cong \Delta I_{mol}(s,t) , \tag{6.5}$$

where t_{ref} refers to the time before the arrival of the pump laser that initiates the molecular structure change. $I_{total}(s,t_{ref})$ is the static diffraction pattern of the molecules in the ground state and can be used to remove the atomic scattering intensity and most of the experimental background. Correspondingly, we can define the $\Delta sM(s,t)$ as

$$\Delta sM(s,t) = \frac{s\Delta I_{mol}(s,t)}{I_{atom}}. \tag{6.6}$$

The fractional difference signal [52, 239, 257] is defined as $FD(s,t) = \Delta I_{mol}(s,t)/I_{total}(s,t_{ref})$. $\Delta sM(s,t)$ and $FD(s,t)$ can be converted into each other by using the factor $sI_{total}(s,t_{ref})/I_{atom}$. The difference of pair distribution function is defined as

$$\Delta f_r(r,t) \cong \int_0^{S_{\max}} \Delta s M(s,t) \sin(sr) e^{-\kappa s^2} ds, \tag{6.7}$$

where $\Delta f_r(r,t) < 0$ indicates a loss of internuclear distance r comparing to the parent molecule, and $\Delta f_r(r,t) > 0$ corresponds to an increase of the internuclear distance r in the product.

6.4 Electron diffraction of CF$_3$I dissociation

We use a UV femtosecond pulse to pump the CF$_3$I molecules to initiate the prompt breakup of C-I bond. I will first present in this section the static diffraction and the corresponding pair distribution functions of CF$_3$I molecules, and then the time-dependent signal of CF$_3$I dissociation. The theoretically calculated diffraction signal using IAM is used to model the electron scattering signal for the products of photodissociation. The temporal evolution of the diffraction signals due to the breakup of C-I bond is used to characterize the temporal resolution of the keV-UED.

6.4.1 Static diffraction and pair distribution function

A static diffraction pattern of CF$_3$I is recorded by setting the arrival time of electron pulse to be ahead of the pump laser pulse. The two-dimensional static diffraction pattern is azimuthally averaged to obtain the one-dimensional $I_{\text{total}}(s)$. The zero values of the theoretically calculated $sM(s)$ is used to fit and remove a background $b(s)$ of the experimental $I_{\text{total}}(s, t_{\text{ref}})$ to obtain the experimental $I_{\text{mol}}(s) = I_{\text{total}}(s) - b(s)$ according to the method introduced in ref. [3].

Figure 6.2 shows the comparison of the experimental and theoretical static diffraction results. The comparison of experimental and theoretical $sM(s)$ is shown in figure 6.2 (a). The pair distribution function of CF$_3$I is calculated using eqn. (6.4), shown in figure 6.2

(b). The experimental data at low s values, $sM(s < 1.3 \text{ Å}^{-1})$, are missing due to the beam stop. The low s values for the experimental data are filled with theoretical values prior to the sine transform. The atom pairs are marked for each pair distribution function in figure 6.2 (b), and the internuclear distances are r_{CF}= 1.33 Å, r_{CI} = 2.14 Å, r_{FF} =2.15 Å and r_{FI} =2.89 Å. The internuclear distances r_{CI} and r_{FF} cannot be resolved with the spatial resolution of the current setup. There is a good agreement between the experimental to theoretical results.
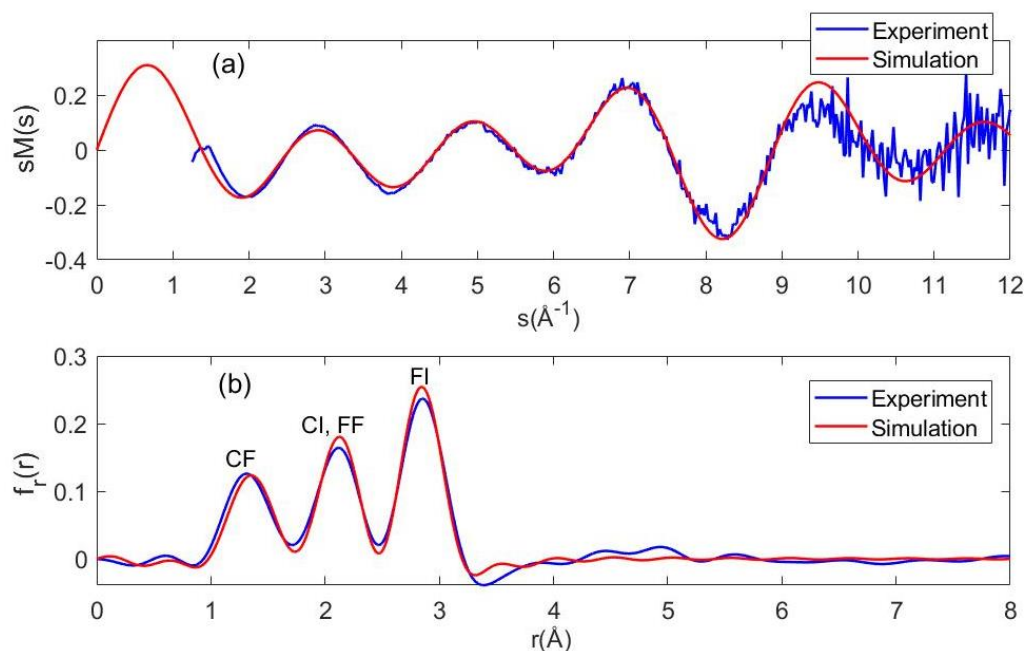
Figure 6.2: Static diffraction signal of CF₃I molecules in ground state. (a) The fitting of experimental to theoretical $sM(s)$. Experimental results are shown in blue curves, and theory in red. The zero values of the theoretical $sM(s)$ is used to fit a background $b(s)$ for $I_{\text{total}}(s)$, including the atomic scattering I_{at} and other background scattering. The experimental molecular scattering term is obtained by $I_{\text{mol}}(s) = I_{\text{total}}(s) - b(s)$. (b) The experimental and theoretical pair distribution functions.

6.4.2 Time-dependent signal

The first UV absorption band of the alkyl iodides, called the A-band continuum between 210 nm and 350 nm, involves promotion of a non-bonding (n) electron from the iodine atom valence shell to the σ^* anti-bonding orbital of the C-I bond, resulting in a rapid fission of the C-I bond [258-262]. The time scale of the rapid bond breakup is on the order of ~100 fs [21, 263]. The A-band consists of three repulsive states that is overlapped in energy, denoted as $^3Q_1$, $^3Q_0$, and $^1Q_1$ in the ascending order by Mulliken [264, 265]. The $^3Q_0$ state excitation involves a transition dipole moment parallel to the C-I bond, and the corresponding photodissociation product is the spin-orbit excited state iodine $I^*(^2P_{1/2})$ [263]. The transition dipole moment for the excitation of $^3Q_1$ and $^1Q_1$ states is perpendicular to the C-I bond, producing ground state of iodine $I(^2P_{3/2})$ followed by the corresponding dissociation [266]. The dominant transition upon 266 nm laser pulse excitation is the $^3Q_0$ state producing $I^*(^2P_{1/2})$. However, $I(^2P_{3/2})$ can be generated by the coupling of $^3Q_0$ and $^1Q_1$ potential energy surfaces through the conical intersection [263, 264].

The photodissociation dynamics through A-band excitation of CF_3I [264, 267-270] exhibit broadly similarities to those observed in CH_3I [262]. The A absorption band of CF_3I is centered around 270 nm, and the excitation results in prompt and direct dissociation via two relaxation channels [260, 271-278], shown below:

$$CF_3I \xrightarrow{h\nu} CF_3 + I(^2P_{3/2}), \tag{6.10}$$

$$CF_3I \xrightarrow{h\nu} CF_3 + I^*(^2P_{1/2}). \tag{6.11}$$

We assume that the double photon excitation is negligible using the pump laser intensity. In this experiment, the end products of the dissociation are neutral CF_3 and iodine atom.
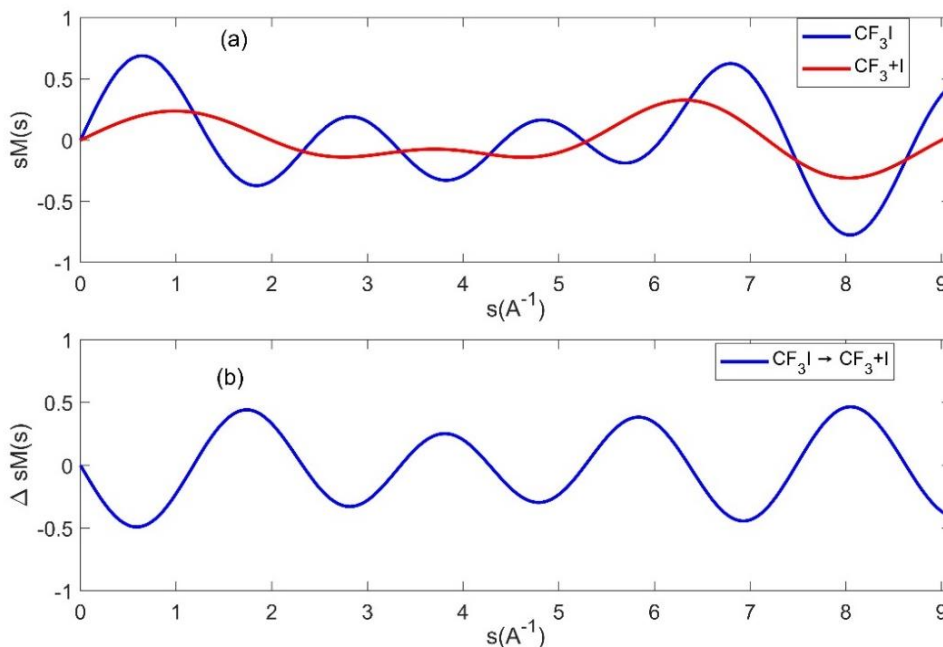
Figure 6.3: Theoretically calculated electron diffraction signal for $CF_3I \rightarrow CF_3 + I$ based on IAM model. (a) $sM(s)$ for CF_3I and CF_3+I. (b) Theoretically calculated $\Delta sM(s) = s\Delta I_{mol}/I_{atom,CF_3I}$, and $\Delta I_{mol} = I_{CF_3}(s) + I_I(s) - I_{CF_3I}(s)$.

UED measurement is directly sensitive to the structure of the molecule, whereas it is difficult to differentiate the iodine atoms in its ground and spin-orbit excited states with the current signal-to-noise level. However, it has been shown in the case of X-ray scattering experiments that electronic excitation manifests as a secondary contribution to the scattering signal [49, 239, 240], and electron scattering signal that cannot be approximated by the independent atom model (IAM) due to electronic excitation is mostly limited to the low *s* range [52]. In addition, no corrections relating to vibrational excitation of the end product CF_3 have been applied to the signal as previous works [241, 242] have demonstrated that the vibrational excitation has minor effects on scattering signals for rigid molecules, even at high temperatures. Therefore, we use the electron scattering theory

based on the IAM to approximate the diffraction signal from the neutral end products of the dissociation, and the vibrational motion of CF_3 is ignored. The level of theory B3LYP, DEF2-SVP is used to optimize the structure of CF_3 in ground state with ORCA [185]. The diffraction-difference intensity for CF_3I dissociation is given by $\Delta I_{mol}(s,t) = I_{CF_3}(s) + I_I(s) - I_{CF_3I}(s)$, and $\Delta sM(s) = s\Delta I_{mol}/I_{atom,CF_3I}$, where I_{atom,CF_3I} is the atomic scattering term of CF_3I. The calculated electron diffraction intensities using IAM are shown in figure 6.3. The blue curve in figure 6.3 (a) corresponds to the $sM(s)$ for CF_3I molecules, and red curve is corresponding to the end products CF_3+I. Figure 6.3 (b) corresponds to $\Delta sM(s)$ for the dissociation of $CF_3I \rightarrow CF_3 + I$.

The pump-probe diffraction patterns are recorded at a series of time delays around the time when UV-induced dissociation starts. The total integration time of the diffraction pattern at each time delay is 10 minutes. The procedures of calculating the experimental $\Delta sM(s,t)$ are described below. 1st, the data behind the beam stop and outliers are removed from each diffraction image for the analysis. 2nd, the 2D diffraction-difference patterns are calculated by taking the difference between diffraction patterns at positive time delays and reference patterns that no dissociation signal is observed, formulated as $\Delta I_{mol}(s,t) = I_{total}(s,t) - I_{total}(s, t_{ref} < 0ps)$. 3rd, $\Delta I_{mol}(s,t)$ is azimuthally averaged to calculate 1D diffraction-difference intensity $\Delta I_{mol}(s,t)$ and the standard error $\sigma(s,t)$ at each s. The experimental $\Delta sM(s)$ at each time delay are calculated using eqn. (6.6). The temporal evolution of the experimental $\Delta sM(s)$ for CF_3I dissociation induced by the UV laser pulse is shown in figure 6.4. The time step is 133.3 fs, and the time zero is defined as the time delay when the signal starts. The signal shows larger statistical variations at larger s due to the lower signal level.
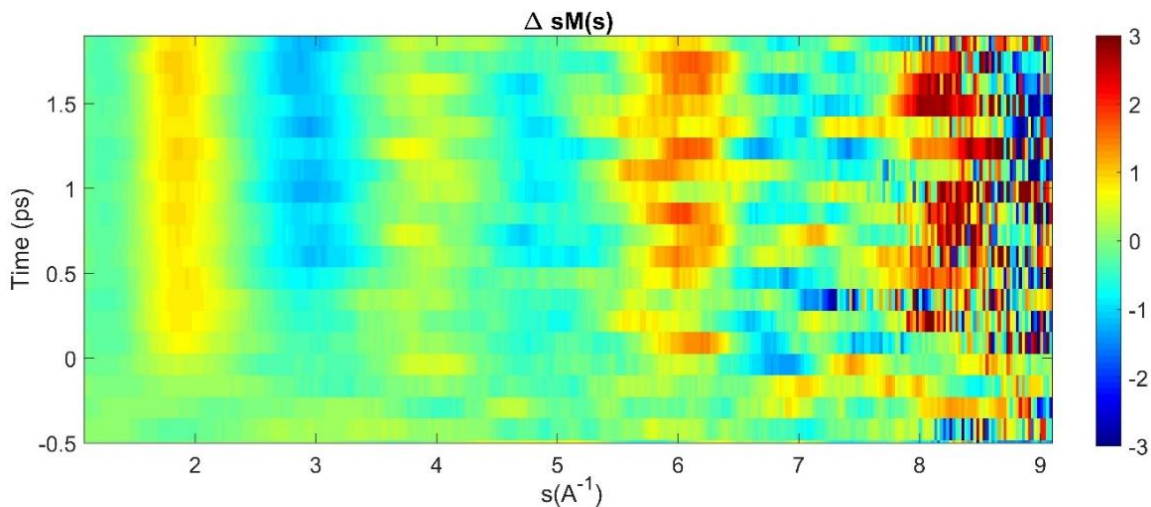
Figure 6.4: Temporal evolution of ΔsM(s,t) for UV laser induced CF_3I dissociation. The integration time of diffraction signal at each time delay is 10 minutes.
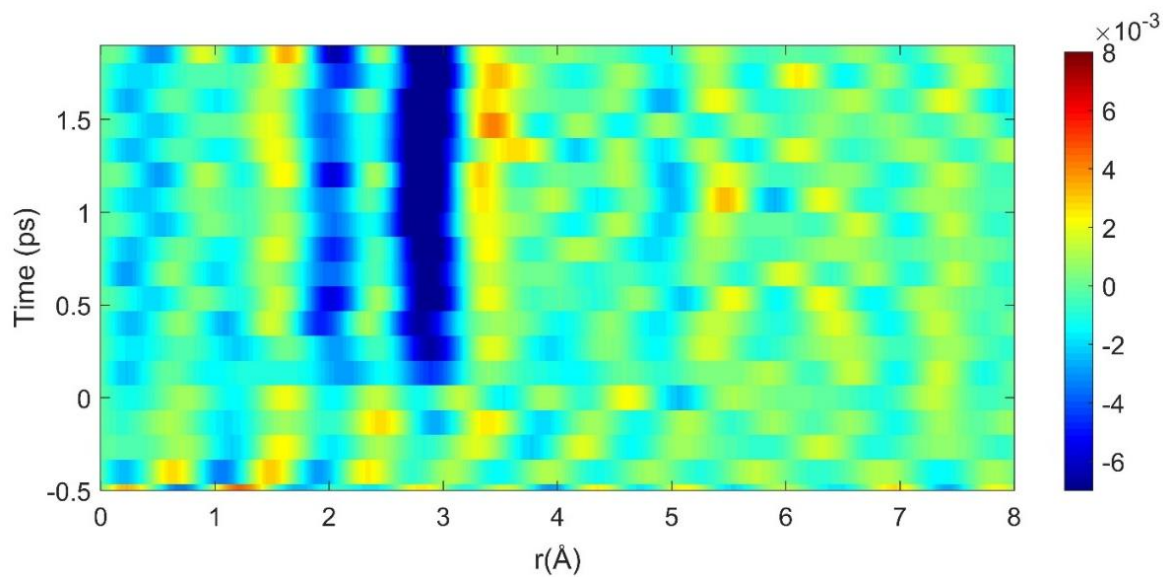
Figure 6.5: Temporal evolution of Δf_r(r, t). For $t > 0$, the signal becomes negative at 2.13 Å, 2.89 Å corresponding to the internuclear distance of CI and IF, which indicates the breakup of C-I bond of CF_3I upon the UV excitation, and forming of end products CF_3 and I.

The sine transform is applied to $\Delta sM(s,t)$ at each time delay to obtain the temporal evolution of $\Delta f_r(r,t)$, shown in figure 6.5. A low pass filter is applied to the experimental $\Delta sM(s, t > 0)$ to remove the fast oscillatory noise, and its low s values ($s < 1.4$ Å^{-1}) are filled with the corresponding theoretical simulated values prior to the sine transform. For $t > 0$, $\Delta f_r(r,t)$ becomes negative around $r = 2.13$ Å, 2.89 Å corresponding to the internuclear distance of CI and IF, which indicates the breakup of C-I bond of CF$_3$I upon the UV excitation, and subsequent forming of end products CF$_3$ and I. To evaluate the excitation ratio of the CF$_3$I molecules, all the images after time zero are averaged to calculate $\Delta sM(s)$, shown in figure 6.6. The blue curve in figure 6.6 (a) is the experimental $\Delta sM(s)$ multiplied by $e^{-0.008s^2}$ to dampen the statistical uncertainty at high s, and the red curve is the theoretically simulated $\Delta sM(s)$.

The experimental $\Delta sM(s)$ is in good agreement to the simulation in figure 6.6 (a). The simulated $\Delta sM(s)$ is scaled by a rescale factor that accounts for the excitation ratio of the sample in the interaction volume. The rescale factor is determined to be 0.016 by comparing the experimental $FD(s)$ to its simulated counterpart, which indicates that 1.6% of sample in the interaction region is excited by the UV pulse. The sine transform is applied to the experimental and theoretically calculated $\Delta sM(s)$ to obtain the $\Delta f_r(r,t)$, shown in figure 6.6 (b). The data points corresponding to $s < 1.4$ Å^{-1} that are missing due to the beam block are filled with the corresponding theoretical simulated values before the sine transform. The experimental and simulated $\Delta f_r(r,t)$ are in good agreement. The negative values of $\Delta f_r(r,t)$ at 2.13 Å, 2.89 Å corresponds to the fission of C-I bond of CF$_3$I molecules upon the UV excitation, and forming of end products CF$_3$ and I.
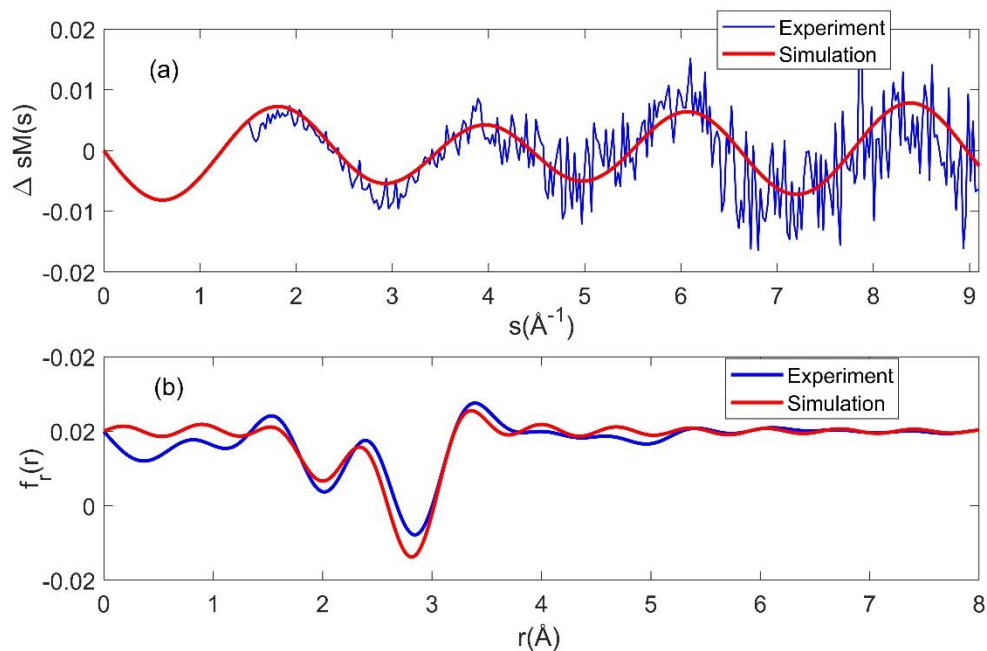
Figure 6.6: Fitting of the experimental ΔsM to its corresponding simulation. (a) The blue curve stands for the experimental $\Delta sM(s)$, and the red curve for the theoretically calculated $\Delta sM(s)$ with IAM. The fitting gives an excitation ratio of 1.6%. (b) The sine transform is applied to the $\Delta sM(s)$ to obtain $\Delta f_r(r,t)$. The experimental $\Delta f_r(r,t)$ is shown in blue, and simulated counterpart in red.

6.4.3 Instrumental temporal resolution

The temporal evolution of the $\Delta sM(s,t)$ or $FD(s,t)$ with s range of 1.6 $\text{Å}^{-1} < s < 2.2$ Å^{-1} can be used to characterize the instrumental temporal resolution. The intrinsic relaxation time of the molecules and temporal resolution of the UED setup are encoded in the experimental measurement $i_E(t)$, defined as $i_E(t) = \int_{1.6}^{2.2} FD(s,t)\,ds$. The measurement is a convolution of the response function of the molecular system to the laser excitation and instrumental response function [53]. The response of the molecule can be modeled by an error function, which is a convolution of a Heaviside step function $h(t)$ and a gaussian

function $g_1(t)$ whose width corresponding to the molecular intrinsic response time τ_1 upon the laser excitation. The response function of the instrument is modeled by a gaussian $g_2(t)$ and the temporal resolution is indicated by the width τ_2. Therefore, the measurement is described by $i_M(t) = h(t) \otimes g(t)$, where $g(t) = g_1(t) \otimes g_2(t)$, and the width of $g(t)$ is given by $\tau = \sqrt{\tau_1{}^1 + \tau_2{}^2}$.
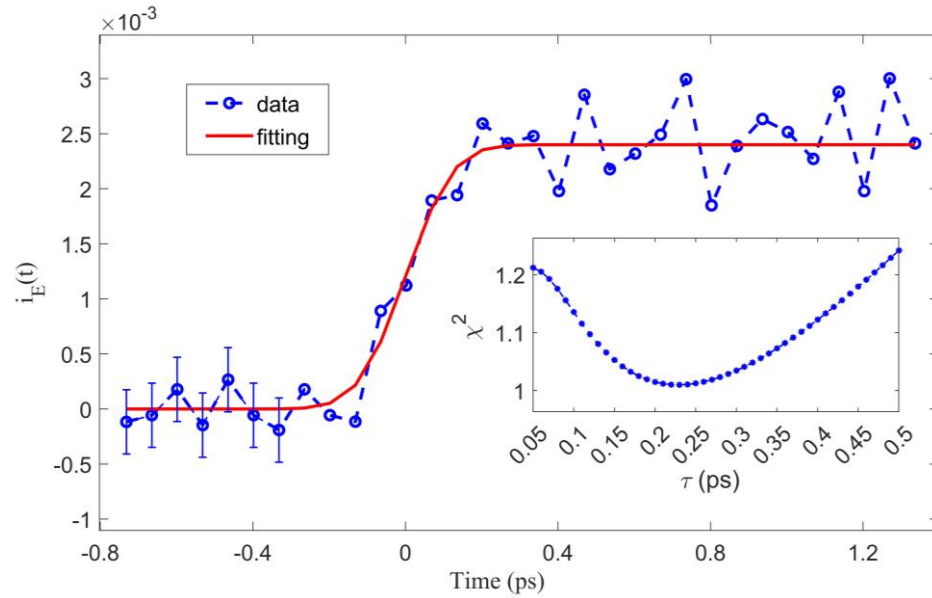
Figure 6.7: Fitting of changes in the i_E(t) with an error function to determine the instrument response time. The fitting of experimental data $i_E(t)$ (blue) to the model $i_M(t)$ (red). The time step in this measurement is 66.7 fs. Statistical error bars for the first seven points, which is the standard error calculated by the data points with negative time delays, are used to estimate the uncertainty of the measurement at each data point. The inset shows the χ^2 value of the fit as a function of τ. The minimum of χ^2 is corresponding to $\tau = 0.23$ ps.

While τ_1 and τ_2 cannot be determined separately from the experimental measurement, τ can be determined by fitting $i_E(t)$ to $i_M(t)$. Figure 6.7 shows the fitting and χ^2 value of the fit as a function of τ (FWHM temporal resolution). The χ^2 function is defined by $\chi^2 =$

$\frac{1}{N-n}\sum_t\left[\frac{i_E(t)-c\times i_M(t,\tau)}{\sigma(t)}\right]^2$, where c denotes the rescale factor for the amplitude of the modeled function, N is the number of the time delays, n is the number of fitted parameters, and $\sigma(t)$ is the standard error estimated by the data points with negative time delays. The best fitting gives $\tau = 0.23$ ps, and it can be considered as an upper limit of the temporal resolution of the experiment as $\tau_2 < \tau$. The time scale of rapid C-I bond fission is estimated to be $\tau_1 \cong 100$ fs [21, 263]. Therefore, the instrumental temporal resolution is $\tau_2 \cong 200$ fs. This result is consistent with the temporal resolution determined by the alignment signal of nitrogen molecules in chapter 4 and in ref. [32].

6.5 Electron diffraction of iodobenzene

In this section, the preliminary experimental results of iodobenzene pumped by an ultrafast UV laser pulse and captured by the keV-UED are presented. The iodobenzene sample was purchased from Millipore Sigma with a purity of 98%. We heated the liquid sample to 70 °C and flowed helium as a carrier gas to increase the diffraction signal. The pump UV laser energy is 80 µJ, which is kept in the range of one phone excitation.

6.5.1 Static diffraction and pair distribution function

A static diffraction pattern of iodobenzene was recorded when the molecules are not pumped by the UV laser pulse. The same procedures described in the CF_3I section were used to calculate and to fit the experimental $sM(s)$ to its theoretical counterpart, shown in figure 6.8. The experimental results are in very good agreement with the simulation. Since many of the internuclear distances are close and the diffraction pattern is truncated at ~10 Å^{-1}, some of the internuclear distances overlap in the pair distribution function.
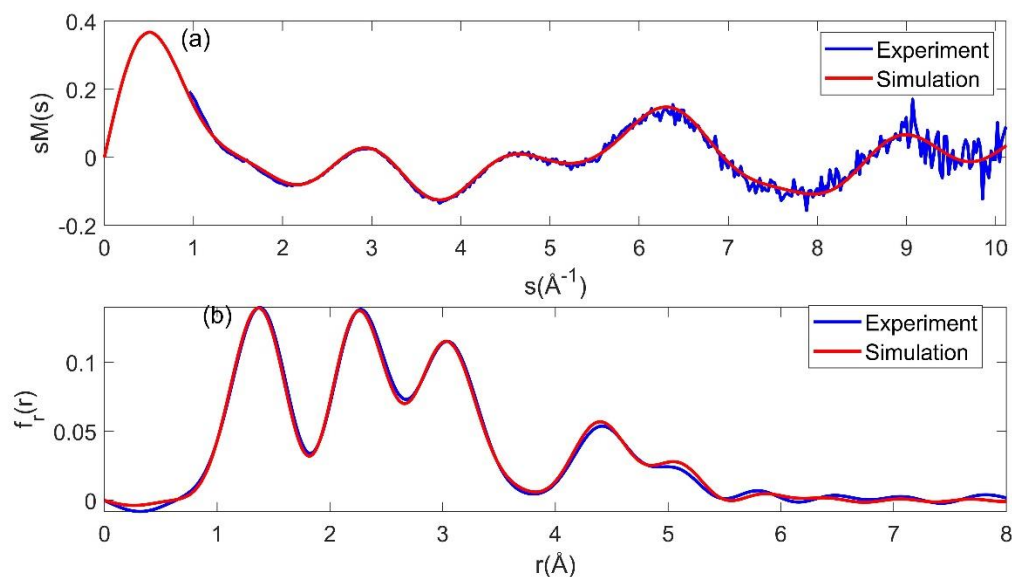
Figure 6.8: Static diffraction signal of iodobenzene molecules in ground state. (a) The fitting of experimental to theoretical $sM(s)$. Experimental results are shown in blue, and simulations in red. The simulated $sM(s)$ is calculated with the IAM. The zeros of the simulated $sM(s)$ are used to fit a background for the total electron diffraction intensity, which is subtracted to calculate the experimental $sM(s)$. (b) The experimental and theoretical pair distribution functions calculated with the sine transform.

6.5.2 UV induced dissociation of iodobenzene

We study the photodissociation of iodobenzene in the A-band, pumped by a UV femtosecond laser pulse centered around 266 nm, using the setup described in the last sections. Comparing to alkyl iodides, aryl halides show additional complexities [279]. Besides the dominant transition $n \rightarrow \sigma^*$ in A band observed in alky iodides, originating from the promotion of a non-bonding (n) electron from the iodine atom valence shell to the σ* anti-bonding orbital of the C-I bond, aryl iodides are supplemented by the dissociative states of $\pi \rightarrow \sigma^*$ excitation which involves the phenyl π orbital, and by bound $\pi \rightarrow \pi^*$

state [261, 262, 280]. The $n \to \sigma^*$ excitation of iodobenzene leads to a rapid direct dissociation that produces a phenyl radical and an iodine atom either in its ground state $I(^2P_{3/2})$ or spin-orbital excited state $I^*(^2P_{1/2})$ [261]. The $\pi \to \pi^*$ and $n \to \sigma^*$ states are overlapped in the same energy region, and the coupling between the two states could make $\pi \to \pi^*$ states predissociative to generate the same products as $n \to \sigma^*$ [261].
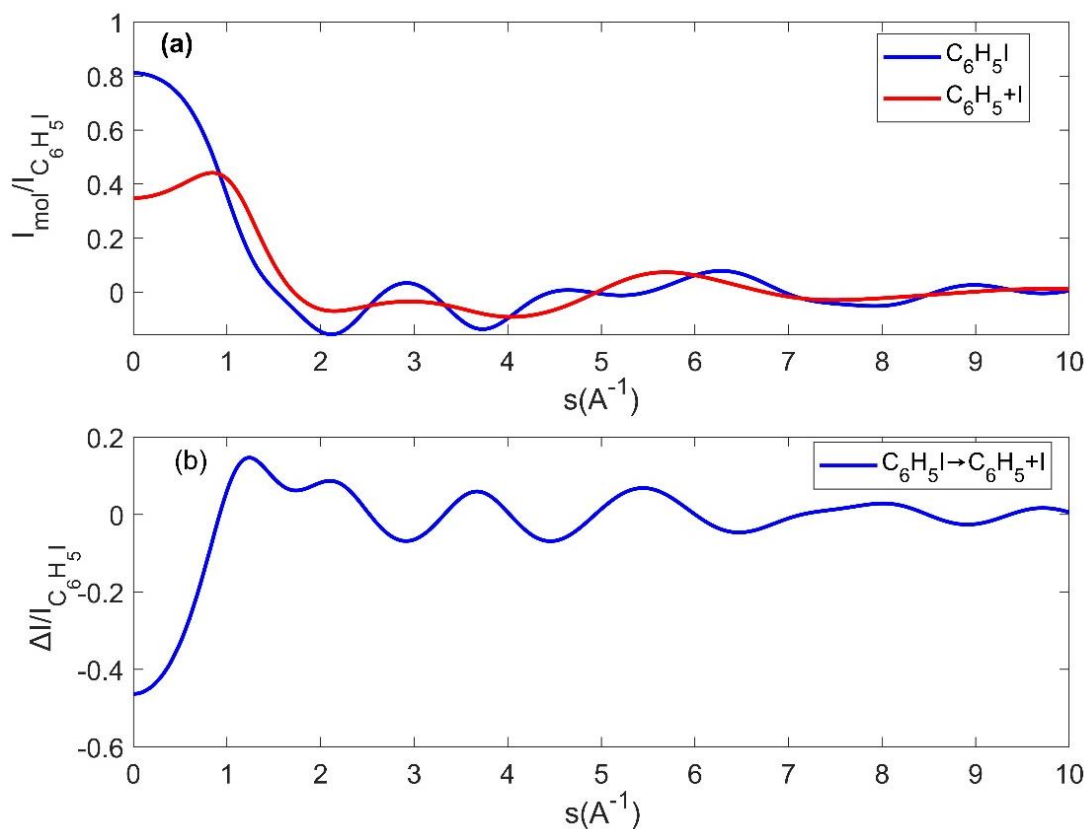
Figure 6.9: Theoretically calculated electron diffraction signal for $C_6H_5I \to C_6H_5+I$ based on IAM model. (a) $I_{\mathrm{mol}}/I_{C_6H_5I}$ for C_6H_5I and C_6H_5+I. (b) Theoretically calculated fractional difference signal $\Delta I/I_{C_6H_5I} = \Delta I_{\mathrm{mol}}/I_{C_6H_5I}$, and $\Delta I_{\mathrm{mol}} = I_I + I_{C_6H_5} - I_{C_6H_5I}$.

The theoretical explanation of the detailed dissociation process requires complex quantum mechanical modeling of the photon excitation and relaxation of the iodobenzene molecule,

and the corresponding electron scattering calculations. Here I present a simple simulation based on the IAM to explain that the dissociation of iodobenzene was captured by the UED setup. Similar to the CF₃I section, the UED setup cannot identify the iodine atom in the ground and excited states, and the vibrations of phenyl radical and iodobenzene are ignored. Therefore, the dissociation is simplified to be $C_6H_5I \xrightarrow{h\nu} C_6H_5 + I$, where the structures of reactant and products are approximated by their ground states structures, respectively. Figure 6.9 shows the calculated electron diffraction intensity for C_6H_5I and dissociated products $C_6H_5 + I$ followed by the UV excitation in (a), and the fractional difference signal $\Delta I/I_{C_6H_5I} = \Delta I_{mol}/I_{C_6H_5I}$ is shown in (b), where $\Delta I_{mol} = I_I + I_{C_6H_5} - I_{C_6H_5I}$.

6.5.3 Time dependent signal of iodobenzene

A series of diffraction patterns at different time delays were recorded to capture the dissociation signal after the UV laser pulse excitation. The diffraction patterns with a negative time delay indicates that the arrival time of electron pulse is prior to that of the laser pulse, which were used as a reference pattern as they contain the signal from iodobenzene in the ground state and other background signals.

The experimental fractional difference signal $\Delta I/I_{C_6H_5I}$ is calculated with the procedure below. 1st, the data behind the beam stop and the wire, and the outliers exceeding the confidence interval with three times of standard deviation, are removed from each diffraction image for the analysis. 2nd, the reference diffraction signal $I_{C_6H_5I}$ is taken by setting the time delay to be negative, denoted as $I_{total}(s, t_{ref} < 0ps)$. the 2D diffraction-difference patterns are calculated by $\Delta I_{mol}(s, t) = I_{total}(s, t) - I_{total}(s, t_{ref} < 0ps)$. 3rd, $\Delta I_{mol}(s, t)$ is azimuthally averaged to calculate $\Delta I_{mol}(s, t)$ and the corresponding standard

error $\sigma(s,t)$. The fractional difference signal is calculated by $FD_E(s,t) = \Delta I_{mol}(s,t)/ I_{total}(s, t_{ref} < 0\text{ps})$. 4th, there is a residual background in $\Delta I_{mol}(s,t)$, which causes the $FD_E(s,t)$ to be tilted. The background is obtained by fitting $FD_E(s,t)$ to a 3rd order polynomial function, which is then subtracted from the $FD_E(s,t)$. To compare the experimental data to the simulation, the same procedure in 4th step is also applied to the theoretically calculated $FD_T(s)$ to correct the offset.

A series of diffraction patterns at different time delays are recorded to calculate the $FD_E(s,t)$, shown in figure 6.10. The experimental data is displayed in blue, and a low pass filter 'rlowess' (Matlab function) is applied to reduce the high oscillatory noise. The theoretically calculated $FD_T(s)$ based on the IAM is displayed with the red curve, and is fitted to the experimental data to obtain the signal amplitude using $\chi^2 = \frac{1}{N-1}\sum_s \left[\frac{FD_E(s,t) - a \times FD_T(s)}{\sigma(s,t)}\right]^2$, where a is the amplitude of the signal, N is the total number of data points. The fitted amplitude of the dissociation at different time delays are shown in figure 6.11.

We see a clear dissociation signal appearing after t = 0 ps, increasing from 0 ps to ~ 1.5 ps, and reaching a plateau after 1.5 ps. Here we compare the experimental data to a simple model in which the C-I bond is broken after the absorption of one UV photon and the phenyl ring remains unchanged. The simulation agrees with the experimental data. To determine the time constants and products from reaction channels $\pi \to \pi^*$ and $n \to \sigma^*$, a more detailed simulation of the molecular dissociation and an *ab-initio* electron scattering calculation are required. Nonetheless, the preliminary experimental demonstrates that the keV-UED setup is sufficient to perform the UV-induced molecular reaction experiments.
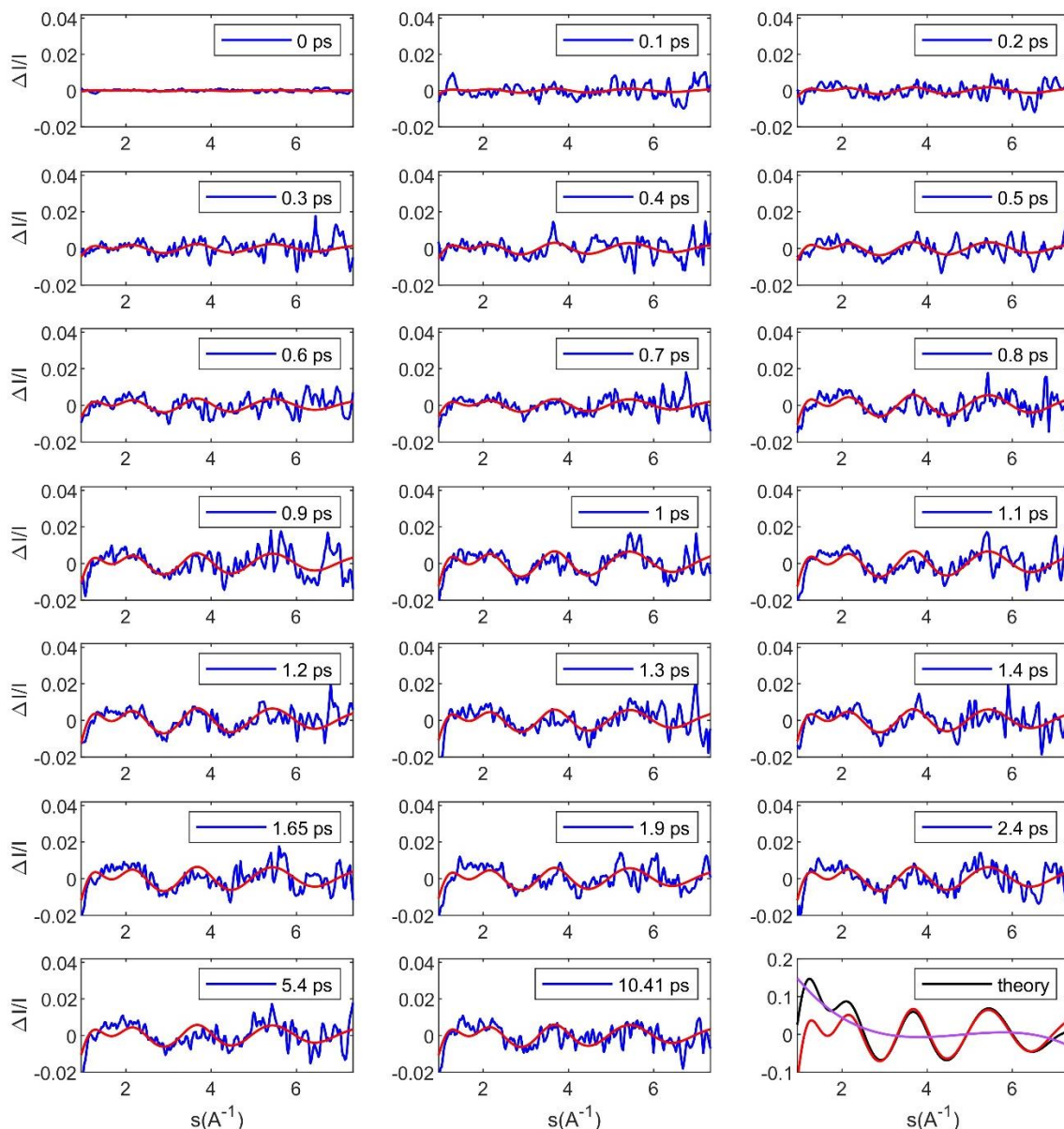
Figure 6.10: Fractional difference signal $FD(s,t)$ taken at different time delays. The experimental data are shown in blue, and the theoretical calculation, displayed in red, is fitted to the data to obtain the signal amplitude. The time zero is determined to be the time that the dissociation signal starts. The last panel is the theoretical calculation. The black curve is the theoretical $FD(s,t)$, purple curve is the third order polynomial to fit an offset, and the red curve is the $FD(s,t)$ with the offset subtracted.
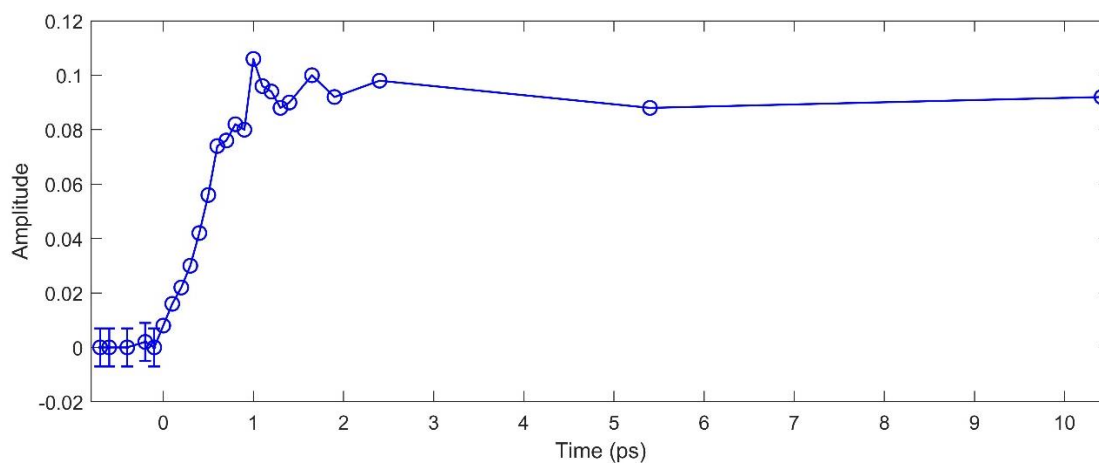
Figure 6.11: Temporal evolution of the dissociation signal amplitude. Statistical error bars for the first five points, which are the standard deviation calculated from data points with negative time delays, are used to show the uncertainty of dissociation amplitude at each time delay.

Chapter 7

Conclusions and outlook

In this chapter, I give a summary of development of the apparatus and demonstration of experiments with the keV-UED in this dissertation, and a brief outlook. In chapter 1, a brief history, and principles of gas phase UED experiments were reviewed, followed by the quantum theory of electron scattering by a Coulomb potential. Based on the far field and first-Born approximations, the scattering amplitude is proportional to the Fourier transform of the potential of the target, and differential cross section, which is the observable, is the square modulus of the scattering amplitude. Using the potential operator, the scattering amplitude can be further written as the Fourier transform of the charge distribution of the target, such as an isolated molecule, divided by s^2. The inelastic electron scattering is shown to be related to the exchange charge density. At last, with the approximation of IAM, the widely used electron scattering formula for an isolated molecule and molecular ensemble are presented.

In chapter 2, I focused on the apparatus development to optimize the temporal resolution of the keV-UED. The temporal resolution of gas phase keV-UED setup has been limited by the long electron pulse duration due to space charge effect, and group velocity mismatch between the laser and electron pulses. A linear space-momentum distribution is developed as the electrons propagating from the cathode to the gas jet due to the space charge Coulomb repulsion. I have used a homemade RF synchronization system, inspired by the system described in Otto et al. [23], to reverse the space-momentum distribution with a time-varying field in a RF cavity so that the electron pulse duration can be compressed on the sample. Optimal compression is achieved when the electron pulse is synchronized to

the RF field accurately, which is demonstrated with a streaking camera. The temporal broadening due to group velocity mismatch is a major factor that deteriorates the temporal resolution of gas phase keV-UED. We use a laser pulse with a tilted intensity front to excite the sample in a geometry that compensates the velocity mismatch between the laser and the electrons. The tilted angle of the pump laser and the angle between the laser and electron beams are designed to be 58.24° with a diffraction grating and an imaging system for matching the speed of 90 keV electron pulse and the longitudinal component of laser velocity. The measurement of the tilted angle and tilted pulse duration are presented, and the analysis of the temporal broadening due to residual velocity mismatch is given. By combining these two techniques in our keV-UED, we achieved an overall resolution of the instrument of 240 fs. The slow timing drift of the instrument is characterized to be on the order of 50 fs rms over several hours.

The contents of chapter 3 focus on the theories required for the experiments of laser induced molecular alignment, which are the theoretical prerequisite for chapter 4. First, we reviewed the quantum theory of nonadiabatic alignment of a molecule by a non-resonant IR ultrafast laser pulse. The rotational wavepacket of a rigid molecule excited by an IR ultrafast laser pulse can be numerically calculated by solving the time-dependent Schrödinger equation with the initial rotational state and laser parameters. For a molecular ensemble with a certain temperature, the molecular orientation distribution (MOD) is obtained by the summation of probability density from each wavepacket weighted by the Boltzmann distribution and nuclear spin statistics. However, in general cases, the MOD for nonlinear molecules cannot be measured directly with experimental methods, except for special cases in which the molecule contains detectable atoms located along the principal

axes of inertia tensor of the molecule. To determine the MOD from the experimental observables, I derived an equation that maps the MOD to the atom-pair angular distributions for nonlinear molecules and developed the retrieval methods for three different cases. In each case, the retrieving process is equivalent to finding solutions of a system of linear equations. The retrieval method is in general working for any molecular alignment methods, like adiabatic and nonadiabatic alignment, and in principle allows for retrieving MOD of an asymmetric-top molecule excited by an arbitrarily polarized pulse. At last, I demonstrated the equation for retrieving the atom-pair angular distributions from the experimentally measured diffraction patterns. The angular distribution and internuclear distance of the atom pairs can be extracted by the inverse Fourier transform, followed by the Abel inversion, to the molecular scattering intensity.

In chapter 4, I presented three experiments of rotational dynamics from laser induced molecular alignment, captured with the keV-UED instrument. First, we captured the full rotational dynamics of impulsively aligned nitrogen molecules. MeV-UED has been demonstrated to be able to capture the fast rotational dynamics of laser induced alignment of nitrogen molecules [19], whereas due to the low electron beam current and signal-to-noise level, the measurement was limited to a few frames of diffraction patterns. With the high electron beam current of our keV-UED, we were able to retrieve a continuous movie of the rotational motion of a nitrogen ensemble with high fidelity and with shorter acquisition time in comparison to the MeV-UED. The fast rotational dynamics of the nitrogen molecules allows us to characterize the instrumental response function and timing drift of the UED setup. The second experiment is the full evolution of rotational dynamics of laser aligned trifluoro-iodomethane (CF_3I) molecules. Due to the overlapping of angular

distributions of CI and FF, we used the angular distribution of FI to successfully retrieve the MOD according to the theory described in chapter 3. The retrieved MOD is in good agreement with the theoretical calculation by directly solving TDSE with the experimental parameters in the experiment. In the last experiment, the detection of isotopes was demonstrated by using the impulsive alignment of isotopologues, captured by the keV-UED. The principle of differentiating isotopes in molecules relies on the difference of alignment dynamics for molecules with different moment of inertia. We demonstrate the technique experimentally by observing the anisotropy in the diffraction signal of chloromethane with two naturally occurring chlorine isotopes ^{35}Cl and ^{37}Cl over multiple revivals. The measurement enables us to determine rotational period, mass difference, and abundance ratio of $CH_3^{37}Cl$ to $CH_3^{35}Cl$ accurately.

In chapter 5, I demonstrated an investigation of ionization, fragmentation and isomerization of toluene generated by a strong IR laser field. We used the keV-UED to determine the structure and yields of the ionized and neutral fragments from ionization and fragmentation of toluene molecules. As multiple products with unknown structures are presented from the reaction induced by the strong IR laser field, it is generally not possible to unambiguously determine the structures of products. Thus, we use a momentum-resolved coincidence time-of-flight ion mass spectrometry (TOF-MS) to determine the mass-to-charge ratio, momentum, and yield of each ion product, and the most abundant products from the TOF-MS measurement are helpful to determine the structures for analysis of UED results. With the help of *ab-initio* electron scattering calculation, the UED measurement is able to determine the relative yields of main reaction channels, which is in good agreement with the TOF-MS measurement. The electron diffraction signal is in good agreement with

ab-initio scattering calculation, while scattering computation based on independent atom model (IAM) is not able to provide a good approximation for electron scattering from ions.

In chapter 6, we used an ultrafast UV laser pump with a central wavelength 266 nm to pump the gas phase sample, trifluoroiodomethane (CF_3I) and iodobenzene (C_6H_5I), and captured the products of reaction with the keV-UED. The frequency of the IR laser pulse from Ti: Sapphire laser is tripled using a commercial trippler to produce the UV laser pulse as the pump laser. To remove the group velocity mismatch, an aluminum-coated grating with the grating constant 400 mm^{-1} is used to generate the UV tilted pulse. The UV pulse excites CF_3I molecules to A-band orbitals, which involves promotion of a non-bonding (n) electron from the iodine atom valence shell to the σ* anti-bonding orbital of the C-I bond [258-262], followed by a rapid fission of the C-I bond with a time scale of ~100 fs [21, 263]. The keV-UED is able to capture the rapid fission of the molecule after UV excitation. The experimental diffraction signal is in good agreement with the electron scattering signal calculated with the theory based on IAM. The time-dependent signal of the rapid fission of C-I bond is used to evaluate the temporal resolution of the UED setup. The best fit of the time-dependent signal to the theoretical model gives a temporal resolution of ~200 fs, which is consistent with the result determined by the impulsive alignment of nitrogen molecules in chapter 4 and in ref. [32]. We also conducted an experiment of iodobenzene dissociation upon UV excitation and presented the preliminary results. The experimental signal of dissociation agrees to the theoretical calculation based on IAM. The dynamics of the signal amplitude has been determined by comparing the experimental fractional difference signal to its theoretical counterpart.

Finally, I will give a brief discussion about the possible future development and experiments with the keV-UED as follows. In the first stage experiments with gas phase samples, we have achieved a temporal resolution of ~ 200 fs for the keV-UED. We expect to further improve the temporal resolution of the setup by optimizing the RF electronics and the velocity matching with the tilted laser pulse. For example, the RF electronics, including the cavity, could be further optimized, or updated, to increase the stability of the phase and amplitude of the time-varying electric field for electron pulse compression. As for the velocity mismatch compensation, further tuning of the imaging system could improve the accuracy of the incidence and tilted angles such that the temporal broadening could be further reduced.

With the MOD retrieval method, only the result of 1D molecular alignment has been demonstrated with CF_3I molecules aligned with a linear polarized laser. It would be interesting to conduct laser induced alignment experiments for asymmetric top molecules using an ultrafast laser pulse with a more complex polarization or using multiple laser pulses with different polarizations. In these experiments, retrieval of MOD for 2D and 3D molecular alignment with the theory developed in chapter 3 will be interesting.

We have replaced the IR laser pulse with a UV laser pulse as a pump to study photodissociation of molecules and conducted the proof-of-principle experiment with CF_3I. We expect to carry out more experiments with molecules that could show more complicated, interesting reaction channels upon the UV excitation. Also, the investigation of photodissociation with additional reaction parameters would be interesting and possible with the high beam current. For example, we can pump the molecules with different excitation conditions, such as different laser wavelengths and pulse energy. Such

comprehensive studies on how the molecules respond to the different excitation conditions would be crucial to the understanding of the underlying mechanisms governing reaction dynamics.

With the higher pulse energy from the updated laser amplifier Astrella, we can also carry out experiments to investigate molecular reactions with two laser pulses, one of which is an IR pulse to produce the alignment of molecules, and the other one is a UV laser pulse to pump the molecules to electronically excited states. In this scenario, the arrival time of the UV laser pulse is synchronized to the molecular alignment or revivals to study the molecular reactions in the molecular frame. One of the previous work was reported in [143]. Another experiment that is interesting to conduct with the two laser pulses is to excite the molecules with the UV laser first, and then determine and products and time scales of the reaction with the IR laser and electron pulses, discussed in section 4.5.2. The keV-UED can also be used to study rotational echoes for more complex molecules than linear molecules [281-283], when both the laser pulses are IR pulses.

Appendix A

Feedback electronics

In this appendix, the feedback electronics in figure 2.3 is shown in figure A1. The circuit contains two amplifier channels. The left one is with the positive gain of the input voltage, and the right one for a negative gain. In the figure, S1, S2 and S3 are triple pole switches. By choosing the 1st connections, the circuit acts as a positive gain circuit, and the gain factor is K(1+R2/R1), where K is determined by potentiometer R0. For the 2nd connections, it acts as a negative gain circuit, and the gain factor is -K(R_2/R_1). The 3rd state is NULL, and gain is 0. The output voltage of the circuit is V1+GAIN ×V2, where V1, GAIN and V2 are corresponding to V_{offset}, A and V_{PDC} in the equation $f_4(t) = A \cdot V_{PDC} + V_{offset}$ (see chapter 2 for details). The voltage V1 is provided by a lead battery, a voltage precision reference chip, and a potentiometer.
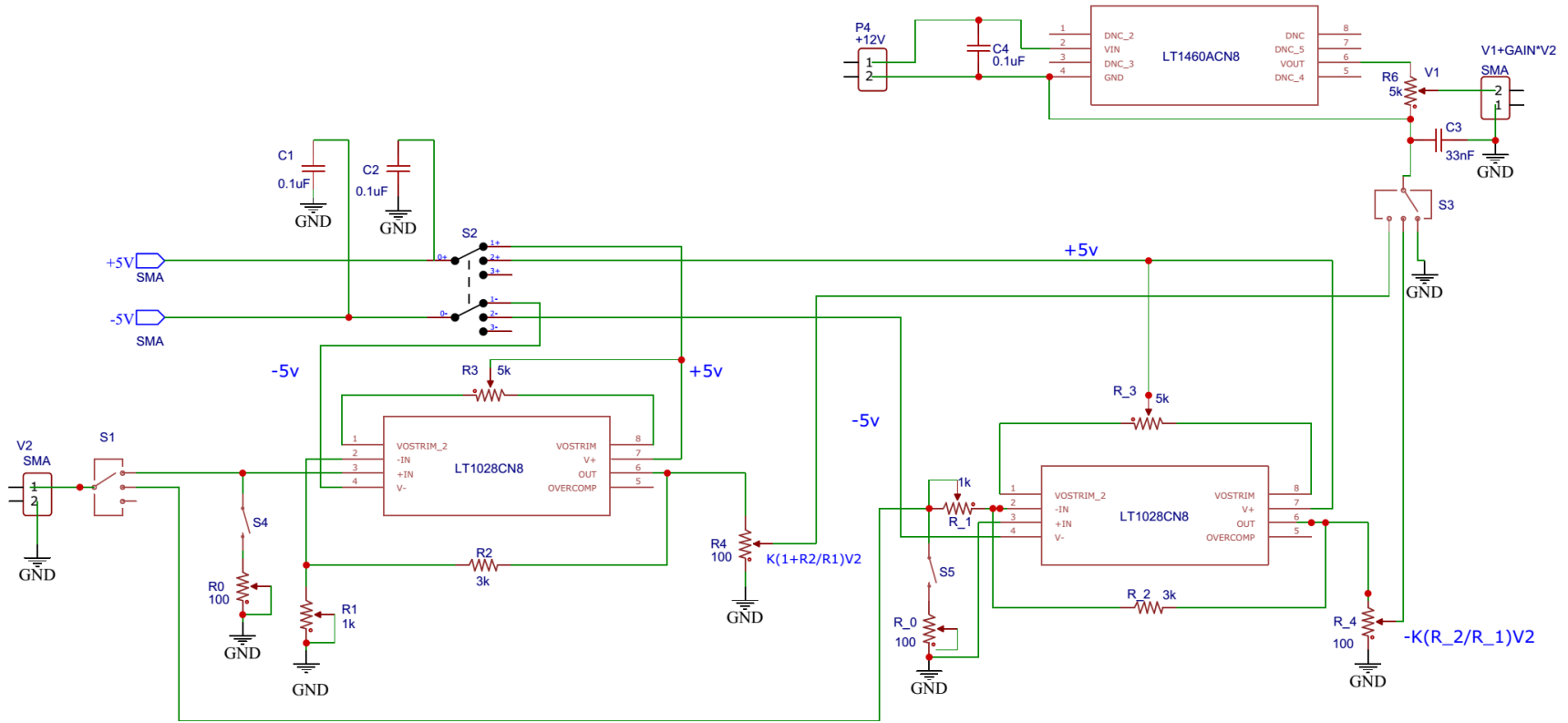
Figure A 1: Feedback electronics. There are two amplifier channels. S1, S2 and S3 are triple pole switches. By choosing the 1st connections, the circuit acts as a positive gain circuit, and the gain factor is K(1+R2/R1), where K is determined by potentiometer R0. For the 2nd connections, we have a negative gain circuit, and the gain factor is -K(R_2/R_1). The 3rd state is NULL. The output voltage of the circuit is V1+GAIN ×V2, where V1, GAIN and V2 are corresponding to V_{offset}, A and V_{PDC} in the equation $f_4(t) = A \cdot V_{\text{PDC}} + V_{\text{offset}}$.

References

[1]   M.T. Hassan, *Atomicroscopy: from femtosecond to attosecond electron microscopy.* Journal of Physics B: Atomic, Molecular and Optical Physics, 2018. **51**(3).

[2]   R. Srinivasan, V.A. Lobastov, C.Y. Ruan, et al., *Ultrafast Electron Diffraction (UED). A New Development for the 4D Determination of Transient Molecular Structures.* Cheminform, 2003. **34**(40): p. 1761-1838.

[3]   H. Ihee, B.M. Goodson, R. Srinivasan, et al., *Ultrafast Electron Diffraction and Structural Dynamics: Transient Intermediates in the Elimination Reaction of C2F4I2.* The Journal of Physical Chemistry A, 2002. **106**(16): p. 4087-4103.

[4]   L. De Broglie, *Recherches sur la théorie des Quanta*, Ph.D Thesis, Migration-universit´e en cours d'affectation, 1924

[5]   C.J. Davisson and L.H. Germer, *Reflection of Electrons by a Crystal of Nickel.* Proceedings of the National Academy of Sciences of the United States of America, 1928. **14**(4): p. 317-322.

[6]   G.P. Thomson and A. Reid, *Diffraction of Cathode Rays by a Thin Film.* Nature, 1927. **119**(3007): p. 890-890.

[7]   H. Mark and R. Wierl, *Über Elektronenbeugung am einzelnen Molekül.* Naturwissenschaften, 1930. **18**(9): p. 205-205.

[8]   G. Mourou and S. Williamson, *Picosecond electron diffraction.* Applied Physics Letters, 1982. **41**(1): p. 44-45.

[9]   A.A. Ischenko, V.V. Golubkov, V.P. Spiridonov, et al., *A stroboscopical gas-electron diffraction method for the investigation of short-lived molecular species.* Applied Physics B, 1983. **32**(3): p. 161-163.

[10]   A.P. Rood and J. Milledge, *Combined flash-photolysis and gas-phase electron-diffraction studies of small molecules.* Journal of the Chemical Society, Faraday Transactions 2: Molecular and Chemical Physics, 1984. **80**(9): p. 1145-1153.

[11]   H.K. Soong and J.B. Malta, *Femtosecond Lasers in Ophthalmology.* American Journal of Ophthalmology, 2009. **147**(2): p. 189-197.e2.

[12]   J.C. Williamson, M. Dantus, S.B. Kim, et al., *Ultrafast diffraction and molecular structure.* Chemical Physics Letters, 1992. **196**(6): p. 529-534.

[13]   C.Y. Ruan, V.A. Lobastov, R. Srinivasan, et al., *Ultrafast diffraction and structural dynamics: the nature of complex molecules far from equilibrium.* Proc Natl Acad Sci U S A, 2001. **98**(13): p. 7117-22.

[14]   H. Ihee, V.A. Lobastov, U.M. Gomez, et al., *Direct imaging of transient molecular structures with ultrafast diffraction.* Science, 2001. **291**(5503): p. 458-62.

[15]   R. Srinivasan, J.S. Feenstra, S.T. Park, et al., *Dark structures in molecular radiationless transitions determined by ultrafast diffraction.* Science, 2005. **307**(5709): p. 558-63.

[16]   G. Sciaini and R.J.D. Miller, *Femtosecond electron diffraction: heralding the era of atomically resolved dynamics.* Reports on Progress in Physics, 2011. **74**(9): p. 096101.

[17]   C. Gerbig, A. Senftleben, S. Morgenstern, et al., *Spatio-temporal resolution studies on a highly compact ultrafast electron diffractometer.* New Journal of Physics, 2015. **17**(4): p. 043050.

[18]   C.J. Hensley, J. Yang, and M. Centurion, *Imaging of isolated molecules with ultrafast electron pulses.* Physical review letters, 2012. **109**(13): p. 7035-7040.

[19]   J. Yang, M. Guehr, T. Vecchione, et al., *Diffractive imaging of a rotational wavepacket in nitrogen molecules with femtosecond megaelectronvolt electron pulses.* Nature communications, 2016. **7**.

[20]   J. Yang, M. Guehr, X. Shen, et al., *Diffractive Imaging of Coherent Nuclear Motion in Isolated Molecules.* Phys Rev Lett, 2016. **117**(15): p. 153002.

[21]   J. Yang, X. Zhu, T.J.A. Wolf, et al., *Imaging CF3I conical intersection and photodissociation dynamics with ultrafast electron diffraction.* Science, 2018. **361**(6397): p. 64-67.

[22]   T. van Oudheusden, P.L. Pasmans, S.B. van der Geer, et al., *Compression of subrelativistic space-charge-dominated electron bunches for single-shot femtosecond electron diffraction.* Phys Rev Lett, 2010. **105**(26): p. 264801.

[23]   M.R. Otto, L.P. Rene de Cotret, M.J. Stern, et al., *Solving the jitter problem in microwave compressed ultrafast electron diffraction instruments: Robust sub-50 fs cavity-laser phase stabilization.* Struct Dyn, 2017. **4**(5): p. 051101.

[24]   P. Baum and A.H. Zewail, *Breaking resolution limits in ultrafast electron diffraction and microscopy.* Proceedings of the National Academy of Sciences, 2006. **103**(44): p. 16105-16110.

[25]   P. Zhang, J. Yang, and M. Centurion, *Tilted femtosecond pulses for velocity matching in gas-phase ultrafast electron diffraction.* New Journal of Physics, 2014. **16**(8): p. 083008.

[26]   O. Zandi, K.J. Wilkin, Y. Xiong, et al., *High current table-top setup for femtosecond gas electron diffraction.* Structural Dynamics, 2017. **4**(4): p. 044022.

[27]   S. Weathersby, G. Brown, M. Centurion, et al., *Mega-electron-volt ultrafast electron diffraction at SLAC National Accelerator Laboratory.* Review of Scientific Instruments, 2015. **86**(7): p. 073702.

[28]   X. Shen, J.P.F. Nunes, J. Yang, et al., *Femtosecond gas-phase mega-electron-volt ultrafast electron diffraction.* Struct Dyn, 2019. **6**(5): p. 054305.

[29]   T.v. Oudheusden, *Electron source for sub-relativistic single-shot femtosecond diffraction.* Ph.D Thesis, Technische Universiteit Eindhoven, 2010

[30]   J. Charles Williamson and A.H. Zewail, *Ultrafast electron diffraction. Velocity mismatch and temporal resolution in crossed-beam experiments.* Chemical Physics Letters, 1993. **209**(1): p. 10-16.

[31]   F. Pennacchio, G.M. Vanacore, G.F. Mancini, et al., *Design and implementation of an optimal laser pulse front tilting scheme for ultrafast electron diffraction in reflection geometry with high temporal resolution.* Struct Dyn, 2017. **4**(4): p. 044032.

[32]   Y. Xiong, K.J. Wilkin, and M. Centurion, *High-resolution movies of molecular rotational dynamics captured with ultrafast electron diffraction.* Physical Review Research, 2020. **2**(4) : p. 043064.

[33]   S. Germán and R.J.D. Miller, *Femtosecond electron diffraction: heralding the era of atomically resolved dynamics.* Reports on Progress in Physics, 2011. **74**(9): p. 096101.

[34]   A.H. Zewail, *4D ultrafast electron diffraction, crystallography, and microscopy.* Annual Review of Physical Chemistry, 2006. **57**(1): p. 65-103.

[35]   J. Yang, J. Beck, C.J. Uiterwaal, et al., *Imaging of alignment and structural changes of carbon disulfide molecules using ultrafast electron diffraction.* Nature Communications, 2015. **6**: p. 8172.

[36]   F. Qi, Z. Ma, L. Zhao, et al., *Breaking 50 Femtosecond Resolution Barrier in MeV Ultrafast Electron Diffraction with a Double Bend Achromat Compressor.* Physical Review Letters, 2020. **124**(13): p. 134803.

[37]   S.P. Weathersby, G. Brown, M. Centurion, et al., *Mega-electron-volt ultrafast electron diffraction at SLAC National Accelerator Laboratory.* Review of Scientific Instruments, 2015. **86**(7): p. 073702.

[38]   X. Yang, J. Li, M. Fedurin, et al., *A novel nondestructive diagnostic method for mega-electron-volt ultrafast electron diffraction.* Scientific Reports, 2019. **9**(1): p. 17223.

[39]   H.W. Kim, N.A. Vinokurov, I.H. Baek, et al., *Towards jitter-free ultrafast electron diffraction technology.* Nature Photonics, 2020. **14**(4): p. 245-249.

[40]   J. Yang, X. Zhu, T.J.A. Wolf, et al., *Imaging CF_3I conical intersection and photodissociation dynamics with ultrafast electron diffraction.* Science, 2018. **361**(6397): p. 64.

[41]   E. Ruska, *Nobel lecture. The development of the electron microscope and of electron microscopy.* Biosci Rep, 1987. **7**(8): p. 607-29.

[42]   C. Varano, *Pioneers in Optics: Ernst Ruska (1906–1988).* Microscopy Today, 2022. **30**(2): p. 46-46.

[43]   R. Glauber and V. Schomaker, *The Theory of Electron Diffraction.* Physical Review, 1953. **89**(4): p. 667-671.

[44]   H.N. Chapman and K.A. Nugent, *Coherent lensless X-ray imaging.* Nature Photonics, 2010. **4**(12): p. 833-839.

[45]   Y.H. Lo, L. Zhao, M. Gallagher-Jones, et al., *In situ coherent diffractive imaging.* Nat Commun, 2018. **9**(1): p. 1826.

[46]   S. Chelkowski, P.B. Corkum, and A.D. Bandrauk, *Femtosecond Coulomb Explosion Imaging of Vibrational Wave Functions.* Physical Review Letters, 1999. **82**(17): p. 3416-3419.

[47]   M. Burt, R. Boll, J.W.L. Lee, et al., *Coulomb-explosion imaging of concurrent CH2BrI photodissociation dynamics.* Physical Review A, 2017. **96**(4): p. 043415.

[48]   M.P. Minitti, J.M. Budarz, A. Kirrander, et al., *Imaging Molecular Motion: Femtosecond X-Ray Scattering of an Electrocyclic Chemical Reaction.* Phys Rev Lett, 2015. **114**(25): p. 255501.

[49]   B. Stankus, H. Yong, N. Zotev, et al., *Ultrafast X-ray scattering reveals vibrational coherence following Rydberg excitation.* Nature Chemistry, 2019.

[50]   H. Yong, X. Xu, J.M. Ruddock, et al., *Ultrafast X-ray scattering offers a structural view of excited-state charge transfer.* Proc Natl Acad Sci U S A, 2021. **118**(19).

[51]   M.P. Minitti, J.M. Budarz, A. Kirrander, et al., *Imaging Molecular Motion: Femtosecond X-Ray Scattering of an Electrocyclic Chemical Reaction.* Physical review letters, 2015. **114**(25): p. 255501.

[52]   J. Yang, X. Zhu, F.N. JP, et al., *Simultaneous observation of nuclear and electronic dynamics by ultrafast electron diffraction.* Science, 2020. **368**(6493): p. 885-889.

[53]   K.J. Wilkin, R.M. Parrish, J. Yang, et al., *Diffractive imaging of dissociation and ground-state dynamics in a complex molecule.* Physical Review A, 2019. **100**(2).

[54]   H. Ihee, V.A. Lobastov, U.M. Gomez, et al., *Direct Imaging of Transient Molecular Structures with Ultrafast Diffraction.* Science, 2001. **291**(5503): p. 458-462.

[55]   C.J. Hensley, J. Yang, and M. Centurion, *Imaging of Isolated Molecules with Ultrafast Electron Pulses.* Physical Review Letters, 2012. **109**(13): p. 133202.

[56]   C.I. Blaga, J. Xu, A.D. DiChiara, et al., *Imaging ultrafast molecular dynamics with laser-induced electron diffraction.* Nature, 2012. **483**: p. 194.

[57]   B. Wolter, M.G. Pullen, A.T. Le, et al., *Ultrafast electron diffraction imaging of bond breaking in di-ionized acetylene.* Science, 2016. **354**(6310): p. 308.

[58]   I. Hargittai and M. Hargittai, *Stereochemical Applications of Gas-Phase Electron Diffraction*, 1988: Wiley.

[59]   R. Shankar, *Principles of Quantum Mechanics*, 2012: Springer US.

[60]   L.O. Brockway, *Electron Diffraction by Gas Molecules.* Reviews of Modern Physics, 1936. **8**(3): p. 231-266.

[61]   L.I. Schiff, *Quantum Mechanics*, 1955: McGraw-Hill.

[62]   V. Schomaker and R.O.Y. Glauber, *The Born Approximation in Electron Diffraction.* Nature, 1952. **170**(4320): p. 290-291.

[63]   N.F. Mott, H.S.W. Massey, and H.S.H. Massey, *The Theory of Atomic Collisions*, 1965: Clarendon Press.

[64]   E.N. Economou, *Green's Functions in Quantum Physics*, 2013: Springer Berlin Heidelberg.

[65]   F. Scheck, *Quantum Physics*. 2 ed, 2013, Berlin, Heidelberg: Springer.

[66]   M. Centurion, T.J.A. Wolf, and J. Yang, *Ultrafast Imaging of Molecules with Electron Diffraction.* Annu Rev Phys Chem, 2021.

[67]   E. Prince, *International Tables for Crystallography Volume C: Mathematical, physical and chemical tables.* 2006. **C**.

[68]   F. Biggs, L.B. Mendelsohn, and J.B. Mann, *Hartree-Fock Compton profiles for the elements.* Atomic Data and Nuclear Data Tables, 1975. **16**(3): p. 201-309.

[69]   Y. Xiong, K. Borne, A.M. Carrascosa, et al., *Strong-field induced fragmentation and isomerization of toluene probed by ultrafast femtosecond electron diffraction and mass spectrometry.* Faraday Discuss, 2021. **228**(0): p. 39-59.

[70]   T. Iijima, R.A. Bonham, and T. Ando, *The Theory of Electron Scattering from Molecules. I. Theoretical Development.* The Journal of Physical Chemistry, 1963. **67**(7): p. 1472-1474.

[71]   H.S.W. Massey and C.B.O. Mohr, *The collision of electrons with molecules.* Proceedings of the Royal Society of London. Series A, Containing Papers of a Mathematical and Physical Character, 1932. **135**(826): p. 258-275.

[72]   L.S. Bartell and R.M. Gavin, *Effects of Electron Correlation in X-Ray and Electron Diffraction.* Journal of the American Chemical Society, 1964. **86**(17): p. 3493-3498.

[73]   J. Karle, *Excited States of Molecules and the Scattering of Fast Electrons.* The Journal of Chemical Physics, 1961. **35**(3): p. 963-969.

[74]   H. Bethe, *Zur Theorie des Durchgangs schneller Korpuskularstrahlen durch Materie.* Annalen der Physik, 1930. **397**(3): p. 325-400.

[75]   N.F. Mott, *The scattering of electrons by atoms.* Proceedings of the Royal Society of London. Series A, Containing Papers of a Mathematical and Physical Character, 1930. **127**(806): p. 658-665.

[76]   P.M. Morse, *Quantum Mechanics of Collision Processes Part II.* Reviews of Modern Physics, 1932. **4**(3): p. 577-634.

[77]   W. Heisenberg, *Über die inkohärente Streuung von Röntgenstrahlen*, in *Original Scientific Papers Wissenschaftliche Originalarbeiten*, W. Blum, H. Rechenberg, and H.-P. Dürr, Editors. 1931, Springer Berlin Heidelberg: Berlin, Heidelberg. p. 627-630.

[78]   C.F. Bunge, J.A. Barrientos, and A.V. Bunge, *Roothaan-Hartree-Fock Ground-State Atomic Wave Functions: Slater-Type Orbital Expansions and Expectation Values for Z = 2-54.* Atomic Data and Nuclear Data Tables, 1993. **53**(1): p. 113-162.

[79]   A.D. McLean and R.S. McLean, *Roothaan-Hartree-Fock atomic wave functions Slater basis-set expansions for Z = 55–92.* Atomic Data and Nuclear Data Tables, 1981. **26**(3-4): p. 197-381.

[80]   P. Debye, *Scattering from non-crystalline substances.* Ann. Physik, 1915. **46**: p. 809-823.

[81] P. Ehrenfest, *On interference phenomena to be expected when Roentgen rays pass through a di-atomic gas.* Koninklijke Nederlandse Akademie van Wetenschappen Proceedings Series B Physical Sciences, 1915. **17**: p. 1184-1190.

[82] D. Shorokhov, S.T. Park, and A.H. Zewail, *Ultrafast electron diffraction: dynamical structures on complex energy landscapes.* Chemphyschem, 2005. **6**(11): p. 2228-50.

[83] H. Ihee, J. Cao, and A.H. Zewail, *Ultrafast electron diffraction: structures in dissociation dynamics of Fe(CO)5.* Chemical Physics Letters, 1997. **281**(1-3): p. 10-19.

[84] B.R. Pauw, *Everything SAXS: small-angle scattering pattern collection and correction.* Journal of Physics: Condensed Matter, 2013. **25**(38): p. 383201.

[85] J.S. Pedersen, D. Posselt, and K. Mortensen, *Analytical treatment of the resolution function for small-angle scattering.* Journal of Applied Crystallography, 1990. **23**(4): p. 321-333.

[86] G. Wignall, *Instrumental resolution effects in small-angle scattering.* Journal of Applied Crystallography, 1991. **24**(5): p. 479-484.

[87] V. Ramakrishnan, *A treatment of instrumental smearing effects in circularly symmetric small-angle scattering.* Journal of Applied Crystallography, 1985. **18**(1): p. 42-46.

[88] G. Sciaini, M. Harb, S.G. Kruglik, et al., *Electronic acceleration of atomic motions and disordering in bismuth.* Nature, 2009. **458**(7234): p. 56-9.

[89] J. Yang, M. Guehr, X. Shen, et al., *Diffractive Imaging of Coherent Nuclear Motion in Isolated Molecules.* Physical review letters, 2016. **117**(15): p. 153002.

[90]   T.J.A. Wolf, D.M. Sanchez, J. Yang, et al., *The photochemical ring-opening of 1,3-cyclohexadiene imaged by ultrafast electron diffraction.* Nature Chemistry, 2019.

[91]   T. van Oudheusden, P.L.E.M. Pasmans, S.B. van der Geer, et al., *Compression of Subrelativistic Space-Charge-Dominated Electron Bunches for Single-Shot Femtosecond Electron Diffraction.* Physical Review Letters, 2010. **105**(26): p. 264801.

[92]   M.R. Otto, L.P. René de Cotret, M.J. Stern, et al., *Solving the jitter problem in microwave compressed ultrafast electron diffraction instruments: Robust sub-50 fs cavity-laser phase stabilization.* Structural Dynamics, 2017. **4**(5): p. 051101.

[93]   T. van Oudheusden, E.F. de Jong, S.B. van der Geer, et al., *Electron source concept for single-shot sub-100 fs electron diffraction in the 100 keV range.* Journal of Applied Physics, 2007. **102**(9): p. 093501.

[94]   B.J. Siwick, J.R. Dwyer, R.E. Jordan, et al., *Ultrafast electron optics: Propagation dynamics of femtosecond electron packets.* Journal of Applied Physics, 2002. **92**(3): p. 1643-1648.

[95]   O. Zandi, *Design and Construction of a High-Current Femtosecond Gas-Phase Electron Diffraction Setup*. 10683670 Thesis, The University of Nebraska - Lincoln: Ann Arbor. p. 176, 2017

[96]   O. Zandi, K. Wilkin, A. DeSimone, et al., *Femtosecond electron pulse generation and measurement for diffractive imaging of isolated molecules*, SPIE Optical Engineering + Applications, Vol. 9956. 2016: SPIE.

[97]   O. Zandi, K.J. Wilkin, and M. Centurion, *Implementation and modeling of a femtosecond laser-activated streak camera.* Review of Scientific Instruments, 2017. **88**(6): p. 063305.

[98]   M. Gao, Y. Jiang, G.H. Kassier, et al., *Single shot time stamping of ultrabright radio frequency compressed electron pulses.* Applied Physics Letters, 2013. **103**(3): p. 033503.

[99]   G.H. Kassier, K. Haupt, N. Erasmus, et al., *A compact streak camera for 150 fs time resolved measurement of bright pulses in ultrafast electron diffraction.* Rev Sci Instrum, 2010. **81**(10): p. 105103.

[100] C. Kealhofer, W. Schneider, D. Ehberger, et al., *All-optical control and metrology of electron pulses.* Science, 2016. **352**(6284): p. 429-33.

[101] M. Gao, C. Lu, H. Jean-Ruel, et al., *Mapping molecular motions leading to charge delocalization with ultrabright electrons.* Nature, 2013. **496**(7445): p. 343-6.

[102] C.T. Hebeisen, G. Sciaini, M. Harb, et al., *Grating enhanced ponderomotive scattering for visualization and full characterization of femtosecond electron pulses.* Optics Express, 2008. **16**(5): p. 3334-3341.

[103] C.T. Hebeisen, R. Ernstorfer, M. Harb, et al., *Femtosecond electron pulse characterization using laser ponderomotive scattering.* Optics Letters, 2006. **31**(23): p. 3517-3519.

[104] M. Gao, H. Jean-Ruel, R.R. Cooney, et al., *Full characterization of RF compressed femtosecond electron pulses using ponderomotive scattering.* Optics Express, 2012. **20**(11): p. 12048-12058.

[105] W.C. Nunnally and R.B. Hammond, *CHAPTER 12 - Optoelectronic Switch for Pulsed Power*, in *Picosecond Optoelectronic Devices*, C.H. Lee, Editor. 1984, Academic Press. p. 373-398.

[106] J. Hebling, *Derivation of the pulse front tilt caused by angular dispersion.* Optical and Quantum Electronics, 1996. **28**(12): p. 1759-1763.

[107] O.E. Martinez, *Pulse distortions in tilted pulse schemes for ultrashort pulses.* Optics Communications, 1986. **59**(3): p. 229-232.

[108] Z. Bor, B. Racz, G. Szabo, et al., *Femtosecond pulse front tilt caused by angular dispersion.* Optical Engineering, 1993. **32**(10): p. 2501-2504.

[109] J.W. Goodman, *Introduction to Fourier optics*. 2nd ed, McGraw-Hill series in electrical and computer engineering,1996, New York: McGraw-Hill. xviii, 441 p.

[110] D. Kreier and P. Baum, *Avoiding temporal distortions in tilted pulses.* Optics Letters, 2012. **37**(12): p. 2373-5.

[111] R. Trebino, K.W. DeLong, D.N. Fittinghoff, et al., *Measuring ultrashort laser pulses in the time-frequency domain using frequency-resolved optical gating.* Review of Scientific Instruments, 1997. **68**(9): p. 3277-3295.

[112] M. Dantus, S.B. Kim, J.C. Williamson, et al., *Ultrafast Electron Diffraction. 5. Experimental Time Resolution and Applications.* J.phys.chem, 1994. **98**(11): p. 2782-2796.

[113] J. Yang, M. Guehr, T. Vecchione, et al., *Femtosecond gas phase electron diffraction with MeV electrons.* Faraday Discuss, 2016. **194**: p. 563-581.

[114] Y. Xiong, K.J. Wilkin, S.K. Saha, et al., *Retrieval of the molecular orientation distribution from atom-pair angular distributions.* Physical Review A, 2022. **106**(3): p. 033109.

[115] K. Lin, I. Tutunnikov, J. Ma, et al., *Spatiotemporal rotational dynamics of laser-driven molecules.* Advanced Photonics, 2020. **2**(02): p. 1.

[116] C.P. Koch, M. Lemeshko, and D. Sugny, *Quantum control of molecular rotation.* Reviews of Modern Physics, 2019. **91**(3): p. 035005.

[117] H. Stapelfeldt and T. Seideman, *Colloquium: Aligning molecules with strong laser pulses.* Reviews of Modern Physics, 2003. **75**(2): p. 543-557.

[118] Y. Ohshima and H. Hasegawa, *Coherent rotational excitation by intense nonresonant laser fields.* International Reviews in Physical Chemistry, 2010. **29**(4): p. 619-663.

[119] S. Fleischer, Y. Khodorkovsky, E. Gershnabel, et al., *Molecular Alignment Induced by Ultrashort Laser Pulses and Its Impact on Molecular Motion.* Israel Journal of Chemistry, 2012. **52**(5): p. 414-437.

[120] M. Lemeshko, R.V. Krems, J.M. Doyle, et al., *Manipulation of molecules with electromagnetic fields.* Molecular Physics, 2013. **111**(12-13): p. 1648-1682.

[121] B. Friedrich and D. Herschbach, *Alignment and Trapping of Molecules in Intense Laser Fields.* Physical review letters, 1995. **74**(23): p. 4623-4626.

[122] B.A. Zon, B.G. Katsnelson, Y.N. Mitin, et al., *Radiative widths of Stark components of fine-structure levels of a hydrogen atom. transition probabilities, electric field strength.* Opt. Spectrosc. (USSR) (Engl. Transl.). (United States), 1976.

[123] T. Seideman and E. Hamilton, *Nonadiabatic Alignment by Intense Pulses. Concepts, Theory, and Directions.* Advances in Atomic Molecular & Optical Physics, 2005. **52**(05): p. 289-329.

[124] R.N. Zare, *Laser control of chemical reactions.* Science, 1998. **279**(5358): p. 1875-9.

[125] J.J. Larsen, I. Wendt-Larsen, and H. Stapelfeldt, *Controlling the Branching Ratio of Photodissociation Using Aligned Molecules.* Physical review letters, 1999. **83**(6): p. 1123-1126.

[126] T. Seideman, *Time-resolved photoelectron angular distributions as a means of studying polyatomic nonadiabatic dynamics.* The Journal of Chemical Physics, 2000. **113**(5): p. 1677-1680.

[127] T. Seideman, *Time-resolved photoelectron angular distributions as a probe of coupled polyatomic dynamics.* Physical Review A, 2001. **64**(4): p. 042504.

[128] J. Itatani, J. Levesque, D. Zeidler, et al., *Tomographic imaging of molecular orbitals.* Nature, 2004. **432**(7019): p. 867-71.

[129] T. Kanai, S. Minemoto, and H. Sakai, *Quantum interference during high-order harmonic generation from aligned molecules.* Nature, 2005. **435**(7041): p. 470-474.

[130] C. Vozzi, M. Negro, F. Calegari, et al., *Generalized molecular orbital tomography.* Nature Physics, 2011. **7**(10): p. 822-826.

[131] M. Zhang, S. Zhang, Y. Xiong, et al., *Quantum state tomography of molecules by ultrafast diffraction.* Nat Commun, 2021. **12**(1): p. 5441.

[132] L. Christensen, J.H. Nielsen, C.B. Brandt, et al., *Dynamic Stark Control of Torsional Motion by a Pair of Laser Pulses.* Physical review letters, 2014. **113**(7): p. 073005.

[133] J. Küpper, S. Stern, L. Holmegaard, et al., *X-Ray Diffraction from Isolated and Strongly Aligned Gas-Phase Molecules with a Free-Electron Laser.* Physical review letters, 2014. **112**(8).

[134] J. Yang, J. Beck, C.J. Uiterwaal, et al., *Imaging of alignment and structural changes of carbon disulfide molecules using ultrafast electron diffraction.* Nature communications, 2015. **6**.

[135] B. Wolter, M.G. Pullen, A.T. Le, et al., *Ultrafast electron diffraction imaging of bond breaking in di-ionized acetylene.* Science, 2016. **354**(6310): p. 308-312.

[136] K.J. Wilkin, Y. Xiong, H. Zhao, et al., *Ultrafast electron diffraction from transiently aligned asymmetric top molecules: Rotational dynamics and structure retrieval.* Structural Dynamics, 2022. **9**(5): p. 054303.

[137] R.A. Bartels, T.C. Weinacht, N. Wagner, et al., *Phase Modulation of Ultrashort Light Pulses using Molecular Rotational Wave Packets.* Physical review letters, 2001. **88**(1): p. 013903.

[138] R. Velotta, N. Hay, M.B. Mason, et al., *High-Order Harmonic Generation in Aligned Molecules.* Physical review letters, 2001. **87**(18): p. 183901.

[139] N. Hay, R. Velotta, M. Lein, et al., *High-order harmonic generation in laser-aligned molecules.* Physical Review A, 2002. **65**(5): p. 053805.

[140] R. Funahashi, M. Mikami, T. Mihara, et al., *A portable thermoelectric-power-generating module composed of oxide devices.* Journal of Applied Physics, 2006. **99**(6): p. 066117.

[141] R.d. Nalda, E. Heesel, M. Lein, et al., *Role of orbital symmetry in high-order harmonic generation from aligned molecules.* Physical Review A, 2004. **69**(3): p. 031804.

[142] A.D. Bandrauk and H. Lu, *Harmonic generation by molecules in intense laser and magnetic fields: Orientation effects.* International Journal of Quantum Chemistry, 2004. **99**(4): p. 431-438.

[143] C.Z. Bisgaard, O.J. Clarkin, G. Wu, et al., *Time-resolved molecular frame dynamics of fixed-in-space CS2 molecules.* Science, 2009. **323**(5920): p. 1464-8.

[144] P. Hockett, C.Z. Bisgaard, O.J. Clarkin, et al., *Time-resolved imaging of purely valence-electron dynamics during a chemical reaction.* Nature Physics, 2011. **7**(8): p. 612-615.

[145] J.L. Hansen, H. Stapelfeldt, D. Dimitrovski, et al., *Time-Resolved Photoelectron Angular Distributions from Strong-Field Ionization of Rotating Naphthalene Molecules.* Physical review letters, 2011. **106**(7): p. 073001.

[146] C.B. Madsen, L.B. Madsen, S.S. Viftrup, et al., *Manipulating the torsion of molecules by strong laser pulses.* Phys Rev Lett, 2009. **102**(7): p. 073007.

[147] M. Gregory, P. Hockett, A. Stolow, et al., *Towards molecular frame photoelectron angular distributions in polyatomic molecules from lab frame coherent rotational wavepacket evolution.* Journal of Physics B: Atomic, Molecular and Optical Physics, 2021. **54**(14): p. 145601.

[148] I.V. Litvinyuk, K.F. Lee, P.W. Dooley, et al., *Alignment-dependent strong field ionization of molecules.* Phys Rev Lett, 2003. **90**(23): p. 233003.

[149] J.E. Bækhøj and L.B. Madsen, *Attosecond transient-absorption spectroscopy on aligned molecules.* Physical Review A, 2016. **94**(4): p. 043414.

[150] J. Wu, P. Lu, J. Liu, et al., *Ultrafast optical imaging by molecular wakes.* Applied Physics Letters, 2010. **97**(16): p. 161106.

[151] K.F. Lee, D.M. Villeneuve, P.B. Corkum, et al., *Phase Control of Rotational Wave Packets and Quantum Information.* Physical review letters, 2004. **93**(23): p. 233601.

[152] T. Seideman, *Rotational excitation and molecular alignment in intense laser fields.* The Journal of Chemical Physics, 1995. **103**(18): p. 7887-7896.

[153] T. Seideman, *Revival Structure of Aligned Rotational Wave Packets.* Physical review letters, 1999. **83**(24): p. 4971-4974.

[154] T. Seideman, *On the dynamics of rotationally broad, spatially aligned wave packets.* The Journal of Chemical Physics, 2001. **115**(13): p. 5965-5973.

[155] J. Ortigoso, M. Rodríguez, M. Gupta, et al., *Time evolution of pendular states created by the interaction of molecular polarizability with a pulsed nonresonant laser field.* The Journal of Chemical Physics, 1999. **110**(8): p. 3870-3875.

[156] J.J. Larsen, H. Sakai, C.P. Safvan, et al., *Aligning molecules with intense nonresonant laser fields.* The Journal of Chemical Physics, 1999. **111**(17): p. 7774-7781.

[157] F. Rosca-Pruna and M.J. Vrakking, *Experimental observation of revival structures in picosecond laser-induced alignment of I2.* Phys Rev Lett, 2001. **87**(15): p. 153902.

[158] E. Hamilton, T. Seideman, T. Ejdrup, et al., *Alignment of symmetric top molecules by short laser pulses.* Physical Review A, 2005. **72**(4).

[159] P.W. Dooley, I.V. Litvinyuk, K.F. Lee, et al., *Direct imaging of rotational wave-packet dynamics of diatomic molecules.* Physical Review A, 2003. **68**(2): p. 023406.

[160] E.T. Karamatskos, S. Raabe, T. Mullins, et al., *Molecular movie of ultrafast coherent rotational dynamics of OCS.* Nature communications, 2019. **10**(1): p. 3364.

[161] V. Kumarappan, C.Z. Bisgaard, S.S. Viftrup, et al., *Role of rotational temperature in adiabatic molecular alignment.* J Chem Phys, 2006. **125**(19): p. 194309.

[162] C.S. Slater, S. Blake, M. Brouard, et al., *Coulomb-explosion imaging using a pixel-imaging mass-spectrometry camera.* Physical Review A, 2015. **91**(5): p. 053424.

[163] C.A. Schouder, A.S. Chatterley, J.D. Pickering, et al., *Laser-Induced Coulomb Explosion Imaging of Aligned Molecules and Molecular Dimers.* Annu Rev Phys Chem, 2022. **73**(1): p. 323-347.

[164] E. Péronne, M.D. Poulsen, H. Stapelfeldt, et al., *Nonadiabatic laser-induced alignment of iodobenzene molecules.* Physical Review A, 2004. **70**(6).

[165] M.D. Poulsen, E. Skovsen, and H. Stapelfeldt, *Photodissociation of laser aligned iodobenzene: Towards selective photoexcitation.* The Journal of Chemical Physics, 2002. **117**(5): p. 2097-2102.

[166] A. Rouzee, V. Boudon, B. Lavorel, et al., *Rotational Raman spectroscopy of ethylene using a femtosecond time-resolved pump-probe technique.* J Chem Phys, 2005. **123**(15): p. 154309.

[167] A. Rudenko, K. Zrost, C.D. Schröter, et al., *Resonant structures in the low-energy electron continuum for single ionization of atoms in the tunnelling regime.* Journal of Physics B: Atomic, Molecular and Optical Physics, 2004. **37**(24): p. L407-L413.

[168] H.V.S. Lam, S. Yarlagadda, A. Venkatachalam, et al., *Angle-dependent strong-field ionization and fragmentation of carbon dioxide measured using rotational wave packets.* Physical Review A, 2020. **102**(4).

[169] J. Mikosch, C.Z. Bisgaard, A.E. Boguslavskiy, et al., *The quantitative determination of laser-induced molecular axis alignment.* J Chem Phys, 2013. **139**(2): p. 024304.

[170] V. Makhija, X. Ren, D. Gockel, et al., *Orientation Resolution through Rotational Coherence Spectroscopy.* Atomic Physics, arXiv:1611.06476 [physics.atom-ph], 2016.

[171] X. Wang, A.-T. Le, Z. Zhou, et al., *Theory of retrieving orientation-resolved molecular information using time-domain rotational coherence spectroscopy.* Physical Review A, 2017. **96**(2): p. 023424.

[172] L.D. Landau and E.M. Lifshits, *Mechanics*. 2nd ed, Course of theoretical physics,1969, Oxford ; New York: Pergamon Press. page 98 -100.

[173] R.N. Zare, *Angular Momentum Understanding spatial aspects in chemistry and physics.* 1988: p. page 77-81, 105.

[174] G. Herzberg, *Molecular Spectra and Molecular Structure Vol II.* Infrared and Raman Spectra of Polyatomic Molecules, 1945. **II** p. 42-49.

[175] T. Seideman, *New means of spatially manipulating molecules with light.* The Journal of Chemical Physics, 1999. **111**(10): p. 4397-4405.

[176]   P.S. Pershan, J.P. van der Ziel, and L.D. Malmstrom, *Theoretical Discussion of the Inverse Faraday Effect, Raman Scattering, and Related Phenomena.* Physical Review, 1966. **143**(2): p. 574-583.

[177]   R.N. Zare, *Angular Momentum Understanding spatial aspects in chemistry and physics.* United States: Wiley, 1988: page 267-277.

[178]   S.C. Wang, *On the Asymmetrical Top in Quantum Mechanics.* Physical Review, 1929. **34**(2): p. 243-252.

[179]   G.W. King, R.M. Hainer, and P.C. Cross, *The Asymmetric Rotor I. Calculation and Symmetry Classification of Energy Levels.* The Journal of Chemical Physics, 1943. **11**(1): p. 27-42.

[180]   B.S. Ray, *Über die Eigenwerte des asymmetrischen Kreisels.* Zeitschrift für Physik, 1932. **78**(1): p. 74-91.

[181]   D.L. Mills, *Nonlinear Optics: Basic Concepts*, 1991: Springer-Verlag.

[182]   H. Hasegawa and Y. Ohshima, *Nonadiabatic Molecular Alignment and Orientation.* 2015. **112**: p. 45-64.

[183]   R.E. Goetz, C.P. Koch, and L. Greenman, *Quantum Control of Photoelectron Circular Dichroism.* Phys Rev Lett, 2019. **122**(1): p. 013204.

[184]   T. Seideman, *The analysis of magnetic-state-selected angular distributions: a quantum mechanical form and an asymptotic approximation.* Chemical Physics Letters, 1996. **253**(3-4): p. 279-285.

[185]   F. Neese, *The ORCA program system.* WIREs Computational Molecular Science, 2012. **2**(1): p. 73-78.

[186] L.F. Shampine and M.W. Reichelt, *The MATLAB ODE Suite.* SIAM Journal on Scientific Computing, 1997. **18**(1): p. 1-22.

[187] G. Herzberg, *Molecular spectra and molecular structure. vol 2: Infrared and Raman spectra of polyatomic molecules.* D. Van Nostrand Company, Toronto, 1945: page 27-29.

[188] D.M. Dennison, *The Infrared Spectra of Polyatomic Molecules Part I.* Reviews of Modern Physics, 1931. **3**(2): p. 280-345.

[189] N. Davidson and N.R. Davidson, *Statistical Mechanics*, 1962: McGraw-Hill.

[190] P.F. Bernath and P.C.P.F. Bernath, *Spectra of Atoms and Molecules*, 1995: Oxford University Press.

[191] M. Machholm and N.E. Henriksen, *Field-free orientation of molecules.* Phys Rev Lett, 2001. **87**(19): p. 193001.

[192] Z. Ma, X. Zou, L. Zhao, et al., *Ultrafast isolated molecule imaging without crystallization.* Proc Natl Acad Sci U S A, 2022. **119**(15): p. e2122793119.

[193] E.R. Peterson, C. Buth, D.A. Arms, et al., *An x-ray probe of laser-aligned molecules.* Applied Physics Letters, 2008. **92**(9): p. 094106.

[194] P.J. Ho, M.R. Miller, and R. Santra, *Field-free molecular alignment for studies using x-ray pulses from a synchrotron radiation source.* J Chem Phys, 2009. **130**(15): p. 154310.

[195] V.K. Rohatgi and A.K.M.E. Saleh, *An Introduction to Probability and Statistics*, 2001: Wiley. page 133-135.

[196] Y. Xiong, H. Zhao, S.K. Saha, et al., *Isotope detection in molecules with ultrafast electron diffraction and rotational spectrometry.* Journal of Physics Communications, 2022. **6**(5): p. 055006.

[197] Y. Xiong, K.J. Wilkin, S.K. Saha, et al., *Diffractive imaging of a rotational wavepacket in nonlinear molecules*, April 11, 2022: PREPRINT (Version 1) available at Research Square [https://doi.org/10.21203/rs.3.rs-1483307/v1].

[198] M.A. Blanco, M. Flórez, and M. Bermejo, *Evaluation of the rotation matrices in the basis of real spherical harmonics.* Journal of Molecular Structure: THEOCHEM, 1997. **419**(1-3): p. 19-27.

[199] M. Planitz, *Inconsistent Systems of Linear Equations.* The Mathematical Gazette, 1979. **63**(425): p. 181-185.

[200] T.J. Holmes, S. Bhattacharyya, J.A. Cooper, et al., *Light Microscopic Images Reconstructed by Maximum Likelihood Deconvolution.* 1995: p. 389-402.

[201] D.S. Biggs and M. Andrews, *Acceleration of iterative image restoration algorithms.* Appl Opt, 1997. **36**(8): p. 1766-75.

[202] P.A. Jansson, *Deconvolution of Images and Spectra: Second Edition*, 2014: Dover Publications.

[203] L. Schåfer, *Electron Diffraction as a Tool of Structural Chemistry.* Applied Spectroscopy, 1976. **30**(2): p. 123-149.

[204] H.B. Bürgi, *Stereochemical Applications of Gas-Phase Electron Diffraction. Edited by I. Hargittai and M. Hargittai. VCH Verlagsgesellschaft, Weinheim/VCH Publishers, New York 1988. Part A: The Electron Diffraction Technique. XVIII, 563 S., geb. DM 210.00. – ISBN 3-527-26691-7/0-89573-337-4; Part B: Structural*

Information for Selected Classes of Compounds. XVIII, 511 S., geb. DM 210.00. – ISBN 3-527-26790-5/0-89573-292-0. Angewandte Chemie, 1989. **101**(12): p. 1756-1757.

[205] X. Shen, J.P.F. Nunes, J. Yang, et al., *Femtosecond gas-phase mega-electron-volt ultrafast electron diffraction.* Structural Dynamics, 2019. **6**(5): p. 054305.

[206] M. Centurion, *Ultrafast imaging of isolated molecules with electron diffraction.* Journal of Physics B: Atomic, Molecular and Optical Physics, 2016. **49**(6): p. 062002.

[207] J. Yang, V. Makhija, V. Kumarappan, et al., *Reconstruction of three-dimensional molecular structure from diffraction of laser-aligned molecules.* Structural Dynamics, 2014. **1**(4): p. 044101.

[208] M. Centurion, T.J.A. Wolf, and J. Yang, *Ultrafast Imaging of Molecules with Electron Diffraction.* Annual Review of Physical Chemistry, 2021.

[209] J.D. Barnes and Z.D. Sharp, *Chlorine Isotope Geochemistry.* Reviews in Mineralogy and Geochemistry, 2017. **82**(1): p. 345-378.

[210] M. Berglund and M.E. Wieser, *Isotopic compositions of the elements 2009 (IUPAC Technical Report).* Pure and Applied Chemistry, 2011. **83**(2): p. 397-410.

[211] J.R.d. Laeter, J.K. Böhlke, P.D. Bièvre, et al., *Atomic weights of the elements. Review 2000 (IUPAC Technical Report).* Pure and Applied Chemistry, 2003. **75**(6): p. 683-800.

[212] W. Von E.Doering and L.H. Knox, *The Cycloheptatrienylium (Tropylium) Ion.* Journal of the American Chemical Society, 1954. **76**(12): p. 3203-3206.

[213]   P. Ausloos, *Structure and isomerization of C7H7+ ions formed in the charge-transfer-induced fragmentation of ethylbenzene, toluene, and norbornadiene.* Journal of the American Chemical Society, 1982. **104**(20): p. 5259-5265.

[214]   T. Baer, J.C. Morrow, J.D. Shao, et al., *Gas-phase heats of formation of C7H7+ isomers: m-tolyl, p-tolyl, and benzyl ions.* Journal of the American Chemical Society, 1988. **110**(17): p. 5633-5638.

[215]   C. Lifshitz, *Tropylium Ion Formation from Toluene: Solution of an Old Problem in Organic Mass Spectrometry.* Accounts of Chemical Research, 2002. **27**(5): p. 138-144.

[216]   P. Jusko, A. Simon, S. Banhatti, et al., *Direct Evidence of the Benzylium and Tropylium Cations as the Two Long-Lived Isomers of C7 H7().* Chemphyschem, 2018.

[217]   T. Nguyen, M. Aparicio, and M.A. Saleh, *Gas Phase Ionization of Toluene: Benzylium Versus Tropylium Pathway.* Current Physical Chemistry, 2019. **9**(2): p. 138-150.

[218]   K.G. Torma, K. Voronova, B. Sztaray, et al., *Dissociative Photoionization of the C7H8 Isomers Cycloheptatriene and Toluene: Looking at Two Sides of the Same Coin Simultaneously.* J Phys Chem A, 2019. **123**(16): p. 3454-3463.

[219]   M. Castillejo, S. Couris, E. Koudoumas, et al., *Ionization and fragmentation of aromatic and single-bonded hydrocarbons with 50 fs laser pulses at 800 nm.* Chemical Physics Letters, 1999. **308**(5-6): p. 373-380.

[220] A.M. Müller, C.J.G.J. Uiterwaal, B. Witzel, et al., *Photoionization and photofragmentation of gaseous toluene using 80-fs, 800-nm laser pulses.* The Journal of Chemical Physics, 2000. **112**(21): p. 9289-9300.

[221] A.M. Müller, B. Witzel, C.J.G.J. Uiterwaal, et al., *White-Light-Induced Fragmentation of Toluene.* Physical review letters, 2001. **88**(2): p. 023001.

[222] X.P. Tang, A. Becker, W. Liu, et al., *Enhanced fragmentation of toluene through linear and nonlinear increase of the focal spot area of an ultrashort laser pulse.* Physical Review A, 2005. **71**(4): p. 045401.

[223] D.W. Squire, M.P. Barbalas, and R.B. Bernstein, *Comparison of multiphoton ionization-fragmentation behavior of benzene, fluorobenzene, and toluene.* The Journal of Physical Chemistry, 1983. **87**(10): p. 1701-1707.

[224] U. Ablikim, C. Bomme, H. Xiong, et al., *Identification of absolute geometries of cis and trans molecular isomers by Coulomb Explosion Imaging.* Scientific Reports, 2016. **6**(1): p. 38202.

[225] S.A. Shlykov, T.D. Phien, Y. Gao, et al., *Structure and conformational behavior of N-phenylpiperidine studied by gas-phase electron diffraction and quantum chemical calculations.* Journal of Molecular Structure, 2017. **1132**: p. 3-10.

[226] S.A. Shlykov, T.D. Phien, and P.M. Weber, *Intramolecular inversions, structure and conformational behavior of gaseous and liquid N-cyanopiperidine. Comparison with other 1-cyanoheterocyclohexanes.* Journal of Molecular Structure, 2017. **1138**: p. 41-49.

[227] A. Lechtken, C. Neiss, M.M. Kappes, et al., *Structure determination of gold clusters by trapped ion electron diffraction: Au(14)(-)-Au(19)(-).* Phys Chem Chem Phys, 2009. **11**(21): p. 4344-50.

[228] D. Schooss, M.N. Blom, J.H. Parks, et al., *The structures of Ag55+ and Ag55- : trapped ion electron diffraction and density functional theory.* Nano Lett, 2005. **5**(10): p. 1972-7.

[229] M. Maier-Borst, D.B. Cameron, M. Rokni, et al., *Electron diffraction of trapped cluster ions.* Physical Review A, 1999. **59**(5): p. R3162-R3165.

[230] T. Soeda, S. Matsumura, J. Hayata, et al., *Quantitative electron diffraction study of cation configuration and irradiation induced displacement in magnesium aluminate spinel crystals.* Journal of Electron Microscopy, 1999. **48**(5): p. 531-536.

[231] J. Yang, M. Guehr, T. Vecchione, et al., *Femtosecond gas phase electron diffraction with MeV electrons.* Faraday Discussions, 2016. **194**(0): p. 563-581.

[232] S. Shibata, H. Sekiyama, K. Tachikawa, et al., *Chemical bonding effect in electron scattering by gaseous molecules.* Journal of Molecular Structure, 2002. **641**(1): p. 1-6.

[233] Y. Malakar, W.L. Pearson, M. Zohrabi, et al., *Time-resolved imaging of bound and dissociating nuclear wave packets in strong-field ionized iodomethane.* Physical Chemistry Chemical Physics, 2019. **21**(26): p. 14090-14102.

[234] J. Ullrich, R. Moshammer, A. Dorn, et al., *Recoil-ion and electron momentum spectroscopy: reaction-microscopes.* Reports on Progress in Physics, 2003. **66**(9): p. 1463-1545.

[235]   J. Ullrich, R. Moshammer, R. Dörner, et al., *Recoil-ion momentum spectroscopy.* Journal of Physics B: Atomic, Molecular and Optical Physics, 1997. **30**(13): p. 2917-2974.

[236]   N. Zotev, A. Moreno Carrascosa, M. Simmermacher, et al., *Excited Electronic States in Total Isotropic Scattering from Molecules.* J Chem Theory Comput, 2020. **16**(4): p. 2594-2605.

[237]   J. Wang and V.H. Smith, *Evaluation of cross sections for X-ray and high-energy electron scattering from molecular systems.* International Journal of Quantum Chemistry, 1994. **52**(5): p. 1145-1151.

[238]   T. Northey, A. Moreno Carrascosa, S. Schafer, et al., *Elastic X-ray scattering from state-selected molecules.* J Chem Phys, 2016. **145**(15): p. 154304.

[239]   H. Yong, N. Zotev, J.M. Ruddock, et al., *Observation of the molecular response to light upon photoexcitation.* Nat Commun, 2020. **11**(1): p. 2157.

[240]   H. Yong, A. Moreno Carrascosa, L. Ma, et al., *Determination of excited state molecular structures from time-resolved gas-phase X-ray scattering.* Faraday Discuss, 2021. **228**(0): p. 104-122.

[241]   A.M.C. Haiwang Yong, Lingyu Ma, Brian Stankus, Michael P. Minitti, Adam Kirrander, Peter M. Weber,, *Determination of Excited State Molecular Structures from Time-Resolved Gas-Phase X-Ray Scattering.* Faraday Discussions (submitted).

[242]   H. Yong, J.M. Ruddock, B. Stankus, et al., *Scattering off molecules far from equilibrium.* The Journal of Chemical Physics, 2019. **151**(8): p. 084301.

[243] H.-J. Werner, P.J. Knowles, G. Knizia, et al., *Molpro: a general-purpose quantum chemistry program package.* Wiley Interdisciplinary Reviews: Computational Molecular Science, 2012. **2**(2): p. 242-253.

[244] M. Centurion, P. Reckenthaeler, S.A. Trushin, et al., *Picosecond electron deflectometry of optical-field ionized plasmas.* Nature Photonics, 2008. **2**(5): p. 315-318.

[245] M. Centurion, P. Reckenthaeler, F. Krausz, et al., *Picosecond imaging of low-density plasmas by electron deflectometry.* Optics Letters, 2009. **34**(4): p. 539-41.

[246] J.S. Baskin and A.H. Zewail, *Oriented ensembles in ultrafast electron diffraction.* Chemphyschem, 2006. **7**(7): p. 1562-74.

[247] J. Yang, X. Zhu, J.P. F. Nunes, et al., *Simultaneous observation of nuclear and electronic dynamics by ultrafast electron diffraction.* Science, 2020. **368**(6493): p. 885.

[248] M. Centurion, *Ultrafast imaging of isolated molecules with electron diffraction.* Journal of Physics B Atomic Molecular & Optical Physics, 2016. **49**(6).

[249] Y.C. Cheng and G.R. Fleming, *Dynamics of light harvesting in photosynthesis.* Annu Rev Phys Chem, 2009. **60**: p. 241-62.

[250] D. Polli, P. Altoè, O. Weingart, et al., *Conical intersection dynamics of the primary photoisomerization event in vision.* Nature, 2010. **467**: p. 440.

[251] W.J. Schreier, T.E. Schrader, F.O. Koller, et al., *Thymine dimerization in DNA is an ultrafast photoreaction.* Science, 2007. **315**(5812): p. 625-9.

[252] T. Wolf, F. Holzmeier, I. Wagner, et al., *Observing Femtosecond Fragmentation Using Ultrafast X-ray-Induced Auger Spectra.* Applied Sciences, 2017. **7**(7): p. 681.

[253] E. Havinga and J.L.M.A. Schlatmann, *Remarks on the specificities of the photochemical and thermal transformations in the vitamin D field.* Tetrahedron, 1961. **16**(1): p. 146-152.

[254] A.H. Zewail, *Femtochemistry: Atomic-scale dynamics of the chemical bond using ultrafast lasers (Nobel lecture).* Angewandte Chemie - International Edition, 2000. **39**(15): p. 2586-2631.

[255] A. Stolow, A.E. Bragg, and D.M. Neumark, *Femtosecond time-resolved photoelectron spectroscopy.* Chem Rev, 2004. **104**(4): p. 1719-57.

[256] F. Krausz and M. Ivanov, *Attosecond physics.* Reviews of Modern Physics, 2009. **81**(1): p. 163-234.

[257] J.M. Budarz, M.P. Minitti, D.V. Cofer-Shabica, et al., *Observation of femtosecond molecular dynamics via pump–probe gas phase x-ray scattering.* Journal of Physics B: Atomic, Molecular and Optical Physics, 2016. **49**(3): p. 034001.

[258] M. Dzvonik, S. Yang, and R. Bersohn, *Photodissociation of molecular beams of aryl halides.* The Journal of Chemical Physics, 1974. **61**(11): p. 4408-4421.

[259] R.A. Durie, T. Iredale, and J.M.S. Jarvie, *Absorption spectra of substances containing the carbon-iodine bond. Part I.* Journal of the Chemical Society (Resumed), 1950: p. 1181-1184.

[260] G.N.A. Van Veen, T. Baller, A.E. De Vries, et al., *Photofragmentation of CF3I in the A band.* Chemical Physics, 1985. **93**(2): p. 277-291.

[261] P.Y. Cheng, D. Zhong, and A.H. Zewail, *Kinetic-energy, femtosecond resolved reaction dynamics. Modes of dissociation (in iodobenzene) from time-velocity correlations.* Chemical Physics Letters, 1995. **237**(5-6): p. 399-405.

[262] A.G. Sage, T.A. Oliver, D. Murdock, et al., *nsigma* and pisigma* excited states in aryl halide photochemistry: a comprehensive study of the UV photodissociation dynamics of iodobenzene.* Phys Chem Chem Phys, 2011. **13**(18): p. 8075-93.

[263] G. Hancock, A. Hutchinson, R. Peverall, et al., *266 nm photolysis of CF3I and C2F5I studied by diode laser gain FM spectroscopy.* Phys Chem Chem Phys, 2007. **9**(18): p. 2234-9.

[264] X.P. Zhang, W.B. Lee, and K.C. Lin, *Nonadiabatic transition in the A-band photodissociation of ethyl iodide from 294 to 308 nm by using velocity imaging detection.* J Phys Chem A, 2009. **113**(1): p. 35-9.

[265] R.S. Mulliken, *Intensities in Molecular Electronic Spectra X. Calculations on Mixed-Halogen, Hydrogen Halide, Alkyl Halide, and Hydroxyl Spectra.* The Journal of Chemical Physics, 1940. **8**(5): p. 382-395.

[266] J.A. Griffiths, K.-W. Jung, and M.A. El-Sayed, *Fluorine Substitution Effects on the Photodissociation Dynamics of Iodobenzene at 304 nm.* The Journal of Physical Chemistry, 1996. **100**(19): p. 7989-7996.

[267] M.N. Ashfold, G.A. King, D. Murdock, et al., *Pi sigma* excited states in molecular photochemistry.* Phys Chem Chem Phys, 2010. **12**(6): p. 1218-38.

[268] W.G. Roeterdink and M.H.M. Janssen, *Femtosecond velocity map imaging of dissociative ionization dynamics in CF3IPresented at the Stereodynamics 2000 Conference on Dynamics and Stereodynamics of Chemical Reactions, El Escorial, Madrid, December 1–5, 2000.* Physical Chemistry Chemical Physics, 2002. **4**(4): p. 601-612.

[269] Y.S. Kim, W.K. Kang, and K.H. Jung, *State-selective photofragment imaging of iodine atoms via photodissociation of CF3I at 277 nm.* The Journal of Chemical Physics, 1996. **105**(2): p. 551-557.

[270] F. Aguirre and S.T. Pratt, *Velocity map imaging of the photodissociation of CF3I: Vibrational energy dependence of the recoil anisotropy.* The Journal of Chemical Physics, 2003. **118**(3): p. 1175-1183.

[271] D.C. Clary, *A theory for the photodissociation of polyatomic molecules, with application to CF3I.* The Journal of Chemical Physics, 1986. **84**(8): p. 4288-4298.

[272] K. Pande, C.D. Hutchison, G. Groenhof, et al., *Femtosecond structural dynamics drives the trans/cis isomerization in photoactive yellow protein.* Science, 2016. **352**(6286): p. 725-9.

[273] P. Felder, *The influence of the molecular beam temperature on the photodissociation of CF3I at 308 nm.* Chemical Physics Letters, 1992. **197**(4-5): p. 425-432.

[274] P. Felder, *Photodissociation of CF3I at 248 nm: Kinetic energy dependence of the recoil anisotropy.* Chemical Physics, 1991. **155**(3): p. 435-445.

[275] P. Felder, *Photodissociation of CF3I AT 248 nm: Internal energy distribution of the CF3 fragments.* Chemical Physics, 1990. **143**(1): p. 141-150.

[276] M.D. Person, P.W. Kash, and L.J. Butler, *The influence of parent bending motion on branching at a conical intersection in the photodissociation of CX3I (X=H,D,F).* The Journal of Chemical Physics, 1991. **94**(4): p. 2557-2563.

[277] H.J. Hwang and M.A. El-Sayed, *Photodissociation of trifluoroiodomethane at 304 nm: effects of photon energy and curve crossing on the internal excitation of trifluoromethyl.* The Journal of Physical Chemistry, 1992. **96**(22): p. 8728-8735.

[278] A. Furlan, T. Gejo, and J.R. Huber, *Probing Curve Crossing by Wavelength-Dependent Recoil Anisotropy: The Photodissociation of CF3I at 275−303 nm Studied by Photofragment Translational Spectroscopy.* The Journal of Physical Chemistry, 1996. **100**(19): p. 7956-7961.

[279] K. Han and G. He, *Photochemistry of aryl halides: Photodissociation dynamics.* Journal of Photochemistry and Photobiology C: Photochemistry Reviews, 2007. **8**(2): p. 55-66.

[280] L. Drescher, M.C. Galbraith, G. Reitsma, et al., *Communication: XUV transient absorption spectroscopy of iodomethane and iodobenzene photodissociation.* J Chem Phys, 2016. **145**(1): p. 011101.

[281] G. Karras, E. Hertz, F. Billard, et al., *Orientation and Alignment Echoes.* Physical review letters, 2015. **114**(15): p. 153601.

[282] G. Karras, E. Hertz, F. Billard, et al., *Experimental observation of fractional echoes.* Physical Review A, 2016. **94**(3): p. 033404.

[283] K. Lin, P. Lu, J. Ma, et al., *Echoes in Space and Time.* Physical Review X, 2016. **6**(4).